

NEUTRAL-HYDROGEN OBSERVATIONS OF SPIRAL AND IRREGULAR GALAXIES

Michael Reakes - Darwin College Cambridge

Summary

This thesis describes hydrogen-line observations using the Cambridge Half-Mile telescope. The initial chapters describe observations of two nearby galaxies of late spiral type, namely M33 and NGC 2403. The severe warping of the HI layer in the outer parts of M33 was clearly seen, and the origin of this phenomenon is discussed. Sensitive low-resolution maps reveal only a very slight warp in NGC 2403, while maps at the full resolution allowed the dynamical parameters to be investigated and showed several features associated with spiral structure.

The later chapters describe observations of irregular galaxies, many belonging to the class IrII which was of particular interest. NGC 1569, a dwarf irregular galaxy, has been the subject of interest due to its prominent H α filaments. Observations reveal that the overall HI distribution to be that expected of a disc in normal rotation, although there are several unusual features. Arp 205 consists of an IrII galaxy (NGC 3448) and a dwarf companion less than one diameter away. A model for the HI dynamics is presented which suggests that there has been a planar tidal interaction between these two galaxies. NGC 2805, NGC 2814, NGC 2820 and IC 2458 form a compact group of galaxies of which NGC 2805 is the brightest. HI was detected in all except NGC 2814, and there is good evidence for a HI bridge linking NGC 2820 and IC 2458. It is postulated that the HI bridge and disturbed nature of this group are the result of a gravitational interaction. Less detailed observations of other irregular galaxies are also presented in this thesis, including NGC 3432 and NGC 3310.

NEUTRAL HYDROGEN OBSERVATIONS OF SPIRAL AND IRREGULAR GALAXIES

Michael Reakes

Darwin College Cambridge

A dissertation submitted for the degree
of Doctor of Philosophy in the University
of Cambridge

September 1979

To Mary

The observations described in this dissertation were made at the Mullard Radio Astronomy Observatory, and the data reduced and analysed at the Cavendish Laboratory. The work was carried out between October 1975 and November 1978.

Most of the observations are of neutral hydrogen made with the Half-Mile Telescope. I have been closely involved in the day-to-day operation of the telescope, and with the reduction of the observations, and I have also improved many of the computer programs used in the reduction and display of the data. The work would not have been possible without the assistance of many people, and I would like to thank:

Mr Peter Warner and his assistants, notably Mrs Elizabeth Waldram & Dr Tim Pearson, who originated and developed many of the computer programs used to reduce and display telescope data.

Dr Darrell Emerson & Dr Anthony Winter who originated several programs concerned with the analysis of HI maps.

Ms Sally Hales, Ms Elizabeth Pimm-Smith, Ms Alice Hurley and Ms Stella Laffoley who assisted with much of the initial data reduction.

Irena Tabecka for producing some of the line drawings, and Mr Andrews for some of the photography.

Mr Don Rolph who maintained the mechanical parts of the telescope, Mr Roger Boysen who maintained the electronics and Dr Donald Wilson who originated and maintained the digital spectrometer.

The Cambridge University Computing Service for use of the IBM 370/165 computer.

I would especially like to thank my supervisor, Dr John Shakeshaft, and also Mr Peter Warner and Dr John Baldwin for their guidance throughout the three years.

Except where specifically stated in the text the work presented in this dissertation is my own, and has not been carried out in collaboration with anyone else. This dissertation contains less than 60 000 words (including footnotes, references and appendices), and has not or is not being submitted for any other degree or diploma or other qualification at any other university.

The work presented in Chapters 2, 6 and 7 has been published in Monthly Notices of the Royal astronomical Society (Reakes & Newton 1978; Reakes 1979A; Reakes 1979B).

Michael Reakes

September 1979

CONTENTSCHAPTER 1 INTRODUCTION

1 BACKGROUND AND AIMS OF THE INVESTIGATION	1-1
1.1 Classification of galaxies	1-2
1.2 Integral properties of galaxies	1-4
1.3 Irregular galaxies of type IrI & IrII	1-7
1.4 Warping of normal galaxies	1-8
1.5 Gravitational interactions	1-10
1.6 Aims of the observations	1-12
2 OBSERVING PROCEDURES & DATA REDUCTION	1-14
2.1 The Half-Mile telescope	1-15
2.2 Broad-band continuum emission	1-21
2.3 Hydrogen-line emission	1-23
2.4 Analysis	1-31

CHAPTER 2 THE Sc GALAXY M33

1 INTRODUCTION	2-1
2 OBSERVATIONS	2-2
3 THE NEUTRAL HYDROGEN DISTRIBUTION	2-5
3.1 The large-scale structure	2-5
3.2 Asymmetries	2-11
4 THE RADIAL VELOCITY FIELD	2-16
4.1 Observations	2-16
4.2 Geometry	2-20
5 DISCUSSION	2-26
6 CONCLUSIONS	2-29

CHAPTER 3 THE Scd GALAXY NGC 2403

1 INTRODUCTION	3-1
2 OBSERVATIONS	3-6
3 RESULTS AND ANALYSIS	3-19
3.1 The total HI mass	3-19
3.2 The HI distribution at low resolution	3-19
3.3 The HI distribution at moderate resolution	3-25
3.4 The HI distribution at high resolution	3-27
3.5 Radio Continuum	3-40
3.6 The velocity field	3-43
4 CONCLUSIONS	3-60

CHAPTER 4 THE Im GALAXY NGC 1569 (Arp 210)

1 INTRODUCTION	4-1
2 OBSERVATIONS	4-7
3 RESULTS AND ANALYSIS	4-11
3.1 Radio Continuum	4-11
3.2 The total HI mass	4-11
3.3 Unusual features seen in the channel maps	4-16
3.4 The integrated HI distribution	4-17
3.5 The velocity field	4-19
3.6 The rotation curve	4-19
3.7 Velocity dispersion	4-23
3.8 Total mass	4-23
3.9 Asymmetries in the velocity field	4-23
3.10 Comparison of the H α and HI velocity fields	4-24
4 DISCUSSION	4-25
5 CONCLUSIONS	4-29

CHAPTER 5 IrII GALAXIES

1 A SAMPLE OF ALLEGED IrII GALAXIES	5-1
2 OBSERVATIONS	5-3
2.1 NGC 51	5-3
2.2 NGC 972	5-5
2.3 UGC 02172	5-5
2.4 IC 334	5-6
2.5 NGC 2968	5-6
2.6 NGC 3067	5-7
2.7 NGC 5273	5-7
3 GENERAL PROPERTIES	5-8
3.1 Spectral type and colour	5-8
3.2 Radio Continuum	5-10
3.3 Hydrogen mass/Luminosity ratio	5-10
4 THEORIES	5-13
4.1 A homogeneous class?	5-13
4.2 A tidal origin for all IrIIs?	5-14
5 A SEARCH FOR COMPANIONS	5-15
6 SUMMARY	5-19

CHAPTER 6 THE IrII GALAXY NGC 3448 (Arp 205)

1 INTRODUCTION	6-1
2 OBSERVATIONS	6-3
3 RESULTS	6-5
3.1 The overall HI distribution	6-5
3.2 UGC 6016	6-13
3.3 NGC 3448	6-17
4 ANALYSIS	6-21
4.1 NGC 3448 as a double interacting system	6-21
4.2 Tidal interaction theories	6-22
5 CONCLUSIONS	6-26

CHAPTER 7 THE GROUP OF GALAXIES NGC 2805, NGC 2814, NGC 2820
and IC 2458

1 INTRODUCTION	7-1
2 OBSERVATIONS	7-5
3 RESULTS	7-7
3.1 The HI distribution	7-7
3.2 Radio Continuum	7-16
4 DISCUSSION	7-18
4.1 Dynamics	7-18
4.2 Tidal interaction hypothesis	7-18
5 CONCLUSIONS	7-22

CHAPTER 8 THE PECULIAR GALAXIES NGC 3310 (Arp 217) AND NGC 3432
(Arp 206)

1 INTRODUCTION	8-1
2 OBSERVATIONS	8-7
3 RESULTS AND ANALYSIS	8-16
3.1 NGC 3310	8-16
3.2 NGC 3432	8-23
4 CONCLUSIONS	8-30

CHAPTER 9 SUMMARY 9-1

APPENDIX COMPUTER SIMULATIONS OF GRAVITATIONAL
INTERACTIONS BETWEEN GALAXIES A-1

REFERENCES R-1

CHAPTER 1INTRODUCTION1 BACKGROUND AND AIMS OF THE INVESTIGATION

This thesis describes hydrogen-line observations of galaxies using the Cambridge Half-Mile telescope. The aims of this Chapter are twofold:

- (1) To provide a background to, and give the aims of, the observations.
- (2) To describe the operation and characteristics of the radio telescope, together with the methods of data reduction and analysis.

1.1 Classification of galaxies

The first step in the development of most sciences is a classification of the objects under study. If the classification is useful it may lead to hypotheses and predictions which, if verified, help to form the theoretical foundations of a subject.

The most widely used classification scheme for galaxies is that due to Hubble, and is based on the images obtained by direct photography. The two basic classes of galaxies are the ellipticals and the disk galaxies. Elliptical galaxies are denoted E0-E7, depending upon their apparent axial ratios. Disk galaxies generally possess a nuclear bulge, which is similar in many respects to ellipticals, and a disk in which spiral structure can usually be seen. Disk galaxies without spiral structure are classified as lenticulars (denoted S0), the remaining ones are called spirals.

Spiral galaxies can be subdivided into 'Hubble types' Sa, Sb, Sc & Sd according to:

- (1) The size of the nuclear bulge relative to the disk.
- (2) The openness of the spiral arms.
- (3) The degree of resolution into stars and HII regions of the arms and/or disk.

A 'revised' version of Hubble's original classification scheme is illustrated in Fig. 1.0 and incorporates the additional distinctions of 'ordinary' and 'barred' spirals (SA & SB), and 'ring' and 'spiral' varieties (r & s). As a matter of convenience and history the terms 'early' and 'late' are used to refer to the two ends of the sequence. Thus S0 galaxies are said to be earlier than Sc galaxies, and Sd galaxies are said to be later than Sc galaxies. These terms should not now be regarded as having chronological significance.

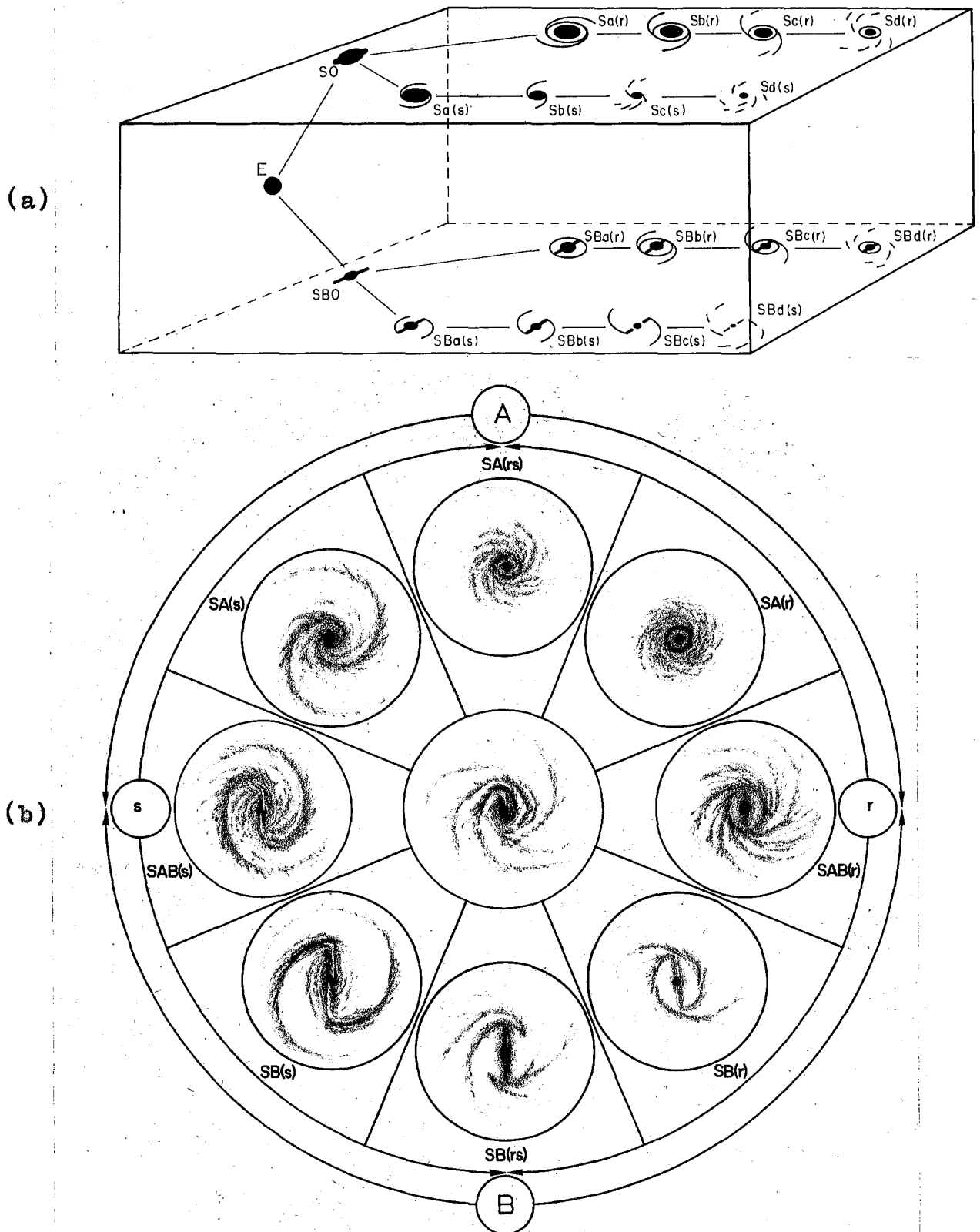


Figure 1.0 (a) Illustration of the Hubble sequence of galaxies in its revised form, taken from Sandage (1975). Here the ordinary and barred spirals are separated onto opposite sides of a box. Within each family, a separation is made into the *r* and *s* strains, depending on whether the arms start from a ring or from the nucleus. (b) A cross-section near the region of the *Sb* and *SBb* spirals, showing the manner in which the transition cases between ordinary (A) and barred (B) families, and the (*r*) and (*s*) strains can be accommodated (from de Vaucouleurs & de Vaucouleurs 1964).

1.2 Integral properties of galaxies

Three main integral properties of a galaxy which can be assigned quantitative values are:

- (1) The total mass of hydrogen, M_H , expressed in units of Solar mass (M_\odot). $M_H \propto \text{distance}^2$.
- (2) The total mass M_T , again in units of M_\odot . $M_T \propto \text{distance}^1$.
- (3) The luminosity L , in units of Solar luminosity (L_\odot).
 $L \propto \text{distance}^2$.

The exact definitions and means of deriving these quantities are explained later, but need not delay us here.

In a statistical study of several hundred galaxies of many different morphological types, it has been found (Roberts 1969; Balkowski 1973) that the parameters M_H/L and M_H/M_T correlate well with Hubble type (Fig. 1.1 and Table 1.1). This correlation shows that Hubble type reflects fundamental characteristics which are important in the formation of the galaxy. However, the physical significance of the classification scheme is still poorly understood.

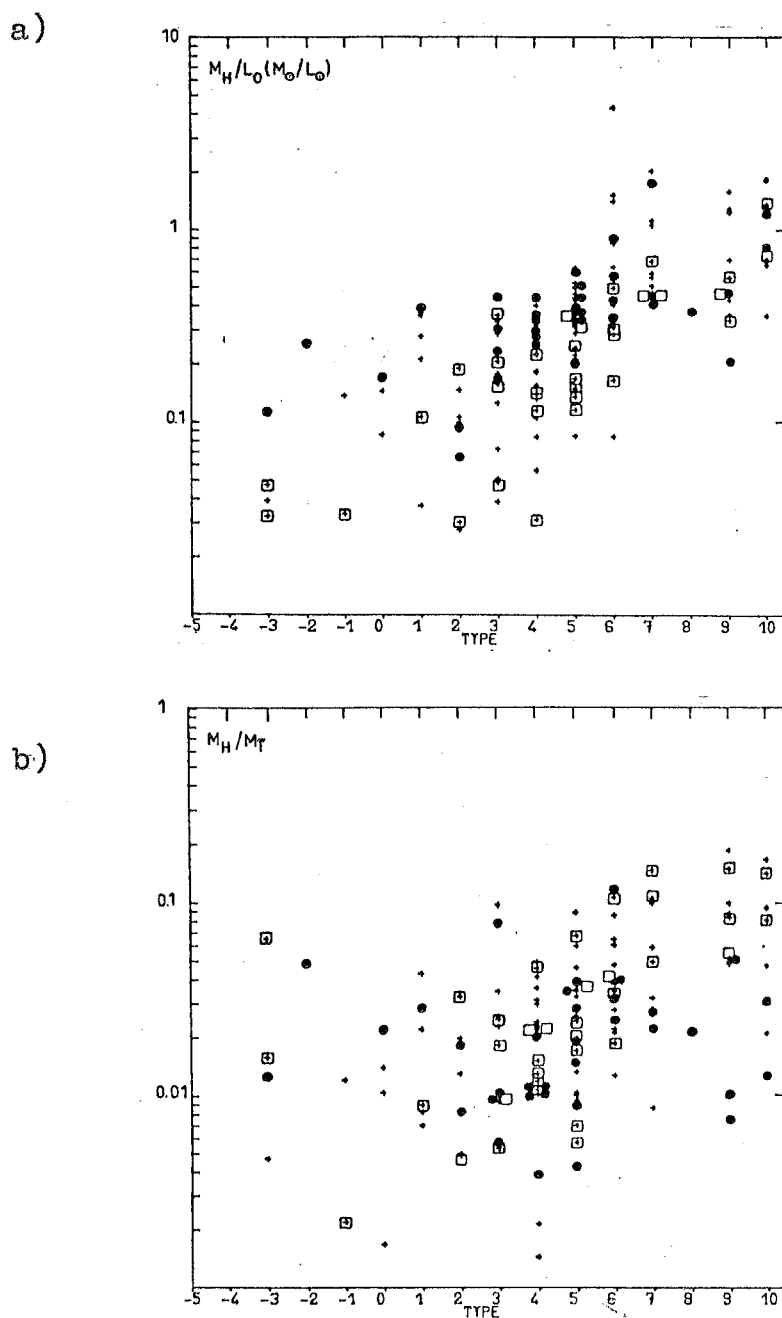


Fig. 1.1 (a) Hydrogen mass to luminosity ratio M_H/L , in solar units, as a function of morphological type T, and (b) hydrogen mass to (indicative) total mass M_H/M_T as a function of T, taken from Balkowski 1973. The symbols refer to the luminosity but are not used here. The revised classification corresponding to a given value of T is given in Table 1.1.

T	revised classification	M_H/L	M_H/M_T
-3 -2 -1 0	E SO IrII	0.079	0.010
1 2	Sa Sab	0.105	0.012
3	Sb	0.161	0.014
4	Sbc	0.178	0.014
5	Sc	0.294	0.017
6	Scd	0.530	0.041
7 8	Sd	0.673	0.038
9	Sd IrI	0.617	0.055
10	IrI	0.942	0.062

Table 1.1 Mean values of the integral parameters M_H/L and M_H/M_T (solar units) as a function of morphological type (from Balkowski 1973).

1.3 Irregular galaxies of type IrI and IrII

Many of the galaxies whose observations are described in this thesis are of an irregular type, and particularly of the sub-type IrII. In this section definitions for the two irregular categories, IrI and IrII, are provided. A detailed discussion of IrII galaxies can be found in Chapter 5.

Irregular galaxies are those which do not fit into the Hubble classification scheme. The distinction between IrI and IrII galaxies was first made by Holmberg (1958) in a study of the integrated colours of galaxies. He defines IrI galaxies as those with a predominant stellar population of type I, and IrII as those with (presumably) a stellar population of type II. The distinction was made primarily in order to preserve continuity of colour across his classification scheme:

E IrII SO Sa Sb Sc IrI

red ←—————→ blue

It also had the effect of reducing the colour dispersion amongst the irregular galaxies.

There were only six objects in Holmberg's original list of IrII galaxies (NGC 520, NGC 2968, M82, NGC 3077, NGC 5195 = M51B, and NGC 5363). All these galaxies have similar optical characteristics (as well as colour) which distinguish them from the IrI category. The properties of the two classes are summarized by Sandage (1961):

IrI galaxies are highly resolved into luminous O and B stars and HII regions. There is no circular symmetry

about a rotation axis. This group is, in effect, a continuation of late Sc galaxies.

IrII galaxies also show no rotational symmetry. The photographic images are smooth in texture and show no signs of resolution into stars. They are often crossed by irregular dust lanes and patches.

The photographs of M81 and M82 in Sandage (1961) illustrate that IrII galaxies are not resolved into stars, since both galaxies are at about the same distance, and although stars are resolved in M81, none are seen in M82.

The first edition of the Reference Catalog of Bright Galaxies (de Vaucouleurs & de Vaucouleurs 1964, RC1) used a subdivision of irregular galaxies similar to that of Holmberg. In the RC1 scheme Im or Magellanic Irregular is equivalent to IrI, and IO (non-Magellanic Irregular) is equivalent to IrII. There are twelve IO galaxies listed in RC1.

1.4 Warping of Normal Galaxies

External galaxies with warped optical discs have been known for a long time. Well-known examples are NGC 3190, 4762, 5866 and the 'Integral-Sign' galaxy (Table 1.2). However, these seemed to have been regarded as rare cases, probably resulting from gravitational interactions (Section 1.5). Our Galaxy is also known to possess a similar large-scale bending in the outer parts of the gas layer (Burke 1957; Kerr 1957). A number of explanations have been proposed to explain this warp, the most favoured being a recent tidal interaction with the Large Magellanic Cloud (Hunter & Toomre 1969).

In recent years 21-cm studies of external galaxies

Table 1.2 Warped Galaxies

<u>Name</u>	<u>Warp Inferred from</u>	<u>References</u>
The Galaxy	HI	Burke 1957 Kerr 1957
NGC 4762	Optical photograph	* Sandage 1961
NGC 5866	do.	* do.
NGC 3190=Arp 316	do.	* Arp 1966
MCG 12-7-28= "Integral sign"	do.	* Richer <u>et al.</u> 1972
M83	HI kinematics	Rogstad <u>et al.</u> 1974
M33	do.	Rogstad <u>et al.</u> 1976 see Chapter 2
NGC 5907	HI distribution	* Sancisi 1976
NGC 4565	do.	* do.
NGC 4244	do.	* do.
NGC 4631	do.	* do.
M31	Optical photograph HI kinematics	Baade 1963 Newton & Emerson 1977
IC 342	HI kinematics	Newton 1978
NGC 2841	do.	Bosma 1978
NGC 5055	do.	do.
NGC 7331	do.	do.

notes: * denotes that the galaxy is viewed nearly edge-on.

Not all references are listed.

have suggested that the neutral hydrogen layers of many apparently normal galaxies may be likewise warped. Where the galaxies are nearly edge-on (NGC 5907, NGC 4565, NGC 4244 & NGC 4631) the warping can be seen directly from maps of integrated HI. However, in the majority of cases the warps are inferred from the kinematics of the HI. The usual model is a set of concentric rings whose position angle and inclination change with radius; it was first suggested by Rogstad *et al.* (1974) for M83. This type of model has now been applied to explain the kinematics observed in M33, M31, NGC 2841, NGC 5055, NGC 7331 & IC 342. In M31 the HI warp is of small magnitude and a slight optical warp is also evident.

Due to problems of resolution and sensitivity, HI warps are very difficult to detect in distant galaxies (≈ 5 Mpc). Since warps in nearby spiral galaxies seem to be a common phenomenon, it may be that all spiral galaxies have warps. Although some warped galaxies have companions which might produce the warps by gravitational interactions, others do not, and the cause of these perturbations is not understood.

1.5 Gravitational Interactions

As far back as 1940 it was suggested that the bridges and tails seen in photographs of peculiar galaxies were the result of gravitational interaction during previous close encounters of galaxies (Holmberg 1940, 1941; Zwicky 1953, 1956). For many years this interpretation did not gain wide acceptance, a notable

critic being Vorontsov-Velyaminov (1961). When fast computers made simulations of galaxy encounters possible (Wright 1972; Clutton-Brock 1972; Toomre & Toomre 1972; Eneev et al. 1973) it became clear that the original ideas of Holmberg and Zwicky were basically correct. These simulations showed that gravity alone can indeed produce bridges and tails during a close encounter of two galaxies, providing the relative velocity is sufficiently low. Although the computer models are relatively simple, remarkably good agreement with the observations has been obtained in several cases, for example:

M81 and NGC 3077	Cottrell 1976 van der Hulst 1977
NGC 4038 and 4039 (The Antennae)	Toomre & Toomre 1972 van der Hulst 1977
NGC 4631 and 4656	Winter 1975 Weliachew, Sancisi & Guelin 1978 Coombes 1978

The distortions in these systems are asymmetric and are distinguished from the symmetric warps seen in relatively normal galaxies (Section 1.4). A tidal hypothesis does not seem to apply in all the cases of symmetrical warps.

The observations of irregular galaxies presented in this thesis show several cases where the HI is severely distorted in an asymmetrical manner, and in these cases a tidal interaction involving the most obvious companion galaxy can explain many observed features of the distortion. The methods used to simulate galaxy interactions, and a description of the types of collision that tend to produce bridges and tails are briefly summarised in the Appendix.

1.6 Aims of the observations

Chapters 2 and 3 describe observations of two nearby galaxies of late spiral type, namely M33 and NGC 2403. Chapters 4 to 8 describe observations of galaxies that are of irregular type or contain peculiar optical features.

M33 is a good example for the further study of the warping phenomenon because it is strongly warped, has a large angular size, and its position in space relative to other nearby galaxies is well known. In previous aperture synthesis observations of M33, emission from the outer regions has been seriously attenuated by the primary response of the antennas. By combining three surveys each with high sensitivity and velocity resolution, it has been possible to make for the first time a detailed study of the neutral hydrogen at large distances from the nucleus of M33.

NGC 2403 is a relatively nearby galaxy of type Scd. In optical photographs it bears a strong resemblance to M33. Sensitive neutral hydrogen observations were made to investigate whether NGC 2403 possesses a large-scale warp similar to that seen in M33. This information is of importance in finding out why many spiral galaxies are warped. High-resolution observations were also made with the aim of resolving the HI spiral structure, so that the density wave theory could be further tested.

The remainder of the observations are of galaxies of irregular or peculiar type. In every case no previous aperture-synthesis observations of HI had been published at the time the observations were planned. Several of the

systems which appear to be very disturbed optically also show a disturbed HI structure. The velocity information gained from such observations enables simple gravitational-interaction hypotheses to be formulated. Many of the irregular galaxies belong to the sub-class IrII. Many data are lacking on these extremely puzzling objects. Their origin is not clearly understood, but it has been suggested that they may all arise as the result of gravitational interactions. One of the prime objectives was to obtain as many 21-cm data as possible on IrII galaxies, with a view to understanding their origins better.

2 OBSERVING PROCEDURES AND DATA REDUCTION

Although hydrogen-line observations using the Half-Mile telescope are in principle straightforward, they are, in practice, very time-consuming. The telescope itself is a complex piece of equipment and great care must be exercised during its operation to ensure that it is properly calibrated and operating satisfactorily. Mechanical or electrical faults can become apparent during the course of observations and often require observations to be delayed or repeated. High winds are also a cause of delay, preventing the dishes from safely being moved along the railtrack, and thunderstorms can cause power supplies to 'trip out' requiring the observations to be repeated. During the last three years I have been allocated a total of 170 days of observing time, of which approximately half have been spent on the sources, the remainder being on calibration and time lost due to faults.

The data reduction for line observations involves many stages and usually takes more time than the observations themselves. Although all the required computer programs exist, many are still in a state of development and have needed modifications by the author on several occasions.

The remainder of this chapter is devoted to a brief description of the telescope, an outline of the data reduction, and a summary of the formulae used to analyse the final maps. Much of this material is not original and can be found elsewhere, but includes

some useful information for future observers of line emission with the Half-Mile telescope which is not documented elsewhere. A few observations were made using the One-Mile or 5-km telescopes which are not described here, but they operate on essentially the same principles as the Half-Mile telescope.

2.1 The Half-Mile Telescope

The Half-Mile telescope (Plate 1.1) was built in the late 1960s and originally comprised only two dishes (Baldwin et al. 1970). Later two more dishes were added, the receiving system was updated, and a digital cross-correlation spectrometer installed in place of the original device, which used a delay cable (Baldwin et al. 1971; Winter 1975).

The telescope operates at a wavelength of 21 cm and can simultaneously record observations both of continuum radiation over a 10-MHz bandwidth and of line radiation using the digital spectrometer. The telescope uses the principle of Earth rotation aperture synthesis (Elsmore, Kenderdine & Ryle 1966). Each of the four parabolic dishes is 9 m (30 feet) in diameter, and they normally track a source between hour angles $(6^{\text{h}} \text{ to } 18^{\text{h}})$. The declination range is from $\delta \sim 18^{\circ}$ to $\delta \sim 90^{\circ}$, and is set by hand. Two of the dishes (C and D in Fig. 1.2) are fixed 60 ft apart at the west end of an east-west rail track 0.5 miles long, while the other two (A and B) are held 120 ft apart by a tie-bar, but can be moved along the railtrack up to a maximum (BC) spacing of 2400 ft, corresponding to a resolution of 47 arcsec at $\lambda = 21$ cm. Phase-switching receivers correlate the

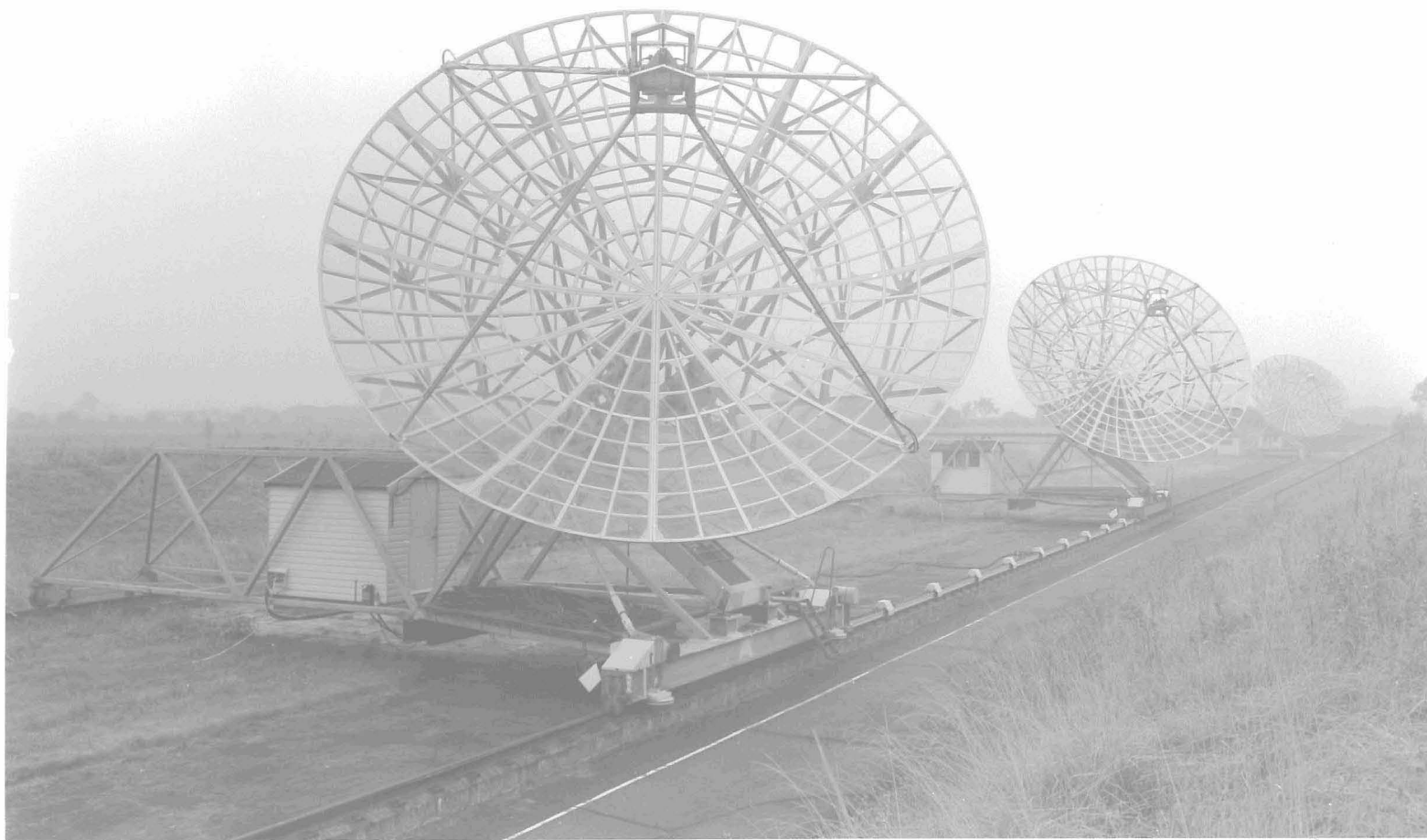


Plate 1.1. The Cambridge Half-Mile Telescope.

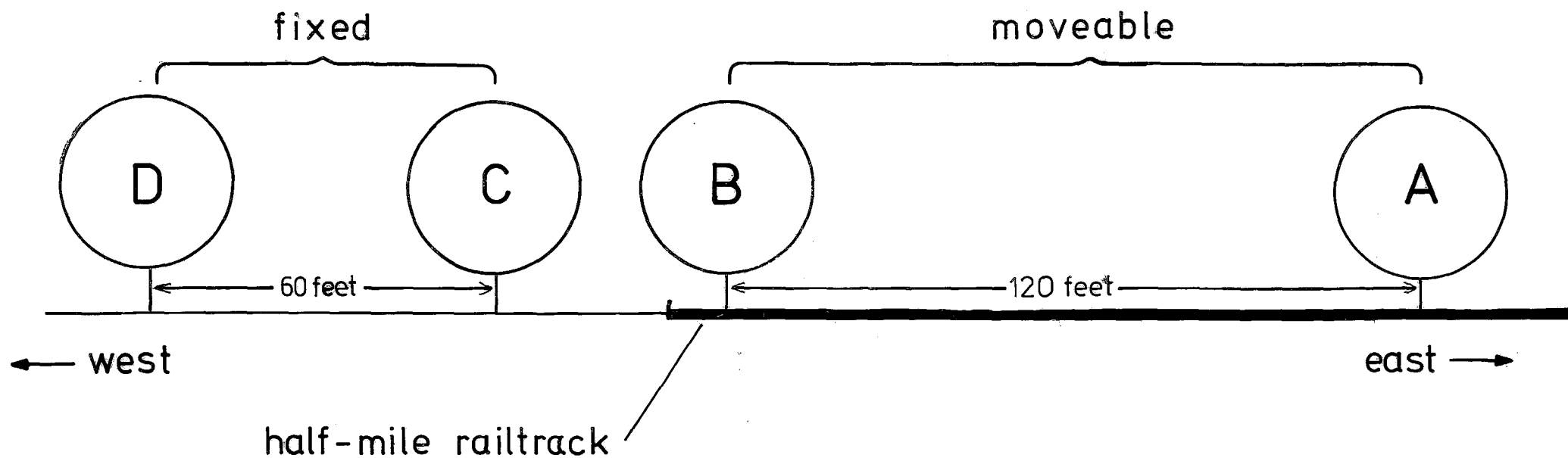


Fig. 1.2 Configuration of the Cambridge Half-Mile Telescope

signals entering a selected pair of dishes to provide the amplitude and relative phase (A and ϕ) data which are recorded during the 12^{h} observing period. These data provide one ring of the complete u - v or aperture plane. In fact, the signal in each of the moveable aerials is correlated with that in each of the fixed aerials, thus providing four equally-spaced rings in the aperture plane after one 12^{h} observing period. The normal observing program is shown in Table 1.3, so that after three 12^{h} periods of observing the source, a fully filled aperture plane from 40 ft to 260 ft has been synthesised (with rings every $2/3$ of the dish diameter). After six periods of observation the aperture plane is fully filled from 40 ft to 500 ft, and so on.

The system needs to be calibrated. This is done by observing a bright source which is unresolved at the maximum resolution used in the survey, and whose flux density is known by other means. Because the path lengths from each receiver to the two dishes are unknown, it is also necessary to calibrate the relative phase. An accurate position for the calibrator (often obtained from the 5-km telescope) is therefore essential. For line work (Section 2.3) the relative amplitude and phase across the intermediate frequency (IF) passband also needs to be measured. The calibrator should therefore have a flat spectrum with no intrinsic absorption or emission features. It is normal to observe a calibrator for a full 12^{h} period prior to each 3 days of source observation (cf. Table 1.3), and also to include as many shorter calibrations as possible (minimum 3^{h} per day).

Table 1.3 typical observing program of the Half-Mile telescope (excluding calibration)

day number	BC spacing (10 ft)	BD spacing (10 ft)	AC spacing (10 ft)	AD spacing (10 ft)	Total number of spacings	resolution in RA (arcmin)	Continuum noise/beam (mJy)	H-Line noise/beam 4-MHz (mJy)	H-Line noise/beam 2-MHz (mJy)
1	4	10	16	22					
2	6	12	18	24					
3	8	14	20	26	12	7.4	2.8	36	44
4	28	34	40	46					
5	30	36	42	48					
6	32	38	44	50	24	3.75	2.0	25	31
7	52	58	64	70					
8	54	60	66	72					
9	56	62	68	74	36	2.5	1.6	21	25
10	76	82	88	94					
11	78	84	90	96					
12	80	86	92	98	48	1.9	1.4	18	21
13	100	106	112	118					
14	102	108	114	120					
15	104	110	116	122	60	1.5	1.2	16	19

The map of the region of sky observed is obtained by performing the two-dimensional Fourier Transform (FT) of the complete (complex) aperture plane. It is usual to weight or 'grade' the aperture plane using a Gaussian function of radius, truncated at 30 %. This results in a synthesised beam (or response to a point source) which has smaller sidelobes than if uniform weighting is used. With uniformly spaced rings in the aperture plane (every 20 ft), the first grating (alias) response which results is at a radius of $\sim 2^\circ$. All emission from any source discussed in this thesis lies within this region, and hence no 'clean' procedures are needed.

Spacings smaller than 40 ft (i.e. less than about 45λ) cannot be physically obtained with two dishes of 15 ft diameter. This means that (1) no structure on a scale larger than about one degree can be detected, and (2) a variation of zero level is introduced across the maps. The latter effect is most noticeable in the case of observations of galaxies of large angular size made with a relatively small number of spacings. This is the case for the observations of M33 (Chapter 2), and a simple correction (detailed in Newton 1978) has been made. Such corrections are not necessary for all the other observations, and have not been applied. In all cases structure greater than one degree is still absent.

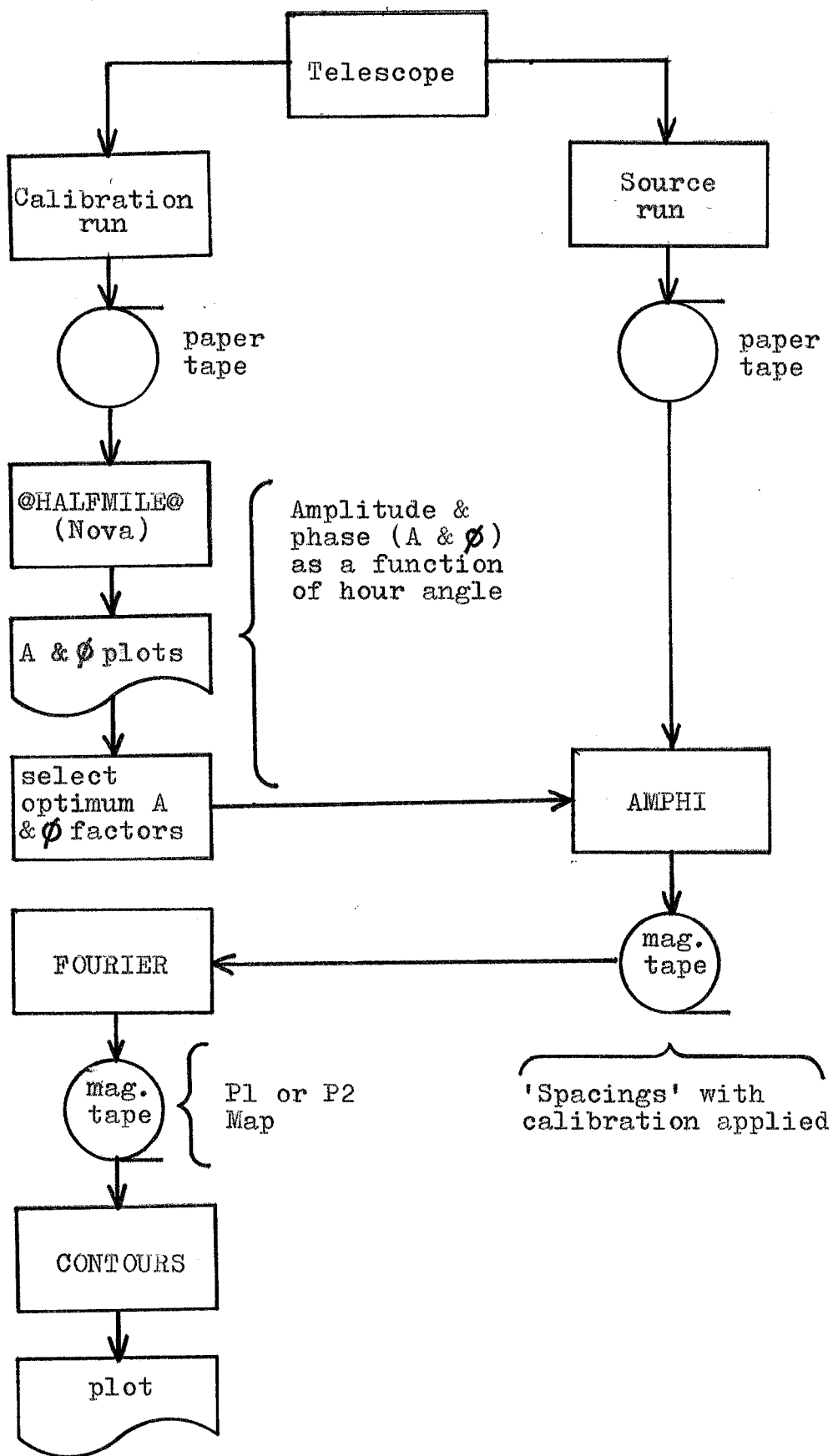
2.2 Broad-band continuum emission

Continuum radiation is correlated over a 10-MHz bandwidth which can be centred at 1411, 1413, 1415, 1417, 1419, 1421 or 1423 MHz by altering the first local-oscillator frequency. Each paraboloid can simultaneously receive linearly polarized radiation at two perpendicular orientations, called P1 and P2 (Stokes' parameters I+Q and I-Q respectively). For each interferometer pair there are three receivers, one which correlates both P1 signals, one which correlates both P2 signals, and one which correlates P1-P2 or P2-P1 (cross-polarization). All the necessary information (A and ϕ) is coded onto punched paper tape at the telescope.

Fig. 1.3 is a block diagram showing the stages of analysis needed to produce a broad-band continuum map. Observations of calibration sources are analysed to produce the required calibration data, and these are then applied to the observations of the source. The calibrated A and ϕ data which result, known as 'spacings', are stored on magnetic tape. The Fourier Transform is then performed, and the resulting map contoured. Full details of the procedures are given by Pearson & Warner 1977.

The receiving system of the telescope has a noise temperature of 120 K, and the noise level on the final maps is shown in Table 1.3, and varies as the number of spacings included.

Fig. 1.3 Continuum data reduction process for the Half-Mile telescope.



2.3 Hydrogen-line emission

Hydrogen line observations utilize the 160-channel digital cross-correlation spectrometer which is fully described by Winter (1975). The spectrometer performs a cross-correlation with the ^{IF} signals from each pair of aerials (i.e. *after path compensation, phase rotation & phase switching*) using a series of time delays. The results are recorded on magnetic tape. The cross-correlation is equivalent to the Fourier Transform of the frequency spectrum. By performing such a Fourier Transform during analysis, it is possible to obtain data for a set of aperture planes, where each is similar to that for the broad-band system but corresponds to a different frequency of observation. By employing the same Fourier Transform procedure as described for the broad-band system to each aperture plane in the set, it is possible to obtain a corresponding set of maps. Each map (referred to as a 'channel' map or 'output' map) corresponds to 21-cm radiation within a different range of frequencies (corresponding to neutral hydrogen within a different range of radial velocities).

/ 320? 4 x 80

The usual arrangement is to share the 160-channels of the spectrometer amongst the four interferometer baselines which are simultaneously observed, and to obtain 32 channel maps. Bandwidths of 2 or 4 MHz are used for extra-galactic observations and correspond to the 32 channels spanning a range of 422 or 844 km/s (respectively) in radial velocity. The individual velocity response and separation of the channels are shown in Table 1.4. Smaller bandwidths are available for Galactic observations.

Table 1.4 Velocity resolution of the digital spectrometer used on the Half-Mile telescope.

BANDWIDTH (MHz)	SEPARATION OF CHANNELS	WIDTH OF CHANNELS (FWHP Gaussian)
2	62.5 kHz 13.2 km/s	75 kHz 15.8 km/s
4	125 kHz 26.4 km/s	150 kHz 31.7 km/s

The second LO frequency determines which part of the IF band (40-50 MHz) is used for the line observations, as illustrated in Fig. 1.4. The centre of the observing bandwidth can be set between 40.0 and 49.9 MHz in 0.1 MHz steps. The absolute frequency and corresponding radial velocity of the observing band depends on both the first and second LO settings.

The digital spectrometer is fed with signals of only one polarization (either P1 or P2). The theoretical noise per beam area on a single-channel map depends upon the number of spacings included and the choice of bandwidth, and is shown in Table 1.3.

The initial stage of reducing line observations are illustrated in Fig. 1.5. Data from the telescope, on magnetic tape, are first checked for correct format. The calibration of the data is similar to that already described for continuum observations, with the additional complication of amplitude and phase variations across the IF passband.

Sometimes the A and ϕ plots show features which are clearly not intrinsic to the source, e.g. terrestrial interference, or correlated signals due to 'aerial overlap': at low declinations the dishes 'look through' one another at $HA \sim 18^h$ and $HA \sim 6^h$. If untreated, such data would give rise to spurious features on the maps. It is therefore necessary to remove discrepant data and, where feasible, replace it with values obtained by interpolation of the good data. This is most easily accomplished manually from A and ϕ plots where the calibration has been applied. The modifications are

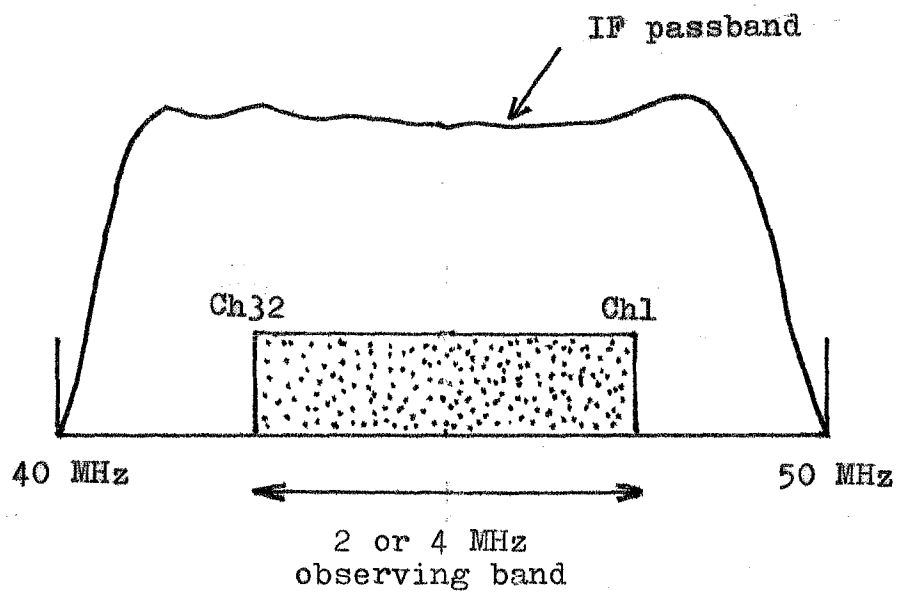


Fig. 1.4 Intermediate frequency band of the Half-Mile telescope. The position of the centre of the observing band (channel 16.75) is set by the second LO frequency.

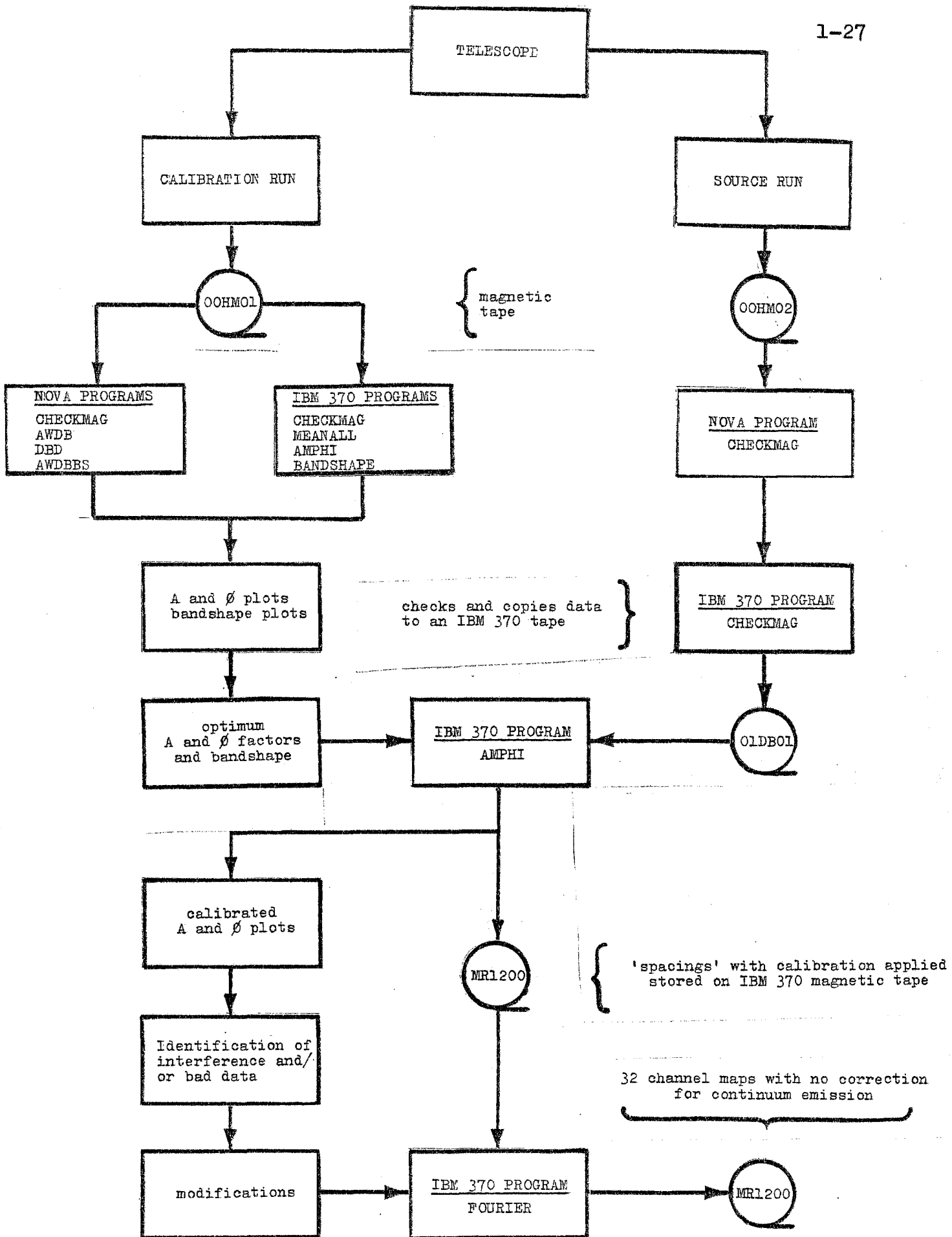


Figure 1.5 The initial stages of the reduction process for hydrogen-line data from the Half-Mile telescope.

made during the FT stage. This procedure can also be employed in the reduction of broad-band data (although this is not illustrated in Fig. 1.3.)

Each of the 32 channel maps will, at this stage, also contain continuum emission. Many galaxies have a continuum source at the nucleus, and several background sources are usually seen in the vicinity of the galaxy. It is desirable to remove these effects to produce maps solely of line emission. This is usually done by averaging the maps which contain no significant line emission and subtracting the resulting map from those which do (Fig. 1.6). The mean value of rms noise on the 'continuum-free' channel maps is denoted σ .

The 'continuum-free' channel maps are combined to produce profiles of HI intensity against radial velocity at each point over the map. (The values are first interpolated using a $\sin \theta / \theta$ function). Each profile is examined in turn, and if the peak value exceeds a specified gate level (usually 1.5σ) then values of 'integrated HI', 'velocity', and 'width' are assigned. The integrated HI corresponds to the area under the profile, and the velocity to the mean of the velocities corresponding to the half-power points. In some cases a least-mean-squares Gaussian fitting procedure is used instead of the standard procedure, since it produces a velocity field which exhibits slightly less noise, but the agreement between the two methods is very high. The integrated HI maps, made in the manner just described, have a noise level of $\sqrt{n} \sigma$, where n is the number of channels included

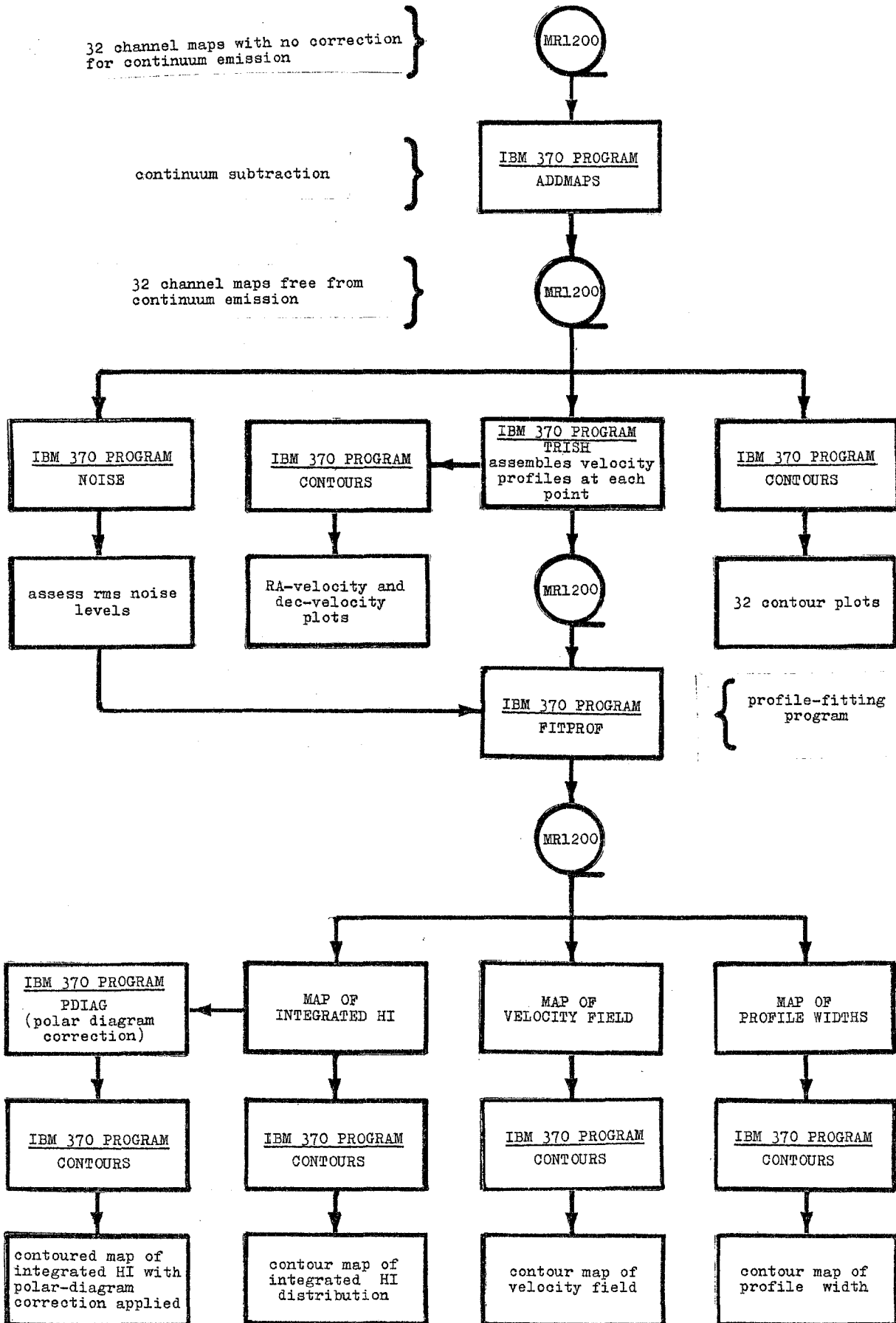


Figure 1.6 The final stages of the reduction process for hydrogen-line data from the Half-Mile telescope.

at any given point (typically $n \sim 3$). The rms error in the velocity field, V , is given by

$$(\overline{\Delta V^2})^{\frac{1}{2}} = w/(2.15(S/N)),$$

and the rms error in the fitted width, w , is given by

$$(\overline{\Delta w^2})^{\frac{1}{2}} = w/(2.4(S/N)),$$

where S is the peak brightness in the profile and N is the rms noise level (Warner, Wright & Baldwin 1973).

All the velocity fields presented in this thesis must be interpreted with caution due the phenomenon called 'beam smearing'. Warner et al. (1973) explain the effect, and show that the only situations where the apparent velocity differs significantly from the actual velocity at the centre of the beam are when: (a) the gradient of surface density has a component in the same direction as the gradient in velocity; (b) the gradient in velocity changes significantly across the beam-width.

A convenient method of displaying both HI intensity and velocity information is by means of a Right Ascension-velocity plot, or declination-velocity plot. These plots are used in Chapters 6 and 7 to illustrate how the HI shifts from channel to channel in a systematic matter (associated with the rotation of the galaxies). The plots are constructed by summing each channel map along lines of declination (for a RA-velocity plot) or lines of RA (for a dec-velocity plot). A gating procedure (similar to that described for maps of integrated HI) is often used to help minimize the effects of noise. In cases where a high gate has been used (e.g. 3σ) the resulting plots are then unsuitable for calculations of the absolute HI mass.

Except where specifically stated, none of the maps presented in this thesis has been corrected for the primary polar diagram of the antennas, since this correction causes a further variation

of noise level over the maps which makes them difficult to interpret.* The correction can be taken as the inverse of a Gaussian of Full-Width-Half-Power (FWHP) 94 arcmin, applied at the map centre. The pointing accuracy of the dishes is estimated to be less than 3 arcmin.

Throughout this dissertation all radial velocities are heliocentric, and all map coordinates are for epoch 1950.0.

* Furthermore, the correction is insignificant in most cases (except M33 and NGC 2403).

2.4 Analysis

This section is intended as a summary of the methods and formulae used to analyse the maps.

a) An unresolved source of flux density S jansky ($1 \text{ Jy} = 10^{-26} \text{ W m}^{-2} \text{ Hz}^{-1}$) will produce the same deflection on a synthesis map as a well-resolved source of brightness temperature T , where

$$T = \frac{D_{\max}^2 \sin(\text{dec}) S}{1380}$$

D_{\max} is the maximum interferometer spacing in meters, and dec is the declination of the map centre.

b) The surface density of HI atoms at any point on a map is given by

$$n_{\text{H}} = 1.82 \times 10^{18} \int T dv \quad \text{cm}^{-2}$$

where T is the observed brightness temperature in K and dv is the linewidth in km/s. A small optical depth is assumed (see below).

c) The total mass of hydrogen in a galaxy is given by

$$M_H = 2.36 \times 10^5 D^2 \int S dv M_\odot.$$

D is the distance to the galaxy in Mpc, and $\int S dv$ is the total integrated flux of the galaxy in units of Jy km/s. $\int S dv$ corresponds to the area under an HI profile constructed by integrating the flux in each of the continuum-free channel maps. The most accurate values for M_H are achieved from channel maps where the emission is (spatially) unresolved. This is because maps at a higher resolution tend to be less sensitive to low-brightness features and also because the numerical integration can introduce errors which become especially significant on noisy maps. The formula for M_H assumes a small optical depth for the HI. This is widely regarded to be the case for most observations of external galaxies.

d) The intrinsic luminosity of a galaxy, L , is related to its apparent magnitude, m , and to its assumed distance, D , by

$$\frac{L}{L_\odot} = \left(\frac{D}{D_\odot} \right)^2 10^{(m_\odot - m)/2.5}$$

L is normally expressed in units of the Solar luminosity L_\odot . D_\odot is the Solar distance (4.84×10^{-12} Mpc), and m_\odot is the apparent magnitude of the Sun (-26.16 in the B system). Whenever possible, apparent magnitudes are values of ' B_T^0 ' taken from de Vaucouleurs, de Vaucouleurs & Corwin (1976, and hereafter referred to as RC2). These are blue magnitudes corrected for Galactic and internal absorption, redshift, and inclination (to 'face-on' view).

e) The inclination of the plane of a disk galaxy to

the line of sight, i , can be estimated using the relation (Holmberg 1946)

$$\cos^2 i = (E^2 - E_0^2)/(1 - E_0^2),$$

where E is the ratio of the observed major to minor axes, and E_0 is the ratio of the intrinsic principal axes of the light distribution. Values of E_0 for different types of galaxy are given by Heidmann, Heidmann & de Vaucouleurs (1971).

f) Where the angular resolution is sufficiently good so that a detailed rotation curve is available, the total mass of a galaxy (and the variation of mass with radius) can be derived using the method of Burbidge, Burbidge & Prendergast (1959). Where the angular resolution is not so good, the total mass, M_T , can be estimated by assuming the gas to be in circular motion about a point mass, and using the relation

$$M_T = 6.79 \times 10^4 D R_m (V_m \operatorname{cosec} i)^2,$$

where R_m is the maximum radius (arcmin) at which HI is observed, and V_m is the corresponding observed velocity (in km/s wrt the systemic velocity of the galaxy), D is the distance of the galaxy in Mpc and i is the inclination. The relation gives the mass interior to a radius of R_m , and the assumption of a point mass is only strictly true in the case of a spherical distribution of matter. The discrepancy is not large, however, and even for a disc of axial ratio 0.1 the mass obtained from this relation is too great only by a factor of two. Where observations are unable to resolve the HI spatially, it is impossible to obtain values for V_m and R_m . In such cases an estimate for the total

mass can be obtained by replacing V_m and R_m by half the width of the global line-profile, and the optical radius (respectively). Masses determined in this way are known as Indicative Total masses.

g) Measurements of the line-of-sight component of velocity do not permit a unique interpretation of the velocity field. Considering the galaxy as a thin inclined plane with rotation dominating over expansion or other peculiar motions, the velocity field may be characterised by the following dynamical parameters (which are not all independent):

- (1) RA_{nuc} and dec_{nuc} , the centre of rotation
- (2) V_{sys} , the systemic velocity
- (3) PA, the position angle of the major axis (measured anticlockwise from north)
- (4) i , the inclination of the plane ($i=0$ is 'face on')
- (5) $V_{rot}(R)$, a rotation curve, where R is a radial distance in the plane of the galaxy from the rotation centre.

A method of obtaining a best-fitting set of parameters is outlined by Warner, Wright & Baldwin (1973). The observed radial velocity, V_{obs} , is then given by

$$V_{obs} = V_{sys} + V_{rot}(R) \cos(\theta) \sin(i)$$

where θ is the azimuthal coordinate in the plane of the galaxy measured from the major axis. Further terms may be added to describe expansion in the plane and motion normal to the galactic plane.

CHAPTER 2THE Sc GALAXY M331 INTRODUCTION

Distortions of the HI disc in the outer parts of M33 have been known for some time (Gordon 1971; Wright Warner & Baldwin 1972; Huchtmeier 1973). They take the form of 'wings' to the NW and SE of the nucleus and have been attributed to symmetrical warping of the galactic plane (Rogstad, Wright & Lockhart 1976) such as that which has been observed directly (Sancisi 1976) in several edge-on galaxies. Perturbations in M83 and M31 have also been interpreted as evidence of warping (Rogstad, Lockhart & Wright 1974; Roberts & Whitehurst 1975; Newton & Emerson 1977). Although some warped galaxies have companions which might produce the warps by tidal interactions, others do not, and the cause of these perturbations is uncertain.

2 OBSERVATIONS

The Cambridge Half-Mile telescope was used to make three separate surveys of M33 (Table 2.1), one centred on the optical nucleus, and the others on the wings to the NW and SE of the nucleus. The former survey was made by Mr K Newton as part of a high-resolution survey, while the two surveys of the wings were made by myself. In each case 12-hr observations were made at 12 interferometer baselines from 12.2 m to 79.2 m in 6.1-m intervals. Complete coverage of the u-v plane was obtained, except in the SE survey where 5 per cent of the data were missing. The resulting low-resolution maps are ideal for the purposes of this study, where sensitivity to large-scale emission of low-surface-brightness is required.

The HI emission was measured using the digital spectrometer over a 2-MHz bandwidth. The output spectrum had a resolution of 16 km/s and was sampled at values of radial velocity separated by 13.2 km/s to provide 32 output maps. Continuum radiation in the 10-MHz bandwidth was also measured and the surveys were calibrated by observations of 3C 48 and 3C 286.

The absence of interferometer spacings smaller than the diameter of the paraboloids (i.e. $\lesssim 45 \lambda$) means that (i) no structure on a scale larger than \sim one degree can be detected and (ii) a variation of zero level is introduced across the maps. A correction for the latter effect has been made (chapter 1), but structure greater than one degree is still absent.

Maps of integrated hydrogen, radial velocity, and velocity dispersion were made from continuum-free channel maps in the way described in chapter 1. The

Table 2.1 Details of the observations of M33 with the Cambridge Half-Mile telescope.

Survey	North	South	Centre
Map centre (1950.0)			
RA (h m s)	01 29 30	01 31 00	01 31 00
Dec (degrees minutes)	31 10	29 40	30 24
Mean epoch of observations	1975.8	1975.9	1975.2
Calibrators			
Name	3C 286	3C 286	3C 286
Assumed flux density (Jy)	14.4	14.4	14.4
Name	3C 48	3C 48	
Assumed flux density	15.3	15.3	
Angular resolution in RA \times dec (arcmin)			
12-spacing observations	7 \times 15	7 \times 15	7 \times 15
60-spacing observations			1.5 \times 3.0
RMS noise over a 16 km/s range of velocity (K)			
12-spacing observations	0.09	0.13	0.09
60-spacing observations			0.82
Heliocentric central velocity (km/s)	-210	+1	-210

three maps of radial velocity were combined in sections divided at the 30° and 31° lines of declination. The maps of integrated hydrogen were similarly combined after application of individual corrections for the primary response of the antennas. The maps were integrated over the velocity range -306 to -28 km/s. The rms noise levels of the surveys are indicated in Table 2.1, but the brightness of the faintest features detectable is determined by the sidelobe level (5 per cent) and varies according to the emission present on each channel map.

The distance to M33 is taken to be 690 kpc (Warner et al. 1973; Rogstad et al. 1976) so that 5 arcmin corresponds to 1 kpc.

3 THE NEUTRAL HYDROGEN DISTRIBUTION

3.1 The large-scale structure

Fig. 2.1 shows the combined integrated hydrogen maps with a resolution of 7×15 arcmin and corrected for the primary response of the dishes; the three map centres are marked as crosses. The outer (dashed) contour is taken from the individual channel maps and indicates the 3σ limit of detected hydrogen. The HI 'wings' extend to about 70 arcmin (14 kpc) from the nucleus in the plane of the sky, both to the NW and the SE. They are features of very low brightness, with low HI masses, and there is no associated excess of optical emission visible on the Palomar Sky Survey prints. The relationship of neutral hydrogen in the outer parts of M33 to the optical emission is illustrated in Plate 2.1.

The observed masses of HI in the wings beyond radius $R = 6$ kpc, and derived from Fig. 2.1 are $2.5 \times 10^7 M_{\odot}$ in the north and $1.0 \times 10^7 M_{\odot}$ in the south. On the assumption that the hydrogen is optically thin, the average column densities in the wings are $\sim 10^{20}$ atom/cm² in the north and $\sim 5 \times 10^{19}$ atom/cm² in the south. The total observed HI mass of M33 is $1.0 \times 10^9 M_{\odot}$. The velocity dispersion (defined as FWHP corrected for the instrumental response) in each wings is ~ 25 km/s, which may be compared with the value 23 km/s for the outer parts of M31 (Newton & Emerson 1977). In the present survey no extended continuum emission has been detected coincident with the HI wings.

Fig. 2.2 shows two maps at 1.5×3 arcmin resolution, integrated over a radial velocity range in which HI emission from the wings was detected at low angular

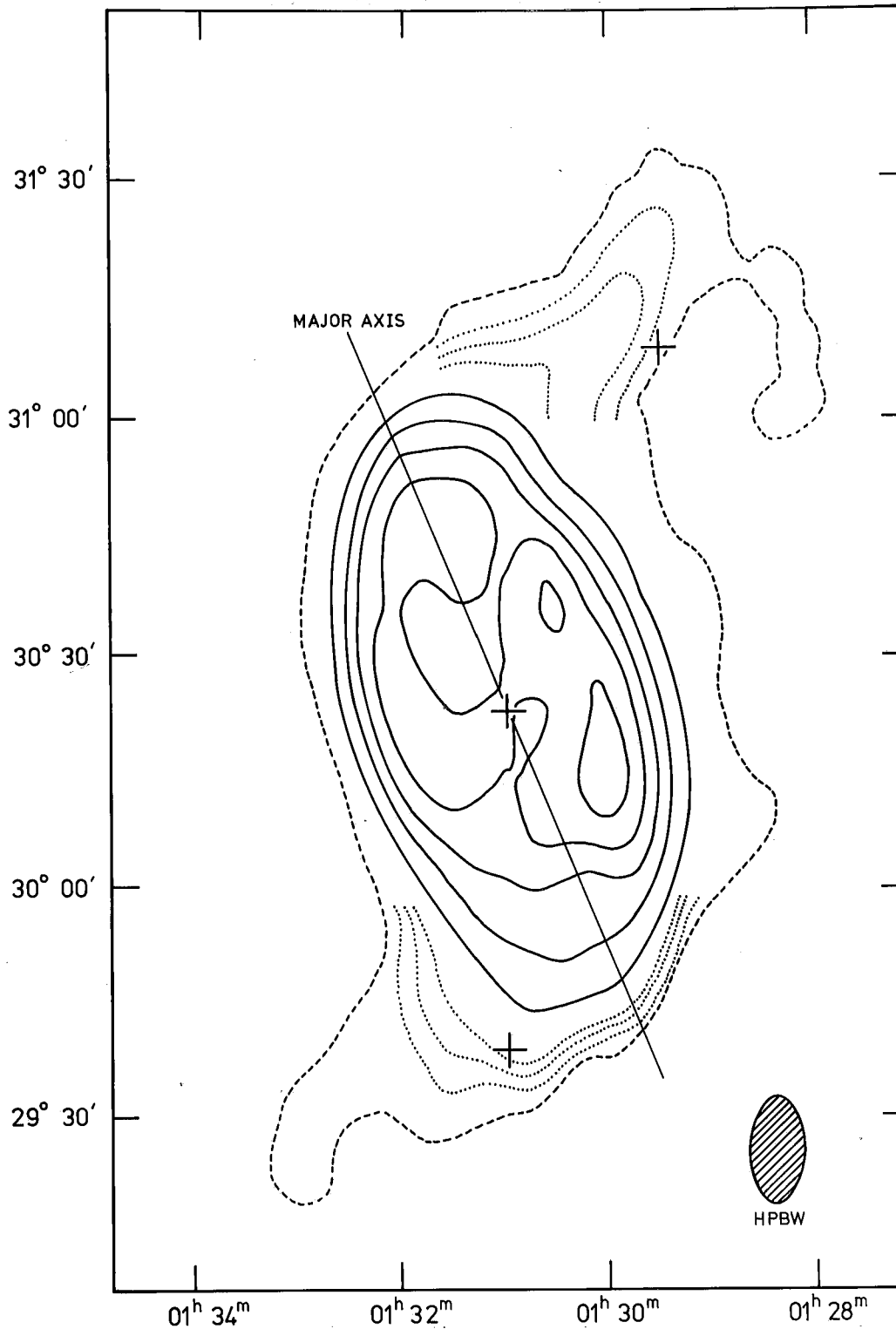


Figure 2.1. Composite integrated HI map of M33. A combination of three separate surveys, corrected for primary beam response, joined along the 31 and 30° lines of declination. The integration was performed over a radial-velocity range -306 to -28 km/s. The map centres are marked with crosses. The outer (dashed) contour shows the 3 σ limit of detected HI from the channel maps. Dotted contours start at 50 K km/s with an interval of 25 K km/s. Dotted contours are not shown around the main body of the galaxy in order to avoid confusion. Solid contours begin at 200 K km/s with an interval of 150 K km/s. The hatched ellipse represents the HPBW of 7 x 15 arcmin. The central disc has an inclination of 54° and a major axis PA of 22° (Warner *et al.* 1973).

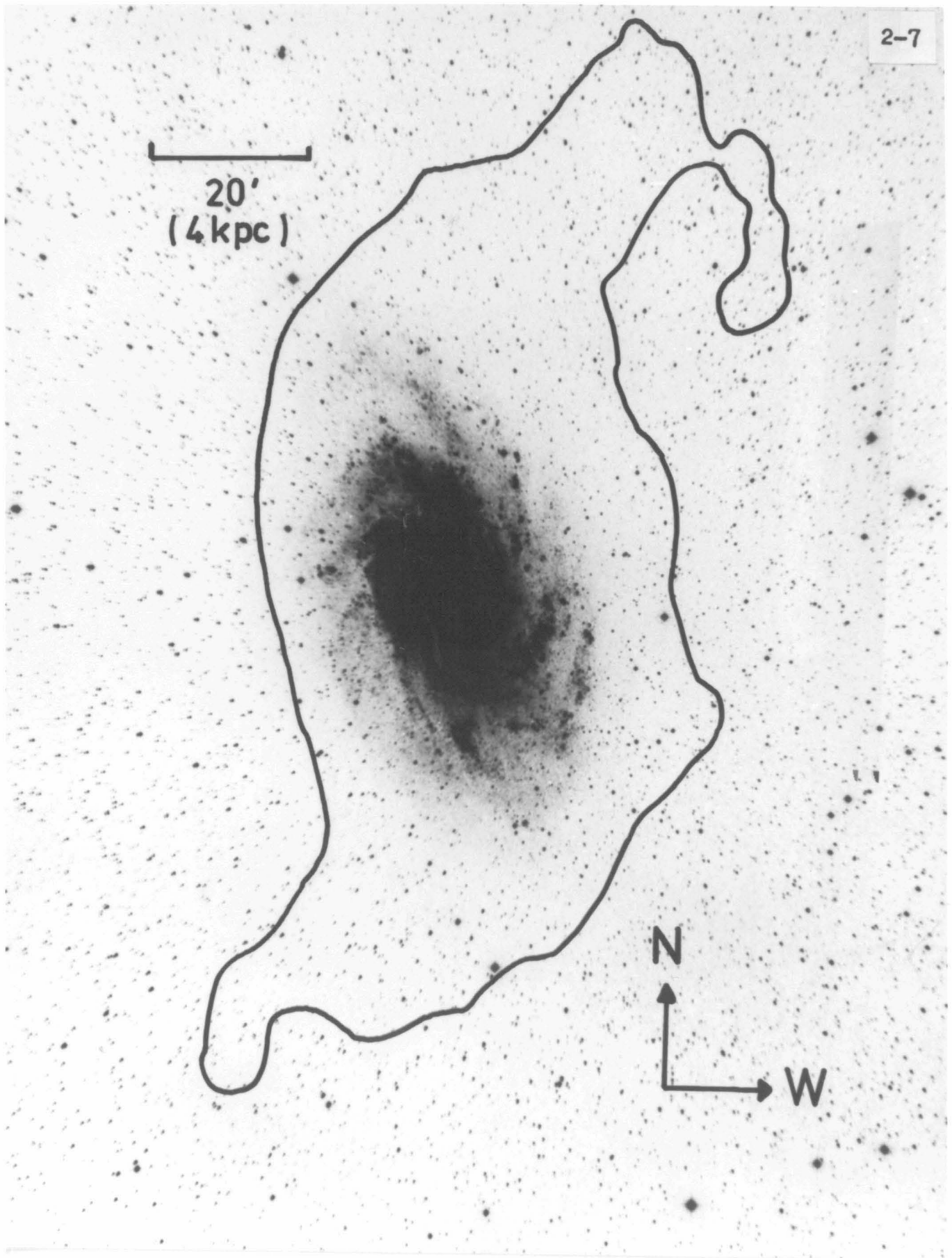


Plate 2.1 Optical photograph of M33 with the outer (dashed) contour from Fig. 2.1 superimposed. The western edge is nearer to the observer if it is assumed that the spiral structure is trailing. (Photograph copyright by the National Geographic Society-Palomar Sky Survey. Reproduced by permission from the Hale Observatories.)

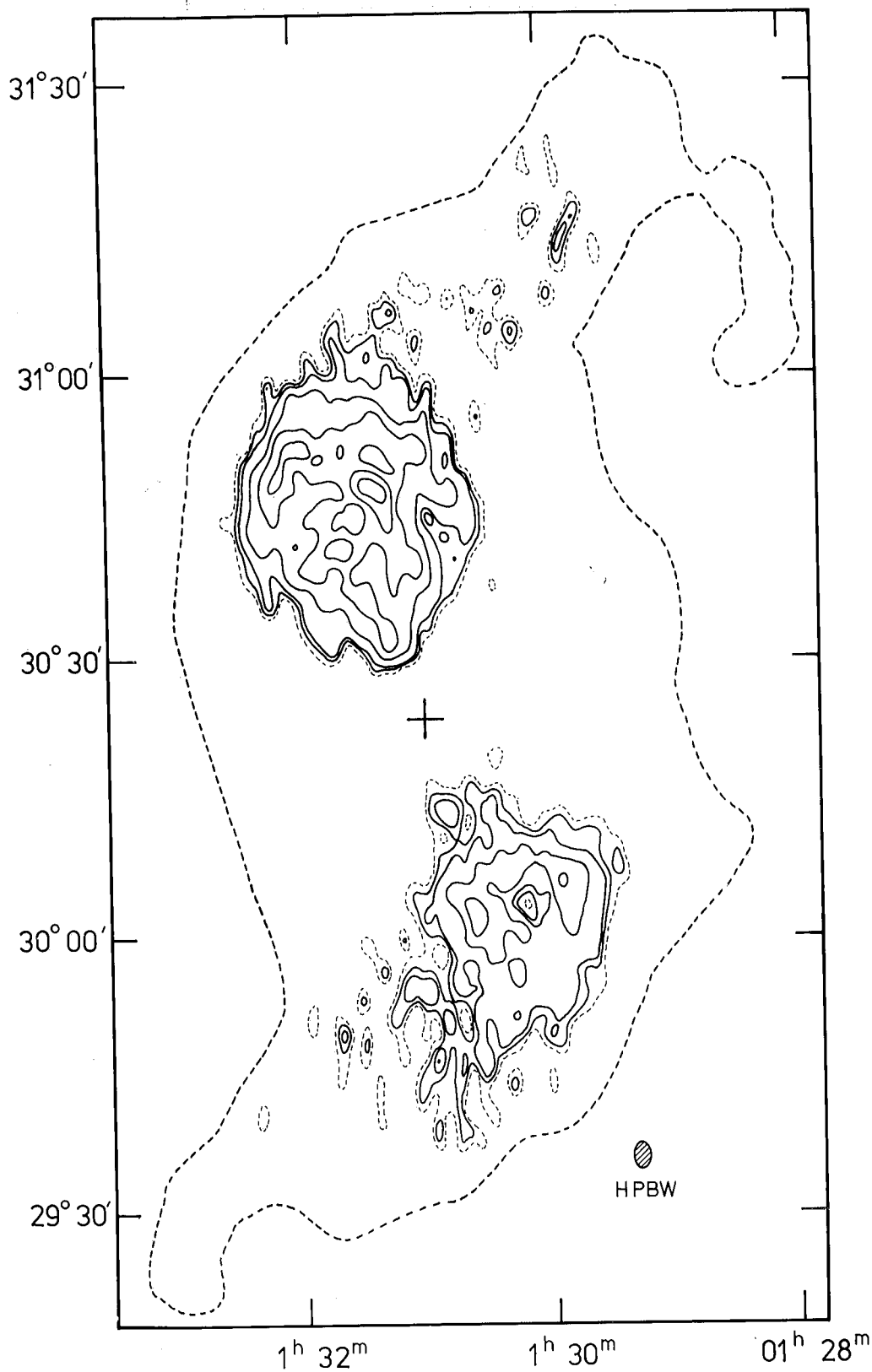


Figure 2.2 Integrated hydrogen maps of the wing areas from the central survey with a resolution of 1.5×3 arcmin (hatched ellipse). The outer (dashed) contour is from the low-resolution maps (Fig. 2.1). The maps were made as described in Chapter 1 using a gate of 3σ , and include HI integrated over the radial velocity range -253 to -292 km/s in the north, and -68 to -95 km/s in the south. No polar diagram correction has been applied. The first contour (dashed) is 50 K km/s . The first two solid contours are 100 and 150 K km/s . Higher contours start at 200 and are in 100 K km/s intervals.

resolution. No correction has been applied for the primary polar diagram, and so the rms noise is uniform over the map. It can be seen that the patchy HI structure revealed in the central disc by high-resolution observations (Wright et al. 1972) extends to the wings.

Fig. 2.3 shows a profile of the total flux density of HI in M33 as a function of radial velocity. The values are about 25 per cent smaller than those of Dean & Davies (1975). This is unlikely to be because a significant fraction of the HI emission has a scale larger than 1° (and hence not detected in the present survey), since:

- (1) Dean & Davies (1975) measured an HI size of only about one degree;
- (2) a discrepancy of similar magnitude was found by Winter (1975) for NGC 4490, a much smaller galaxy also observed both at Jodrell Bank and by the Half-Mile Telescope. It seems more probable that the discrepancy lies in the calibration of brightness.

Rogstad, Wright & Lockhart (1976), in observations made at Owens Valley, found evidence for a weak component of hydrogen superposed on the main disc but with radial velocities differing from the strong component. This weak component exhibits itself as extended or double-peaked emission profiles. The present central survey at high-resolution gives no clear evidence for the weak component but would not be expected to, because of the low signal-to-noise ratio. The 7×15 arcmin data reveal tails to some of the velocity profiles in the central disc, but the low spatial resolution and resulting beam-smearing do not allow detailed measurements to be

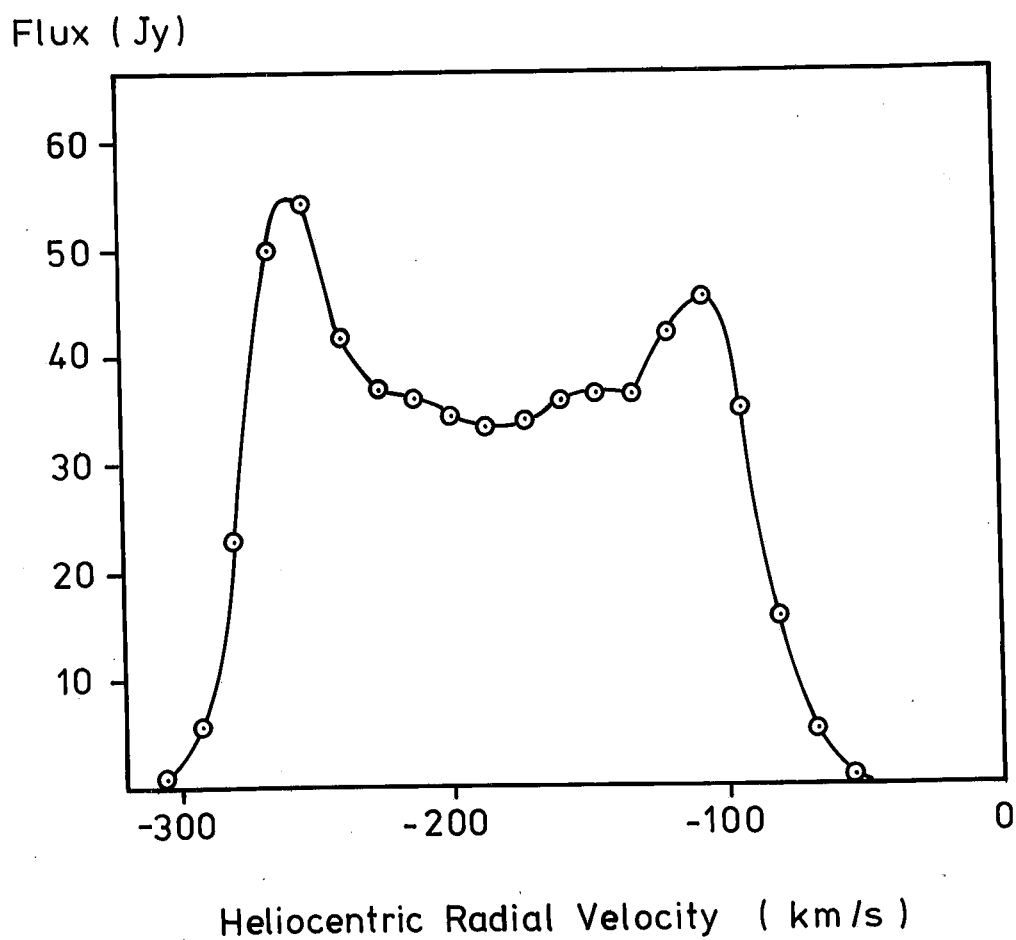


Figure 2.3 Profile of HI flux density in M33 as a function of radial velocity.

made.

3.2 Asymmetries

It is well known that the HI distribution of M33 is not symmetrical (e.g. Wright, Warner & Baldwin 1972). Fig. 2.1 shows that in the central disc, emission to the west of the major axis is brighter than emission to the east, with the brightest in the SW quadrant. Although the linear extent and shapes of both wings in the sky are similar, the NW feature is about twice as bright and more massive than the SE. The high sensitivity of the present observations reveals two further asymmetries in the outermost regions: (i) the low-brightness feature running perpendicular to the end of the NW wing, referred to here as the 'NW turnover', and (ii) extended emission down the west side of the galaxy.

3.2.1 THE NW TURNOVER

This feature is observed on four output maps in the northern survey (Fig. 2.4A from -266 to -227 km/s) with average brightness temperatures of about 0.7 K. It is connected to the main wing both spatially and in radial velocity, at -279 km/s, and there is a radial velocity gradient of ~ 9 km/(s kpc) along its length. This continuity strongly suggests that the feature belongs to M33 and is part of the large-scale distortions of HI at large distances from the nucleus. The observed mass of HI in this feature, derived from individual channel maps is $4 \times 10^6 M_{\odot}$, with an average column density of 2×10^{19} atom/cm². The feature may extend further south, and on the channel maps there

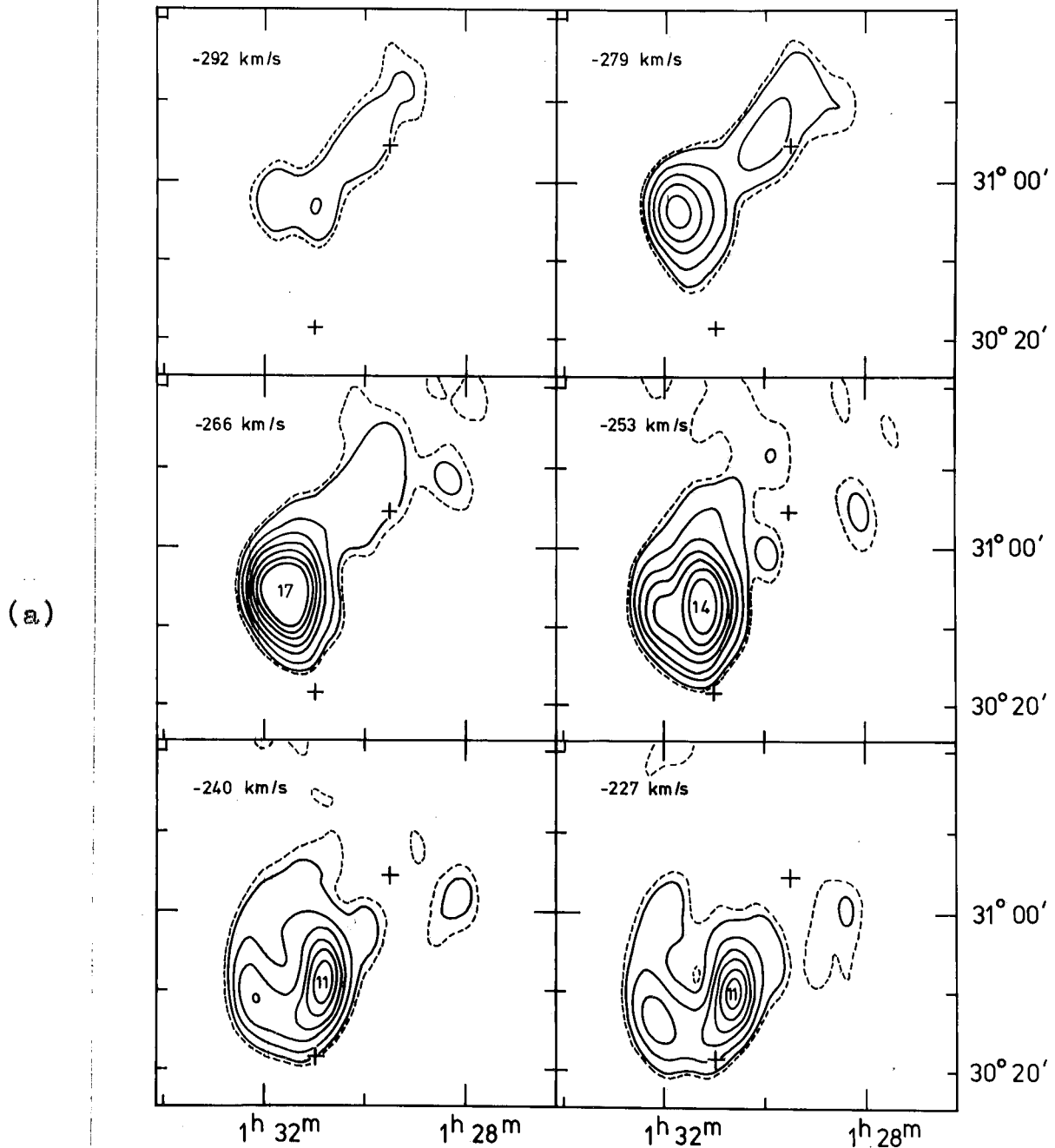


Figure 2.4. Channel maps with a resolution of 7×15 arcmin, each covering a range of 16 km/s in radial velocity. These maps have not been corrected for the primary polar diagram of the dishes, so there is a uniform noise level (Table 2.1) over each map. The dashed contour is 0.3 K. Solid contours are at 0.7, 2, 4, 6, 8, 10 and 12 K. Numbers indicate the peak emission in K. Crosses indicate the map centres. (a) -292 to -227 km/s: from the north survey. The wings are clearly visible, and the westernmost isolated emission at -266 to -227 km/s forms the northern 'turnover'.

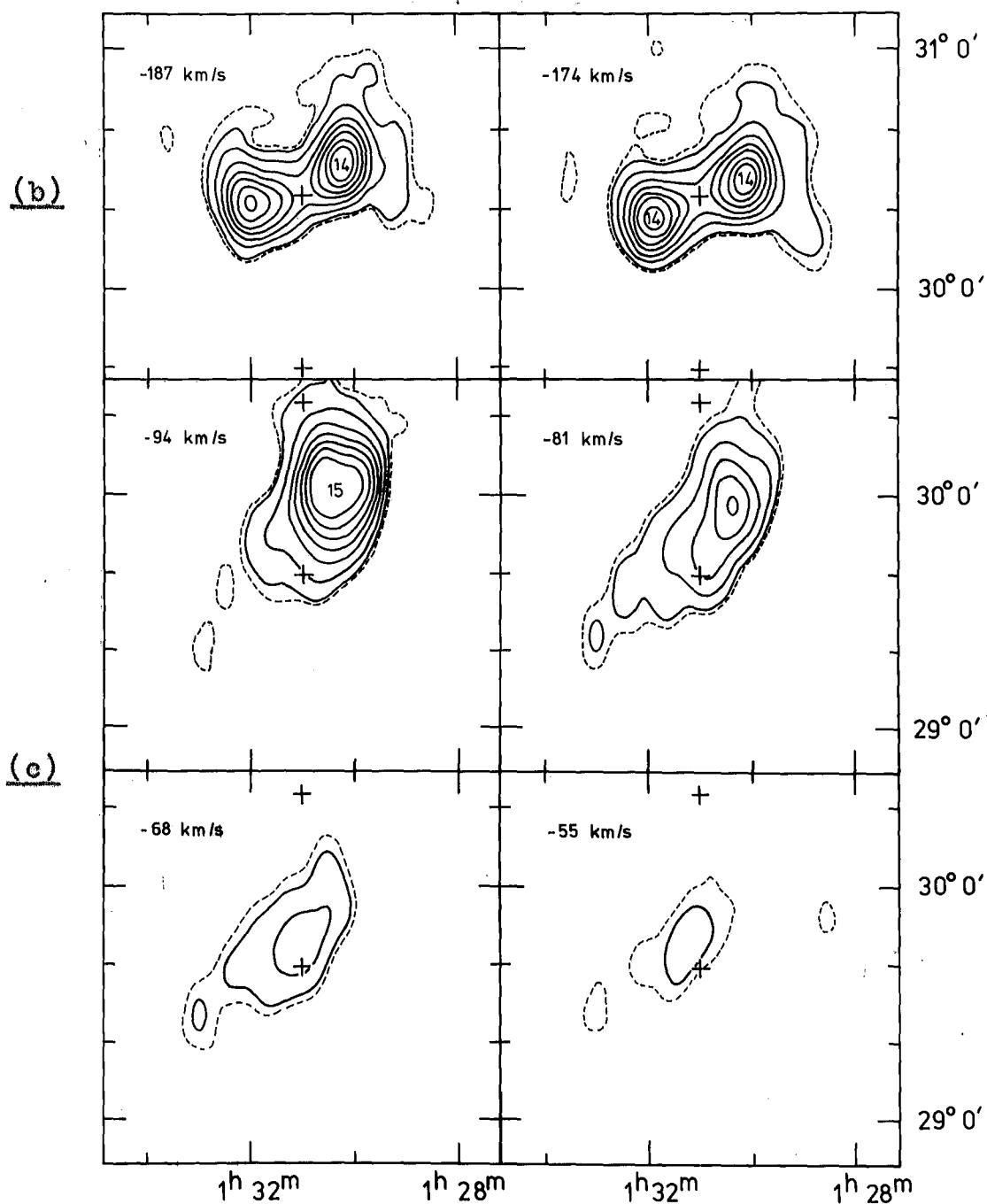


Figure 2.4 (continued). (b) -187 and -174 km/s: channel maps from the central survey, showing the low-brightness feature at the western edge. (c) -94 to -55 km/s: channel maps from the southern survey showing the southern wing.

is some evidence that emission at the 0.3 K level extends from the turnover to join the 'western extension', described below, at about -200 km/s.

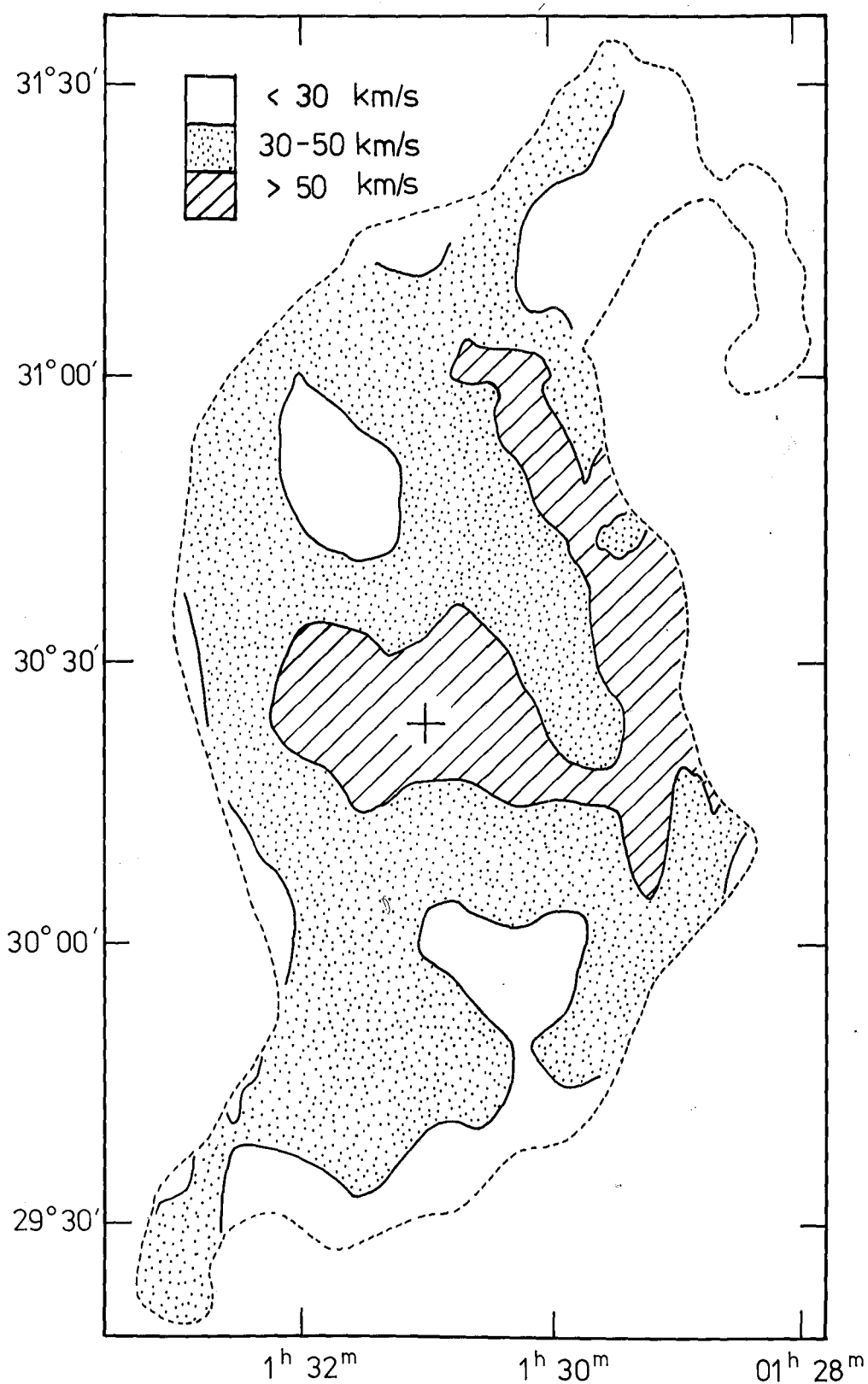
There is no evidence for a similar 'turnover' feature of the SE wing, but such a feature, with a surface-brightness half of that of the 'NW turnover' (reflecting east-west asymmetry), would not have been detected by these observations.

3.2.2 THE WESTERN EXTENSION

The central elliptical distribution of HI exhibits a steep gradient around its edge at a distance of about 7 kpc in the plane of the galaxy, and it can be seen from Fig. 2.1 that to the east this gradient extends to the limit of detected emission, producing a sharp cut-off and an extremely regular outline. This is not the case to the west where, beyond the initial steep gradient, low-brightness HI with an irregular outline extends to greater radii (Figs 2.1 and 2.4B). It may be that this effect is a reflection of the east-west asymmetry in the central regions, and further observations with better sensitivity are required to establish the reality of the eastern cut-off.

The line-profiles in the region of the western extension are broad and flat-topped. Fig. 2.5 shows the variation of dispersion over the galaxy. Dispersions in the western extension are considerably higher than elsewhere in M33 (excepting the nucleus where beam-smearing effects are large), and often reach 70 km/s.

Figure 2.5



Dispersion map of M33. The outer (dashed) contour shows the extent of 3σ HI emission from the single output maps. Dispersions are FWHM values, not corrected for the instrumental response of the telescope.

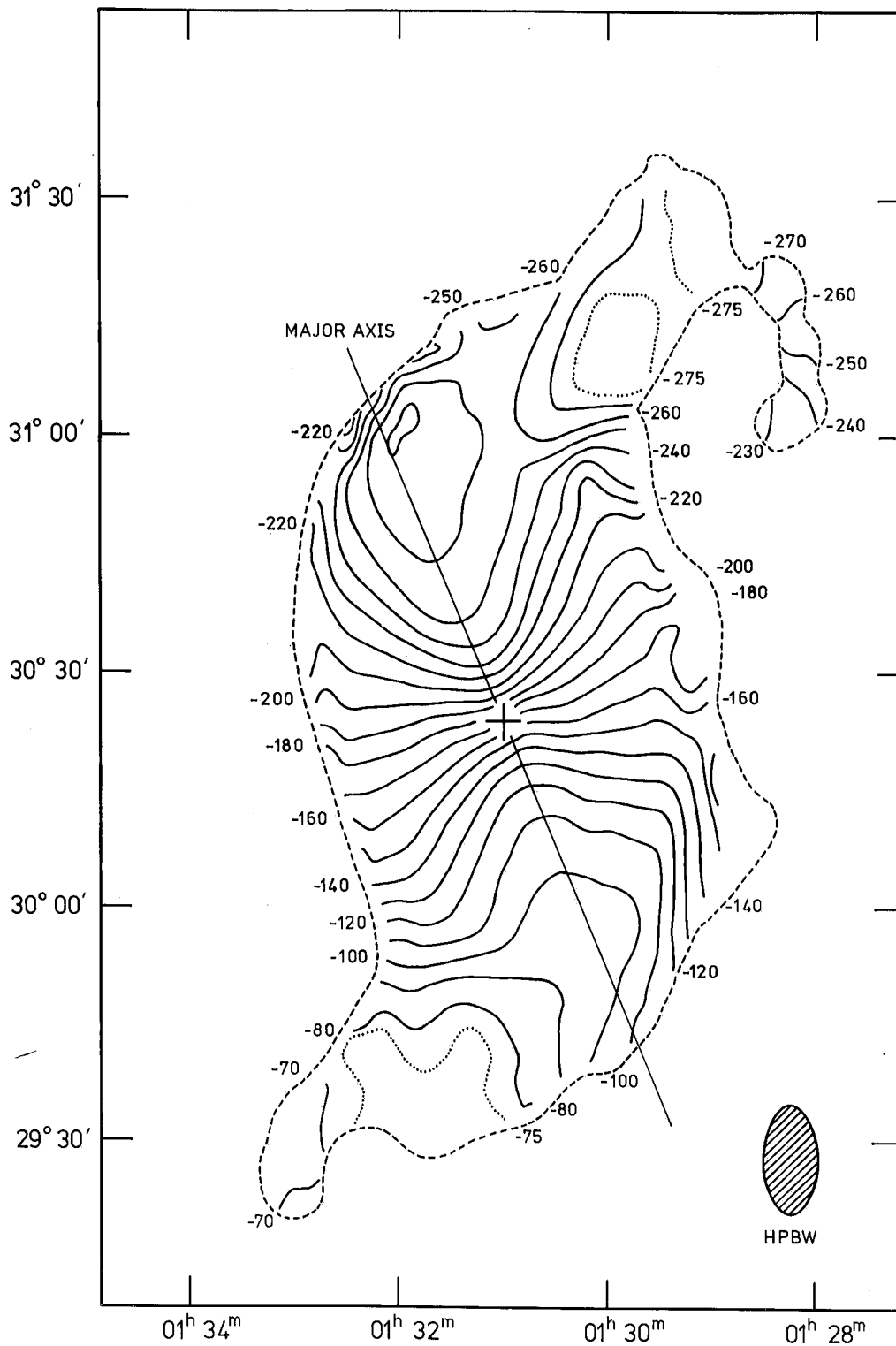
4 THE RADIAL VELOCITY FIELD

4.1 Observations

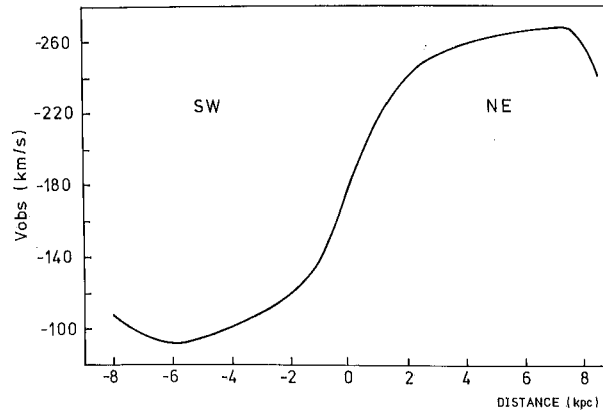
From a plot (Fig. 2.6) of the radial velocity field, it can be seen that the well-behaved central disc, in normal differential rotation, extends to ± 30 arcmin (6 kpc) along the major axis. The variation of observed radial velocity, V_{obs} , with radius along the major axis (PA 22°) is shown in Fig. 2.7A, from which the rotation curve, V_{rot} for $R < 6$ kpc (Fig. 2.7B), has been derived by assuming an inclination of 54° . It should be noted that these curves are smoothed by the resolution of the synthesised beam along the major axis (2.2 kpc). The rotation curve is seen to rise smoothly to $V_{\text{rot}} = 107$ km/s at $R = 6$ kpc. A decrease in V_{rot} beyond $R = 6$ kpc would explain Fig. 2.7A, but in view of the perturbations to orbits at larger radii, discussed below, calculations of V_{rot} cannot be extrapolated with any certainty. According to the model presented in section 4.2, radial velocities in the wings are consistent with a flat rotation curve having $V_{\text{rot}} = 107$ km/s at larger radii.

Fig. 2.8 shows the residual velocity field obtained by subtracting model radial velocities from those observed. The model used was a thin flat disc with inclination 54° and major axis PA 22° , with the measured rotation curve for $R < 6$ kpc, and a constant $V_{\text{rot}} = 107$ km/s at greater radii (Fig. 2.7B). In the outer parts of M33 there are residuals as large as 70 km/s and the velocity perturbations themselves show some asymmetry; the magnitudes of the residuals at corresponding positions in the two wings differ by up to 30 km/s.

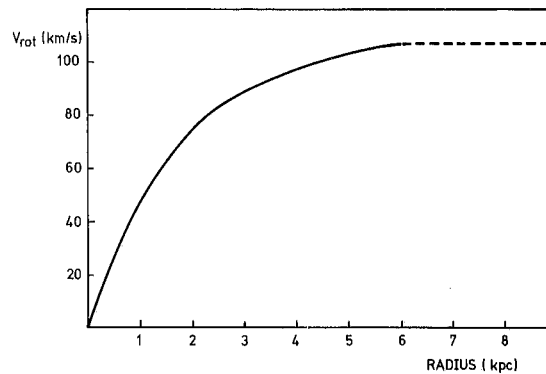
Figure 2.6



Combined radial-velocity field after projecting the three surveys on to a common grid and joining along the 30 and 31° declination lines. The velocity resolution is 16 km/s. The contours are drawn only in regions where there is a sufficiently large signal to noise ratio. Dotted contours are in 5 km/s intervals, and solid contours in 10 km/s intervals. The outer limit to HI from the single output map is shown dashed. The hatched ellipse represents the HPBW resolution of 7×15 arcmin. The map centre of the central survey is marked with a cross and the major axis is marked at PA 22°.



(a)



(b)

Figure 2.7 (a) Observed velocities, V_{obs} , in M33 northwards and southwards along the major axis, PA 22° . (b) Rotation curve for M33, calculated for $R < 6$ kpc from (a) above, assuming an inclination of 54° , PA 22° , and $V_{\text{sys}} -180$ km/s. The rms error in V_{obs} and V_{rot} is ~ 2 km/s, and both curves are smoothed by the resolution of the synthesised beam along the major axis (2.2 kpc).

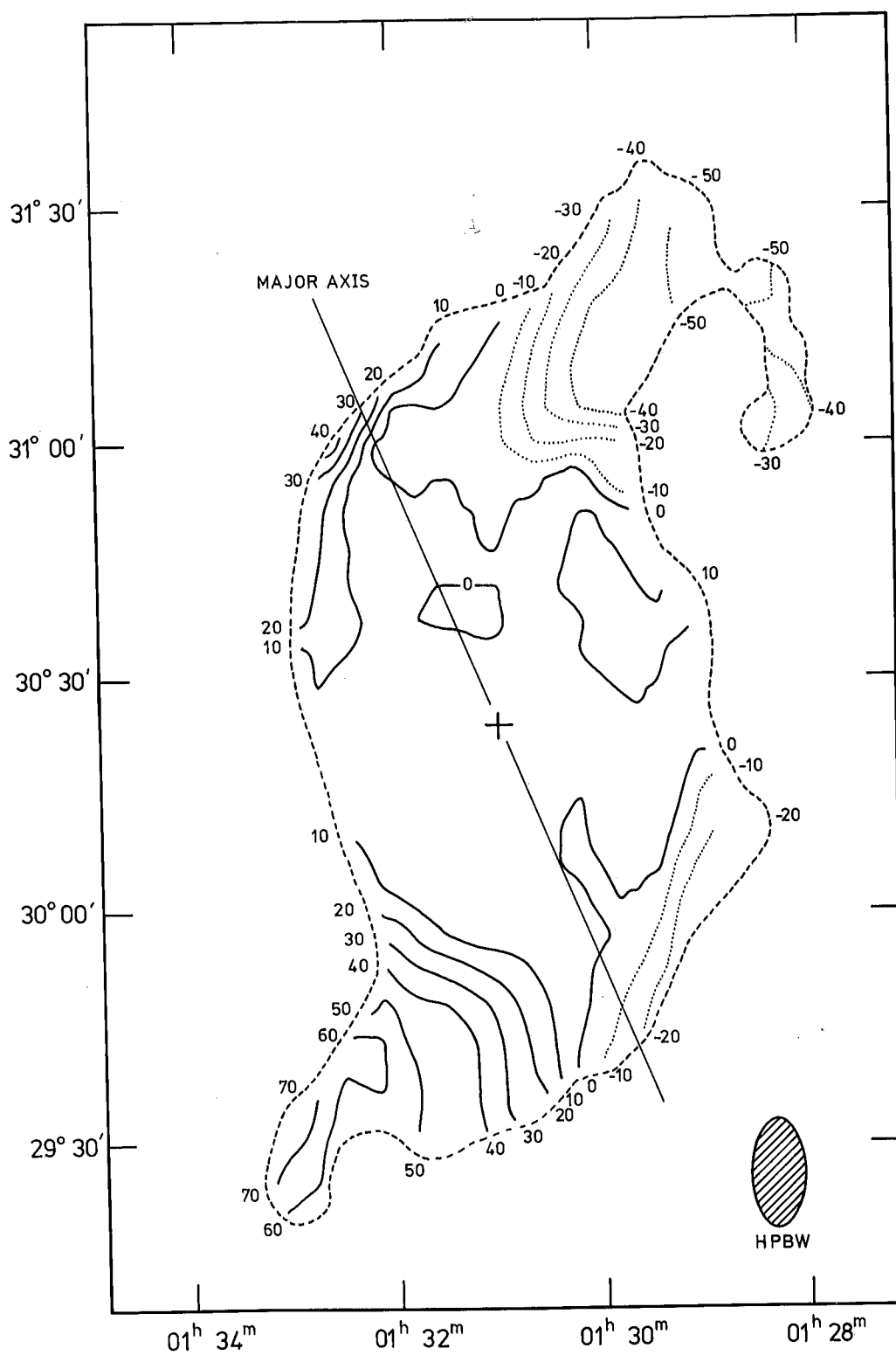


Figure 2.8 Residual velocities between observations (Fig. 2.6) and a model of normal differential rotation ($v_{\text{sys}} -180$ km/s; major axis PA 22° ; inclination 54°). Solid contours are positive, dotted are negative. The contouring interval is 10 km/s. The outer limit of HI from the single output maps is shown dashed. The HPBW of 7×15 arcmin is represented by the hatched ellipse. The map centre of the central survey is marked with a cross and the major axis is marked at PA 22° .

4.2 Geometry

These new observations of HI and radial velocity distribution in the wings shed more light on the geometry of the perturbations. Rogstad, Wright & Lockhart (1976) have interpreted the wings in terms of hydrogen rotating about the nucleus in circular orbits whose inclination and PA of the (projected) major axis vary with radius. A similar interpretation has been made of distortions in the outer parts of other galaxies (cf. Ch 1, sec.1.4). This model explains the wings as due to the enhancement of the column density for lines of sight through the ends of each orbit.

The model by Rogstad et al. was produced to explain three main phenomena: (i) the shape of the HI wings, (ii) the steep cutoff in HI density on the minor axis, and (iii) the 'weak' component of HI in front of the main disc, discussed in section 3 above. In its original form, the model is not consistent with these new observations, as may be seen from the perspective drawing of the model, shown in Fig. 2.9 together with an outer HI contour from the present survey. It is clear that the wings observed in the present survey extend much further from the nucleus than the corresponding features in the model, even after convolution with our beam. Furthermore the model does not account for the observed radial velocity field in the wings, since both the inclination and PA of the major axis increase too quickly with radius in the model, nor with the western extension on the minor axis. It can be seen from Fig. 2.6, nevertheless, that the position

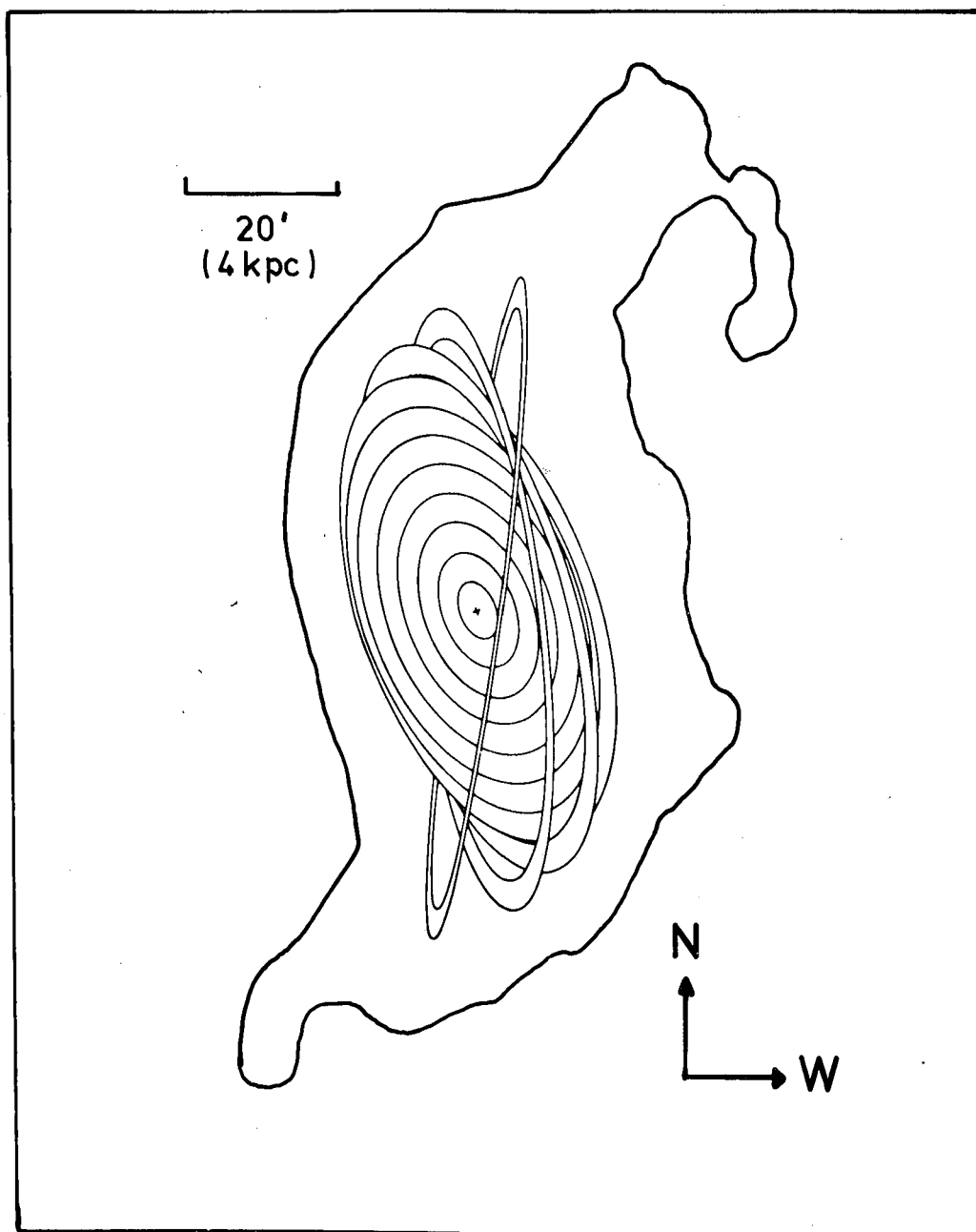


Figure 2.9 Outer HI contour of Fig. 2.1 superimposed on a perspective drawing of the bending model for M33 by Rogstad *et al.* (1976). The plane of the sky corresponds to the plane of the paper. The map centre is shown as a cross.

angle of the dynamical major axis (defined as the locus of maximum deviation from systemic velocity), deviating in opposite senses in the NW and SE, changes comparatively smoothly with radius, while the radial velocities towards the ends of each wing are consistent with HI rotating in orbits edge-on to the line of sight at $R \approx 14$ kpc, and with $V_{\text{rot}} = 107$ km/s. The narrowing of the wings towards their ends also implies a change of inclination with radius. If one assumes the western extension to be one aspect of the overall asymmetry in brightness distribution, so that similar emission may exist along the eastern edge but below the sensitivity of this survey, then a model not constrained by the 'cut-off' can be constructed, although it must still explain the high gradient of emission observed in these regions.

The proposed model (Fig. 2.10) is inherently symmetrical, and therefore does not describe the asymmetries noted above, but it indicates well the sense and magnitude of the observed perturbations. It is similar to that of Rogstad et al., but with orbital parameters changing more slowly with radius. In Fig. 2.11 the radial velocities calculated from this model are shown, together with a contour indicating the extent of the model HI distribution, for comparison with Fig. 2.6. The differences between the observed and model radial velocities do not exceed 30 km/s, and over most of the region are less than about 10 km/s. Since asymmetries in the observed velocity field reach 30 km/s, any symmetrical model must leave residuals of at least 15 km/s. The fits in both HI shape and velocity for

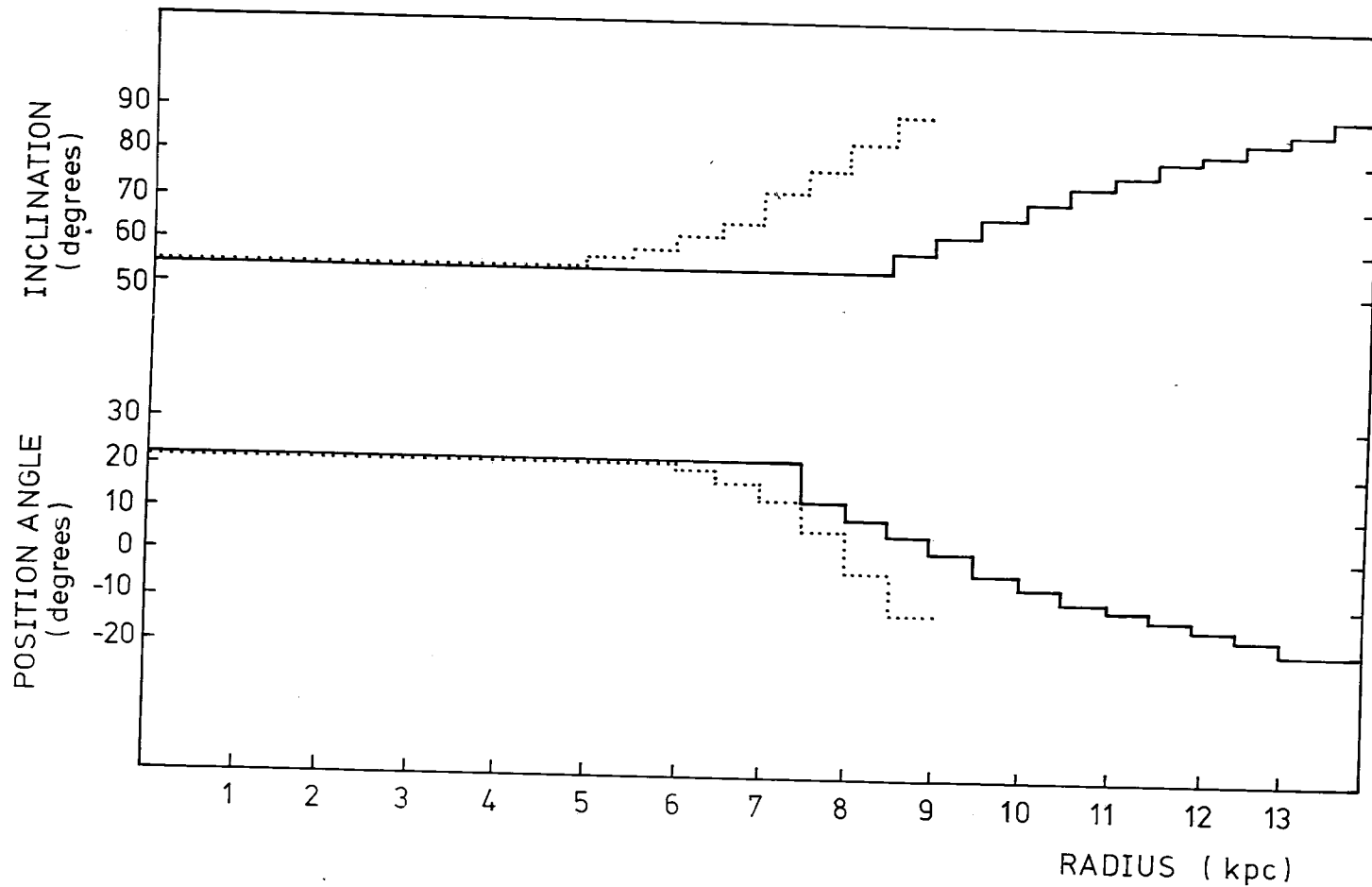


Figure 2.10 The parameters of a warped disc model of M33. The solid line represents parameters giving an optimum fit to the HI and radial velocity in both the NW and SE wings of M33. The dotted line is the model of Rogstad *et al.* (1976). Inclinations and PAs are defined relative to the plane of the sky (i.e. inclination 90° is edge-on; PA 0° is north-facing).

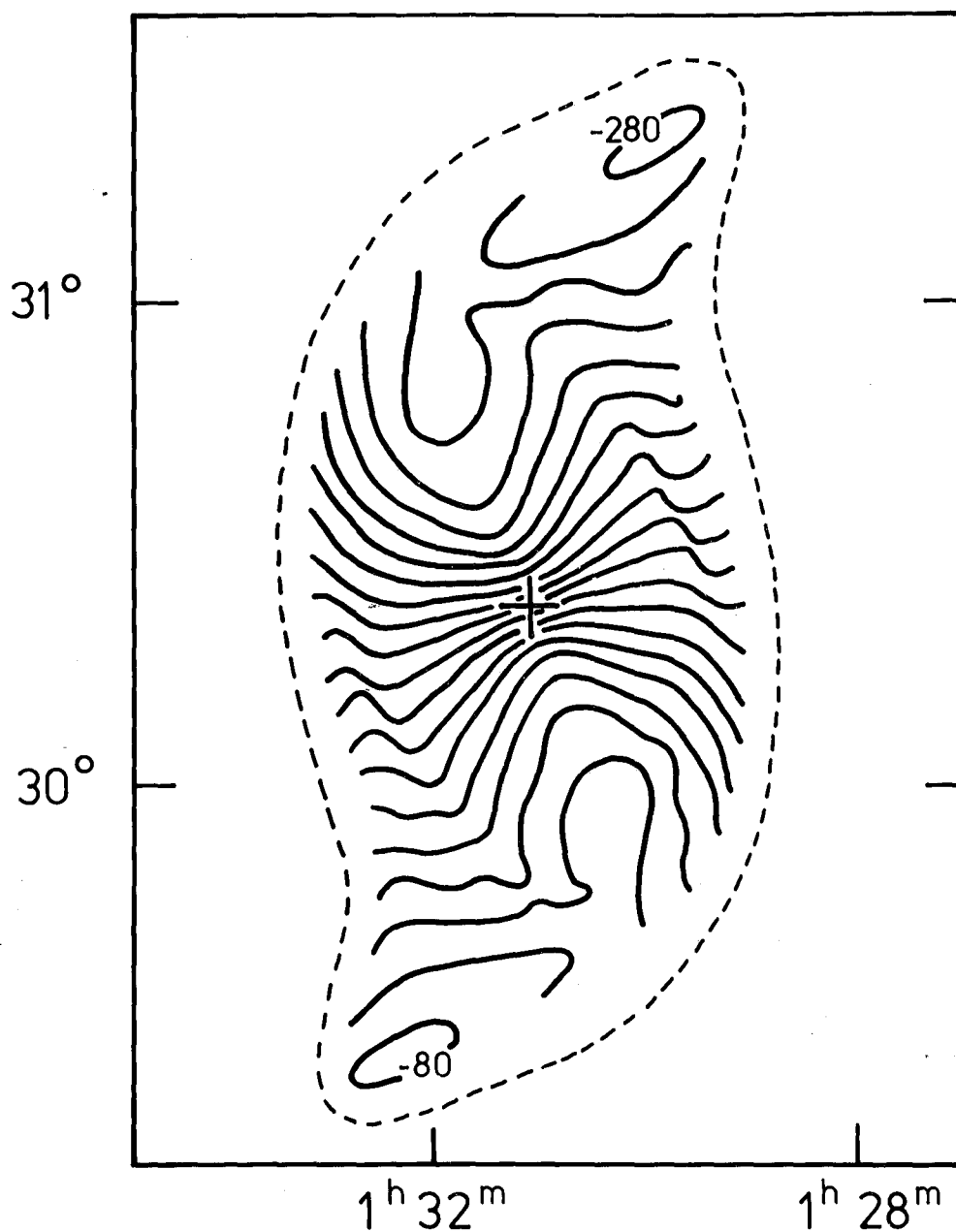


Figure 2.11 Radial-velocity distribution of the model of Fig. 2.10 (solid curve), surrounded by the approximate HI extent obtained by convolution of the model HI distribution with the telescope beam. This diagram should be compared with Fig. 2.6.

either one of the wings could be improved, but not without worsening the fit to the other. If the variation of PA and inclination in our model is extrapolated to greater radii, then velocities in the region of the 'NW turnover' are similar to those observed, but the extrapolated model cannot reproduce the exact velocity gradient or HI shape of the 'turnover' feature.

Such a model puts hydrogen in front of and behind the main disc, with radial velocities differing from those of the main disc ($R < 6$ kpc). One of the reasons given by Rogstad et al. for the rapid variation of inclination and of the major axis PA in their model was to obtain a gradient in radial velocity of the weak component across the disc steep enough to fit their observations. The model presented here displays a smaller gradient, but fits observations of the weak component by Rogstad et al. to about ± 20 km/s.

5 DISCUSSION

Although gravitational interaction between galaxies is capable of producing violent distortions of stars and gas (e.g. Hunter & Toomre 1969) there are, in the case of M33 and several other warped galaxies (e.g. Sancisi 1976), no obvious companions nearby. Since M33 is the warped galaxy for which we perhaps have the most detailed information concerning the kinematics of the bending phenomenon, it is important to discover whether or not a tidal explanation is possible.

In view of the gross distortions in M33, the most likely candidate for an interaction is M31 and evidence in favour of such an interaction is given below:

- (1) M31 is the nearest galaxy to M33.
- (2) Recently M31 has been found to be symmetrically warped in its outer parts (Newton & Emerson 1977). The distortions in M33 are relatively much more severe than in M31 as would be expected from the fact that M31 is 10 times more massive than M33. Calculations by Baldwin (1978) show that the ratio at which warping occurs in the two galaxies is consistent with a tidal origin.
- (3) The present separation of the two galaxies is only about 180 kpc or three times the HI diameter measured by Newton & Emerson (1977), and their radial velocities differ by only 64 km/s (corrected for galactic rotation).
- (4) Although the force currently exerted by M31 on M33 is unlikely to be large enough to have any significant effect, it is easy to envisage an orbit such

that M33 would have had a perigalacticon distance from M31 of about 40 kpc, some 1.3×10^9 yr ago (Baldwin 1978). This interval would correspond to about two rotation periods of M31 and M33 in the regions of the warps.

One of the factors affecting the lifetime of a warp is differential precession (Kahn & Woltjer 1959). Rogstad, Lockhart & Wright (1974) have discussed the effects of differential precession in relation to M83. Their model for the HI distribution in M83 is similar to that for M33, and they find that, for a reasonable mass distribution, the variation of position angle of the orbit with radius, after differential precession over a period of 2×10^9 yr, is not very different from the best-fitting values to their observations. Calculations of precession rate are highly dependent on the mass distribution at large radii, which is not known, but if warps can last for about 10^9 yr then the time scales for differential precession and an interaction between M33 and M31 may be consistent.

Two other theoretical explanations for the warping phenomenon which also involve an interaction with the medium external to the galaxy, are (i) accretion of intergalactic gas clouds (Haud, in preparation), (ii) the 'intergalactic wind' hypothesis of Kahn & Woltjer (1959), in which the pressure distribution around a galaxy caused by its movement relative to the intergalactic medium may result in symmetrical bending of the disc.

There are other explanations which treat the galaxy as an isolated system and the warping as an inherent instability (e.g. Lynden-Bell 1964). However, the HI clouds seen near M31 (Davies 1975; Newton & Emerson 1977), together with the 'NW

turnover' and large perturbations of HI in M33, are suggestive of an external interaction rather than an inherent instability. A tidal interaction between M31 and M33 is an attractive explanation for the warps. More sensitive observations of the gas around and between galaxies of the Local Group would be the best way of solving this problem.

6 CONCLUSIONS

The most important conclusions of this study are summarised here:

- (1) The HI 'wings' of M33 extend to 70 arcmin (14 kpc) from the nucleus, both to the NW and SE, with masses of 2.5×10^7 and $1.0 \times 10^7 M_{\odot}$ respectively. The total HI mass observed is $1.0 \times 10^9 M_{\odot}$.
- (2) Although the rotation is normal for $R < 6$ kpc, there are gross deviations from normal differential rotation in the outer parts of the galaxy reaching 70 km/s in the wings. The wings are not completely symmetrical in radial velocity or HI distribution.
- (3) A feature of $4 \times 10^6 M_{\odot}$ is detected, which runs perpendicular to the end of the NW wing and is continuous spatially and in radial velocity with the wing. No equivalent feature is detected in the SE.
- (4) While the eastern edge of the main HI disc has a sharp cut-off, the western edge has a 'plateau' of low-brightness emission, with large velocity dispersions.
- (5) A model (Figs 2.7B & 2.10) comprising HI in a set of inclined circular orbits indicates the sense and magnitude of the distortions in the outer regions of M33.
- (6) A gravitational interaction between M31 and M33 involving a close passage with perigalacticon of about 40 kpc, some 1.3×10^9 yr ago (Baldwin 1978), is a possible explanation for the large-scale distortions observed in both galaxies.

CHAPTER 3THE Scd GALAXY NGC 24031 INTRODUCTION

NGC 2403 is a bright Scd galaxy, and the illustration in The Hubble Atlas of Galaxies (Sandage 1961) is reproduced in Plate 3.1. It has an indistinct nucleus, broad and ill-defined spiral arms, pronounced resolution into stars, and closely resembles the local-group galaxy M33. The main optical parameters are summarized in Table 3.1.

NGC 2403 is at the western edge of the M81 group of galaxies, at a distance estimated by Tammann & Sandage (1968) as 3.25 Mpc. This value is adopted here, although values in the range 2.2 to 3.4 Mpc have been quoted elsewhere (Sandage & Tammann 1974; Madore 1976; Sandage & Tammann 1976).

The neutral hydrogen in NGC 2403 has been previously mapped at high resolution by Shostak & Rogstad (1973) and Love (1975). A comparison of the resolution and sensitivity of these and the present surveys is given in Table 3.2. Love's observations were made with the Half-Mile telescope; since then there has been a considerable improvement in sensitivity and velocity resolution (cf. chapter 1, section 2.1) and it was used again for the present survey. Both the spatial and velocity resolution of the latter are somewhat greater than that of Shostak & Rogstad's survey, although the sensitivity at this high resolution is not so good. Throughout this chapter the results of all these surveys are compared in detail.

An important aim of these observations was to investigate whether NGC 2403 possesses a large-scale warp similar to that seen in M33. The low-resolution maps from the present survey

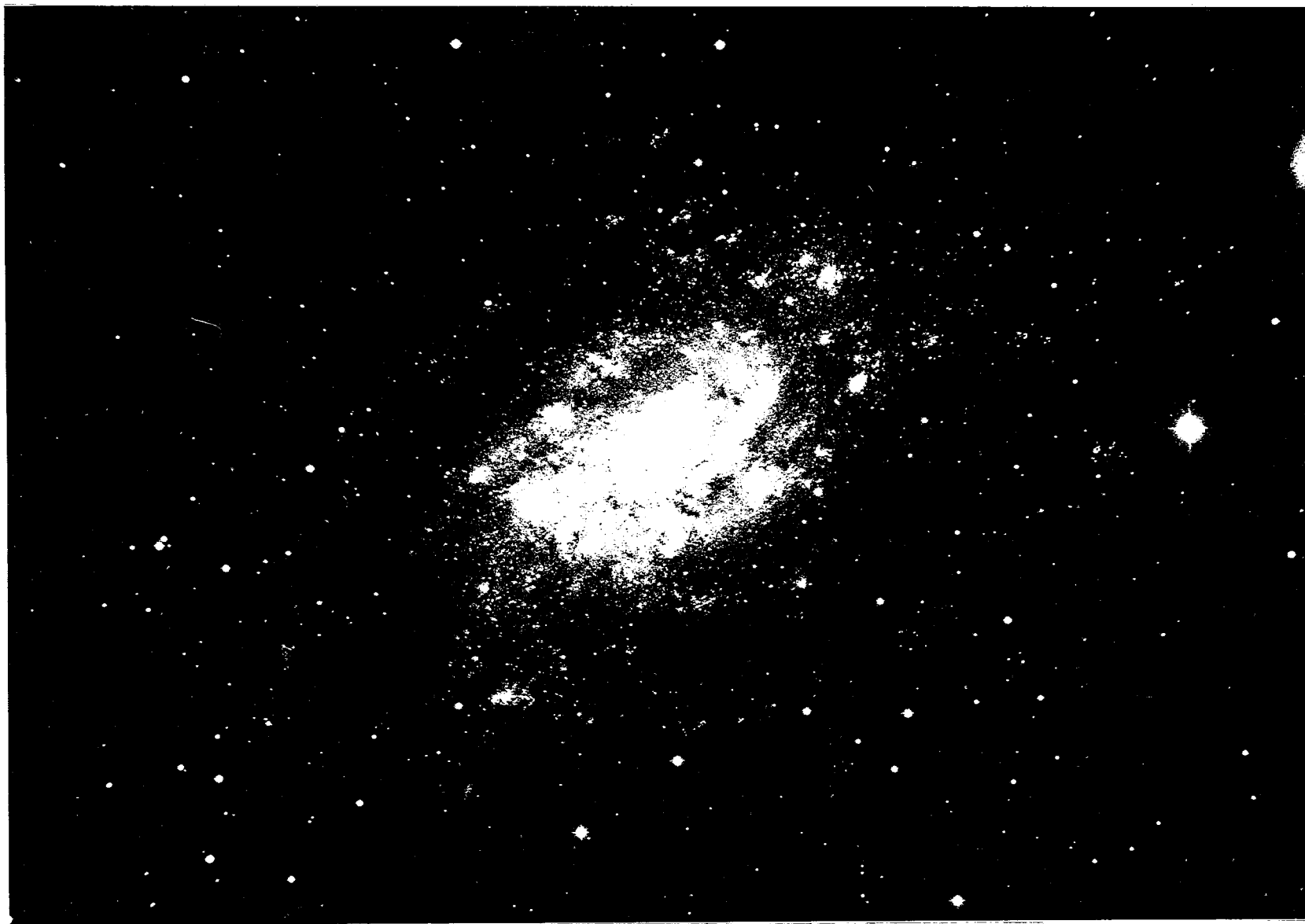


Plate 3.1 Photograph of NGC 2403 reproduced from The Hubble
Atlas of Galaxies. Copyright - Hale Observatories.

Table 3.1 Optical Parameters of NGC 2403

Parameter	Value
Coordinates of nucleus (1950)	
- RA	7 ^h 32 ^m .05
- dec	65 ^o 42'.7
Classification (revised type)	SAB(s)cd
Total 'face-on' B magnitude corrected for galactic and internal absorption	8.30
Isophotal major diameter corrected to 'face-on'	17.0 arcmin
Ratio of apparent major to apparent minor diameter	1.62±0.02
Heliocentric radial velocity	131±4 km/s
Corrected colour index (B-V)	0.37
Assumed distance [*]	3.25 Mpc

Notes: Values are from de Vaucouleurs *et al.* (1976)
except that marked ^{*}, which is from Tammann &
Sandage (1968).

Table 3.2 Comparison of recent aperture-synthesis observations of HI in NGC 2403.

Survey	Shostak & Rogstad (1973)	Love (1975)	Reakes (this chapter)
Resolution in RA (arcmin)	2.0	1.05	1.5
Velocity resolution of one channel (km/s)	21	39	16
Measured rms noise per beam area per channel	0.6	6.8	1.8

are more sensitive per beam area than those previously published, and are ideal for mapping low-brightness features such as warps.

The high-resolution maps were made with the aim of more clearly seeing the HI spiral structure, as a result of the improved resolution, and thus further testing the density wave theory.

2 OBSERVATIONS

The survey consisted (initially) of 12-hr observations at 60 equally-spaced interferometer baselines as indicated in Table 3.3. Results at some of the small baselines were subject to considerable interference from the Sun, mainly between hour angles (HA) 18^{h} and 21^{h} . The first six hours of these observations ($18^{\text{h}} \lesssim \text{HA} \lesssim 24^{\text{h}}$) were replaced by additional interference-free data, collected at a later time of the year. Although a small amount of data was lost due to residual 'spikes' of interference, almost complete coverage of the u-v plane was achieved.

The HI emission was measured using the digital spectrometer over a 2-MHz bandwidth. The output spectrum had a resolution of 16 km/s and was sampled at values of radial velocity separated by 13.2 km/s to provide 32 channel maps. Continuum radiation in the 10-MHz bandwidth was also measured and the surveys were calibrated by observations of 3C 309.1.

Channel maps were made at three different spatial resolutions by selecting different sets of interferometer baselines (Table 3.3). The maps made at low resolution were more sensitive to low-brightness features than those at the full resolution. A correction for continuum emission was made by forming a map of average continuum emission from those channel maps which contained no line emission (-73 to -7 km/s inclusive, 270 to 296 km/s inclusive, plus the channel at 322 km/s. The channels at 309 and 336 km/s were not included because they exhibited a greater than average noise level). The resulting map was then subtracted from each of the channel maps in turn to obtain continuum-free maps (Figs 3.1a, 3.1b and 3.1c).

Maps of integrated hydrogen, radial velocity, and velocity dispersion were made from the continuum-free channel maps in the way described in Chapter 1.

Table 3.3. Details of the observations of NGC 2403 with the Cambridge Half-Mile telescope.

Dates	1978 February			
Map centre (1950)	RA	7 ^h 32 ^m 01 ^s .20		
	dec	65° 42' 57".00		
Interferometer baseline				
	total number	60		
	smallest	12.2 m		
	increment	6.1 m		
	largest	298.7 m		
Calibration source	name	3C309.1		
	flux density	7.9 Jy		
	reference	Kellermann <u>et al.</u> (1969)		
Largest structure present		≤ 1°		
Diameter of first grating response		~ 2°		
Continuum	bandwidth	10 MHz		
	centre frequency	1419 MHz		
Hydrogen line	bandwidth	2 MHz		
	velocity range	-73 to +336 km/s (heliocentric)		
	channel separation	13.2 km/s		
	channel width	16 km/s (FWHP Gaussian)		
Number of interferometer baselines included				
		12	36	60
resolution	RA x dec (aromin)	7.4x8.1	2.5x2.7	1.5x1.6
		(low)	(medium)	(high)
Brightness temperature				
Conversion Factor (K/Jy)		4.15	33.6	91.3
Rms noise levels (mJy/beam)				
	continuum	2.8*	1.6*	1.2*
	one HI-line channel	46	26	20

Note * theoretical value

Figure 3.1 Channel maps of NGC 2403, free of continuum emission. The numbers at the top left of each box indicate the heliocentric velocity in km/s. The large cross is the map centre, and the small crosses are the positions of stars for alignment with optical photographs. The crosses are the same on subsequent figures. In all cases solid contours are positive, dashed contours are negative, and the zero contour has been omitted.

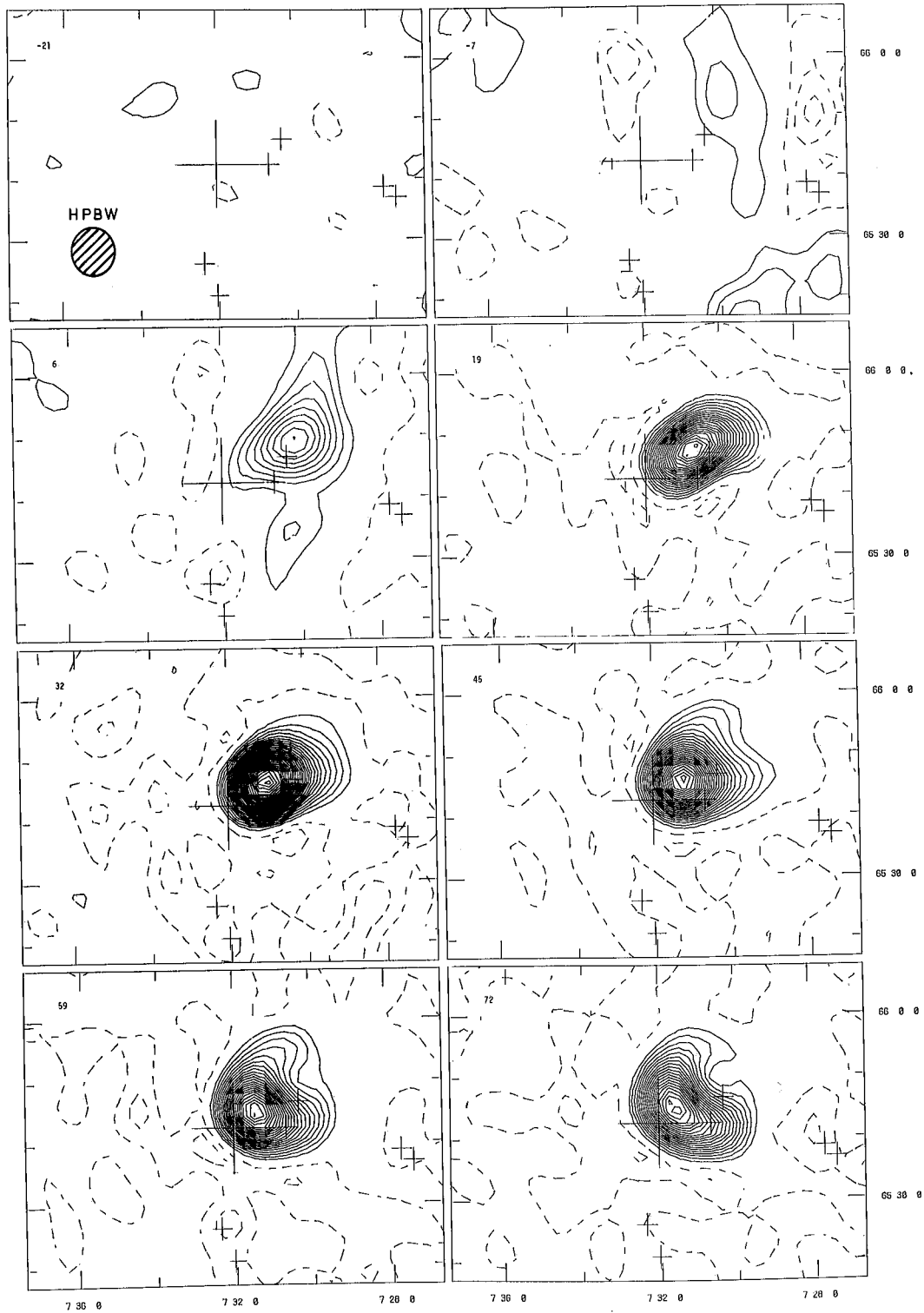


Figure 3.1a Resolution 7.4×8.1 arcmin, contour interval 50 mJy ($\sigma = 46$ mJy).

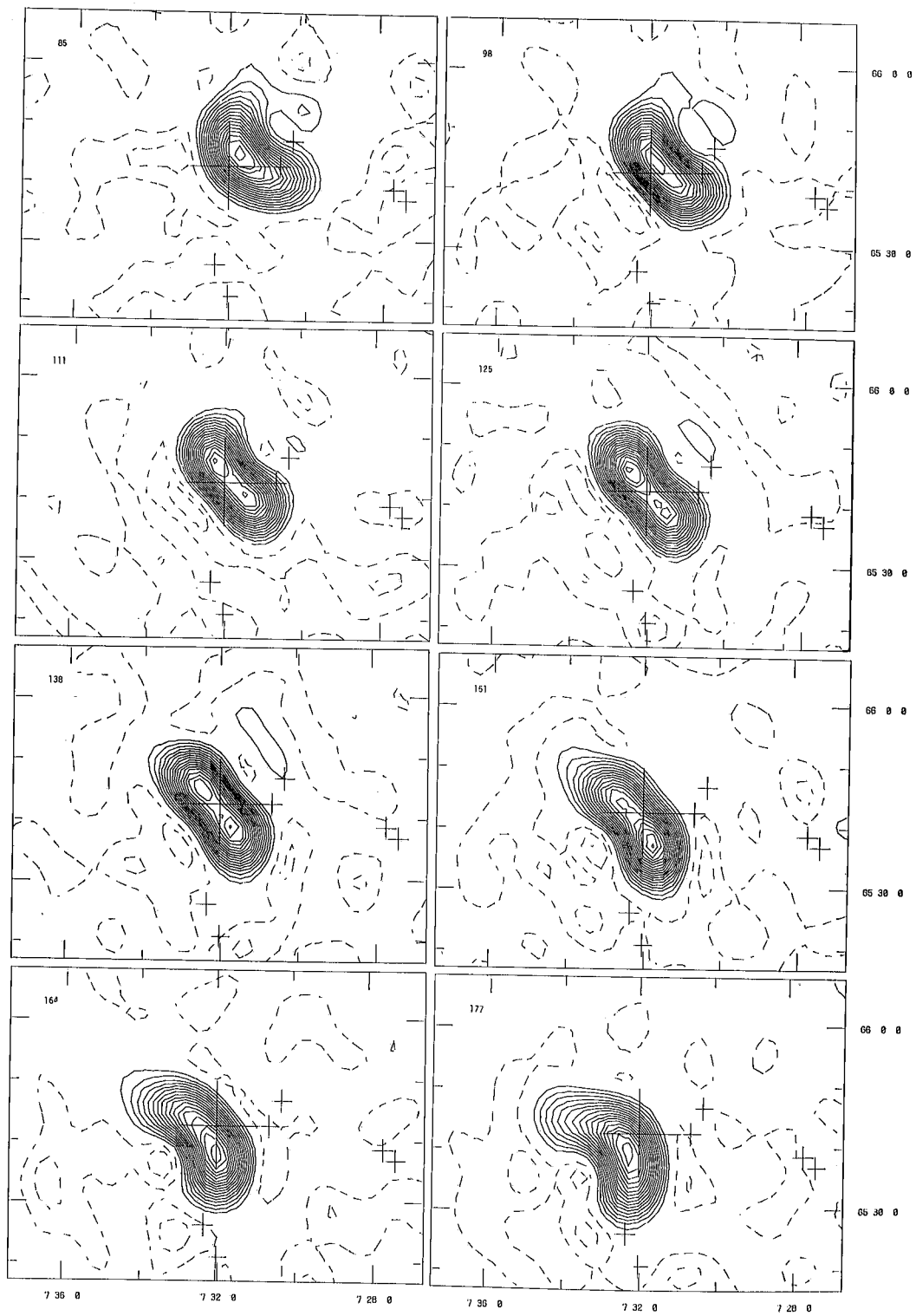


Figure 3.1a continued

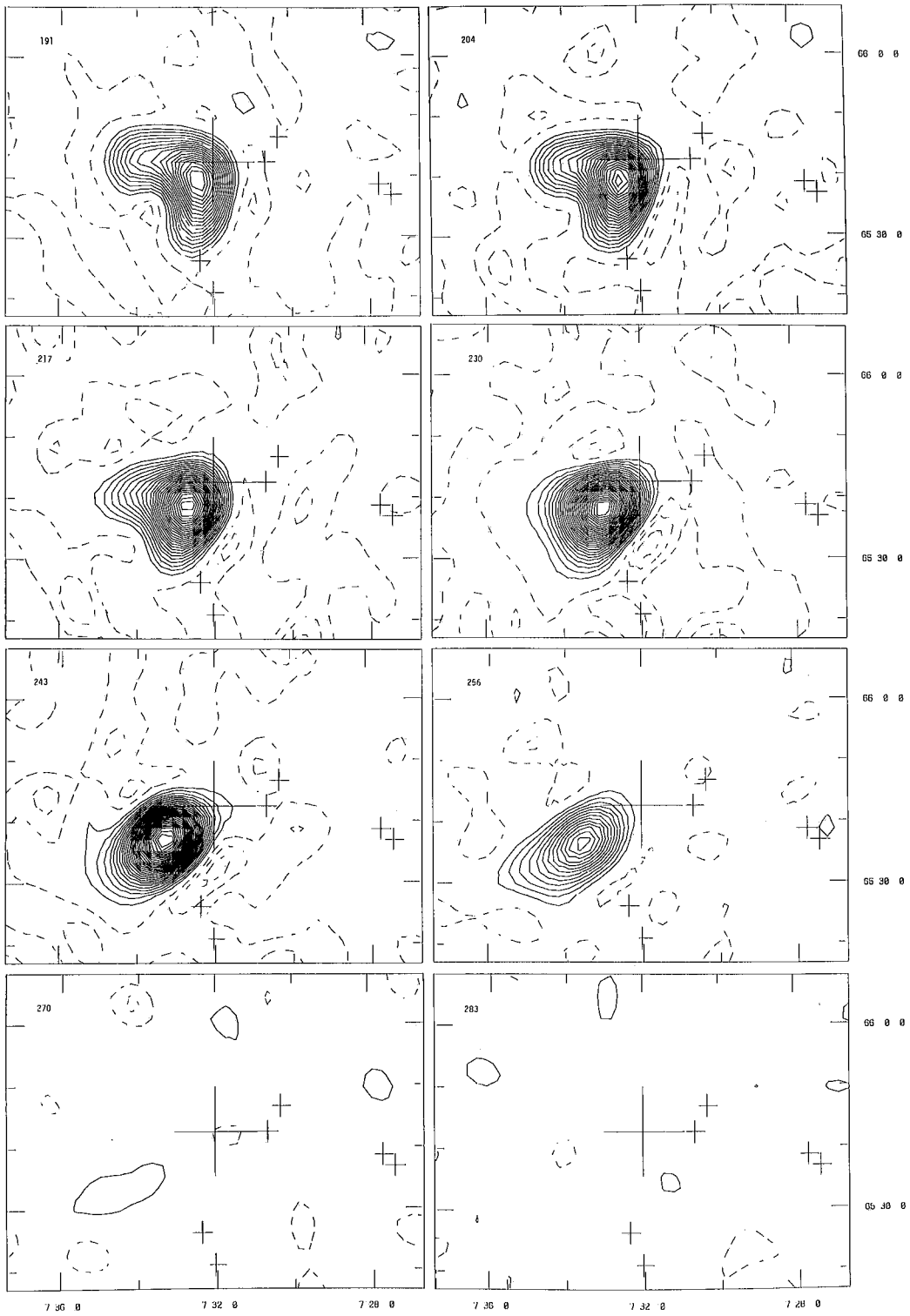


Figure 3.1a continued

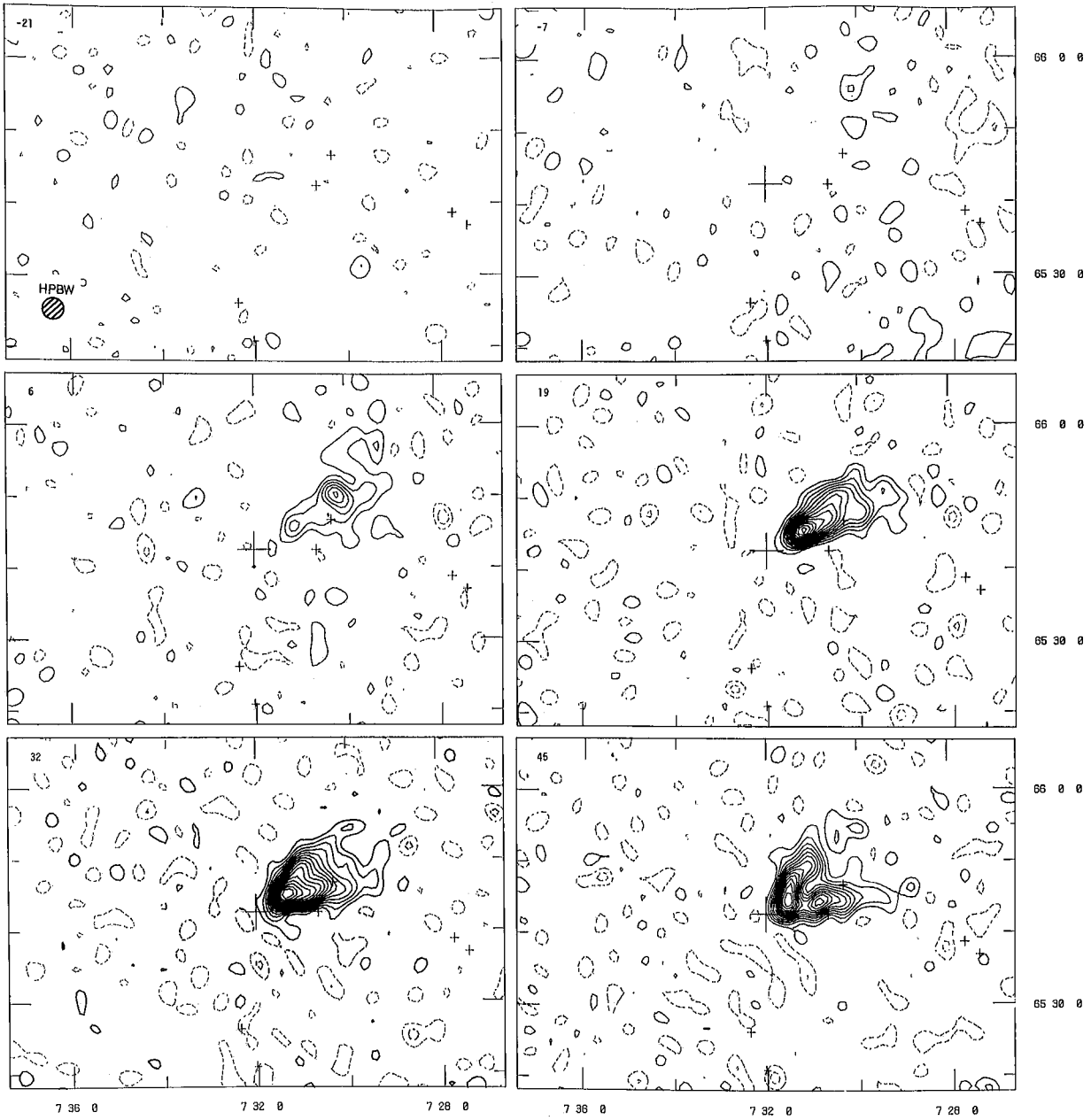


Figure 3.1b Resolution 2.5×2.7 arcmin, contour interval
50 mJy ($\sigma = 26$ mJy).

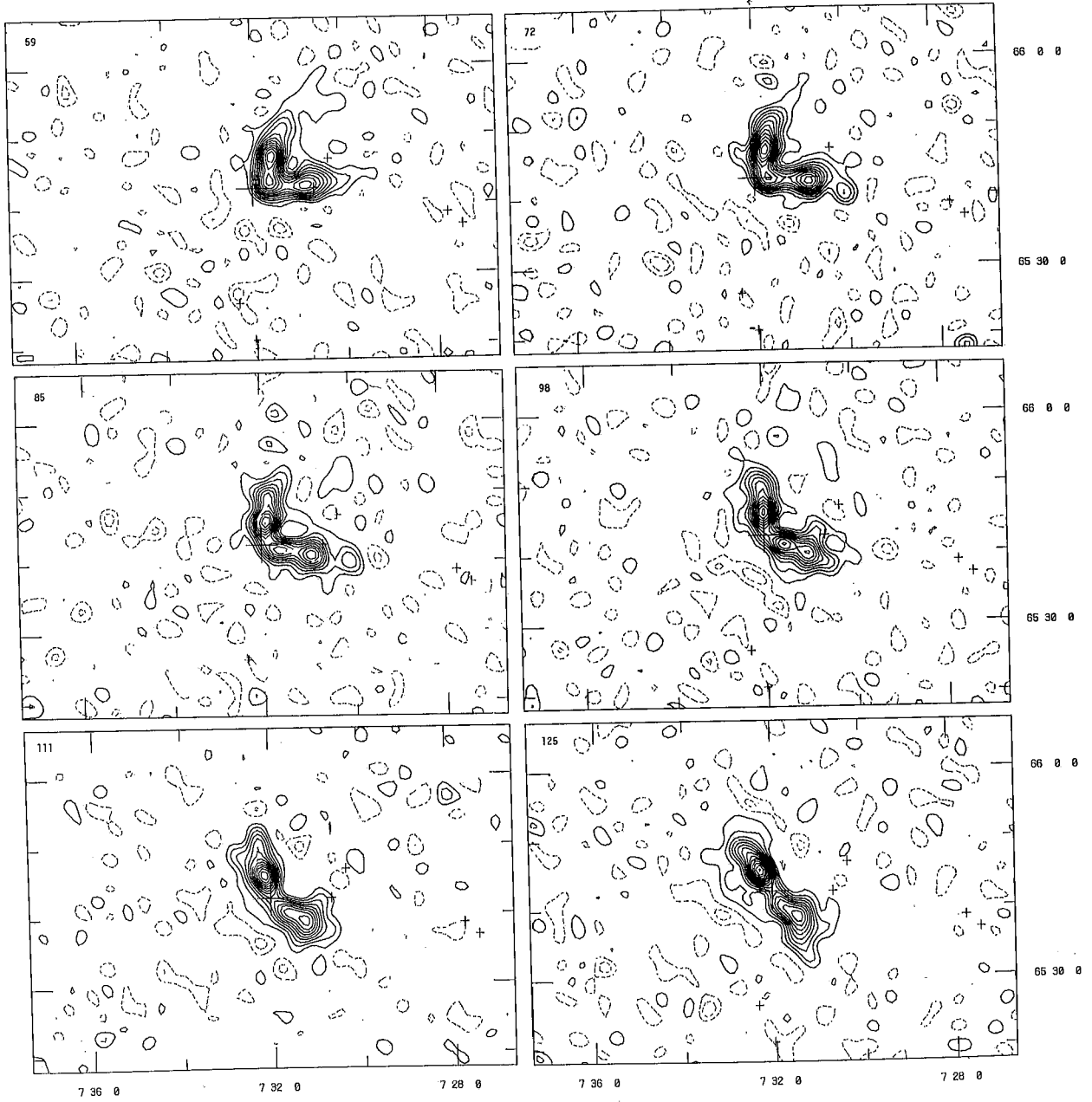


Figure 3.1b continued

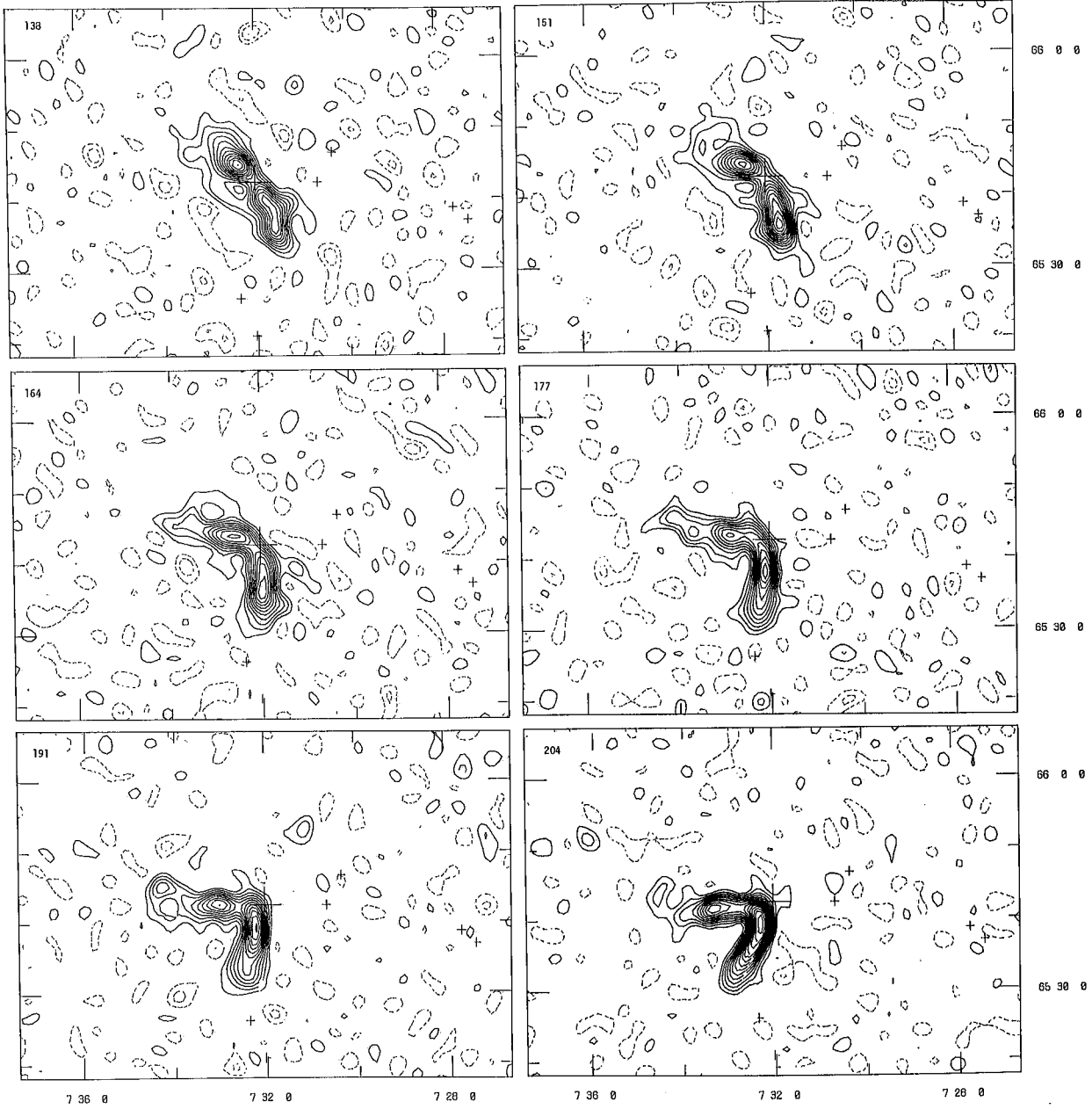


Figure 3.1b continued

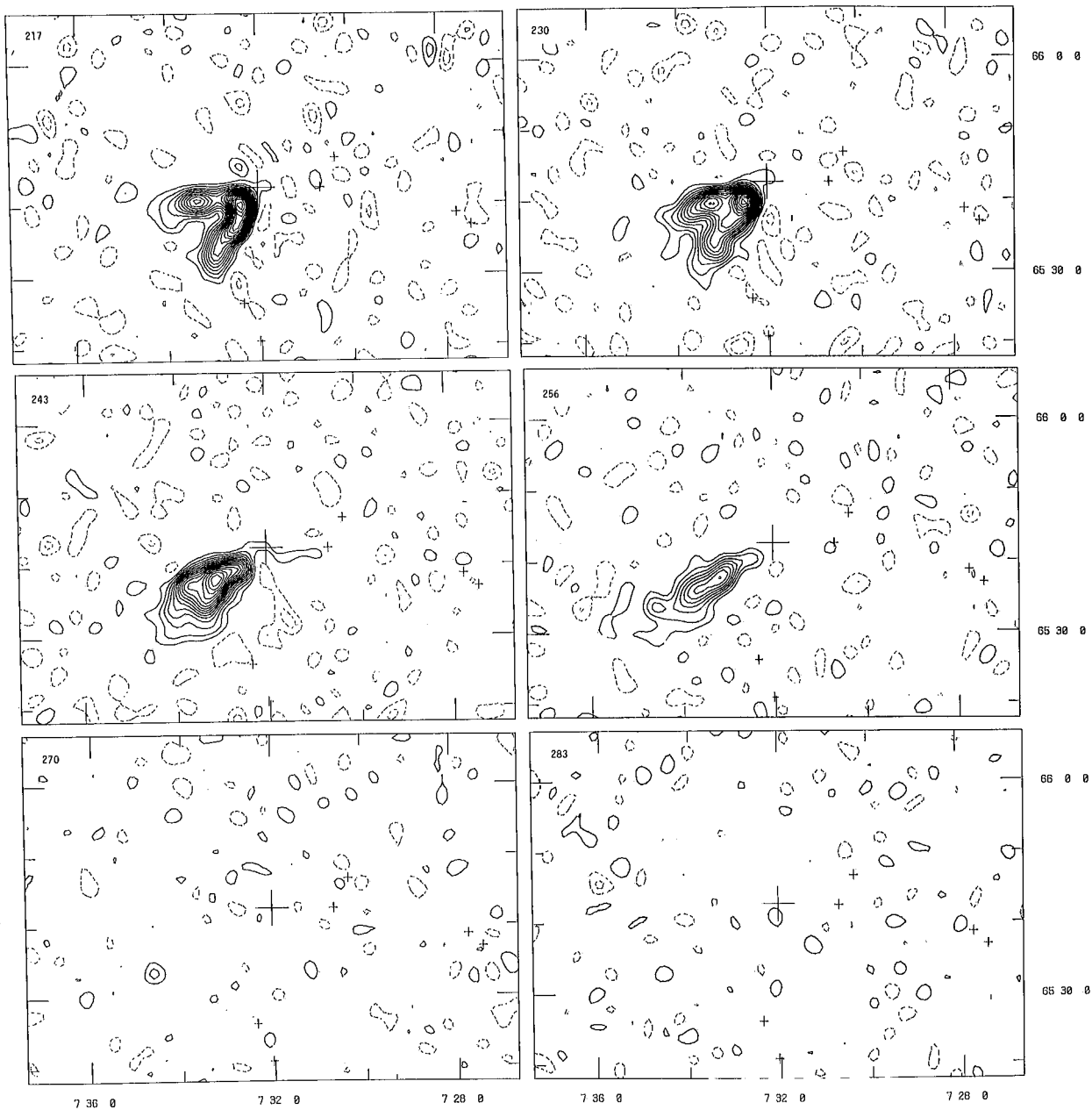


Figure 3.1b continued

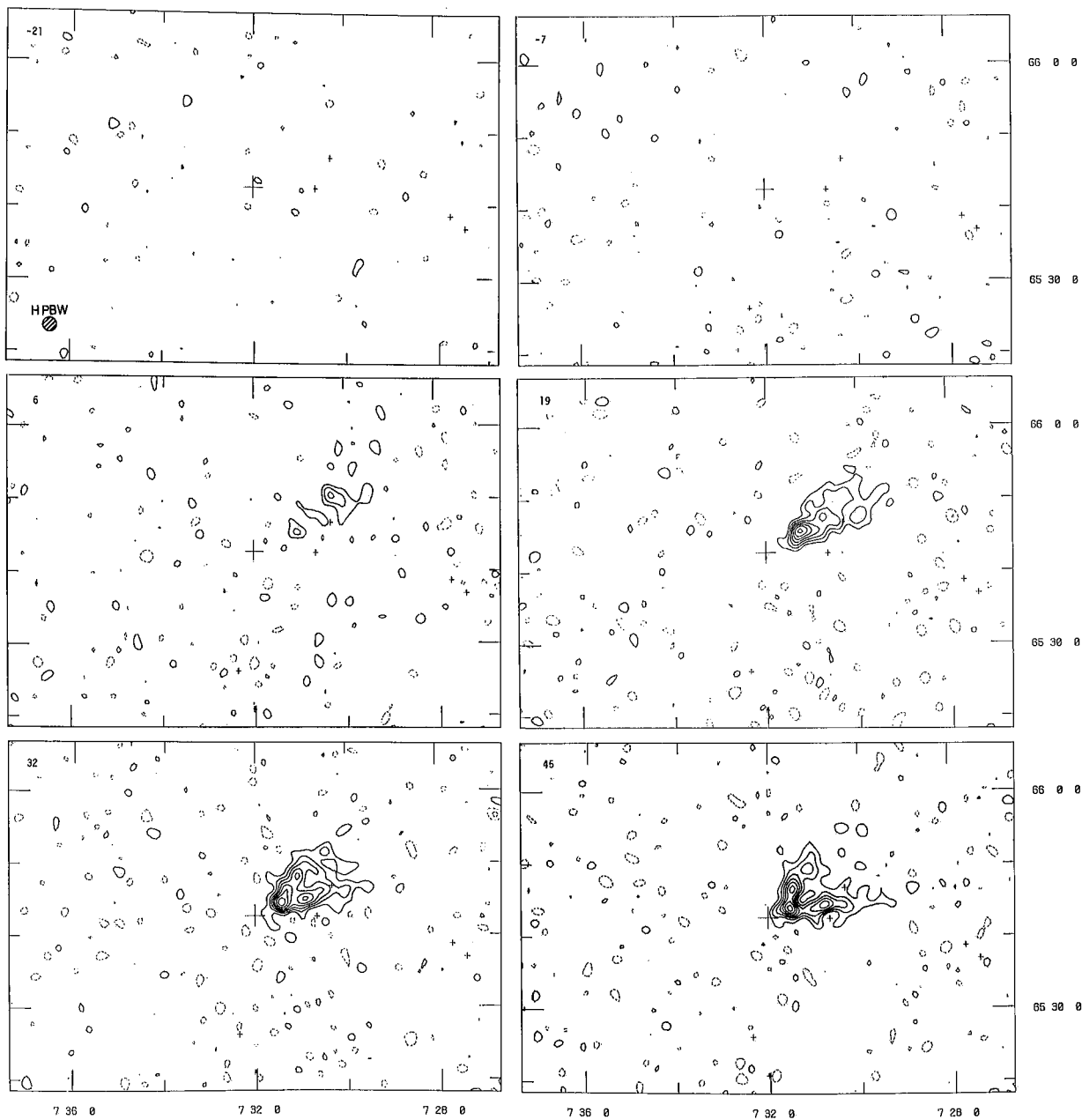


Figure 3.1c Resolution 1.5 x 1.6 arcmin, contour interval
50 mJy ($\sigma = 20$ mJy).

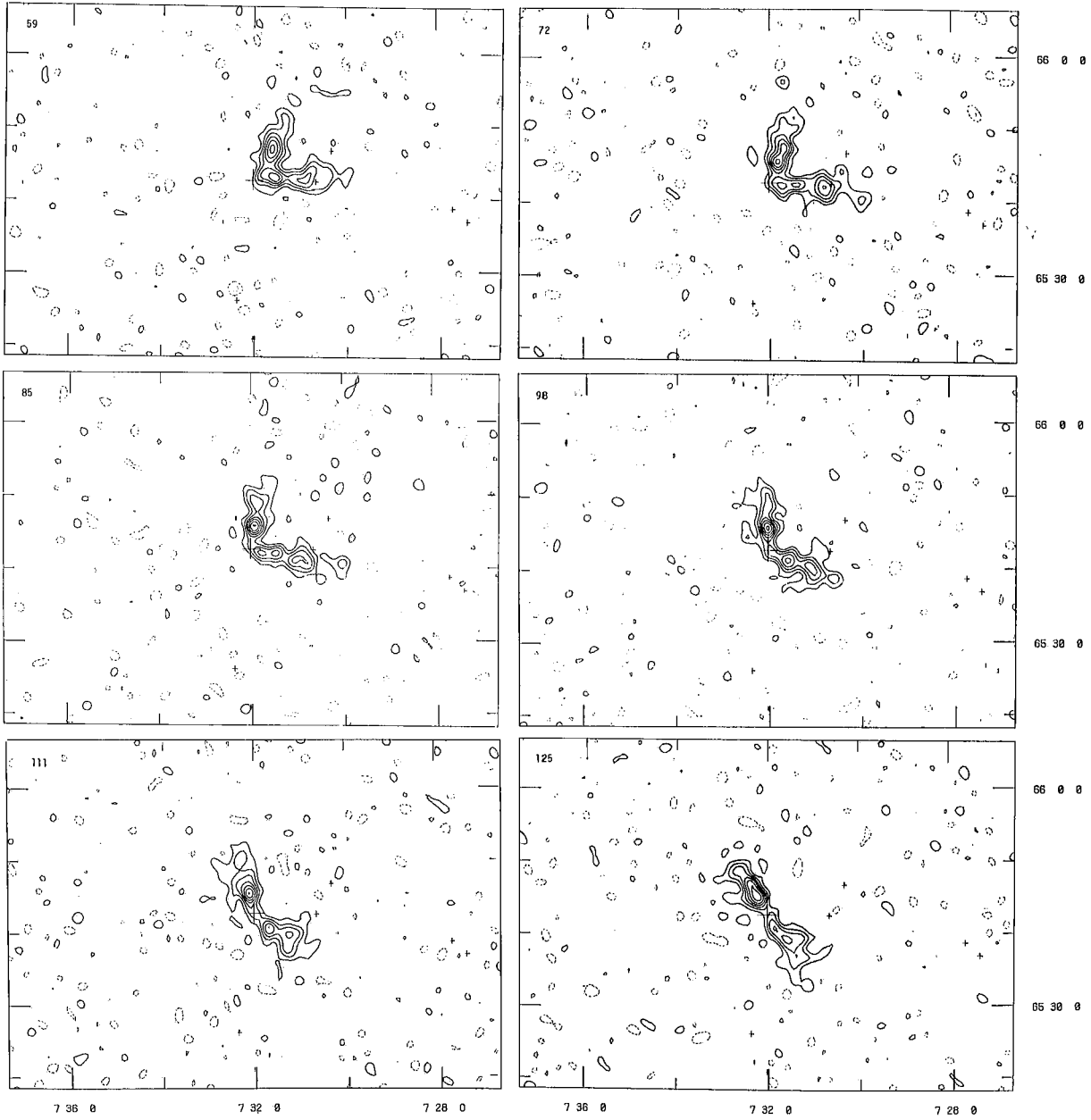


Figure 3.1c continued

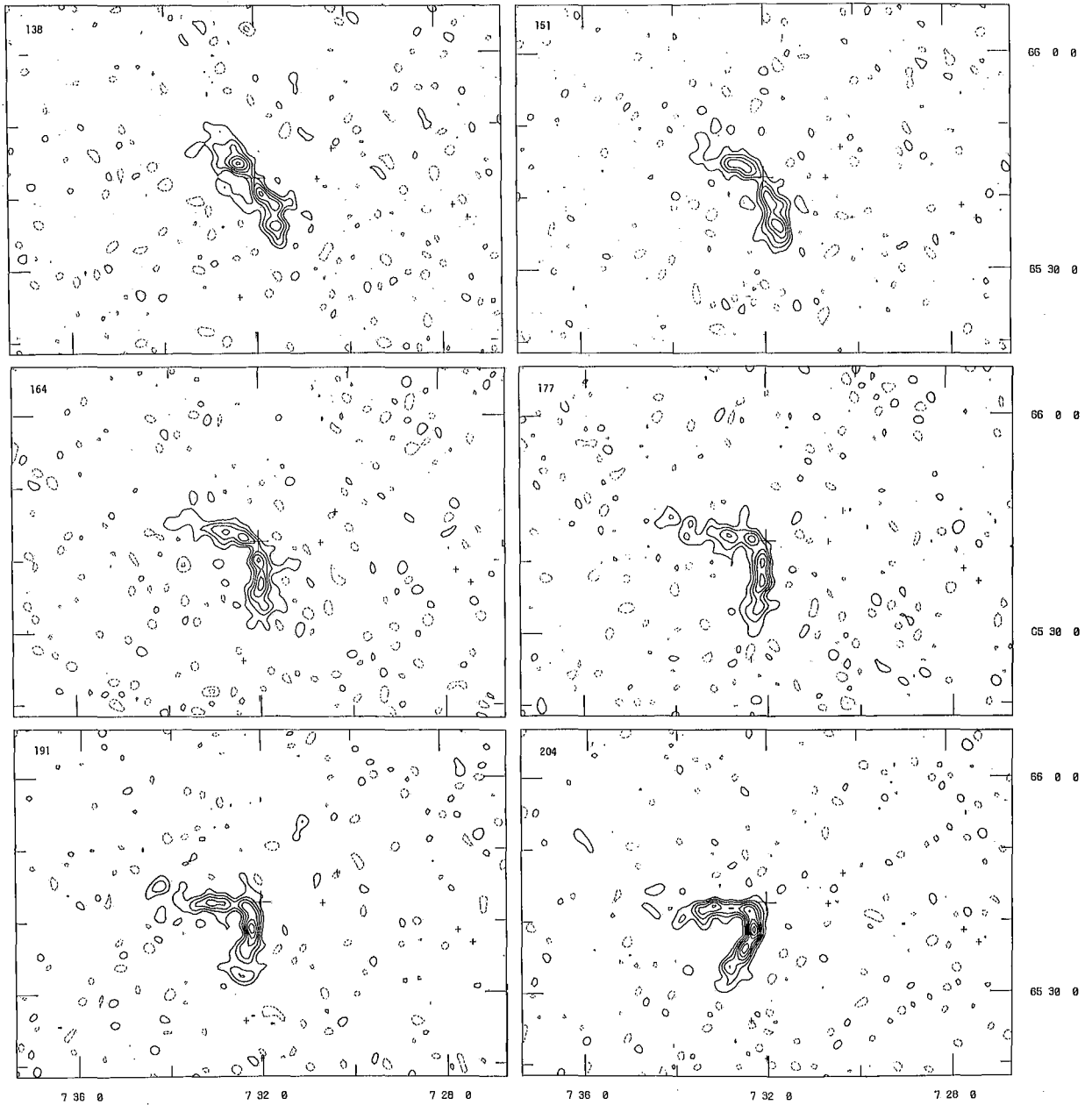


Figure 3.1c continued

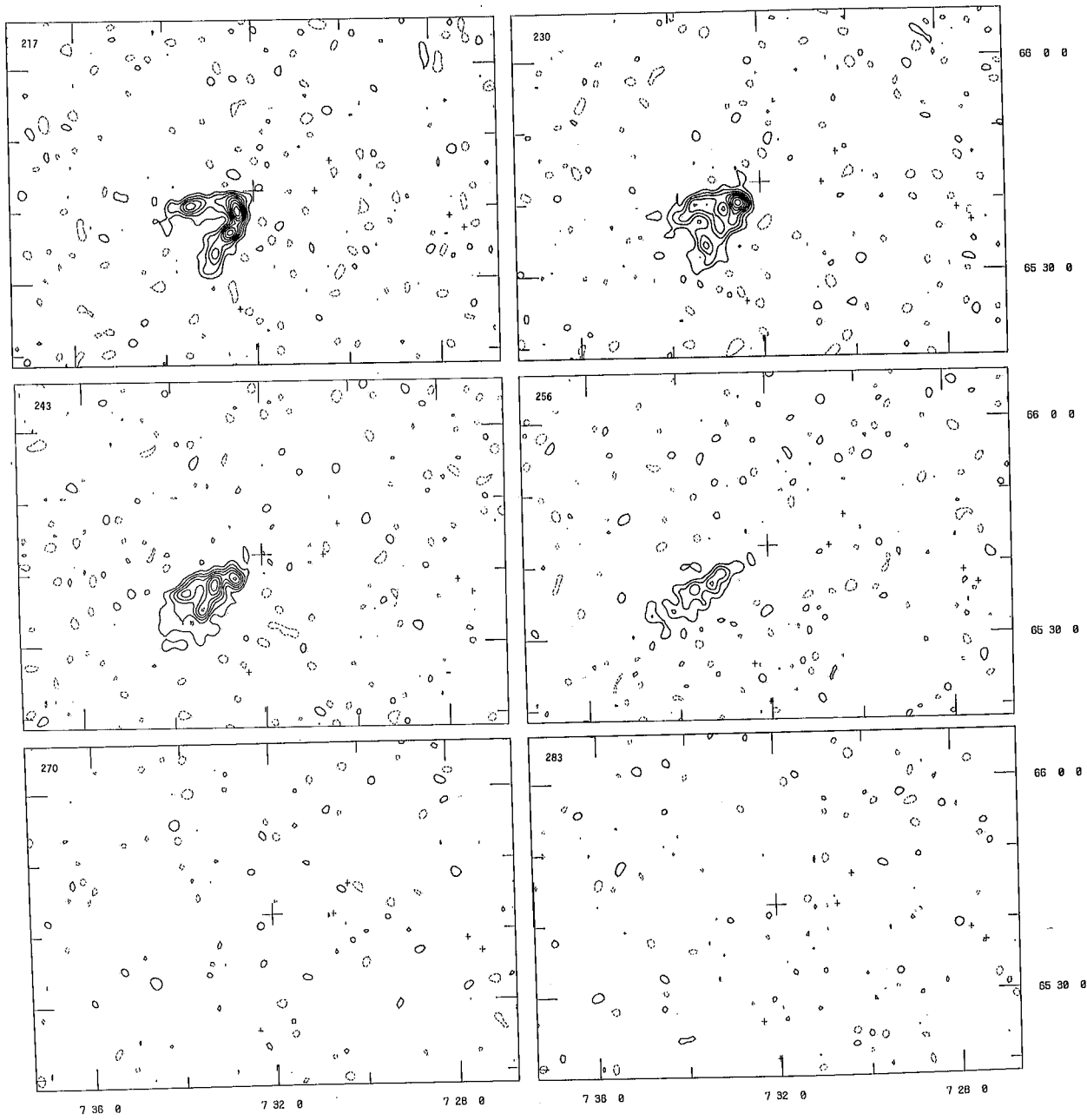


Figure 3.1c continued

3 RESULTS AND ANALYSIS

3.1 The total HI Mass

The integrated HI spectrum for NGC 2403 is shown in Fig. 3.2. This was constructed by integrating the flux from NGC 2403 observed in the continuum-free channel maps with a resolution of 7.4×8.1 arcmin (Fig. 3.1a). The area under the curve was used to evaluate the total HI mass, M_H , as described in section 2.4c of chapter one. M_H obtained in this way is $(3.2 \pm 0.3) 10^9 M_\odot$, in agreement with values obtained by other means. Table 3.4 includes a comparison of the M_H values of various authors. The values are consistent with the exception of those of Roberts (1962) and Burns & Roberts (1971), which are significantly higher. The discrepancy is probably the result of differences in calibration, rather than the absence of large-scale structure ($\approx 1^\circ$) in the present observations.

3.2 The HI distribution at low-resolution

The continuum-free HI maps at low resolution are shown as Fig. 3.1a, and have been combined to produce an integrated HI map (Fig. 3.3). These maps are more sensitive to low-brightness emission than the high-resolution maps presented later, and show emission clearly associated with NGC 2403 over the velocity range -7 to $+270$ km/s, and up to distances of 22 arcmin (21 kpc) from the nucleus (allowing for the beam size).

The channel maps at -7 and $+6$ km/s show, apart from the peaks of emission associated with NGC 2403 at RA $\sim 7^h 30^m$ & dec $\sim 65^\circ 50'$, other emission in the form of a 'spur' running both to the north and south for about 20 arcmin. This may be due to hydrogen in our Galaxy, as is almost certainly the case for emission at RA $\sim 7^h 28^m$ & dec $\sim 65^\circ 21'$ in the -7 km/s channel.

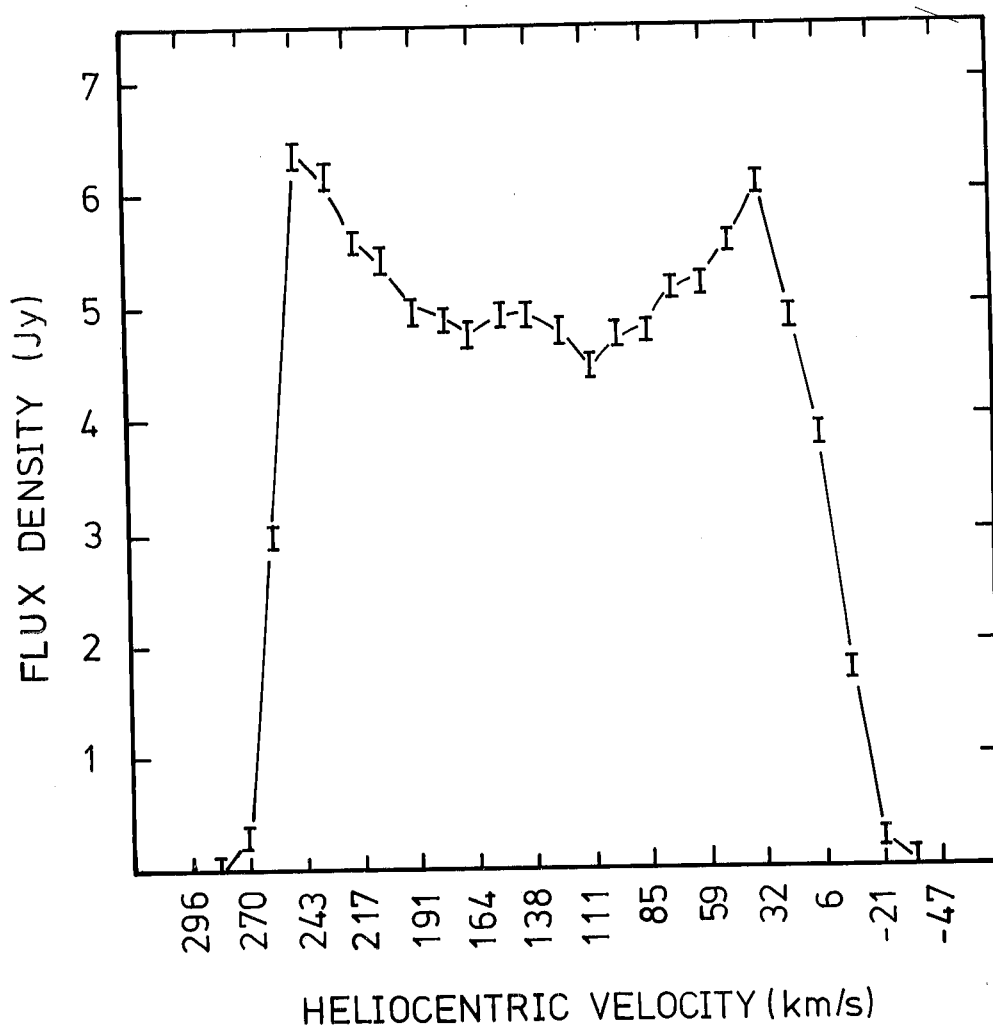


Figure 3.2 The integrated HI spectrum for NGC 2403

Table 3.4 Integral Parameters for NGC 2403

<u>Parameter</u>	<u>Value</u>	<u>References</u>
HI mass, M_H	$(3.2 \pm 0.3) 10^9 M_\odot$	this chapter
	$(3.2 \pm 0.4) 10^9 M_\odot$	Love (1975)
	$(3.5 \pm 0.7) 10^9 M_\odot$	Shostak & Rogstad (1973)
	$4.6 \times 10^9 M_\odot$	Burns & Roberts (1971)
	$4.6 \times 10^9 M_\odot$	Roberts (1962)
Total mass, M_T		
	R < 18 arcmin	$(4.0 \pm 1.6) 10^{10} M_\odot$ Fig. 3.15
	R < 13.5 arcmin	$(3.3 \pm 0.5) 10^{10} M_\odot$ Fig. 3.15
	R < 13.5 arcmin	$(3.6 \pm 0.3) 10^{10} M_\odot$ Shostak & Rogstad (1973)
R < 21 arcmin	$(4.1 \pm 0.9) 10^{10} M_\odot$ Love (1975)	
Luminosity, L	$6.7 \times 10^9 L_\odot$	Seielstad & Whiteoak (1965)
M_H/L	$0.48 \pm 0.04 M_\odot/L_\odot$	this table
M_T (R < 18 arcmin)/L	$6.0 \pm 2.4 M_\odot/L_\odot$	this table
	6.1 M_\odot/L_\odot	Love (1975)
M_H/M_T (R < 18 arcmin)	0.08 ± 0.04	this table
	0.08 ± 0.03	Love (1975)

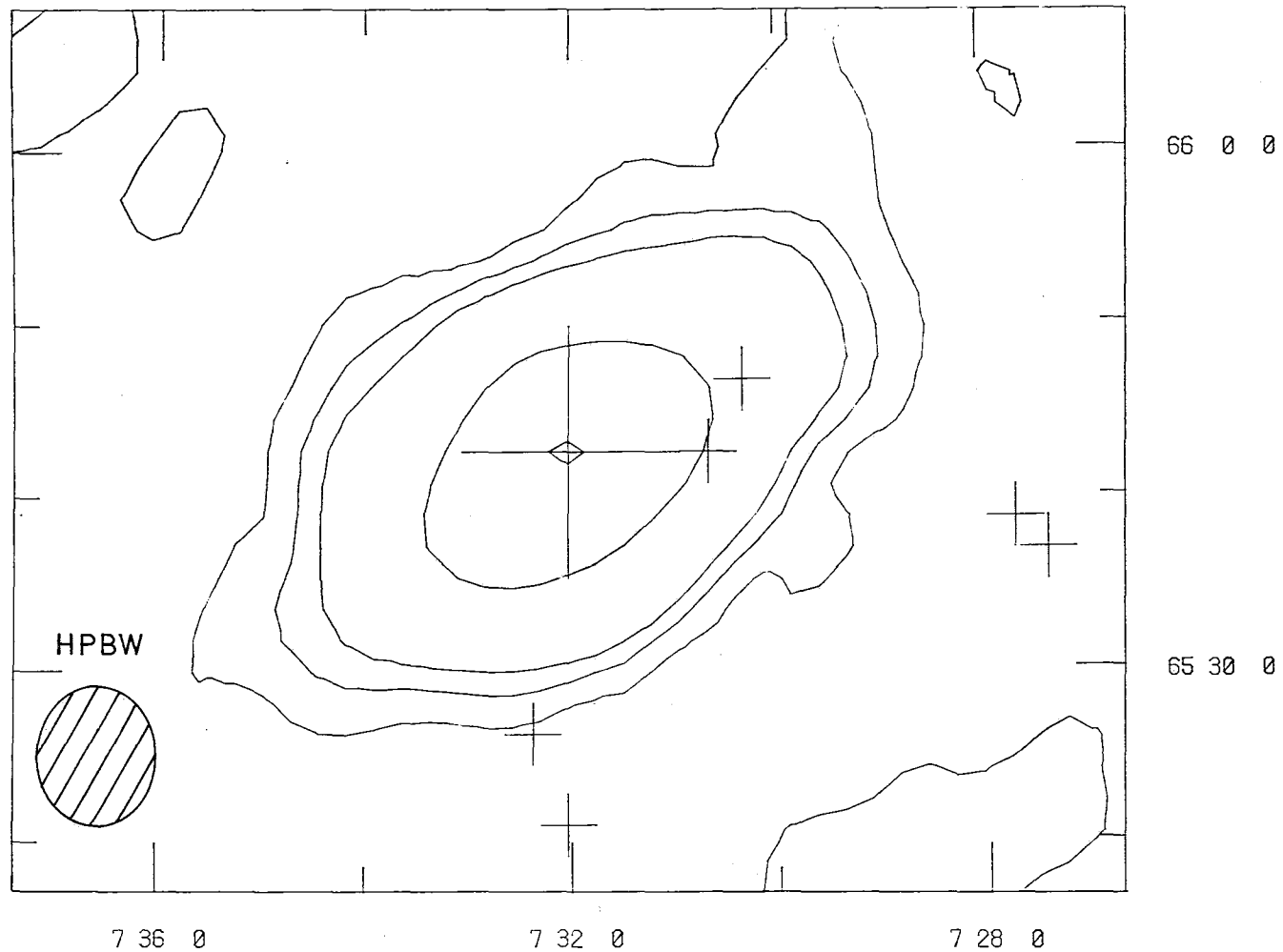


Figure 3.3 Integrated HI map of NGC 2403 at a resolution of 7.4 x 8.1 arcmin (hatched ellipse). The contours are 10, 50, 100, 500, and 1000 K km/s. The gate employed in construction was 80 mJy ($\sim 2\sigma$).

All the channels from 85 to 138 km/s show a region of low-brightness emission about 15 arcmin to the NW of the bright emission associated with normal differential rotation. This feature is isolated at velocities 98-138 km/s and shows little systematic change in position from channel to channel, except where it blends with the brighter emission at 85 km/s. It is possible that this feature is an instrumental artefact, although it does not possess the characteristics of either a spatial or a frequency sidelobe. There is no sign of a corresponding feature in the south of NGC 2403.

Recent work (cf. section 1.4 of chapter 1) has shown that the HI in many nearby spiral galaxies is warped out of the plane of the optical disc. A particularly severe warp is seen in M33 (chapter 2), a galaxy which closely resembles NGC 2403 in optical appearance and is of similar Hubble type. Other physical properties of M33 and NGC 2403 are compared in Table 3.5. The values of the parameters for NGC 2403 depend upon its distance which lies in the range 2.2-3.4 Mpc (with 3.25 Mpc adopted elsewhere in this chapter). M33 and NGC 2403 have very similar properties if the latter is assumed to be at a distance of 2.2 Mpc and, if a warp of magnitude similar to that of the NW wing of M33 existed in NGC 2403, it would be detected in the channel maps (Fig. 3.1a) at about the 1σ level. The adoption of 3.25 Mpc as the distance to NGC 2403 implies that it is a galaxy of about twice the size of M33, and any warp would have to be correspondingly larger to be detected at the same confidence level.

The present observations show some evidence for a large-scale warp in NGC 2403. Direct evidence can be seen in the channels at 19 and 32 km/s (Fig 3.1a) which show emission

Table 3.5 Comparison of the properties of M33 and NGC 2403.

PARAMETER	M33	NGC 2403	NGC 2403
distance (D)	0.69 Mpc	2.2 Mpc	3.25 Mpc
optical diameter ^{*1}	15.9 kpc	17.2 kpc	25.3 kpc
luminosity ^{*2} ($\propto D^2$)	$2.9 \times 10^9 L_{\odot}$	$2.7 \times 10^9 L_{\odot}$	$6.0 \times 10^9 L_{\odot}$
HI diameter	~ 28 kpc	~ 28 kpc	~ 42 kpc
M_H ($\propto D^2$)	$1.0 \times 10^9 M_{\odot}$	$1.5 \times 10^9 M_{\odot}$	$3.2 \times 10^9 M_{\odot}$
Rotation curve	~ 107 km/s beyond 6.5 kpc	~ 130 km/s beyond 10 kpc	as for 2.2Mpc
M_T ^{*3} ($\propto D^1$)	$2.9 \times 10^{10} M_{\odot}$	$3.9 \times 10^{10} M_{\odot}$	$5.8 \times 10^{10} M_{\odot}$

*1 Photometric diameter reduced to face-on view at the galactic pole (Balkowski 1973)

*2 Intrinsic luminosity reduced to face-on view at the galactic pole (Balkowski 1973)

*3 Indicative total mass (Balkowski 1973)

bending westward at the north-western edge. At the southern end of the galaxy, emission at 243, 256 and 270 km/s shows a marginal bend in the opposite sense. Indirect evidence of warping is also provided by the skewing of the velocity contours on the higher resolution maps (section 3.6.4).

More sensitive observations are required for a detailed study of warping in NGC 2403. Huchtmeier (1975) has made very sensitive observations of the HI along the major axis of NGC 2403 in order to obtain details of the rotation curve in the outer parts. His rotation curve is flat at large radii, while the warp in M33 produced rotation velocities along the major axis which dropped steeply at large radii unless the distortions due to the warp were taken into account (cf. Fig. 2.7a in chapter 2). Nevertheless, these facts do not preclude a large-scale warp in NGC 2403 of a different geometry.

If one accepts that NGC 2403 is warped, one may speculate that the 'spurs' of emission, previously assumed to be Galactic, are really associated with the warp. Similarly the isolated feature seen on the channels at 98-138 km/s and which blends with the bright emission at 85 km/s may also be associated with the warp; similar extensions to the bright emission were seen in the channel maps of M33 (e.g. the -227 km/s channel in Fig. 2.4a of chapter 2). Further interpretation of both features is not justified without better observations.

3.3 The HI distribution at moderate resolution

The integrated HI map made from the smallest 36 spacings is shown in Fig. 3.4. This map is in excellent agreement with that presented by Shostak & Rogstad, and both maps show the distinctive 'ring' of three peaks of emission surrounding the nucleus, although there is a difference in the relative heights

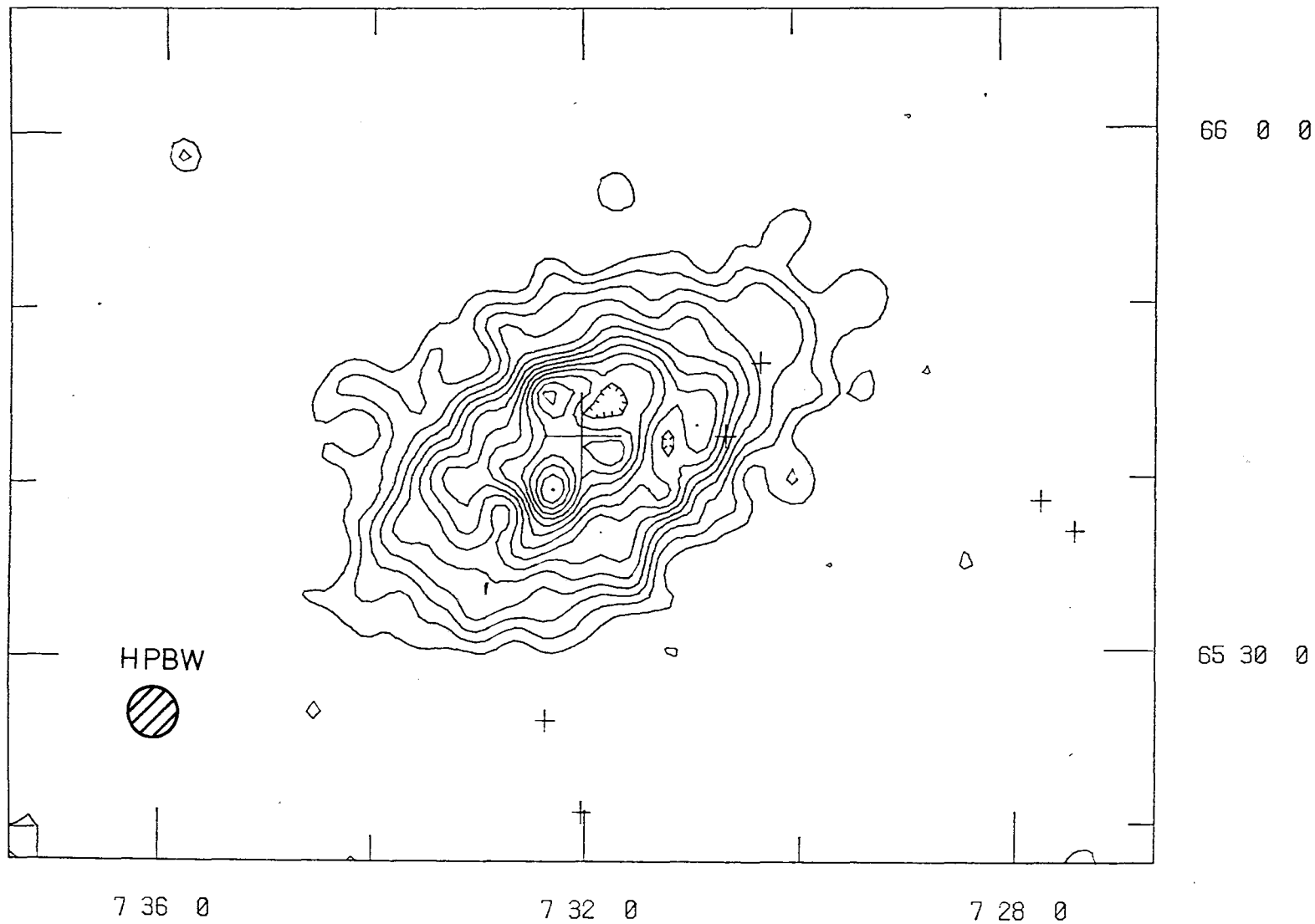


Figure 3.4 Integrated HI map of NGC 2403 at a resolution of 2.5×2.7 arcmin (hatched ellipse). The first contour is 100 K km/s and higher contours are at intervals of 100 K km/s. The gate employed in construction was 50 mJy ($\sim 2\sigma$).

of the three peaks, the westernmost peak being relatively less bright on the present map. The general reliability of the two maps is confirmed by the similarity of many features, including some at low-brightness levels. Common features include:

- (1) The depressions between the two brightest peaks.
- (2) The ridge running SW from the westernmost peak.
- (3) The low-brightness ridge running eastwards at the NE edge of the galaxy.
- (4) The trough running North-South to the east of the easternmost peak.
- (5) The NS ridge to the W of the westernmost peak.
- (6) The ridge running NE from the northernmost peak.

3.4 The HI distribution at high resolution

3.4.1 INTRODUCTION

The full-resolution integrated HI map is shown in Fig. 3.5 and Plate 3.2. The map shows a ridge of HI, not previously detected, which starts near the nucleus and spirals outwards, anticlockwise through $\sim 180^\circ$, towards the limit of detected HI at the northern edge of the galaxy. The broad arm which runs NW-SE from the northernmost HI peak is a feature mentioned by Shostak & Rogstad.

The radial distribution of the HI is analysed in Sec. 3.4.2, and asymmetries in Sec. 3.4.3. A detailed discussion of the HI spiral structure is presented in Sec. 3.4.4 (see also Sec. 3.6.4 for velocity perturbations associated with spiral structure), and the correlations of spiral arms with HII regions and dust are examined in Sections 3.4.5 and 3.4.6.

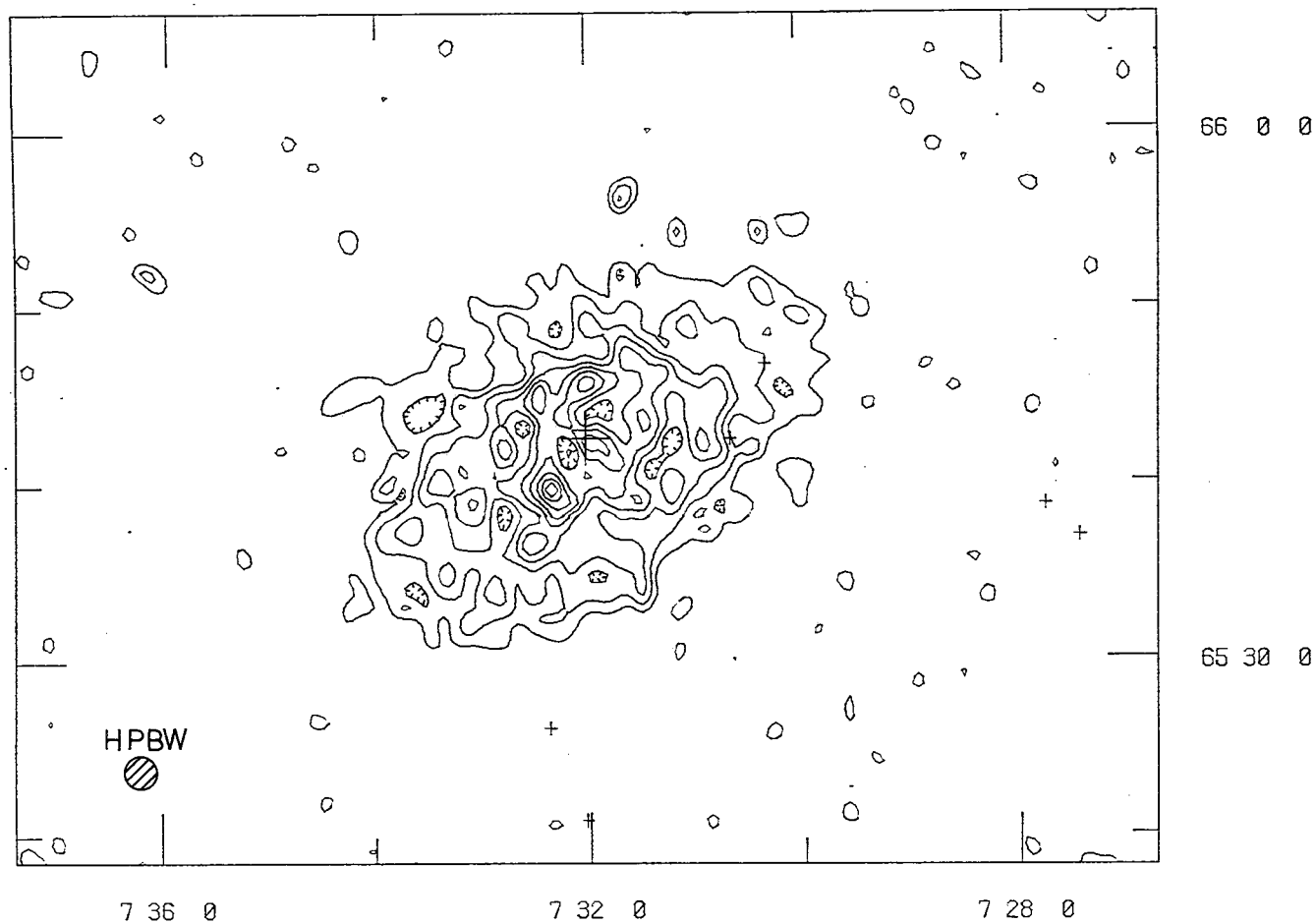


Figure 3.5 Integrated HI map of NGC 2403 at a resolution of 1.5 x 1.6 arcmin (hatched ellipse). The first contour is 200 K km/s and higher contours are at intervals of 200 K km/s. The gate employed in construction was 30 mJy (~1.5 σ).

3.4.2 RADIAL DISTRIBUTION

The variation of HI brightness with radius is shown in Fig. 3.6. This has been derived by sampling the high-resolution map (Fig. 3.5) in ellipses in the sky, corresponding to an inclination of 60° and a position angle of the major axis of 125° (i.e. the dynamic parameters found by Shostak 1973 - see section 3.6.2). The points plotted are the mean of twenty sampling points around each ring, and the rings are separated by 1 arcmin.

The radial distribution of HI presented by Love (1975) at a resolution of 1.5 arcmin is in good agreement with Fig. 3.6, which shows a fairly flat distribution out to a radius $R = 4$ arcmin, although a slight minimum is evident at $R = 2$ arcmin. Beyond $R = 4$ arcmin the HI brightness falls off steeply to about $R = 7$ arcmin, where the gradient becomes less steep. (The edge of the optically bright galaxy is at $R = 4.8$ arcmin).

Okamura, Takase & Kodaira (1977) have performed detailed surface photometry of NGC 2403 and note a 'ring-like' region ($2 \text{ arcmin} < R < 4 \text{ arcmin}$) with an excess of B luminosity relative to the smooth exponential distribution. The ring is just inside the ring of three bright HI peaks on Fig. 3.4, and Okamura *et al.* suggest that it may be due to the presence of abundant young stars.

Love (1975) also presents the radial distribution of HI at a resolution of 63×68 arcsec and claims that this reveals a central minimum. It is likely that this result is spurious, and due to the high noise level of his maps. No such minimum is apparent from his data at a resolution of 1.5 arcmin. There is no significant central minimum in the HI distribution in M33.

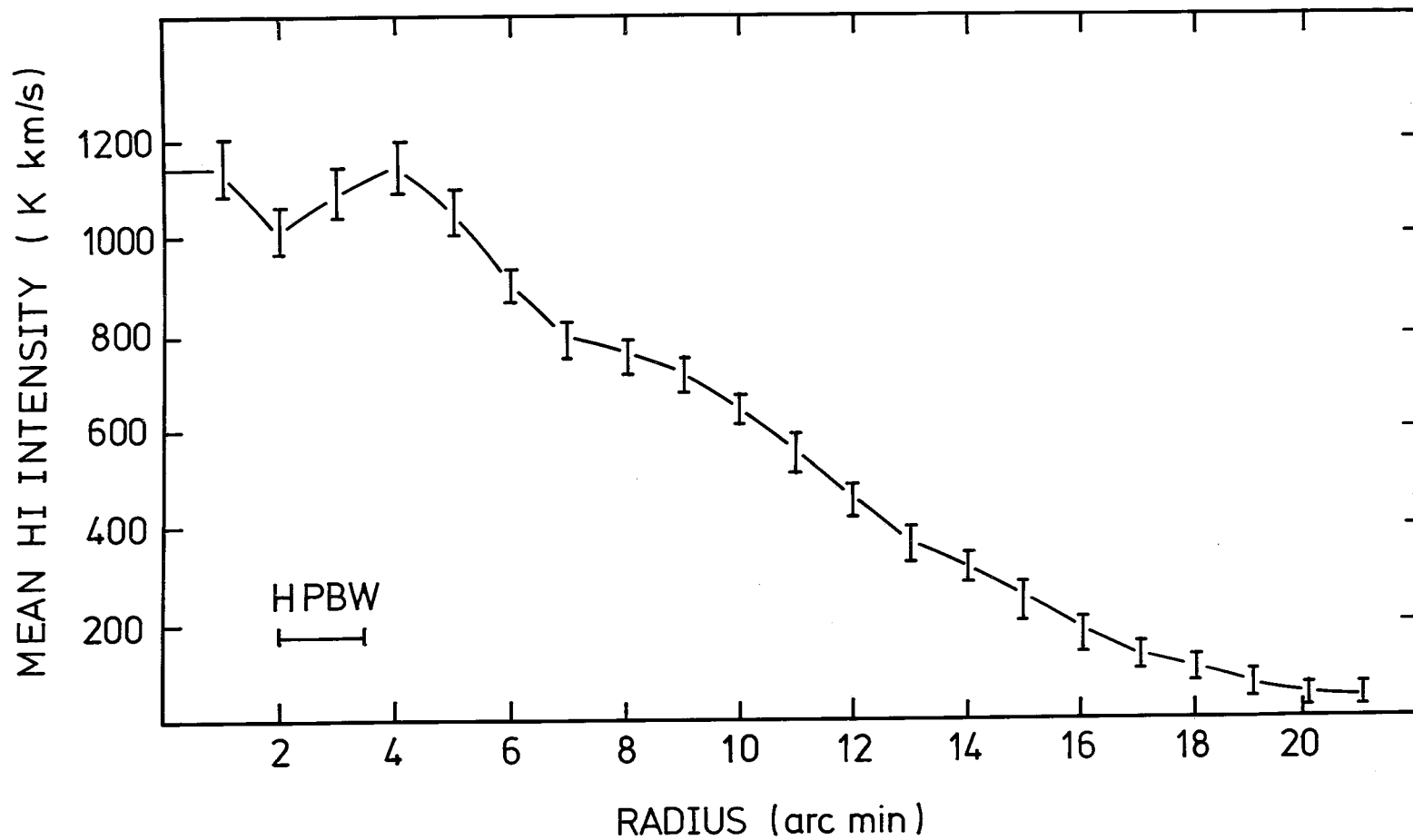


Figure 3.6 Radial distribution of HI in NGC 2403, constructed from Fig. 3.5 as described in the text.

3.4.3 ASYMMETRIES

Love's observations at a resolution of 63×68 arcsec show an asymmetry in the outer parts of the integrated HI distribution, with the southern half of the galaxy containing more HI than the north. He found the ratio South/North for HI between the radii 10 and 15 kpc to be ~ 1.8 . I have carried out a similar analysis on the integrated HI map of Fig. 3.5 (resolution 1.5×1.6 arcmin). The HI was sampled in ellipses using Shostak's parameters, as described earlier. The ratios of the HI on either side of the major and minor axes are plotted in Fig. 3.7, as a function of radius.

There is a slight, but not significant, indication of a North-South asymmetry with HI_N/HI_S ($1 \leq R \leq 18$ arcmin) = 0.92 ± 0.17 (the error is σ for the mean). However, an East-West asymmetry at large radii is significant, where HI_W/HI_E ($11 \leq R \leq 20$ arcmin) = 0.82 ± 0.08 . Such asymmetries are by no means unusual for late-type galaxies.

The poor signal-to-noise ratio of Love's observations probably account for this discrepancy.

3.4.4 THE SPIRAL STRUCTURE

The HI is distributed (Fig. 3.5 and Plate 3.2) in the form of bright 'knots', an effect not due to noise. The nucleus does not coincide with either a knot or a hole, and so is in accord with the study of the radial distribution of HI (section 3.4.2). Bright knots of HI are usually seen in high-resolution HI maps of spiral galaxies, and recent surveys of M33, M31 and IC 342 (Newton 1978) have shown a good correlation

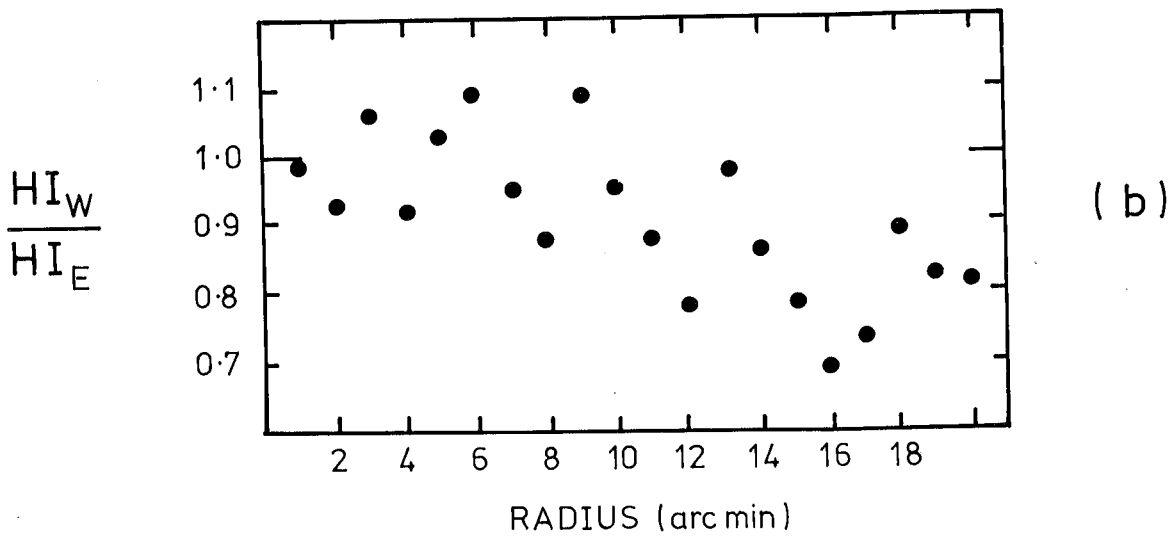
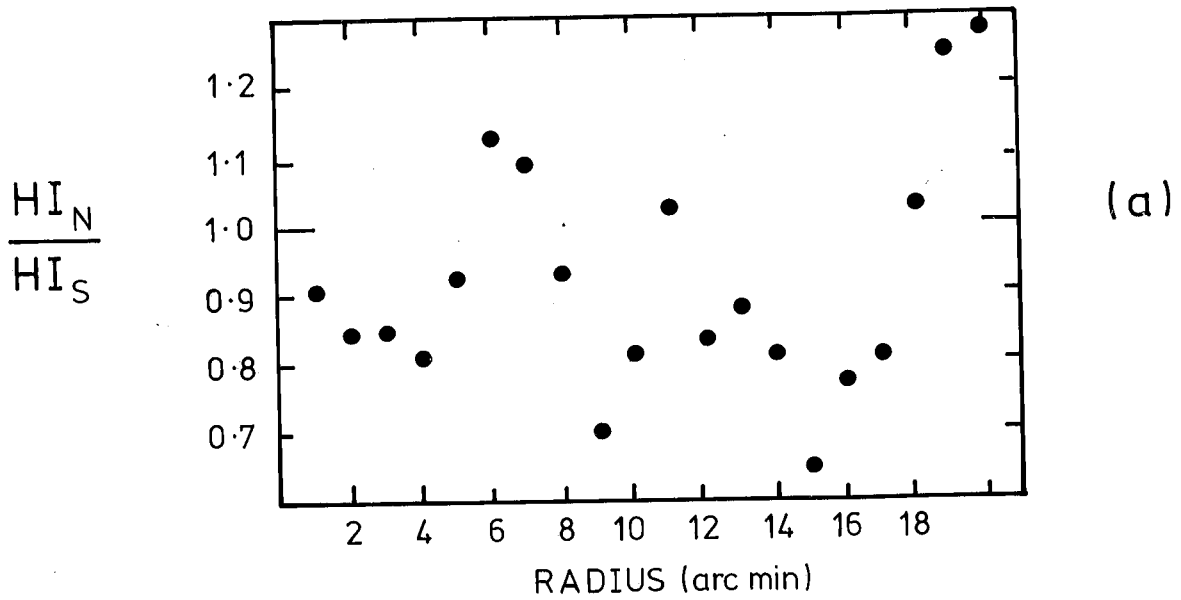


Figure 3.7 Asymmetry of the HI distribution in NGC 2403 (Fig. 3.5).
 (a) Ratio of 'HI to the north of the minor axis' to 'HI to the south of the minor axis', as a function of radius. (b) Ratio of 'HI to the west of the major axis' to 'HI to the east of the major axis', as a function of radius.

between HI spiral features and the optical tracers of spiral arms. As has already been mentioned, spiral features can be discerned in NGC 2403, and it is tempting to examine if the correlation also exists here.

The most obvious features of the HI distribution which could be interpreted as spiral arms are sketched in Fig. 3.8. It should be emphasised that these are purely subjective. Unambiguous spiral patterns are very difficult to trace even in the best observations, and here the angular resolution is only just sufficient to resolve any spiral structure, so that great caution must be exercised.

The distribution shows no single underlying spiral pattern. The most prominent features are 1, 2 and 8, whose lengths are 15, 10 and 15 arcmin respectively, while the others are of order 5 arcmin in length. The arm-interarm contrast ratio is defined as

$$C = (B_{\max} - B_{\min}) / (B_{\max} + B_{\min}),$$

where B is the brightness temperature of the HI. The parameter is of importance when comparing observations with density wave theories. Arms 1, 2 and 8 have $C = 0.3 \pm 0.1$, while the other features have $0.1 < C < 0.5$. These values are similar to those found for other galaxies, but there are serious difficulties (notably lack of resolution) in determining this parameter.

The pitch angle of spiral arms, t , is defined as the angle between the arm (viewed face-on) and a circle at that radius. Shostak (1973) measured the mean value of t for the optical arms of NGC 2403 as $t \approx 18^\circ$. The HI arms 1, 2 and 9 seem to have a roughly constant pitch angle, while features 3-8 show

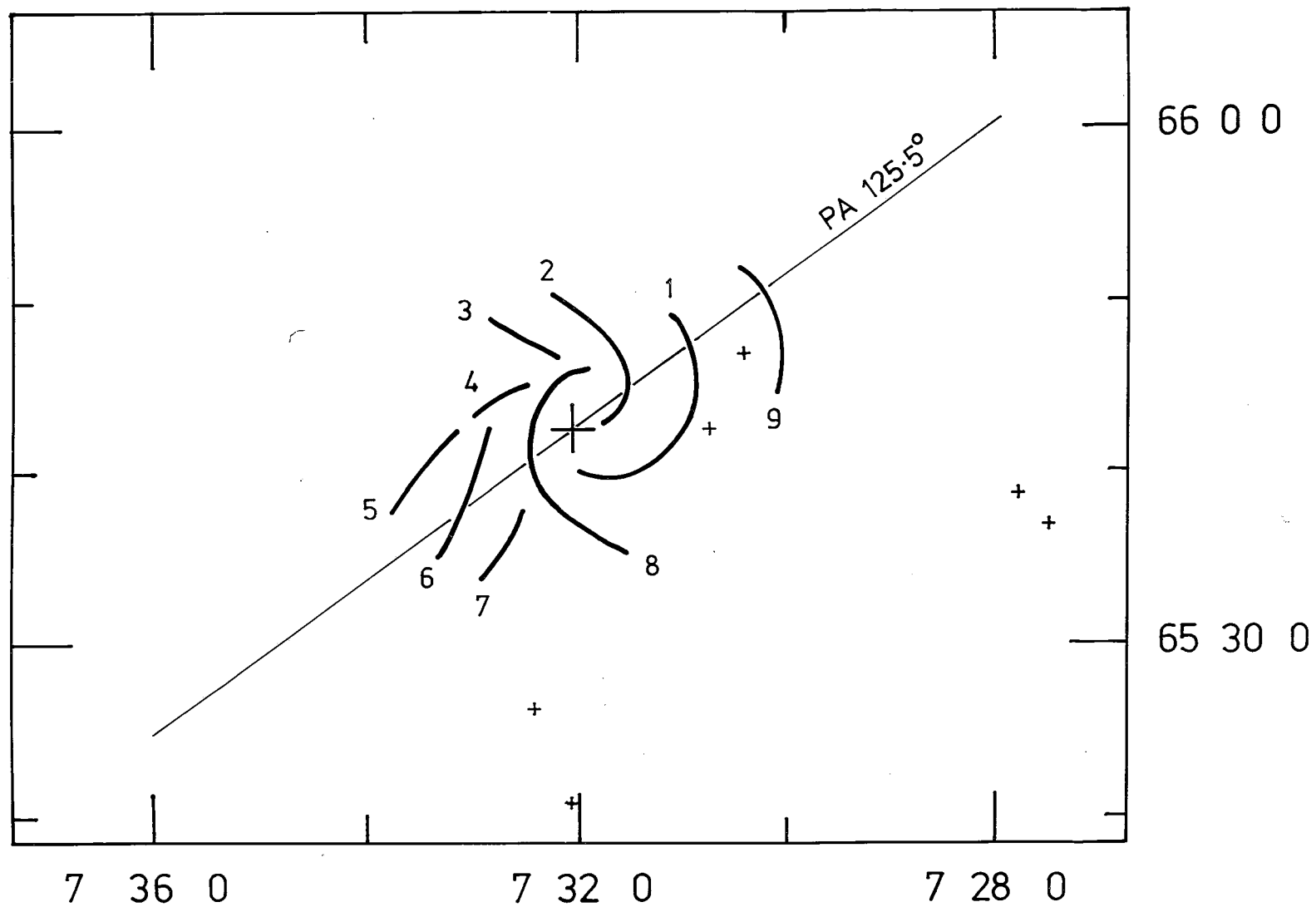


Figure 3.8 Subjective sketch of the HI spiral features in NGC 2403 (derived from Fig. 3.5 and Plate 3.2).

a much greater dispersion in values of t .

A sketch of the optical spiral arms is shown superimposed on the HI distribution in Plate 3.3. The sketch was constructed from a combination of the Palomar Sky Survey prints and the Hubble Atlas photograph (Plate 3.1). The latter was used to trace the spiral structure in the inner regions where the Sky-Survey prints were 'burnt-out'. As with the HI distribution the optical arms do not show a single underlying spiral pattern; the pattern is multi-armed and complicated, with several bifurcations. Only in the very centre of the nucleus does the pattern resemble a classical two-arm spiral. There is much less dispersion in pitch angle in the optical arms than was found for the HI. All the segments appear to belong to the same basic type of spiral.

The general agreement between the spiral patterns seen in the HI and optical distributions (Fig. 3.8 and Plate 3.3) is remarkably good, although no detailed quantitative fitting to logarithmic spirals has been attempted. Probably the best agreement occurs for HI in arms 4 and 6, which are in almost exact agreement with two of the outer arms seen on the PSS prints. HI arm number 5 can be considered as an extension of arm number 4, where the optical arm is too faint to be visible. There is also no optical counterpart to arms 3 or 9. Arms 1 and 2 lie very close to several optical arms, and have very similar pitch angles to them. Arm number 8 is not in such good agreement, and appears to cut across several optical arms, having a different pitch angle from them. The worst agreement is for feature 7 which cuts radially across the ends of two optical arms.

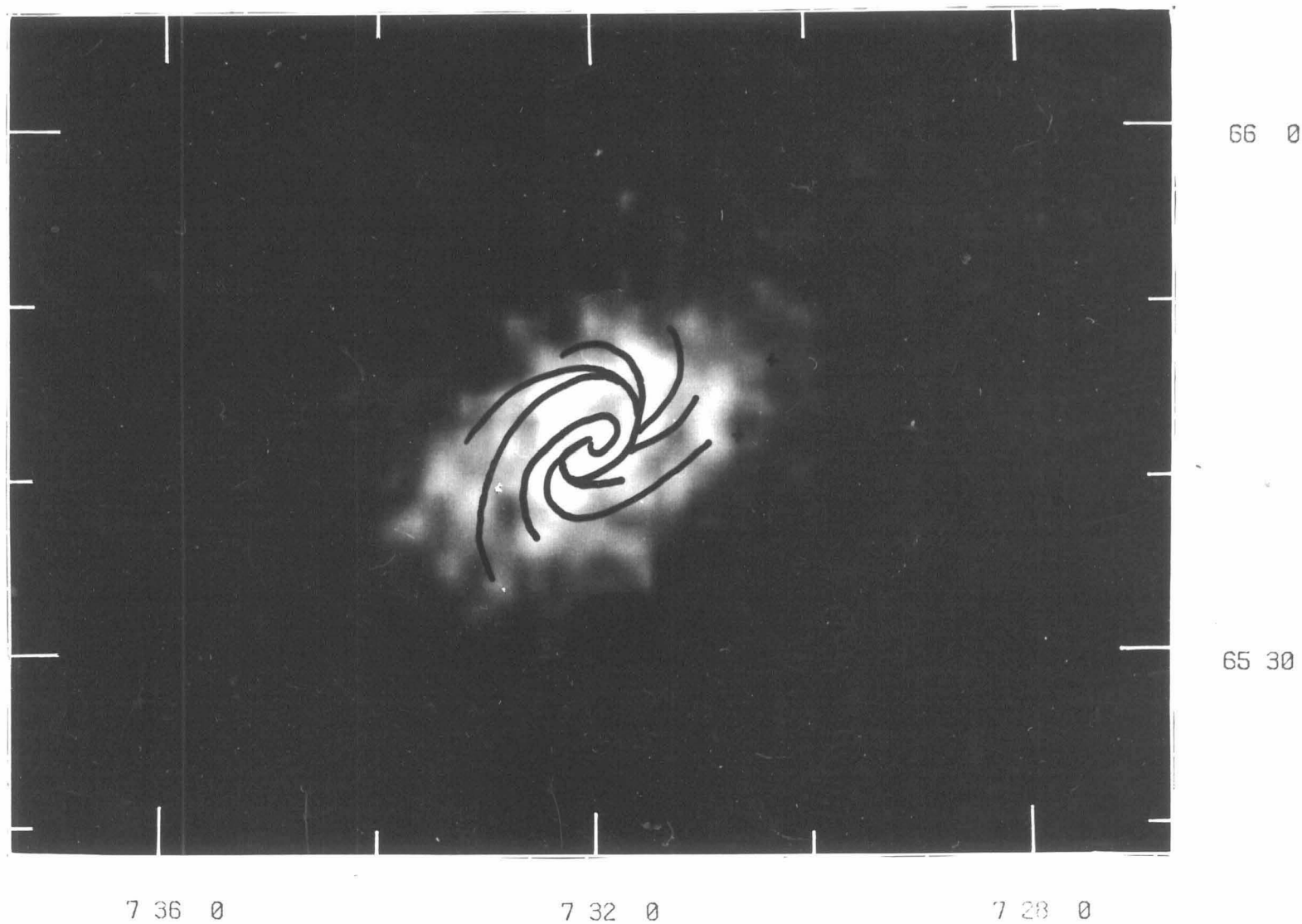
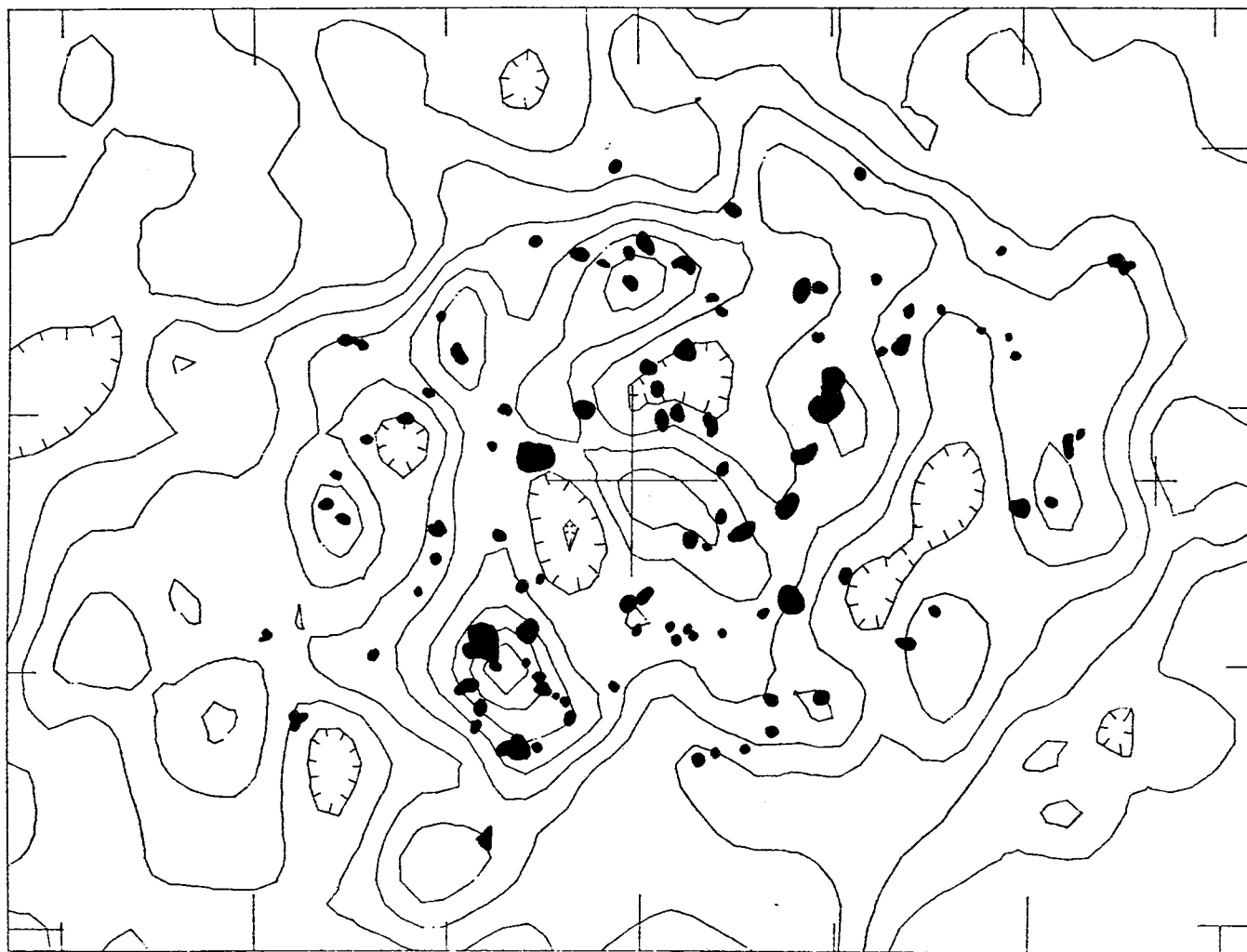


Plate 3.3 Subjective sketch of the optical spiral arms in NGC 2403, superimposed on a photographic representation of the integrated HI map at a resolution of 1.5 x 1.6 arcmin (Plate 3.2).

3.4.5 HII REGIONS

Véron & Sauvayre (1965) catalogued 52 HII regions in NGC 2403, the largest of which are similar to NGC 604 in M33 and 30 Doradus in the LMC. Hodge has extended the work and catalogues 109 HII regions (1969A), and discusses their radial distribution (1969B). Searle (1971) discusses evidence for gradients in the composition of the HII regions across the discs of spiral galaxies (including NGC 2403), while Deharveng & Pellet (1970) derive a rotation curve for NGC 2403 from the radial velocities of the HII regions (see Section 3.6). Hamijima & Tosa (1975) have found a correlation of a power-law type between the rate of star formation measured by the surface density of HII regions, and the HI gas density from Shostak & Rogstad's map.

Fig. 3.9 shows the HII regions mapped by Hodge (1969A) superimposed on the integrated HI map at a resolution of 1.5 arcmin. As has been previously reported, there is a good correlation between the position of the HII regions and the peaks and ridges of HI emission. A ring of HII regions surrounds the peak of brightest HI emission to the SE of the nucleus. The existence of a ring rather than a centrally condensed group of HII regions is probably due to increased optical obscuration at the HI peak. Hodge's HII regions clearly show a spiral pattern which is well aligned with several of the HI spiral features noted earlier (particularly features 1, 2, 4 and 8 in Fig. 3.8). The HII regions seem to correlate better with the apparent HI spiral arms (Fig. 3.8) than the sketch of optical spiral arms (Plate 3.3).



65 48 0

65 36 0

7 33 0

7 32 0

7 31 0

Figure 3.9 The HII regions of Hodge (1969A) superimposed on the high-resolution integrated HI map of NGC 2403 (Fig. 3.5).

3.4.6 DUST

Plate 3.4 shows the high-resolution integrated HI map superimposed on the Hubble Atlas photograph of NGC 2403. There are several regions where optical obscuration by dust is evident, but such regions are not clearly correlated with the HI emission. Such a correlation has been found in other galaxies (e.g. M31, M82, and M33) but would not necessarily be visible in the present observations on account of the limited angular resolution and sensitivity.

3.5 Radio Continuum

Van der Kruit (1973) has presented high-resolution observations of NGC 2403 in the radio continuum at 1415 MHz. His map shows an absence both of a nuclear radio source, and of radio spiral structure. The highest peak in the radio brightness corresponds to the brightest HII region, and he suggested that the emission may be non-thermal, by analogy with 30 Doradus.

Fig. 3.10 shows the broad-band continuum map from the present survey, centred at 1419 MHz. Both the sensitivity and angular resolution of this map are similar to that of van der Kruit's map, although comparison is difficult because Fig. 3.10 includes line emission diluted over the 10-MHz bandwidth. After correction for the HI emission, an upper limit of 10 mJy (approximately 1 K) can be placed on any nuclear source. The peak of emission 1.8 arcmin to the east of the nucleus is partly a genuine continuum feature and in fact corresponds to the brightest HII region, discussed above and also seen in van der Kruit's map.

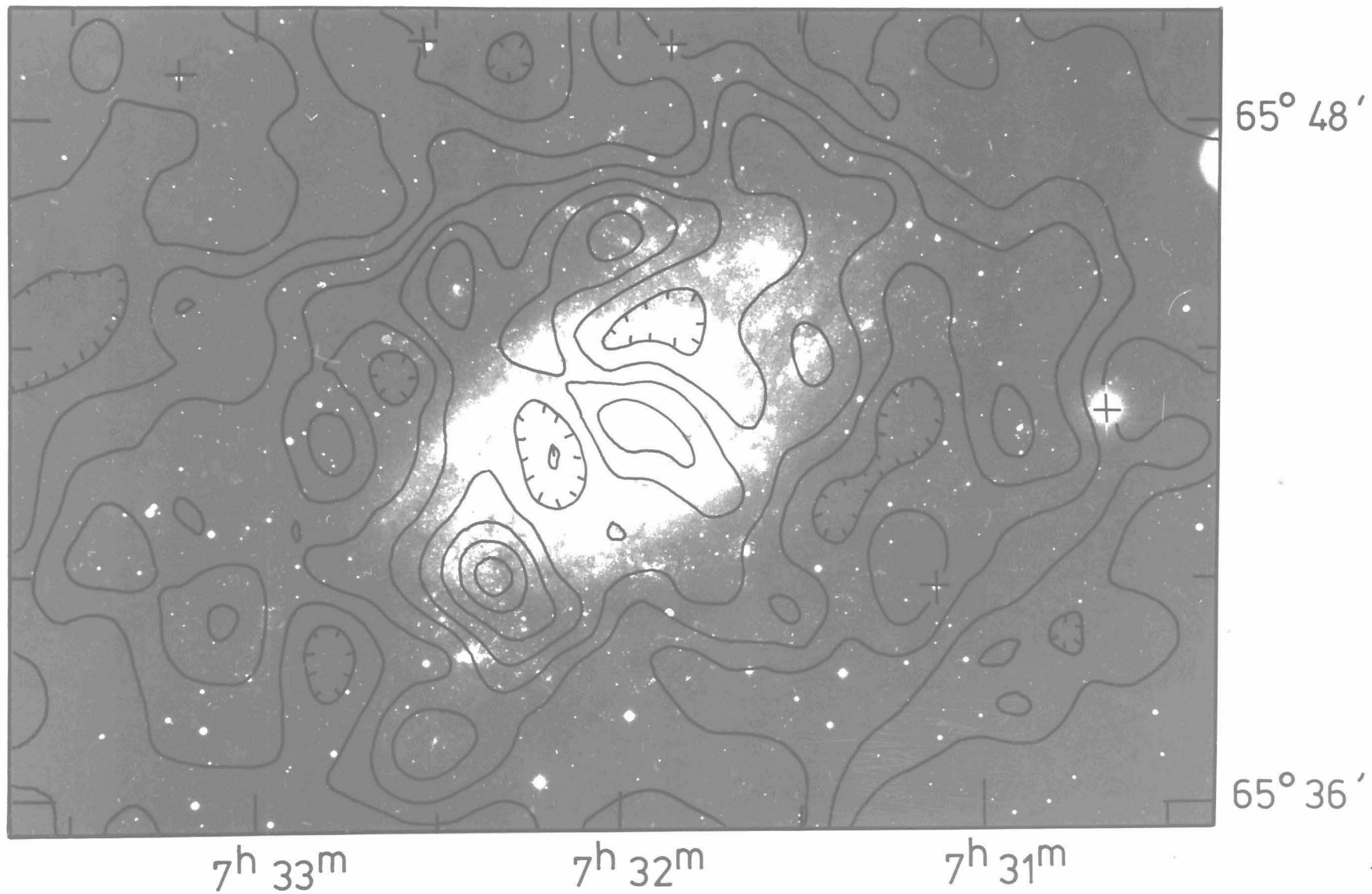


Plate 3.4 Contours of integrated HI in NGC 2403 (resolution 1.5×1.6 arcmin) superimposed on The Hubble Atlas photograph (copyright - Hale Observatories).

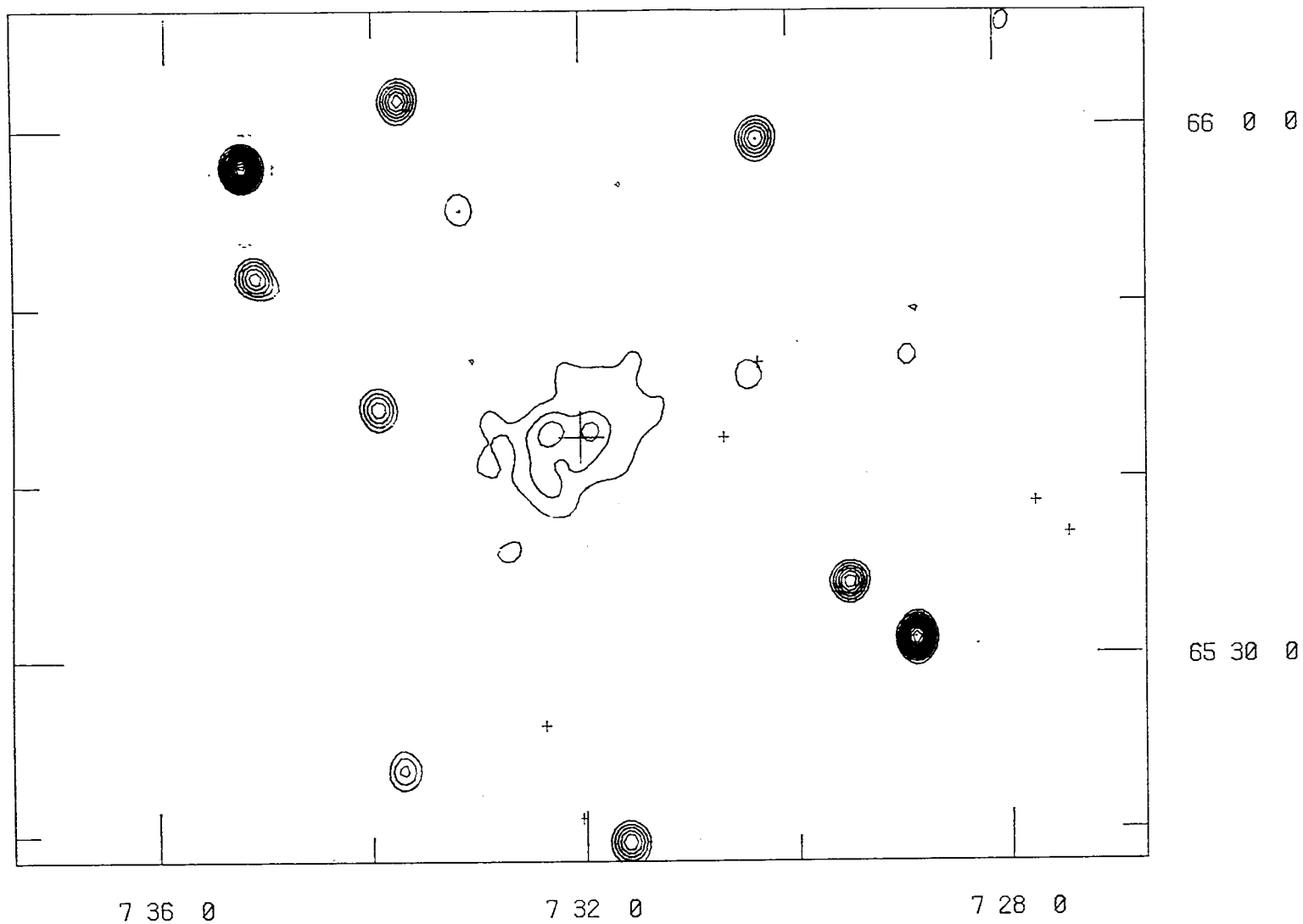


Figure 3.10 Broad-band radiation centred at 1419 MHz, and thus including line emission diluted over the 10-MHz band. The rms noise level is 1.2 mJy and the resolution is 1.5 x 1.6 arcmin. The contours are in intervals of 10 mJy (zero omitted). All the unresolved sources are from background objects, not associated with NGC 2403.

3.6 The Velocity Field

3.6.1 INTRODUCTION

Fig. 3.11 shows the velocity field of NGC 2403 at a resolution of 2.5×2.7 arcmin; it was produced by means of the Gaussian-fitting procedure as described in Section 2.3 of Chapter 1. Plate 3.5 shows the velocity field at a resolution of 1.5×1.6 arcmin, superimposed on the optical representation of the integrated HI distribution. The latter velocity field was produced using the standard fitting-procedure and has a noise level of about 3 km/s. Plate 3.5 is in excellent agreement with that presented by Shostak & Rogstad (1973), and generally similar to the 1.5 arcmin-resolution velocity field presented by Love (1975). Love's map is, however, much more noisy than that presented here, and he interprets several features as real which are most probably only noise (e.g. the 'kink' in the 108 km/s and adjacent contours at a position about 2 arcmin north of the nucleus).

3.6.2 DYNAMICAL PARAMETERS AND THE ROTATION CURVE

The dynamical parameters for a galaxy are defined in Section 2.4 (g) of Chapter 1, and a method of deriving them from observations is outlined. Values of the dynamical parameters for NGC 2403 obtained by both Love (1975) and Shostak (1973) are compared in Table 3.6. Clearly there are some discrepancies between the two values for dec and i , although Shostak does not quote any errors. The new data obtained from the present survey reveal that Shostak's values are more nearly correct than those of Love.

Because of difficulties with the computing, and lack of time, it was not possible to derive new dynamical parameters from the present observations using the method mentioned above.

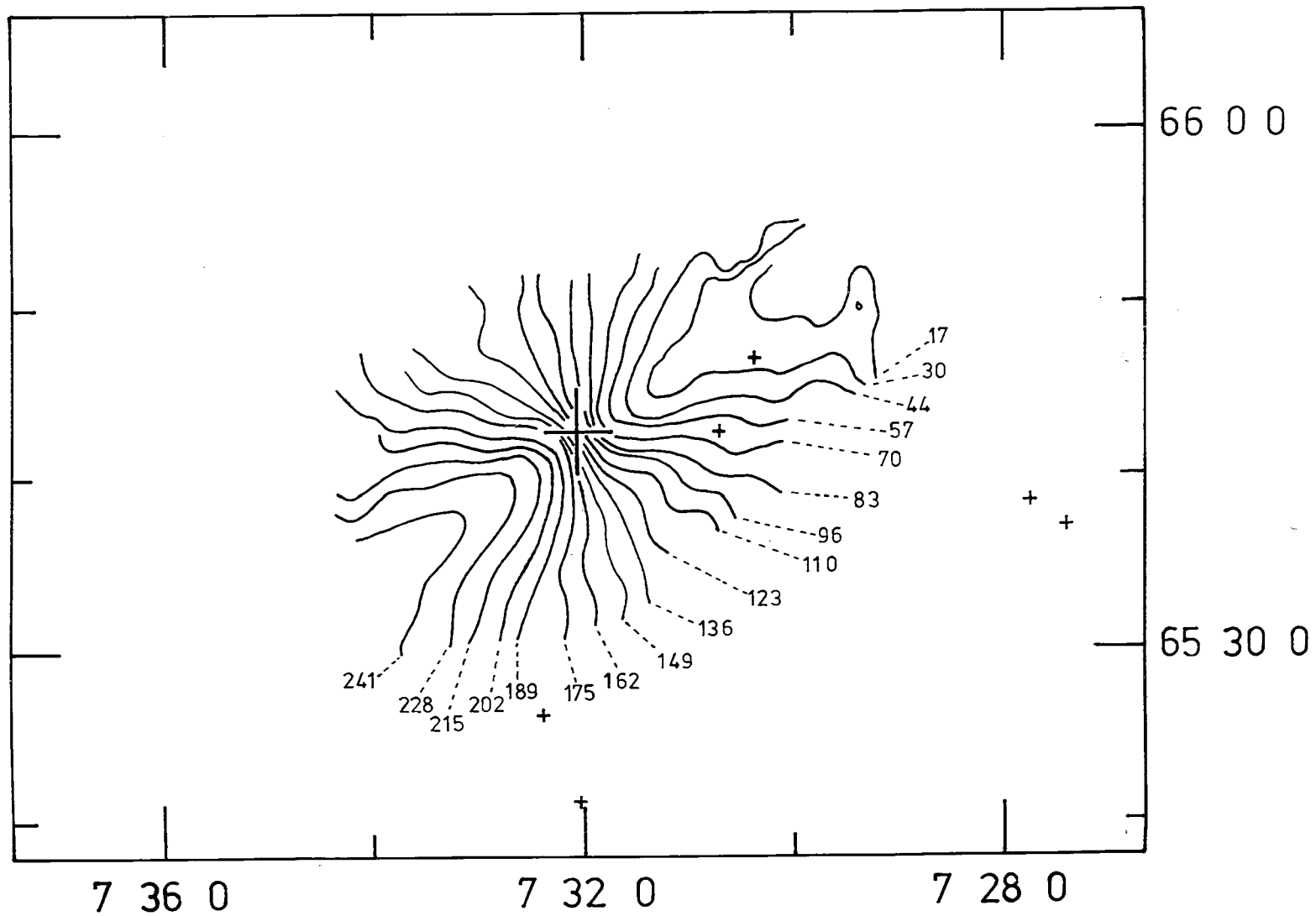
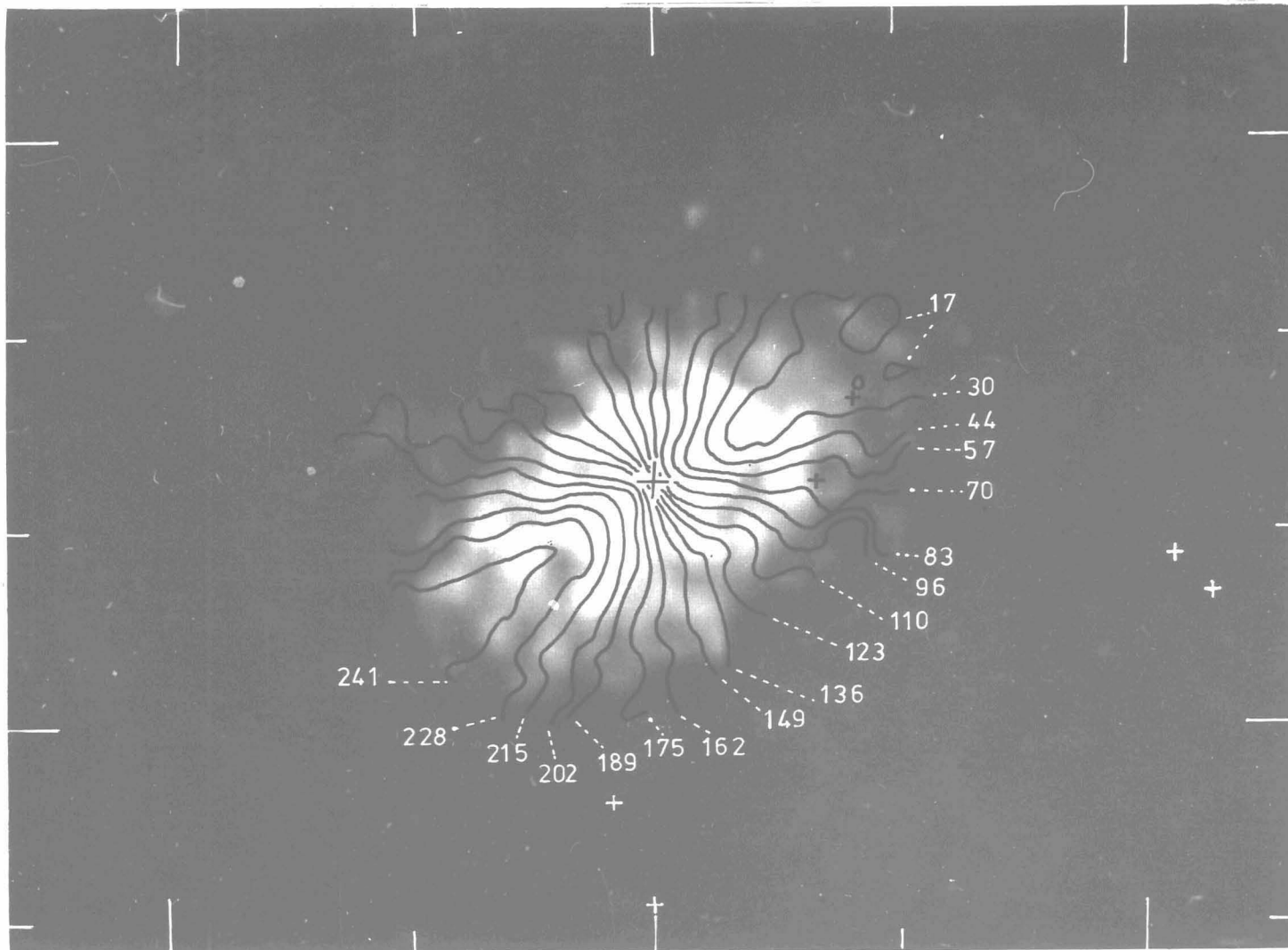


Figure 3.11 Velocity field of NGC 2403 at a resolution of 2.5 x 2.7 arcmin.



66 0 0

65 30 0

7 36 0

7 32 0

7 28 0

Plate 3.5 Contours of velocity in NGC 2403 (resolution 1.5 x 1.6 arcmin) superimposed on a photographic representation of the integrated HI (Plate 3.2). The numbers indicate the velocity in km/s, and the rms error is typically about 3 km/s.

Table 3.6

Summary of HI dynamic parameters for NGC 2403

	SHOSTAK (1973)	LOVE (1975)
RA	07 ^h 32 ^m 01.2 ^{s*}	07 ^h 31 ^m 51 ± 4 ^s
dec	65 ^o 42' 57" [*]	65 ^o 42' 17 ± 8"
V _{sys}	128 ± 3 km/s	138 ± 2 km/s
PA	125.5 ± 1 ^o	126 ± 1 ^o
i	60 ^{o*}	55 ± 2 ^o

NOTES

* no error quoted.

Instead, the analysis was restricted to producing two maps (Fig. 3.12) of 'residual-velocity' differences between the present high-resolution velocity field and a model of circular rotation for each set of parameters. It is clear from the greater magnitude of the residuals in Fig. 3.12(a) that Shostak's parameters are more nearly correct than those of Love. More specifically the residuals resulting from Love's parameters have an overall negative excess of about 10 km/s, which corresponds to V_{sys} being too high by the same amount. When this effect is removed a systematic residual still remains whose symmetry corresponds to an error in the position of the nucleus along the minor axis of the galaxy. When both these corrections are applied to Love's parameters, they bring them into good agreement with those of Shostak.

It is difficult to discern any large-scale systematic error in the residual field based on Shostak's parameters, except a slight hint of the symmetry which corresponds to an error in the position of the nucleus along the major axis. There is, however, a localised positive residual of ~ 10 km/s running northwest-southeast in a band about 3 arcmin south of the nucleus. This is coincident with an optical spiral arm, and will be discussed presently.

The dynamical parameters quoted by Shostak (1973) describe well the large-scale motions of HI in NGC 2403, and are adopted for the derivation of the rotation curve. This was obtained from the high-resolution velocity field using the method of Warner *et al.* (1973, see Chapter 1 Section 2.4) and is displayed in Fig. 3.13. Rotation velocities rise steeply for $R < 4$ arcmin and then flatten to a plateau of about 130 km/s at greater radii. For $R \gtrsim 15$ arcmin, $V_{\text{rot}} = 130$

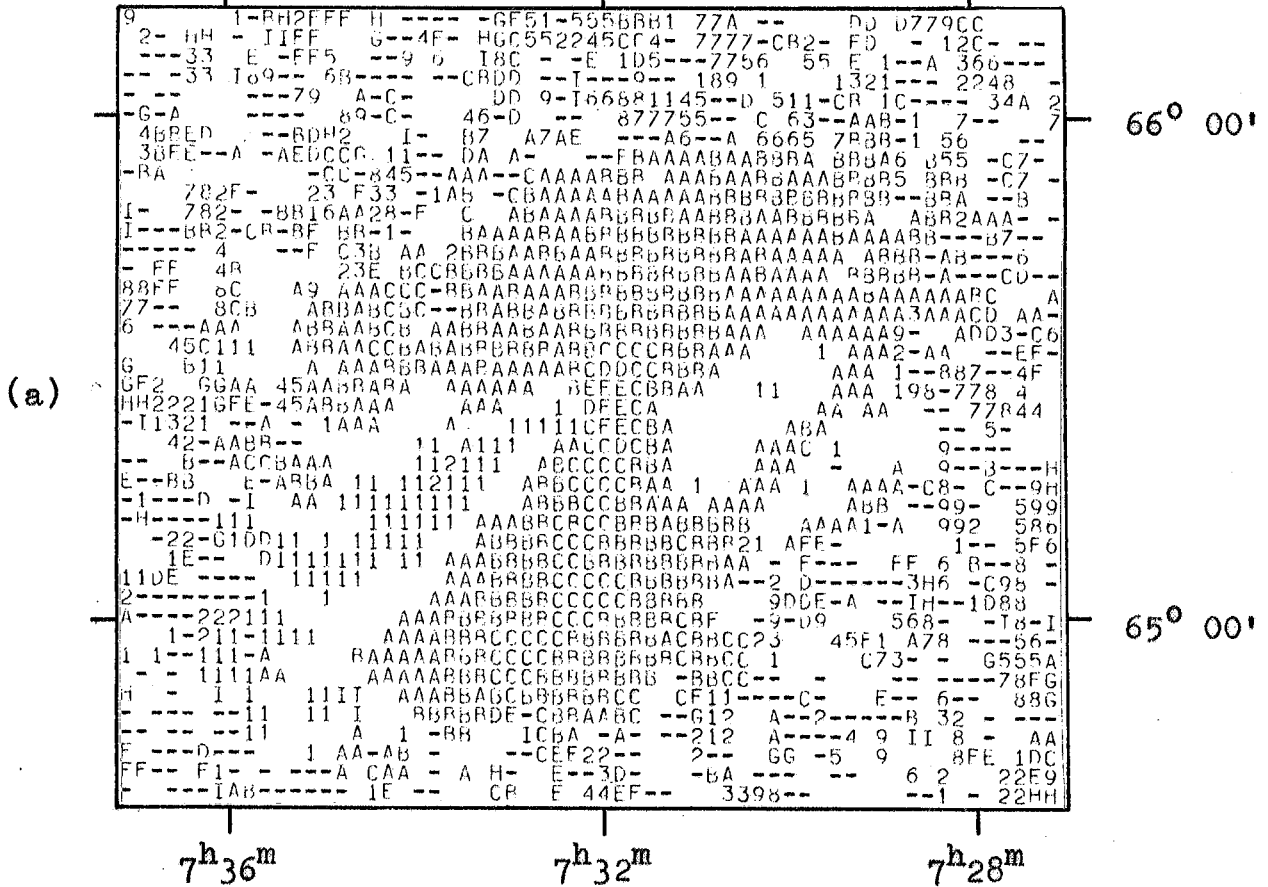


Figure 3.12 Residual velocity fields made by subtracting model velocity fields from the observed velocity field (Plate 3.5). (a) A model using the parameters of Love (1975). (b) A model using the parameters of Shostak (1973). In both cases the numerals 1-9 represent positive residuals, the letters A-I represent negative residuals, the character interval is 9 km/s, a blank character represents a zero residual, and a dash represents a residual of magnitude greater than 90 km/s. The values of residual velocity are only meaningful in regions where the observed radial velocity field is well-defined (cf. Plate 3.5).

(b)

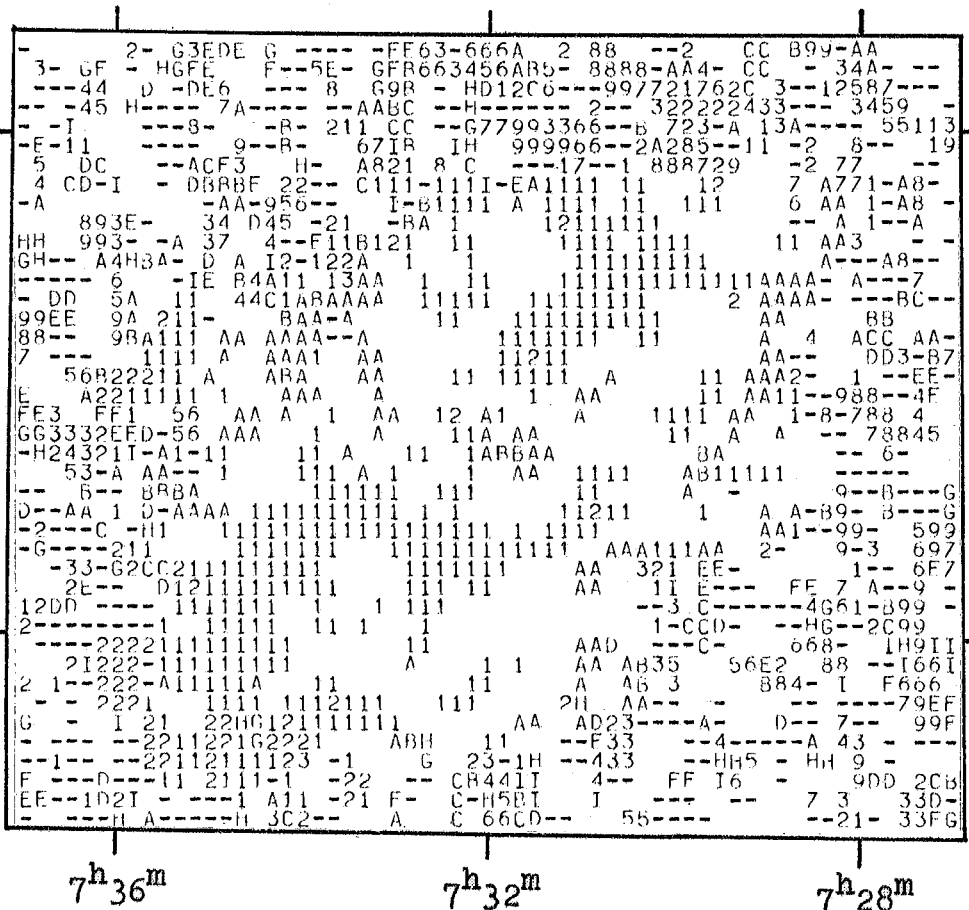


Figure 3.12 (continued)

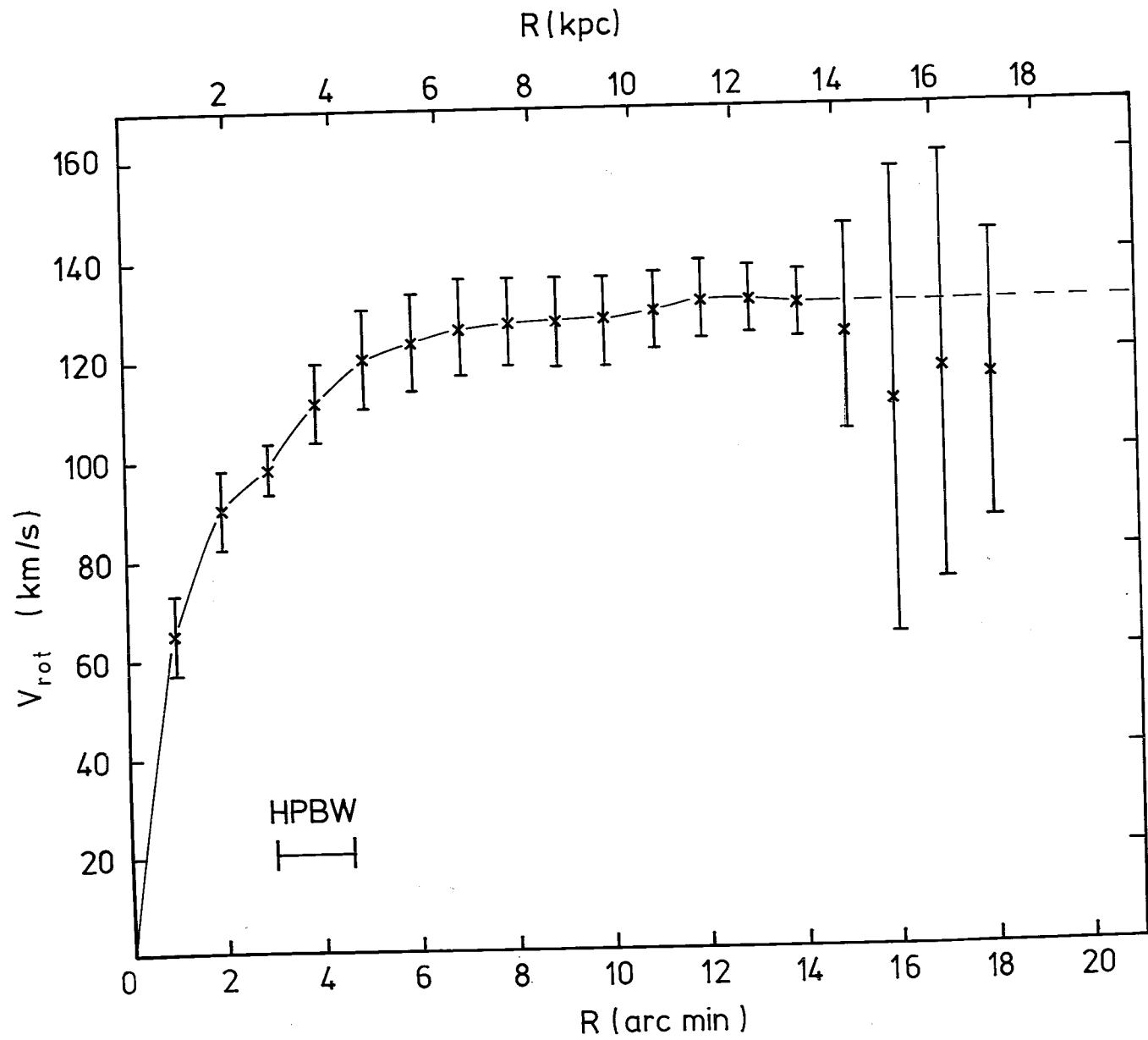


Figure 3.13 Rotation curve for NGC 2403, derived from the high-resolution velocity field (Plate 3.5) as described in the text, assuming the dynamic parameters of Shostak (1973).

km/s is assumed since the rms errors are high. This is seen to be a fair assumption from Fig. 3.14, which shows V_{rot} obtained from the maps at a resolution of 7.4×8.1 arcmin, using the same method. These observations are more sensitive to low-brightness emission in the outer parts of the galaxy and allow V_{rot} to be determined with reasonable accuracy out to 20 arcmin from the nucleus. Beam-smearing is important at this resolution and accounts for the underestimated values of V_{rot} at small radii, but the effect is negligible at large radii ($R \gtrsim 14$ arcmin) where the rotation curve is approximately flat. There is some indication of rotational velocities at $R \approx 18$ arcmin greater than 130 km/s, but generally these data, those of Huchtmeier (1975) and those of the extrapolated high-resolution rotation curve, are consistent (within the errors) with a fairly flat rotation curve at large radii.

Deharveng & Pellet (1970) derive a rotation curve for $R < 6$ arcmin from the radial velocities of the HII regions. Both Love (1975) and Shostak (1973) noted that these rotational velocities were systematically higher than those obtained from HI data. While part of this discrepancy may be attributed to resolution effects, the remainder is probably real and may be due to the gas in the spiral arms (where the HII regions are located) rotating faster than in the disc - see Section 3.6.4.

3.6.3 THE MASS DISTRIBUTION

The rotation curve can be used to derive the variation of mass with radius, by modelling the galaxy by concentric spheroids (Burbidge, Burbidge & Prendergast 1959). The intrinsic axial ratio of these spheroids was taken as 0.1 in

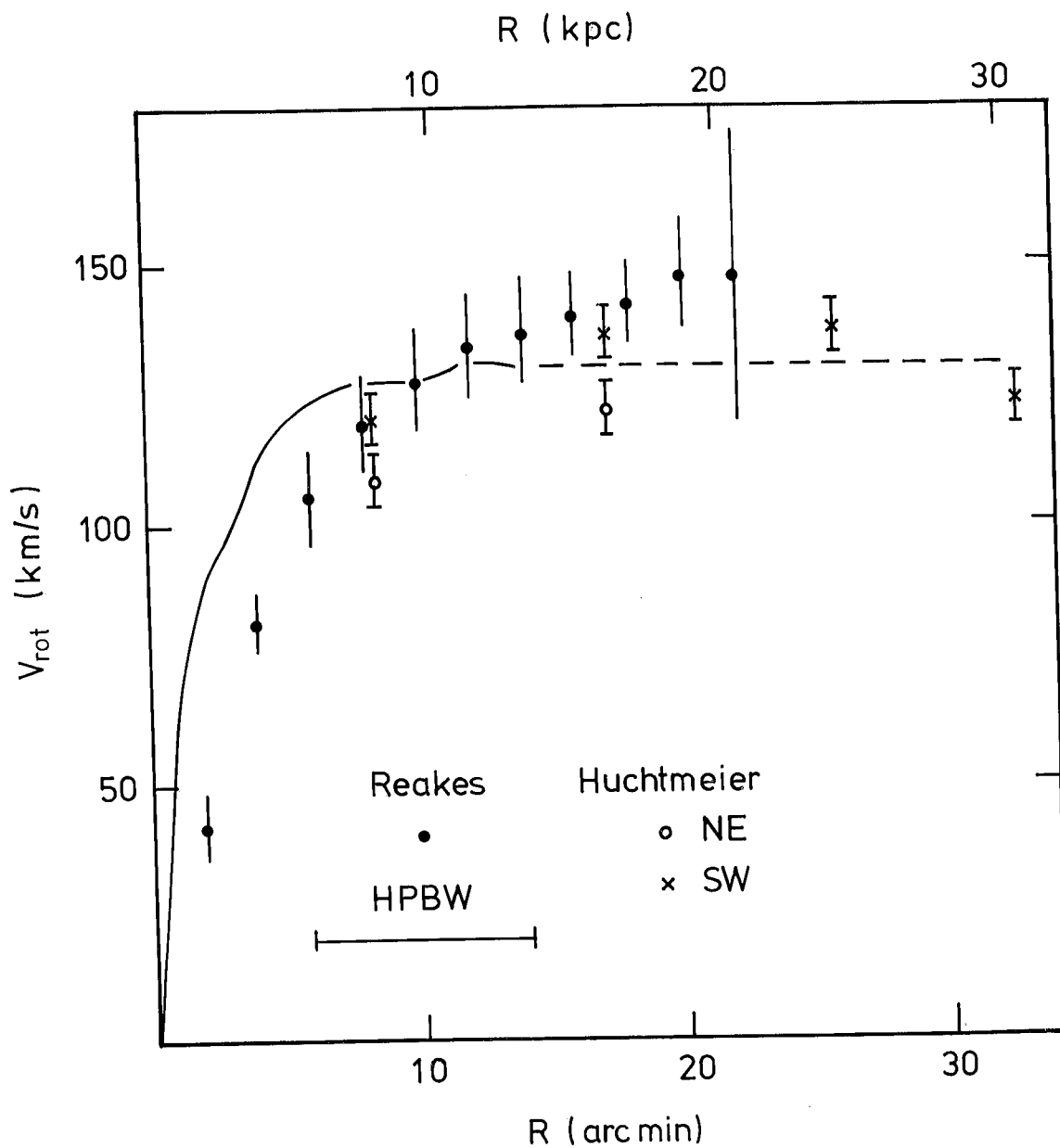


Figure 3.14 Comparison of the rotational velocities in the outer parts of NGC 2403. The filled circles are derived from the present observations assuming the dynamic parameters of Shostak (1973). The HPBW resolution for these points is shown by the horizontal bar. The open circles and crosses are data from Huchtmeier (1975). The solid line is the high-resolution rotation curve shown in Fig. 3.13.

accordance with the mean value for Scd galaxies (Heidmann, Heidmann & de Vaucouleurs 1971). The cumulative total mass, M_T , as a function of radius, R , derived using this method, is shown in Fig. 3.15. The errors were derived by repeating the analysis using the maximum and minimum rotation curves allowed by the errors in Fig. 3.13. The total mass within a radius of 18 arcmin is $(4.0 \pm 0.1) 10^{10} M_\odot$, a value similar to that of other authors (Table 3.4, page 3-21).

Also shown in Table 3.4 are the integrated parameters for NGC 2403. According to Balkowski (1973), the ratio M_H/L adopted here is typical of an Scd type galaxy. The ratio M_H/M_T seems to indicate an earlier type (Sab or earlier), but this comparison requires considerable caution because of the many ways in which M_T can be defined. The ratio M_T/L is close to the type-independent mean of 11 ± 1 found by Dickel & Rood (1978).

3.6.4 VELOCITY PERTURBATIONS AND SPIRAL STRUCTURE

Many authors have compared the velocity fields of spiral galaxies with the predictions of the linear density-wave theory for spiral structure (e.g. Lin, Yuan & Shu 1969). The theory assumes broad, symmetrical spiral arms (usually two), unlike the narrow multi-armed features seen in NGC 2403 or other similar galaxies (e.g. M33 and IC 342, Newton 1978). Therefore, since this theory is not likely to represent well the gas dynamics in NGC 2403, it will be compared only qualitatively.

The main velocity-perturbations expected from the linear density-wave theory are illustrated in Fig. 3.16. Along the major axis (where the Θ -component is visible) the theory predicts an increase in rotational velocity on the outside of an arm and a decrease on the inside, with no change at the

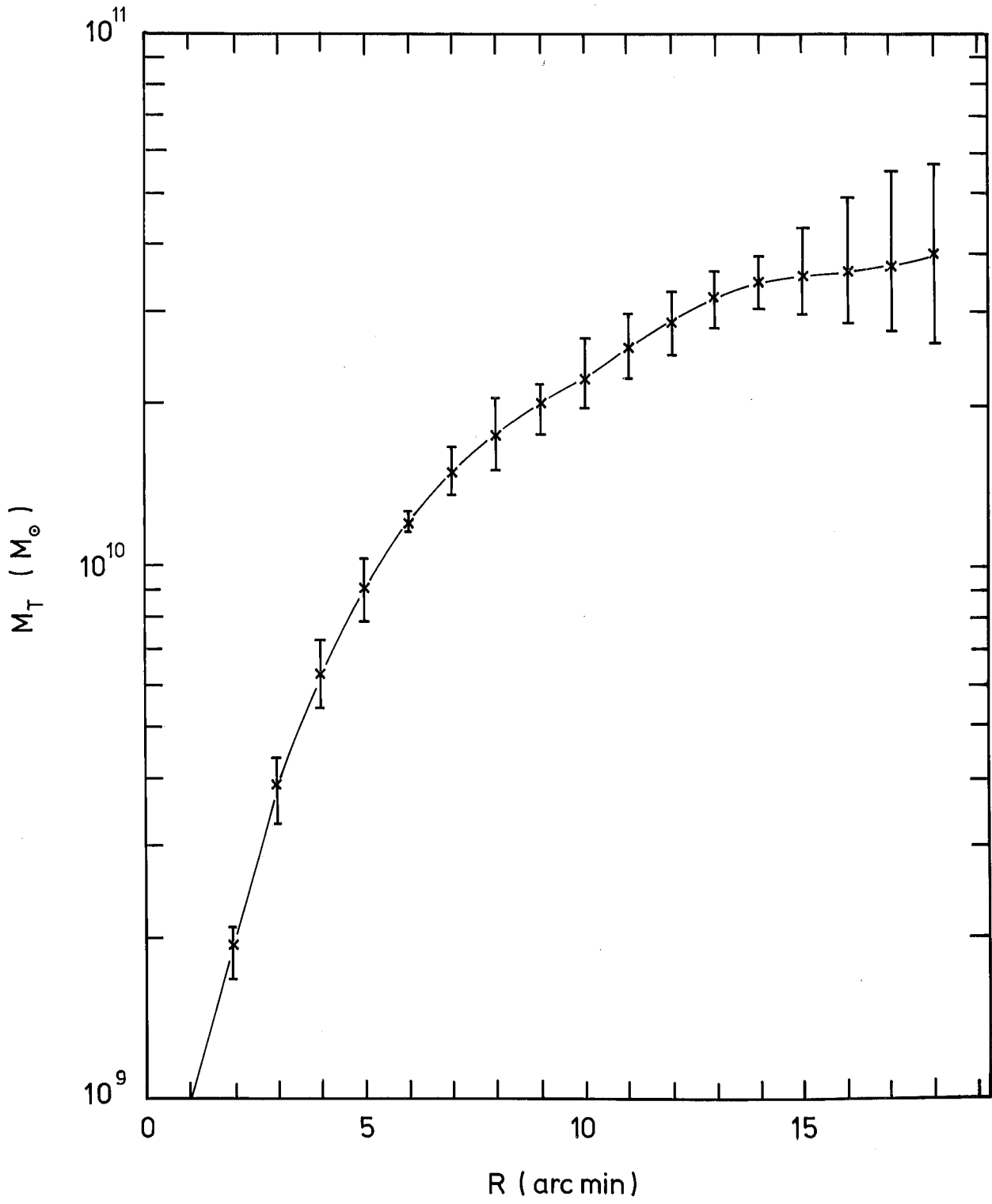


Figure 3.15 Cumulative total mass as a function of radius for NGC 2403, $M_T(R)$.

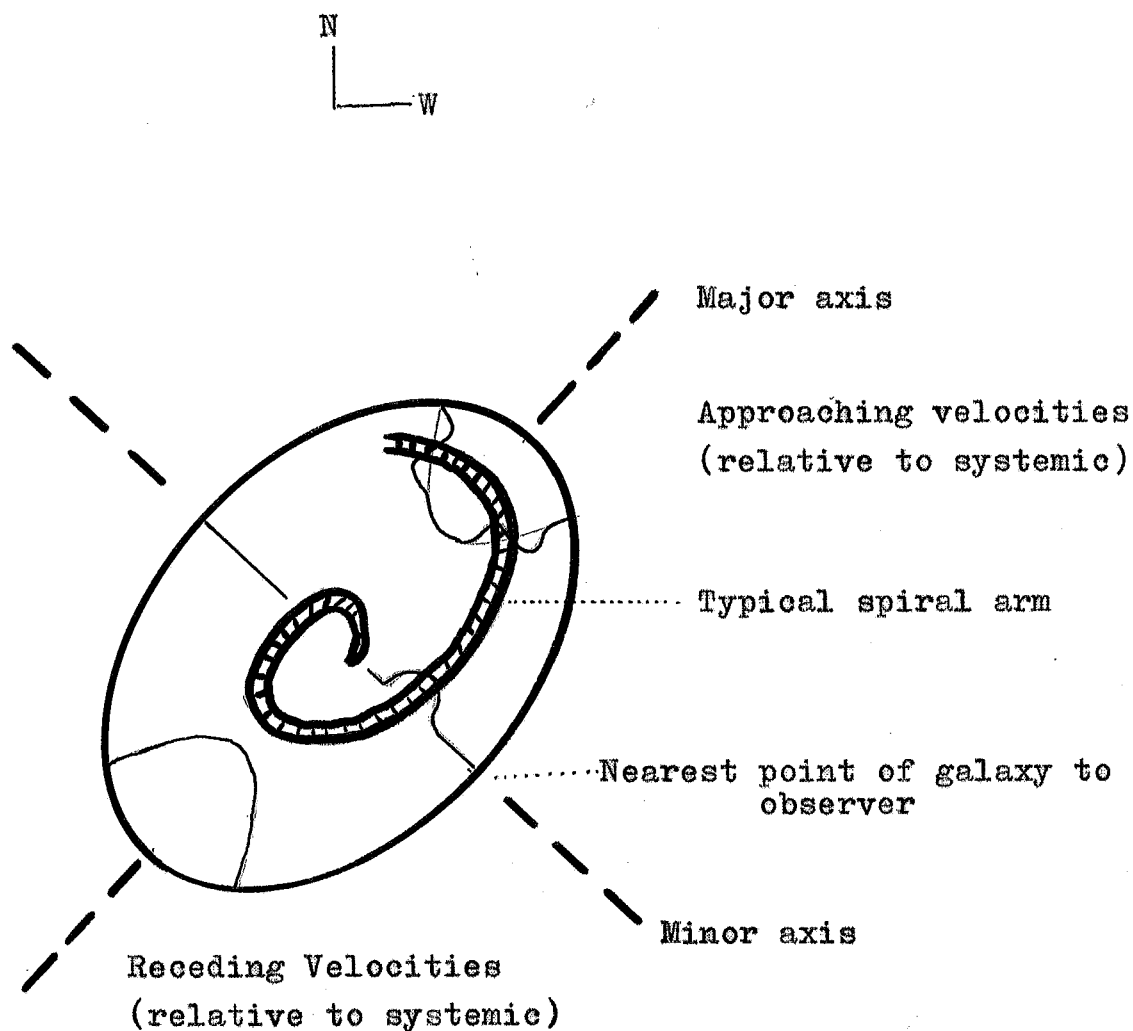


Figure 3.16. Schematic representation of the perturbations to lines of constant velocity in NGC 2403, expected on the basis of a density-wave theory of spiral structure. If the spirals are trailing, the SW end of the minor axis is closest to the observer. Along the minor axis, perturbations are equivalent to an apparent radial contraction of the gas, while along the major axis the perturbations are equivalent to a decrease in rotational velocity on the inside of the arm and an increase on the outside.

centre of the arm. Along the minor axis (where the r motion is visible) the theory predicts an apparent radial contraction of the gas in the arm, relative to the interarm gas. This assumes that all points are within the co-rotation radius, at which the pattern speed equals the rotation speed of the gas. Outside this radius the sense of the velocity perturbations are reversed. Spiral arms are unlikely to occur at the co-rotation radius, where a resonance exists, and Roberts, Roberts & Shu (1975) argue that this is probably the radius at which the 'easily visible' optical spiral structure ceases. In the case of NGC 2403 this is approximately 12 kpc. The pattern speed can then be determined from the rotation curve as $\Omega_p \sim 11 \text{ km s}^{-1} \text{ kpc}^{-1}$ (cf. $20 \text{ km s}^{-1} \text{ kpc}^{-1}$ for M81 quoted by Rots & Shane 1975; $11 \text{ km s}^{-1} \text{ kpc}^{-1}$ for M31 quoted by Guibert 1974). The maximum amplitude of the velocity perturbation is given by

$$\tan(t) = V(R) - \Omega_p R,$$

where t is the pitch angle of the spiral as previously defined. With $t=18^\circ$ (Shostak 1973), velocity perturbations of about 10 km/s result, although 'non-linear' effects discussed by Roberts (1969) can result in amplitudes of up to about 20 km/s.

Love (1975) and Shostak (1973) noticed several velocity peculiarities of amplitude about 10 km/s, which they claim are in qualitative agreement with the density-wave theory. Many of these features are clearly reproduced in the new high-resolution velocity field (Fig. 3.17).

The velocity contours at the ends of the major axis are slightly skewed, having a smaller position angle than the best estimate from model-fitting (125.5°). This effect would be

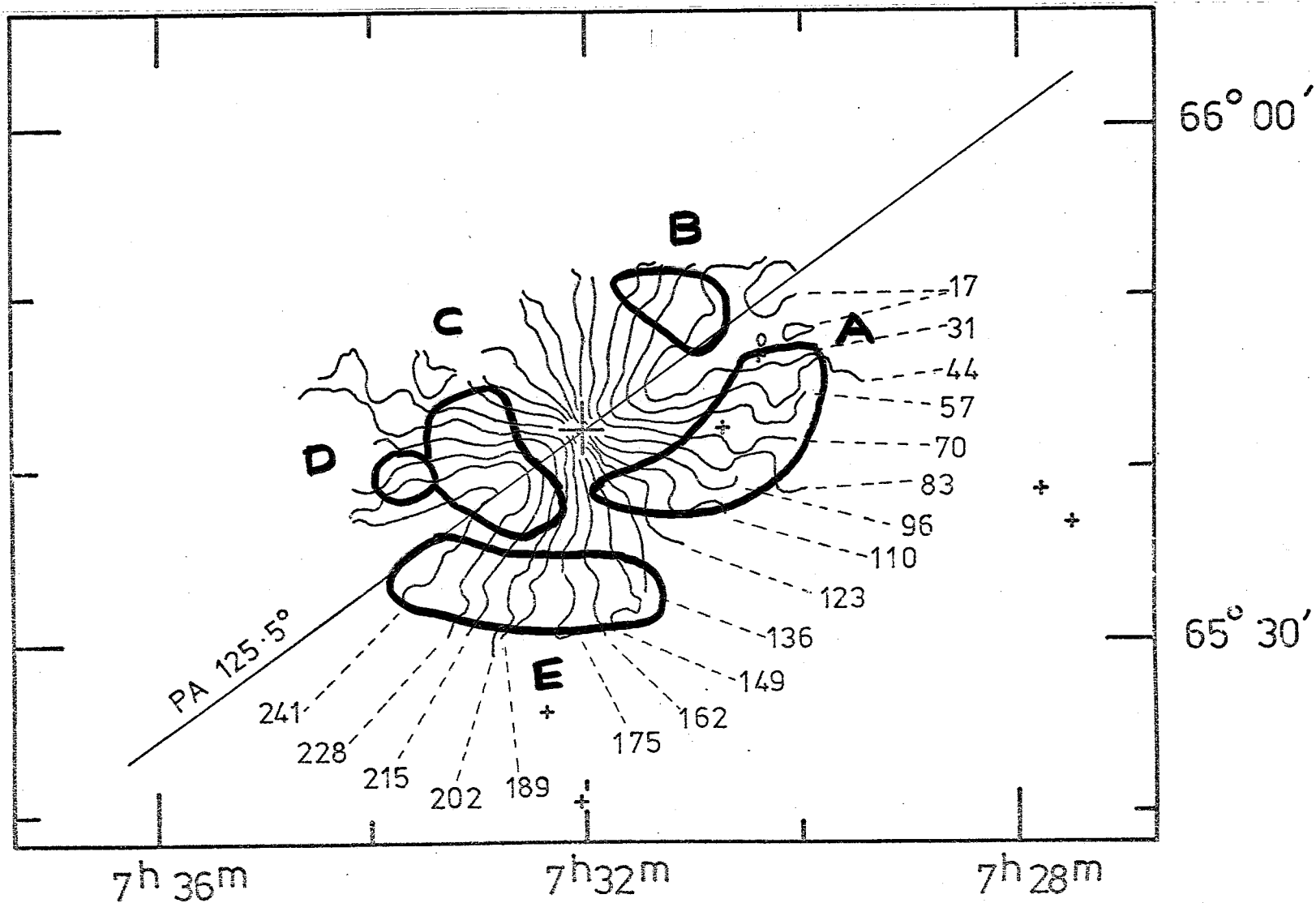


Figure 3.17 High-resolution velocity field (as Plate 3.5) showing the major axis at PA 125.5°. A-E represent areas of velocity peculiarities associated with spiral structure. The rms error in the velocity field is about 3 km/s.

expected from the density-wave theory, but could easily be due to other reasons, such as an error in the dynamical parameters, or a warp in the HI plane (see Section 3.2).

The velocity perturbations seen within region A (Fig. 3.17) are the clearest evidence in favour of density waves in NGC 2403 (cf. Fig. 3.16). They were noticed by Love and by Shostak but are more clearly seen in the present observations. The easternmost end of the line of perturbations closely follows the outermost spiral arm to the SW of the nucleus, while at the NW end it follows HI spiral feature 9 (Fig. 3.8). This indicates that the HI and optical spiral segments are part of the same feature.

Other evidence for density waves can be seen in the areas B, C, D and E. Region B is in good agreement with the most prominent HI spiral arm - feature 1 in Fig. 3.8. The 'double-wave' evident in the two velocity contours passing through both regions C and D has previously been reported by Love, and is confirmed here; the perturbations seem to be associated with the two easternmost optical arms (Plate 3.3). Although region E shows some velocity peculiarities, the evidence does not confirm a large-amplitude 'wave' in a contour at 168 km/s, reported by Love. There is no clear optical or HI spiral feature in this region.

3.6.5 VELOCITY DISPERSION

The HPFW, w , of the line-profiles measured in high-resolution observations have been evaluated in concentric rings in the plane of NGC 2403. These widths are a measure of the velocity dispersion of the gas within the synthesised beam area, convolved with the velocity response of each channel of the

spectrometer (Gaussian with a HPFW, w_c , of 15.84 km/s). The latter effect can be corrected using

$$\sigma_{\text{rms}} = (w^2 - w_c^2)^{\frac{1}{2}} / 2.36,$$

where the constant in the denominator corrects to rms values.

Values of σ_{rms} decrease from about 35 km/s at a radius of 3 arcmin, to 15 ± 4 km/s at larger radii (mean of 15 to 25 arcmin). The majority of this effect is due to the larger velocity-gradient across the synthesised beam at small radii. Model fitting is necessary to investigate the intrinsic velocity dispersion as a function of radius, but at large radii the dispersion quoted above is similar to that reported for the gas in other galaxies (Table 3 in Allsopp 1978).

4 CONCLUSIONS

The main conclusions of this study of HI in NGC 2403 are summarised here:

- (1) HI is seen between velocities of -7 and $+270$ km/s (heliocentric) and up to 21 kpc from the nucleus. The total mass of HI is $(3.2 \pm 0.3) 10^9 M_{\odot}$.
- (2) The HI disc is slightly warped. There is direct evidence of this in Fig. 3.1a, and indirect evidence in the skewing of the velocity contours (Fig. 3.17).
- (3) A low-brightness feature seen in the north of NGC 2403 (Fig. 3.1a between 85 and 138 km/s) requires confirmation.
- (4) The radial distribution of HI shows no significant central minimum.
- (5) The HI distribution shows no significant north-south asymmetry, but does show a significant east-west asymmetry for radii greater than 11 arcmin.
- (6) Several HI spiral features are seen and these appear (as far as the limited resolution allows) to be correlated with the optical spiral arms and HII regions.
- (7) The dynamical parameters suggested by Shostak (1973) represent the underlying circular rotation of NGC 2403 better than those suggested by Love (1975), (cf. Table 3.6).
- (8) The rotation curve for radii greater than 14 arcmin has an approximately constant value of 130 km/s.
- (9) The total mass and integral parameters of NGC 2403 are displayed in Table 3.4.
- (10) The high-resolution velocity field of these observations (Plate 3.5 and Fig. 3.17) clearly shows several perturbations associated with the spiral arms. The perturbations are in qualitative agreement with the density-wave theory

of spiral structure (summarised in Fig. 3.16).

- (11) The rms velocity dispersion of the HI gas in NGC 2403 is (15 ± 4) km/s, a value typical of many galaxies.

CHAPTER 4THE Im GALAXY NGC 1569 (ARP 210)1 INTRODUCTION

NGC 1569 is No. 210 in the Arp (1966) Atlas of Peculiar Galaxies (Plate 4.1a). It is well resolved into stars and HII regions and has been classified as a 'Magellanic irregular with a bar' (IBm) in RC2. A summary of the optical parameters is given in Table 4.1. Ables (1971) presents isophotes and discusses two bright centrally-located star-like objects, A and B (Plate 4.1b), which he suggests may be foreground stars. He estimates the distance to be 3.3 Mpc so that 1 arcmin \cong 0.96 kpc; this value is adopted here. NGC 1569 is probably associated with the G2 (= M81 = Ursa Major - Camelopardalis) group of galaxies (de Vaucouleurs 1975).

H α plates (Hodge 1974; Plate 4.1c) reveal that the whole galaxy is contained in an intense H α envelope, with an extensive filamentary system reaching out to a radius twice that of the optical. De Vaucouleurs, de Vaucouleurs & Pence (1974) estimate that the H α emission is an order of magnitude more intense than for an average Im system. The fainter filaments have a radial trend, while the brightest filament, originally detected by Butslov et al. (1962), curves out of the most southerly region of the galaxy and could be considered as a spiral arm.

De Vaucouleurs et al. (1974) have obtained Fabry-Perôt interferograms of the H α filaments in order to derive the velocity field. This is chaotic, apparently not consistent with normal rotation of a disc galaxy, but displaying a general velocity gradient perpendicular to the major axis of 116° determined from the outer isophotes.

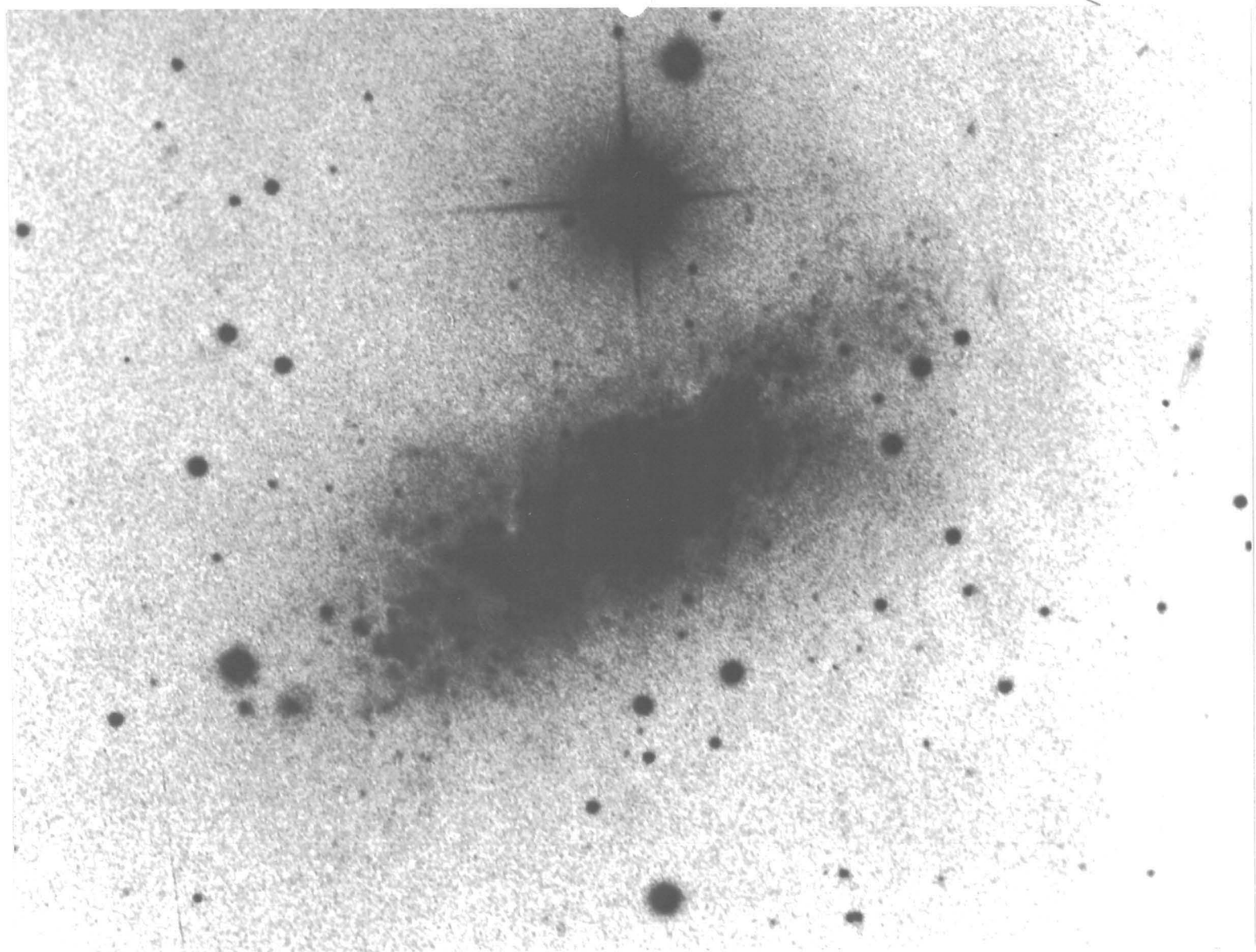
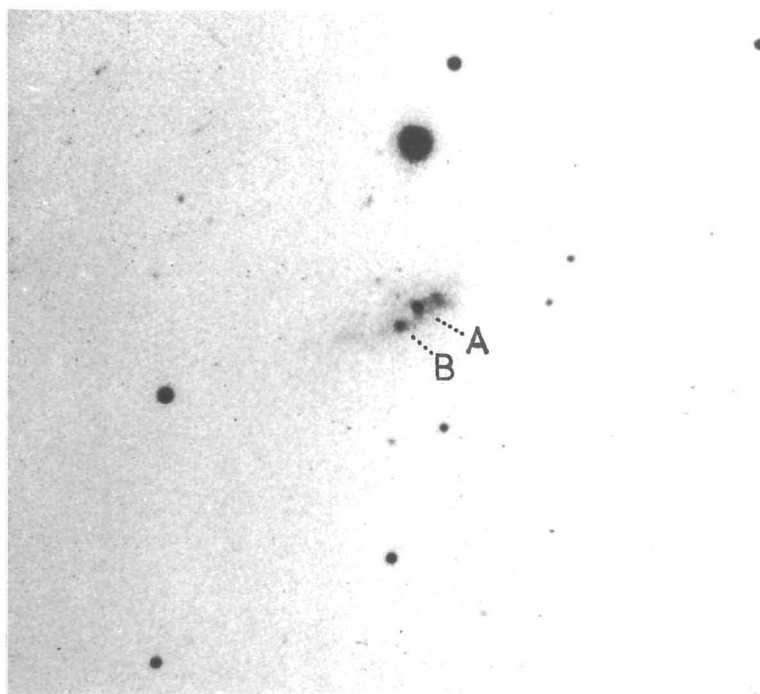


Plate 4.1 Three photographs showing different aspects of NGC 1569. In all cases north is at the top and east is on the left. (a) Long-exposure plate from Arp (1966). (b) Short-exposure plate from Hodge (1974) showing the two 'star-like' objects A and B. (c) $H\alpha$ plate from Hodge (1974) showing the extensive radial filaments and 'arm'.

(b)



(c)

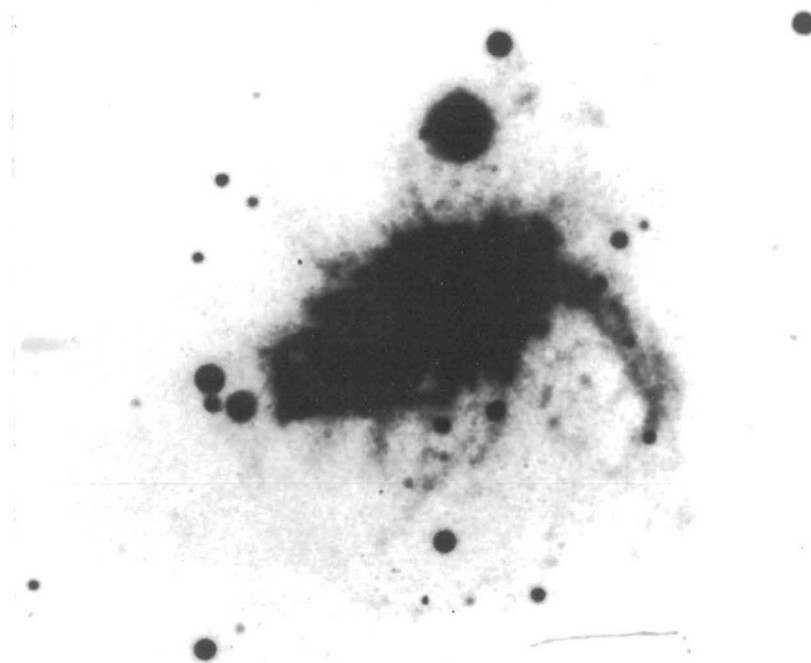


Plate 4.1 (continued)

Table 4.1 Optical parameters for NGC 1569.

Parameter	Value	Source
Coordinates of nucleus (1950)		
RA	04 ^h 26 ^m 04 ^s .5	RC2
dec	64°44'24"	RC2
Classification		
revised type	IBm	RC2
Holmberg type	IrI	RC2
Total 'face-on' B magnitude corrected for galactic and internal absorption		
	10.58 mag	RC2
(correction	1.4 mag	RC2)
Isophotal major diameter corrected to 'face-on'		
	2.75 arcmin	RC2
Ratio of minor to major diameter, R_{25}		
	0.49	Ables (1971)
Major axis PA		
	116°	Ables (1971)
Systemic radial velocity (Heliocentric), V_{sys}		
	-87 km/s	RC2
Distance, D		
	3.3 Mpc	Ables (1971)
Colour index (B-V)		
	0.23 mag	Roberts (1968)
Inclination		
	63°	Ables (1971)
Luminosity, L [$\propto D^2$]		
	9.4 x 10 ⁸ L _⊙	from magnitude and D given in this Table.

Lequeux (1971) has observed the radio continuum from the galaxy at 1420 MHz using an interferometer. He found an extended disc component plus an unresolved source (< 1 arcmin) at a position close to the two star-like objects. However, the radio position was too inaccurate for a certain identification.

Zwicky (1971) and Hodge (1974) have suggested that the appearance of NGC 1569 results from an explosion within the galaxy. De Vaucouleurs et al. (1974) also support this view, on the basis of their observations of the chaotic and intense $H\alpha$ emission. They argue that the two star-like objects may be part of the galaxy and that the unresolved radio component of Lequeux (1971), which has a flat radio spectrum unusual for a late-type galaxy, might arise from A or B. Indeed, NGC 1569 exhibits many of the features characteristic of IrII galaxies such as M82.

The most recent observations of NGC 1569 have been in the radio continuum at 2695 and 8085 MHz with high resolution (Seaquist & Bignell 1976). Their map at 2695 MHz closely resembles the isophotal maps by Ables (1971), with the brightest radio emission coinciding with the brightest region of blue light in the west of the galaxy. This is consistent with the observations of Lequeux (1971), and the high-resolution map now shows that neither of the star-like objects coincides with any radio continuum feature. Seaquist & Bignell have, therefore, strengthened the suggestion of Ables (1971) that A and B are foreground stars, although association with the galaxy cannot yet be excluded. The map at 8085 MHz shows the emission to be due to many unresolved sources, some of which coincide with HII regions. The spectra of many of these sources

are rather flat, indicating thermal emission from an optically thin ionized gas. The strongest source, however, contains a nonthermal component and is coincident with the brightest continuum feature on a blue photograph of the galaxy (excluding A and B).

The present observations are of both radio continuum and neutral hydrogen. The latter provide maps of the integrated HI and velocity fields with the highest angular resolution available to date. (Limited observations of HI using the Westerbork Synthesis Radio Telescope are also known to exist in an unpublished form; de Bruyn, private communication). In Section 2 details of the observations are briefly described, while in Section 3 the resulting maps are presented and analysed. Further discussion is presented in Section 4, and the main conclusions are summarised in Section 5.

2 OBSERVATIONS

The survey of NGC 1569 consisted of 48 equally-spaced interferometer baselines as detailed in Table 4.2. The HI emission was measured using the digital spectrometer over a 2-MHz bandwidth. Continuum radiation in the 10-MHz bandwidth centred at 1419 MHz was also measured and both the surveys were calibrated by observations of 3C 309.1.

In order to correct for the presence of continuum emission, the eight channel maps which contained no significant line emission (-258 to -192 and +72 to +98 km/s inclusive) were averaged and subtracted from those which did. The resulting 'continuum-free' channel maps at a resolution of 1.9 x 2.1 arcmin, are shown in Fig. 4.1.

Table 4.2 Details of the observations of NGC 1569 with the Cambridge Half-Mile telescope

Dates	1977 November/December
Map centre (1950)	
RA	04 ^h 26 ^m 54 ^s
dec	64° 44' 24"
Interferometer baselines	
number	48
smallest	12.2 m
increment	6.1 m
largest	298.7 m
Calibrator	
name	3C 309.1
flux density	7.9 Jy
reference	Kellermann <u>et al.</u> (1969)
Response	
synthesised beam (HPFW)	
RA x dec	1.9 x 2.1 arcmin
structure absent	>1°
radius of first grating	
response in RA	~2°
Continuum Survey	
bandwidth	10 MHz
centre frequency	1419 MHz
theoretical sensitivity	
per beam area	1.6 mJy
Hydrogen-line survey	
bandwidth	2 MHz
heliocentric velocity	
range	-284 to +125 km/s
channel separation	13.2 km/s
channel width	16 km/s (FWHP Gaussian)
mean rms sensitivity	
per beam area	21 mJy

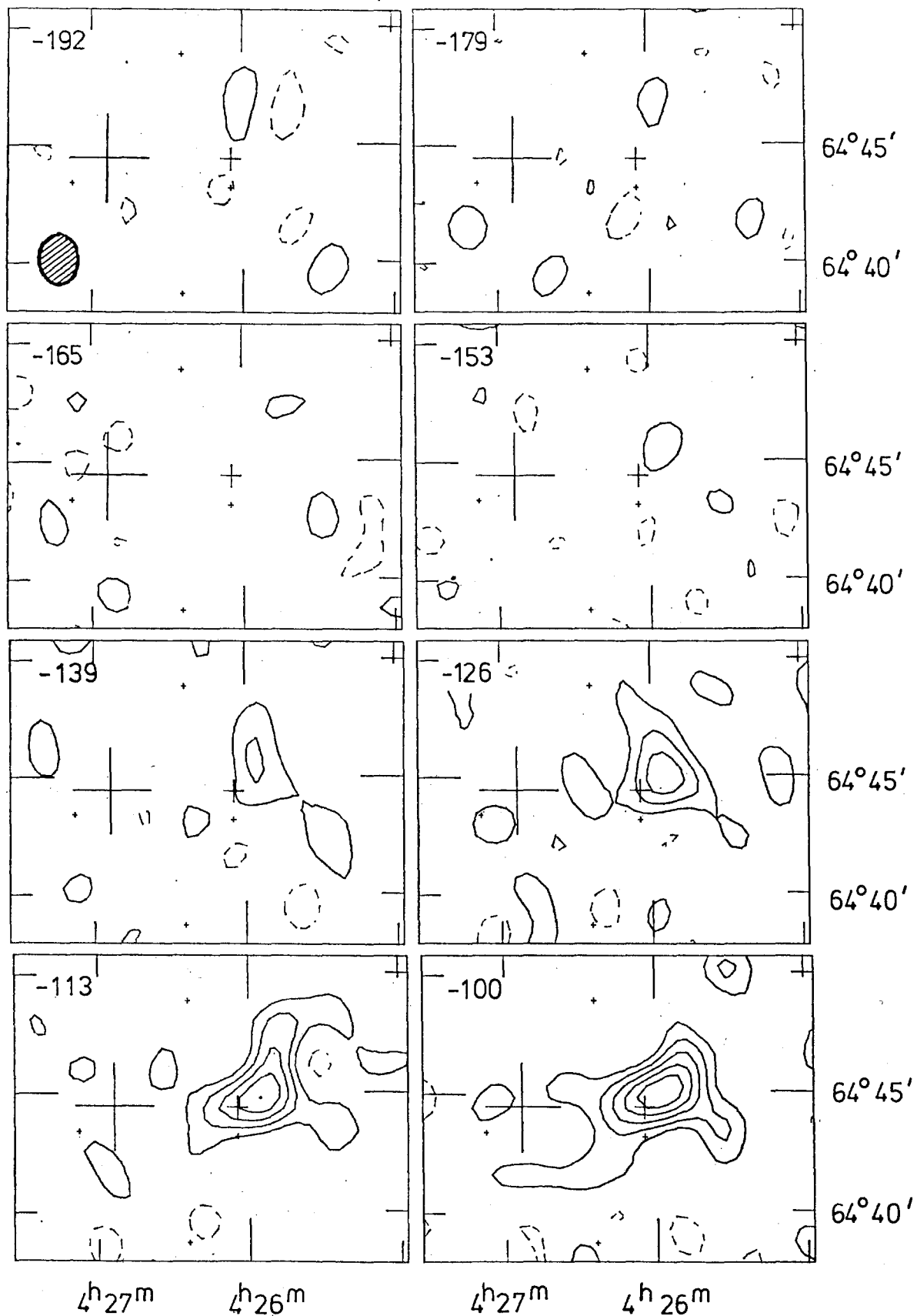


Figure 4.1. Continuum-free channel maps of NGC 1569 at a resolution of 1.9×2.1 arcmin (hatched ellipse). The contour interval is 50 mJy (per beam area) with the first positive contour (solid) at 50 mJy ($\sim 2\sigma$) and the first negative contour (dashed) at -50 mJy. The zero contour is omitted. Each map corresponds to HI within a 16 km/s range of radial velocities centred at the velocity (km/s) shown at the top left of each panel. The large crosses represent the map centres, the medium crosses represent the optical nucleus of the galaxy (Table 4.1), and the small crosses are star positions. No polar diagram has been applied.

correction

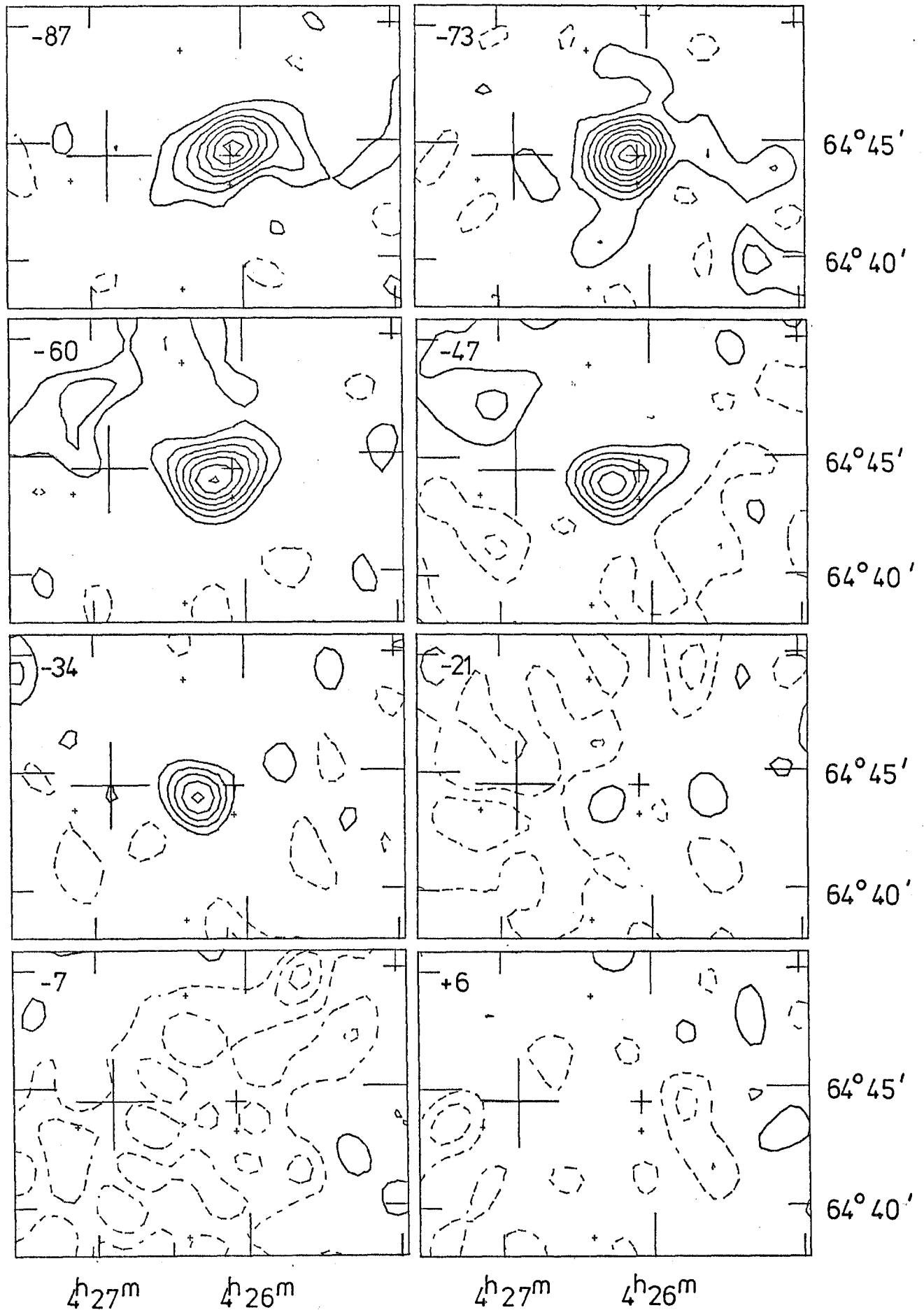


Figure 4.1 (continued)

3 RESULTS AND ANALYSIS

3.1 Radio Continuum

The broad-band continuum map centred at 1419 MHz is shown in Fig. 4.2. At the resolution of 1.9×2.1 arcmin, the emission from NGC 1569 is slightly resolved along a position angle of about 117° , in good agreement with the optical major axis (Table 4.1). Most of the features outlined by the -5 and $+5$ mJy ($\sim 3\sigma$) contours are not real, but result from the side-lobes of the synthesised beam. The extensions of the $+5$ mJy contour along the major axis may, however, be partly real.

The coordinates of the peak of emission (Table 4.3) are in excellent agreement with the position of the optical nucleus determined by Ables and shown by the medium-sized cross in Fig. 4.2. The integrated flux density is estimated to be 450 ± 20 mJy, in agreement with the spectrum presented by Seaquist & Bignell (1976). The present line observations reveal that approximately 30 mJy of the flux may be attributed to the line emission.

3.2 The total HI mass

The integrated HI spectrum for NGC 1569 (Fig. 4.3) was obtained from observations at the twelve smallest interferometer baselines (giving a resolution of 7.4×8.2 arcmin). Assuming the HI to be optically thin, the total HI mass is $(1.9 \pm 0.2) \times 10^8 M_\odot$ (Table 4.4). NGC 1569 lies only 11° out of the galactic plane, and the effects of large-scale Galactic hydrogen are evident in both the strong negative feature seen at -7 km/s (Fig. 4.3) and the large-scale negative features seen on the channel maps centred from -21 to $+6$ km/s (Fig. 4.1). These effects result from Galactic ^{structure in the} hydrogen

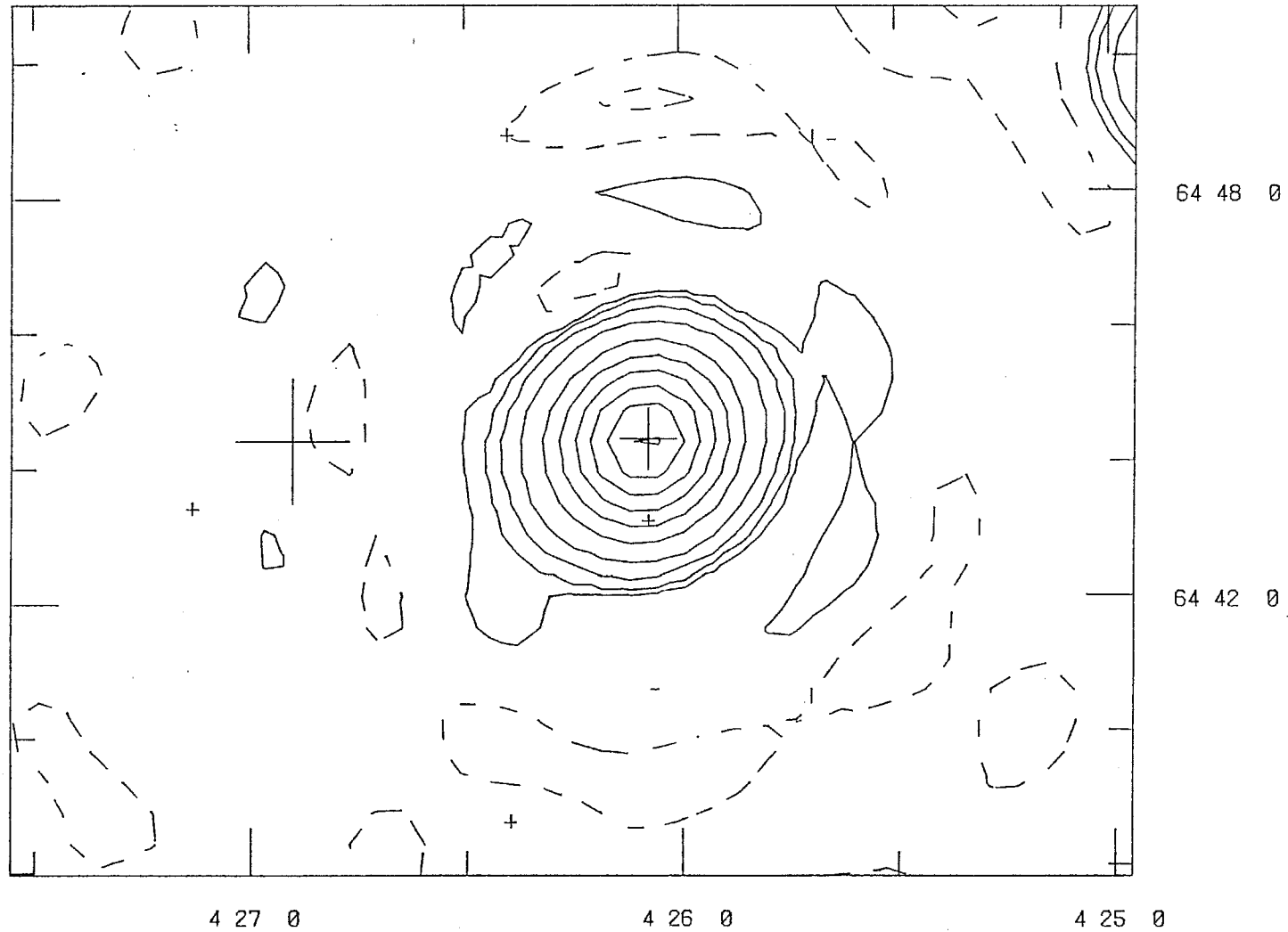


Figure 4.2 Map of radio continuum emission over a 10-MHz bandwidth centred at 1419 MHz. The HPBW resolution is 1.9×2.1 arcmin. Solid contours are 5 10 20 40 80 160 200 240 and 280 mJy. Dashed contours are -5 and -10 mJy. The crosses are the same as for Fig. 4.1.

Table 4.3 Parameters resulting from the observation of radio continuum in NGC 1569 centred at 1419 MHz

Parameter	Value	Source
Coordinates of peak emission (1950)		
RA	$04^{\text{h}}26^{\text{m}}04^{\text{s}}.6 \pm 1.2$	Fig. 4.2
dec	$64^{\circ}44'26'' \pm 7$	Fig. 4.2
Integrated flux density	450 ± 20 mJy	Fig. 4.2
Coordinates of optical nucleus (1950)		
RA	$04^{\text{h}}26^{\text{m}}04^{\text{s}}.5$	Table 4.1
dec	$64^{\circ}44'24''$	

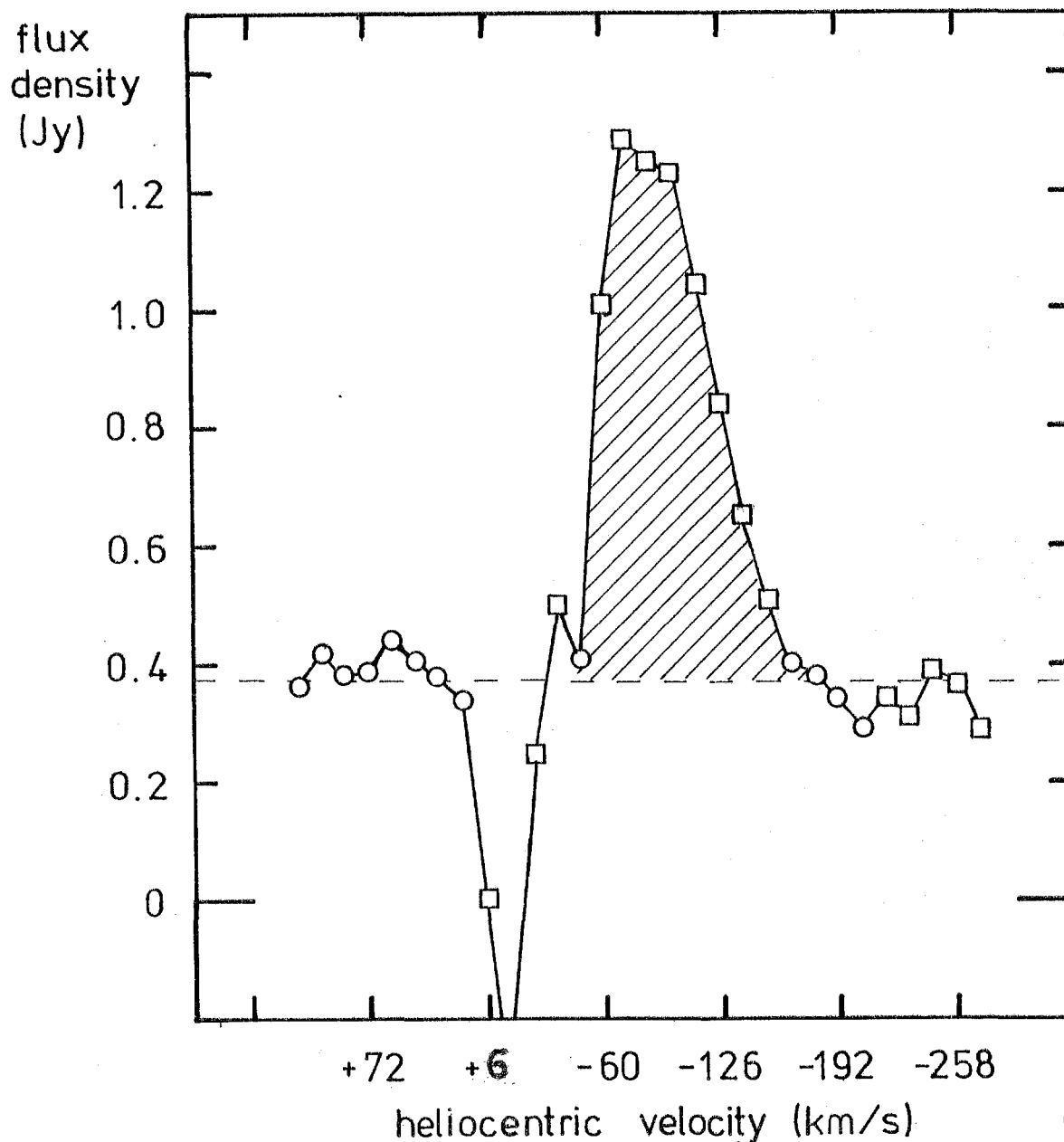


Figure 4.3 The integrated HI spectrum of NGC 1569. The squares and circles represent the peak flux centred on NGC 1569 seen in the 12-spacing channel maps (not corrected for continuum emission). The horizontal dashed line represents the mean level of continuum emission, and was obtained by averaging the data represented by circles. (These channels were also used for continuum subtraction from the high-resolution maps). The shaded area was used to evaluate the total HI mass. The velocity range -34 to +19 km/s is affected by local HI.

Table 4.4 HI parameters for NGC 1569

Parameter	Value	Source
Coordinates of nucleus (1950)		Plate 4.2
RA	$04^{\text{h}}26^{\text{m}}06^{\text{s}}.5 \pm 1.2$	
dec	$64^{\circ}44'24'' \pm 7$	
HI dimensions at the 200 K km/s level after deconvolution with the telescope beam		Plate 4.2
major axis	5.9 ± 0.4 arcmin	
minor axis	2.8 ± 0.4 arcmin	
ratio (minor/major)	0.48 ± 0.01	
Major axis position angle		
channel maps	$124 \pm 3^{\circ}$	Fig. 4.1
HI distribution	$117 \pm 1^{\circ}$	Plate 4.2
Systemic radial velocity (heliocentric)	-77 ± 1 km/s	Fig. 4.4
Integrated profile width (FWZP), ΔV	119 ± 13 km/s	Fig. 4.3
HI mass, $M_{\text{H}} [\propto D^2]$	$(1.9 \pm 0.2) \times 10^8 M_{\odot}$ cf. $0.3 \times 10^9 M_{\odot}$	Fig. 4.3 Roberts (1968)
Mean rms velocity dispersion	12 ± 4 km/s	corrected to $D=3.3$ Mpc see text
Total mass, $M_{\text{T}} [\propto D]$	$7 \times 10^8 M_{\odot}$	Fig. 4.1
Luminosity, $L [\propto D^2]$	$9.4 \times 10^8 L_{\odot}$	Table 4.1
Integral parameters		
$M_{\text{H}}/L [\propto D^0]$	0.20 ± 0.02 cf. 0.20	this table Roberts (1968)
$M_{\text{T}}/L [\propto D^{-1}]$	0.52 ± 0.06	this table
$M_{\text{H}}/M_{\text{T}} [\propto D]$	0.39 ± 0.09	this table

~~Continuum radiation from NGC 1569~~, and may mask some HI emission from the galaxy at these velocities, thus accounting for part of the asymmetry of the profile. If the hydrogen mass is computed using a symmetrical profile, by doubling the area under the half of the profile further from the effects of Galactic HI, the hydrogen mass, M_H , is about $2.0 \times 10^8 M_\odot$, a value not significantly different from that adopted.

Both M_H and the luminosity, L (Table 4.4), of NGC 1569 are consistent with an Im galaxy, although these parameters are not strongly correlated with type. The ratio M_H/L normally correlates well with type but the value for NGC 1569 is unusual for an Im type, being that more commonly found in galaxies of Sc or Sd type (Balkowski 1973).

3.3 Unusual features seen in the channel maps

HI associated with NGC 1569 can be seen in the channel maps (Fig. 4.1) centred on velocities from -165 to -21 km/s and the general pattern of emission resembles that expected from an inclined disc in differential rotation. However, apart from the underlying rotation, several interesting features are observed, which are discussed below.

(1) Several of the channel maps show low-brightness extensions emerging radially from the brighter emission. This is seen especially clearly at -73 km/s, but is also evident at -113 and -100 km/s.

(2) Isolated patches of emission are seen at about 7 arcmin to the NE of the nucleus (RA $4^h 27^m$, dec $64^\circ 47'$ at -60 and -47 km/s) and a similar distance to the SW (RA $4^h 25^m 20^s$, dec $64^\circ 40'$ at -73 km/s).

Features (1)-(3) should be treated with caution, and require independent confirmation;

One possibility is that they are due to Galactic emission, since, at these coordinates, the bright Galactic HI exists in the (heliocentric) velocity range -20 to $+20$ km/s (Weaver & Williams 1973), and HVC and IVCs have been reported nearby (Vershur 1973). The present high-resolution observations are not sensitive to large-scale emission ($\geq 1^\circ$).

If the emission in features (1) and (2) originates from the vicinity of NGC 1569, it indicates that the galaxy is disturbed not only in its optical appearance, but also in its HI distribution.

(3) The bright emission from NGC 1569 seen on the channels at -60 and -47 km/s has clear extensions to the NW along the major axis. These extensions are on the opposite side of the nucleus to the bright emission and may be due to the velocity dispersion of the gas or indicate a component of HI rotating about NGC 1569 in the opposite sense to the bright emission.

3.4 The Integrated HI Distribution

The integrated HI map is shown superimposed on a blue photograph from the Palomar Sky Survey in Plate 4.2. Two distinctive features are visible at low brightness (i.e. in the 200 K km/s contour): (i) an isolated patch of emission to the NE of the nucleus (corresponding to feature (2) of the channel maps), and (ii) an 'arm-like' extension towards the ~~SE~~^W from the ~~easternmost~~^{west} end of the major axis (corresponding mostly to feature (1) of the channel maps). The arm-like extension is much larger than the H α arm noted in Section 1 (Plate 4.1c),

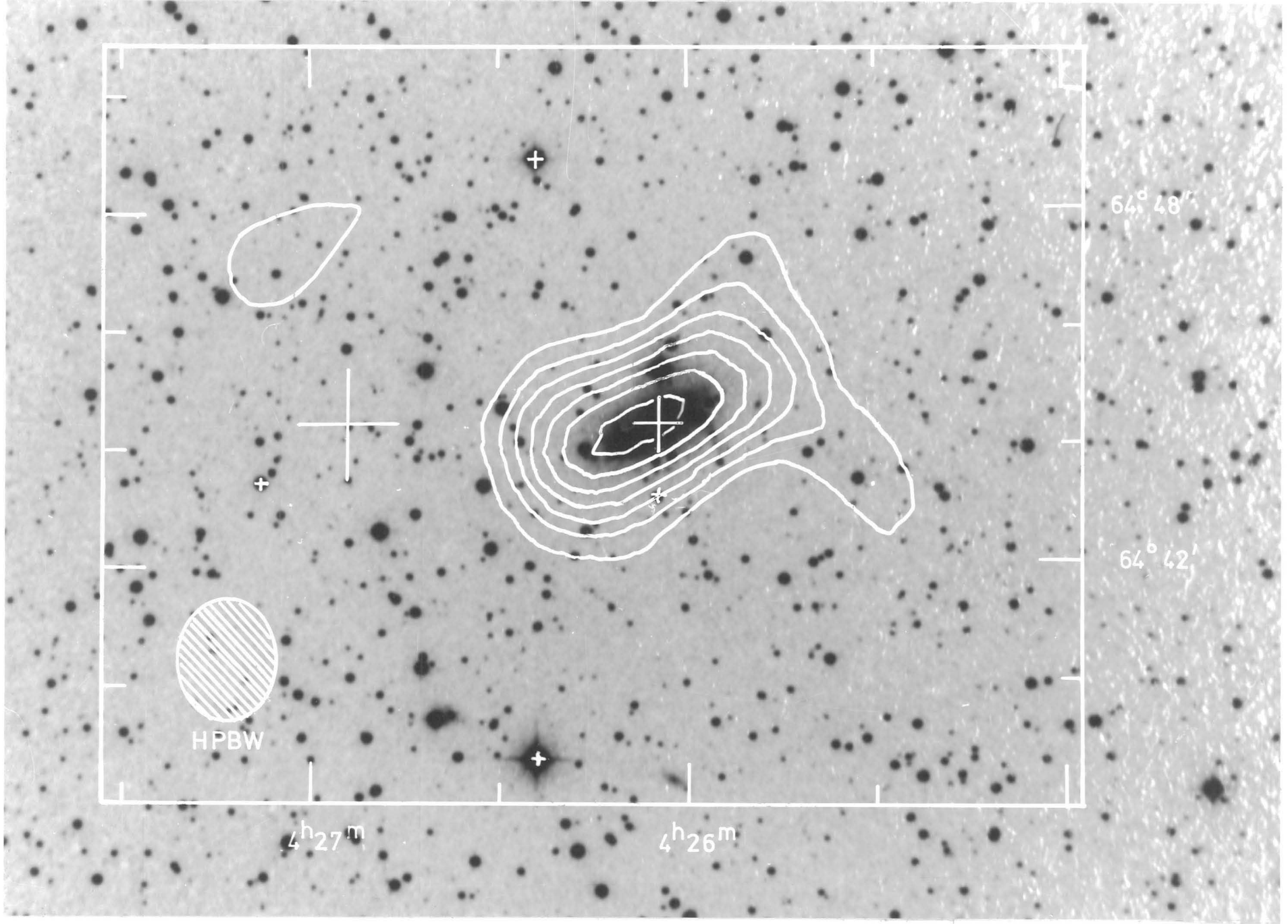


Plate 4.2 Integrated HI map of NGC 1569 superimposed on the blue PSS plate (copyright Hale Observatories). The map incorporates 10 continuum-free channel maps over the velocity range -139 to -21 km/s. The HPBW resolution is 1.9×2.1 arcmin (hatched ellipse). The contours start at 200 K km/s and are at intervals of 100 K km/s. The noise varies as the number of channels included at any point, and is typically ~ 30 K km/s. The crosses are explained in Fig. 4.1

and does not coincide with it, but both arms appear to have a common root. Apart from this correspondence, neither of the two HI features has any obvious optical feature coincident with it.

The contours of brighter emission (≥ 300 K km/s) show good axial symmetry, although they are not perfectly elliptical. Parameters derived from Plate 4.2 (including the coordinates of the peak emission, the dimensions of the HI and the position angle of the HI) are shown in Table 4.4. The HI parameters are in good agreement with the optical values (Table 4.1), except that the HI extends about twice as far from the nucleus as does the optical emission.

3.5 The Velocity Field

Fig. 4.4 shows the velocity field obtained from the line observations. The velocity contours are approximately perpendicular to the major axis ($PA \sim 117^\circ$) defined by both the optical and integrated HI distributions, thus confirming that the galaxy is rotating.

The velocities observed along the major axis, V_{obs} , are displayed in Fig. 4.5. The steep drop in velocities occurring beyond 2 arcmin from the nucleus is partly a manifestation of the peculiar radial extensions seen in the channel maps (Section 3.2), since these extensions comprise HI at large distances from the nucleus with velocities close to that of the system as a whole.

3.6 The Rotation Curve

A rotation curve for NGC 1569 was derived by assuming that circular rotation predominates, so that

$$V_{\text{rot}}(R) = (V_{\text{obs}}(R) - V_{\text{sys}}) / \sin(\text{inclination}).$$

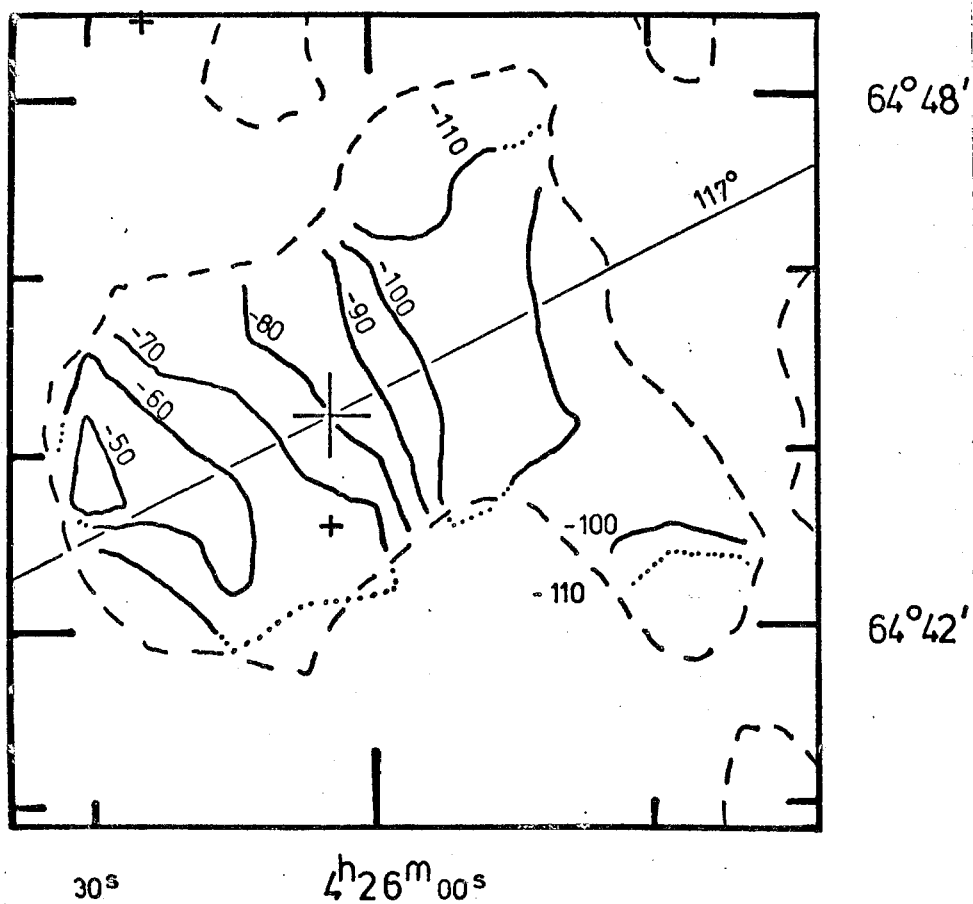


Figure 4.4 Velocity field for NGC 1569. The contours of constant heliocentric velocity are shown as solid lines, except in regions of low signal-to-noise ratios where they are shown dotted. The dashed lines are the 100 K km/s contours of the integrated HI. The velocity resolution is 16 km/s and the spatial resolution is 1.9×2.1 arcmin. The crosses are the same as in Fig. 4.1, and the line marks a PA of 117° .

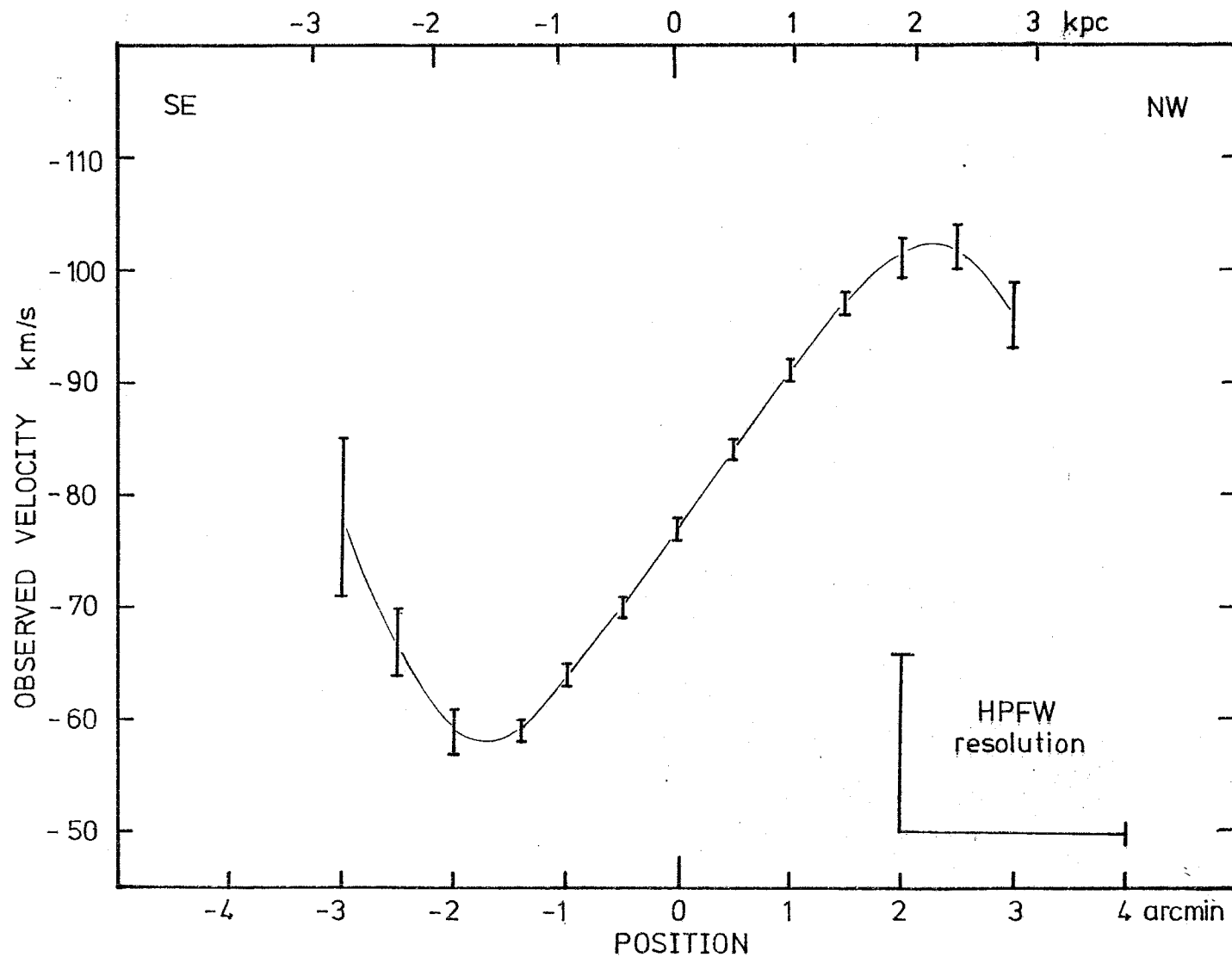


Figure 4.5 Observed velocities at 0.5 arcmin intervals along the major axis of NGC 1569. The values were centred at RA $4^{\text{h}}26^{\text{m}}07^{\text{s}}$ dec $64^{\circ}44'24''$ and measured along a PA of 117° . The error bars were computed according to a formula in Warner *et al.* (1973). No allowance has been made for beam smearing.

The systemic velocity, V_{sys} , of NGC 1569 evaluated from Fig. 4.5 is -77 ± 1 km/s. This value is confirmed in Fig. 4.4 since the -80 km/s contour passes very close to the cross marking the position of the optical nucleus, but the value is not significantly different from the optical value of -87 km/s ± 8 (Table 4.1). Adopting the values $V_{\text{sys}} = -77$ km/s, inclination = 63° and the curve of V_{obs} (Fig. 4.5), the resulting values of V_{rot} rise in direct proportion to radius, R , reaching a peak value of about 25 km/s at $R = 2$ arcmin, and then fall steeply beyond $R = 2$ arcmin, to $V_{\text{rot}} \sim 10$ km/s at $R = 3$ arcmin. This rotation curve has, however, been significantly affected by the instrumental response of the telescope. Such 'beam-smearing' effects were mentioned in Chapter 1, and tend to make the observed rotation curve rise less steeply at small radii than is actually the case. Calculations of the velocity profiles expected from a model galaxy have been made, taking due account of the telescope's velocity resolution and synthesised beam size. One particular model which can provide a good match to the V_{obs} curve (Fig. 4.5) comprises a true rotation curve which rises linearly to $V_{\text{rot}} \sim 40$ km/s at $R = 2$ arcmin, and then falls to $V_{\text{rot}} \sim 20$ km/s at $R = 3$ arcmin. This linear increase of V_{rot} with radius is that expected for a rigid disc in rotation, and is typical of the dynamics found by Tully et al. (1977) for several dwarf irregular galaxies. The rapid fall of V_{rot} beyond $R = 2$ arcmin (faster than the Keplerian law, $V_{\text{rot}} \propto R^{-1}$) is highly atypical for a rotation curve, but is not so surprising in this case, since unusual HI emission is known to exist, which would not necessarily be expected to exhibit circular rotation.

3.7 Velocity Dispersion

The modelling procedure just described also allows the velocity dispersion of the gas in NGC 1569 to be evaluated. This was done by comparing the widths (FWHP) of the HI line-profiles predicted by the model with those observed at several points over the face of the galaxy. Since the model allows for both beam smearing and velocity convolution, any excess width has been interpreted as the intrinsic velocity-dispersion of the gas. The rms velocity-dispersion within one synthesised beam area was found to have an approximately uniform value over the face of the galaxy of 12 ± 4 km/s. This value is typical of many galaxies (Allsopp 1978, Table 3).

3.8 Total Mass

An estimate for the total mass of NGC 1569 (Table 4.4) was calculated using the formula given in Section 2.4(f) of Chapter 1. This is based on HI associated with NGC 1569 existing in channels 60 km/s away from the systemic velocity and up to 3 arcmin from the nucleus. The pressure term in the equation of motion has been ignored, but the method of Tully *et al.* (1977) shows the effect to be less than 10 per cent. The value of M_T is low for an Im galaxy, although not inconsistent with this type of galaxy.

3.9 Asymmetries in the velocity field

The velocity contours of Fig. 4.4 resemble the pattern expected of a flat disc in normal rotation, but also show a significant deviation from axial symmetry. The -90 and -110 km/s contours to the NW of the nucleus are nearly perpendicular to the major axis, while the -60 and -70 km/s contours to the SE are clearly not perpendicular, but have a signific-

antly greater PA. One explanation of this effect is that a localized region of NGC 1569 (to the SE of the nucleus) is exhibiting a radial expansion of about 10 km/s. (It is necessary to assume that the northern edge of NGC 1569 is nearer to the observer.)

Alternatively, it may be that the simple model of circular orbits is not adequate for NGC 1569. Like other galaxies with an optical bar (Bosma 1978) NGC 1569 may be warped. The orbits may be elliptical rather than circular, and the isophotal major axis may no longer be coincident with the dynamical major axis (line of nodes). A non-uniform HI field may also distort the velocity contours. The present observations are unable to distinguish which of these possibilities is the correct one. *The most likely explanation is a non uniform HI field caused by those features noted in 3.3.*

3.10 Comparison of the HI and H α velocity fields

A comparison of the HI velocity field (Fig. 4.4) with the H α velocity field presented by de Vaucouleurs et al. (1974) has been made in the region where they overlap (approximately 4 arcmin² surrounding the nucleus). It is clear that there are no features in common. While the velocity field of the HI shows a fairly uniform gradient consistent with a rotating disc (PA 117^o, inclination 63^o), the velocity field of the H α shows, as reported in Section 1, a chaotic pattern inconsistent with normal rotation and having a general velocity gradient perpendicular to the major axis.

A velocity gradient of 1 arcmin per 13 km/s at a sensitivity of 50 mJy should be clearly visible

4 DISCUSSION

The similarity of many optical properties of NGC 1569 with those of the much-studied galaxy M82 was mentioned in Section 1 and is summarised in Table 4.5. NGC 1569 is approximately the same size and luminosity as M82, although the former is much lower in both HI and total mass.

The most important similarity is the extensive system of luminous H α filaments arranged in a radial pattern in both galaxies. The similarity is even more striking since the velocity gradient of the filaments in M82 is perpendicular to the major axis, exactly as for NGC 1569.

Lynds & Sandage (1963) originally interpreted the filaments in M82 in terms of ionized material that had been ejected from the nucleus in an explosion. Later, an accumulation of additional radio and optical data (notably that the emission lines were found to be polarized identically to the continuum) brought this theory into disfavour, and the luminous filaments in M82 are now interpreted in terms of an extensive halo of dust particles scattering light from the main body of the galaxy. M82 is known to be enveloped in a giant HI cloud which engulfs the whole of the M81 group, and Solinger *et al.* (1977) suggest that M82 is merely an interloper in the group, moving through this dusty HI cloud in such a way that its drift velocity accounts for the observed Doppler shift seen in reflection.

So far, all the publications concerning the origin of H α filaments in NGC 1569 favour an explosion. In view of the close similarity between the properties of M82 and NGC 1569, it seems clear that a model involving the scattering of light by dust should be investigated for NGC 1569, similar to that for M82.

Table 4.5 Comparison of the properties of M82 and NGC 1569

<u>M82</u>	<u>NGC 1569</u>
Distance 3.2 Mpc	Distance 3.3 Mpc
Optical magnitude 9.2	Optical magnitude 10.6
Optical diameter ~ 13 kpc	Optical diameter ~ 10 kpc
Luminosity $1.8 \times 10^9 L_{\odot}$	Luminosity $0.9 \times 10^9 L_{\odot}$
Exhibits chaotic dust lanes.	Dust lanes present.
Optical image not resolved into stars.	Optical image resolved into stars and HII regions.
Galaxy surrounded by intense H α filaments with a radial orientation.	Galaxy surrounded by intense H α filaments with a radial orientation, although the brightest filament curves out of the SW part of the galaxy in an 'arm'.
H α filaments above and below the galactic plane show Doppler shifts with the opposite sense.	H α filaments show a chaotic velocity field with a general gradient perpendicular to the major axis.
Over-luminous central region.	Two star-like objects may be part of the galaxy.
Radio source in nucleus has a complex geometry. Components have complex spectra, and no polarization is observed.	The radio continuum at 8085 MHz consists of a number of unresolved point sources, many having flat spectra. The strongest source contains a non-thermal component and is coincident with the brightest optical continuum feature (except the star-like objects).
Emission lines from the luminous filaments are polarized.	No data.
$M_H \sim 1.7 \times 10^9 M_{\odot}$	$M_H \sim 0.2 \times 10^9 M_{\odot}$
$M_T \sim 1.0 \times 10^{10} M_{\odot}$	$M_T \sim 0.1 \times 10^{10} M_{\odot}$

Perhaps NGC 1569 was once a normal late-type spiral or Im galaxy which has drifted into a tenuous cloud of dust and gas that is postulated to pervade at least part of the G2 group of galaxies? Its sudden immersion into this ambient gas caused a burst of star formation in the galaxy and accounts for its peculiar optical appearance. The dust particles in the cloud act like 'moving mirrors' and reflect the H α light from the nucleus. The drift of NGC 1569 relative to the cloud causes the light reflected at the leading edge of the galaxy to be blue-shifted, and that at the trailing edge to be red-shifted. Thus the velocity gradient perpendicular to the major axis is explained. Measurements of the polarization of the filaments in NGC 1569 are desirable, since a high degree of polarization almost certainly indicates that the light is scattered, rather than being emitted directly.

The hypothesis described above may also help to account for the unusual HI features reported in Section 3.3. In this view they could be localized enhancements of HI caused by the passage of NGC 1569 through the cloud of gas and dust.

There are, of course, some differences between NGC 1569 and M82. For example, the image of NGC 1569 is well resolved into stars and HII regions while none can be seen in M82, and this is the reason for their different classifications. In the hypothesis described above it is the dust in M82 which obscures the star images. We must therefore presume that there is enough dust around NGC 1569 to reflect H α light, but not enough to cause its stars to be obscured. Another difference between the two galaxies is that in M82 there are clear signs of a tidal interaction with the nearby galaxy M81. For NGC 1569 there are no bright companions within a radius of

25 arcmin (9 diameters), so that a tidal interaction is unlikely. But the hypothesis proposed is capable of explaining all the disturbances seen in the galaxy without the need to invoke a tidal interaction.

5 CONCLUSIONS

The observations presented in this Chapter have yielded the following information about NGC 1569:

- (1) The radio-continuum parameters, summarised in Table 4.3, and the HI parameters in Table 4.4.
- (2) The overall HI distribution is that expected of a disc in normal rotation, but there are several unusual features, namely:

** These are somewhat speculative and require independent confirmation.*

 - (a) Low-brightness extensions with a radial trend, on the channels at -73, -113 and -100 km/s;
 - (b) Isolated patches of HI about 7 arcmin both to the NE and SW of the nucleus;
 - (c) Bright emission at -60 and -47 km/s which is extended along the major axis, and may indicate HI in a retrograde orbit.
- (3) The integrated HI map shows a prominent HI extension towards the SW of the nucleus, and an isolated patch of HI to the NE.
- (4) The galaxy appears to be rotating as a rigid body for $R \lesssim 2$ arcmin, but the rotation velocities fall steeply at larger radii.
- (5) The velocity field to the NW of the nucleus shows a more or less normal rotation, but to the SE of the nucleus the velocity gradient is at a PA significantly greater than that defined by the optical and HI distributions. This could be due to a radial expansion of ~ 10 km/s, but it is not possible to distinguish between this and other explanations.
- (6) The HI gas has a velocity dispersion of 12 ± 4 km/s, a value typical of many other galaxies.

(7) There is no correspondence between the HI velocity field (Fig. 4.4) and the H α velocity field of de Vaucouleurs et al. (1974). The former shows normal rotation, while the latter is chaotic and exhibits a general velocity gradient perpendicular to the major axis.

It is proposed that the unusual properties seen in NGC 1569 (notably the velocity gradient of the H α) are due to the galaxy having drifted into a tenuous cloud of dust and gas, as originally advocated by Solinger et al. (1977) for M82. An important test of this hypothesis would be measurement of the polarization of the H α filaments.

CHAPTER 5
IrII GALAXIES

1 A SAMPLE OF ALLEGED IrII GALAXIES

Holmberg's introduction of the IrII category of galaxies, and their properties, were described in Chapter 1 (Page 1-7). Holmberg named six galaxies belonging to this type. An equivalent classification, IO (RC1), was also mentioned and contains twelve galaxies. To date, more than 40 galaxies have been suggested as being of IrII type (Table 5.1), although it should be emphasised that the classifications of many of these are uncertain.

Many of the less distant galaxies in Table 5.1 were the subject of a preliminary observing program, with the intention of selecting objects suitable for further study. Both radio continuum and neutral hydrogen were observed and the results are described in Section 2.

A large amount of optical and radio data was assembled on the alleged IrII galaxies. These data were examined to see if the sample possessed any well-defined properties or displayed any unusual correlations. The results of this work are described in Section 3. In Section 4, theories for IrII galaxies are reviewed, while in Section 5 the hypothesis that 'IrII galaxies tend to have more close companions than other types of galaxies' is investigated. Section 6 is a summary.

	name	source	weight		name	source	weight
1	NGC 51	COR ?	3	24	NGC 3955	RCL	10
2	NGC 442	UGC (1)	3	25	NGC 4194	COR ?	3
3	NGC 520	HOL	10	26	NGC 4248	RCL ?	5
4	NGC 942	COR ?	3	27	NGC 4253	K+H	6
5	NGC 972	RCL	10	28	NGC 4433	K+H	6
6	NGC 1012	UGC (2)	4	29	NGC 4438	K+H	6
7	UGC 2172	UGC (1)	3	30	NGC 4691	K+H ?	3
8	NGC 1275	UGC (3)	4	31	NGC 4753	RCL	10
9	UGC 2824	UGC (3)	4	32	NGC 4922B	COR ?	3
10	NGC 2388	COR ?	3	33	NGC 5195	HOL	10
11	NGC 2415	COR ?	3	34	NGC 5253	K+H	6
12	NGC 2814	RCL ?	5	35	NGC 5273	CHR	7
13	NGC 2968	HOL	10	36	NGC 5360	RCL	10
14	NGC 3034	HOL	10	37	NGC 5363	HOL	10
15	NGC 3067	MAR	7	38	NGC 5393	K+H	10
16	NGC 3077	HOL	10	39	NGC 6185	UGC (1)	3
17	UGC 5456	RC2 ?	5	40	NGC 6240	RC2 ?	5
18	NGC 3341	UGC (2)	5	41	NGC 6622	COR ?	3
19	NGC 3448	RCL	10	42	NGC 7070A	RCL	10
20	NGC 3499	RCL ?	5	43	NGC 7250	UGC (1)	3
21	NGC 3656	RCL	10	44	NGC 7625	DEM	6
22	NGC 3912	UGC (1)	3	45	NGC 7752	COR ?	3
23	NGC 3952	RCL	10	46	NGC 7800	RCL ?	5

Table 5.1 Sources of galaxies alleged to be of IrII type.

Abbreviations are as follows:

?	Uncertain classification
HOL	Holmberg (1958)
RCL	de Vaucouleurs & de Vaucouleurs (1964)
RC2	de Vaucouleurs, de Vaucouleurs & Corwin (1976)
UGC	Nilson (1973). The numbers in parentheses indicate the certainty which Nilson placed in the classification, and range from 5 ('under little dispute') to 0 ('very doubtful').
K+H	Krienke & Hodge (1974)
COR	Corwin (1970)
CHR	Chromey (1973)
MAR	Markarian (1963)
DEM	Demoulin (1969)

The columns headed 'weight' display the Author's estimate of the certainty which can be placed in the IrII classification. Weights lie in the range 0-10, with large weights implying a certain classification as IrII.

2 OBSERVATIONS

This section briefly describes preliminary observations of seven of the alleged IrII galaxies from Table 5.1. The majority of the observations were made with the Half-Mile telescope, although two One-Mile observations are reported and one optical spectrum was obtained using the Isaac Newton telescope.

Optical parameters for the seven galaxies are displayed in Table 5.2; these galaxies were selected as being amongst the nearest and brightest of the IrII sample, with the largest angular diameters (excluding well-studied galaxies such as M82 and NGC 3077).

The observations were designed to identify objects suitable for further study, particularly by detailed HI mapping with the Half-Mile telescope. In fact none proved suitable for further study since the instrument was unable to detect HI in any of these seven galaxies. Two other IrII galaxies are described elsewhere in this thesis - NGC 3448 in Chapter 6, and NGC 2814 (a member of the NGC 2805 group) in Chapter 7.

2.1 NGC 51

NGC 51 is the brightest in a group of six galaxies. The galaxy was observed for one day in 1977 October using the Half-Mile telescope (spacings of 40, 100, 160 and 220 ft). In the absence of a redshift, the radial velocity range 527-1345 km/s was chosen for the 4-MHz bandwidth. No hydrogen line was detected with a 3σ upper limit of 200 mJy, and no 1419-MHz continuum radiation was detected from the galaxy (3σ upper limit of 120 mJy).

Table 5.2 Optical parameters for seven IrII galaxies.

Name	NGC 51	NGC 972	UGC 02172	IC 334	NGC 2968	NGC 3067	NGC 5273
Coordinates (1950)							
RA	00 ^h 11 ^m 57 ^s	02 ^h 31 ^m 18 ^s	02 ^h 38 ^m 54 ^s	03 ^h 38 ^m 48 ^s	09 ^h 40 ^m 12 ^s	09 ^h 55 ^m 24 ^s	13 ^h 39 ^m 48 ^s
dec	47°58'42"	29°05'	43°09'	76°29'	32°10'	32°07'	35°54'
Redshift (km/s)	unknown	1555	unknown	3300±500 [#]	1608	1506	1022
Distance (Mpc) [*]	unknown	21	unknown	44	22	21	14
Photographic mag							
apparent	14.6	12.1	14.6	13.2	13.1	12.7	12.7
absolute	unknown	-19.5	unknown	-20.0	-18.6	-18.9	-18.0
Optical dimensions							
arcmin	1.4 x 1.3	3.7 x 1.7	1.8 x 1.1?	6 x 6	2.4 x 1.7	2.2 x 0.8	2.8 x 2.3
kpc	unknown	23 x 10	unknown	77 x 77	15 x 11	13 x 5	11 x 9

Notes

* Assumes $H_0 = 75 \text{ km s}^{-1} \text{ Mpc}^{-1}$

Not available at time of observations.

? Uncertain

Most data are from UGC.

2.2 NGC 972

A photograph of NGC 972 appears on page 23 of The Hubble Atlas of Galaxies (Sandage 1961). McCutcheon & Davies (1970) found $M_H/D^2 = (5.1 \pm 3.7) \times 10^6 M_\odot/\text{Mpc}^2$. The galaxy was observed for six days in 1976 September using the Half-Mile telescope (see Table 1.3, page 1-19, for details). No hydrogen line was detected in the velocity range 1120-1937 km/s with a 2σ upper limit of 70 mJy. Assuming $D = 21$ Mpc (Table 5.2), this corresponds to $M_H \lesssim 2.3 \times 10^9 M_\odot$, a result consistent with that of McCutcheon & Davies.

The radio continuum source coincident with the galaxy was found to have a flux density of 0.31 ± 0.05 Jy, using the Half-Mile telescope. The galaxy was observed for two days with the One-Mile telescope, which revealed a 408-MHz flux density of 0.48 ± 0.08 Jy. The 1407-MHz observations detected the galaxy, but grating rings from other nearby sources prevented a reliable analysis. Both the continuum fluxes quoted here are in agreement with previous determinations (Haynes et al. 1975).

2.3 UGC 02172

UGC 02172 was observed for a single day in 1977 October using the Half-Mile telescope (spacings of 40, 100, 160 and 220 ft). In the absence of any optical redshift, the radial velocity range 528-1345 km/s was chosen for the 4-MHz bandwidth. No hydrogen line was detected, with a 3σ upper limit of 200 mJy. No 1419-MHz continuum radiation was detected from the galaxy (3σ upper limit of 120 mJy).

2.4 IC 334

The nuclear region of IC 334 (alias UGC 02824) appears bright and complex, and an absorption lane runs eastward from the centre. Three days of observation were undertaken in 1976 November using the Half-Mile telescope (Table 1.3, page 1-19). The spectrometer used a 4-MHz bandwidth and, in the absence of an optical radial velocity, a range of 950-1767 km/s was chosen. No hydrogen line was detected with a 3σ upper limit of 160 mJy, and no 1417-MHz radio continuum was observed from the galaxy (3σ upper limit of 20 mJy).

Subsequent to these observations (1977 January), an optical spectrum was taken with the Isaac Newton telescope. The spectrum of IC 334 showed a strong NaD absorption line, a strong H β emission line, Ca:K and Ca+Fe absorption features, and weak Ca:H and CaI:g absorption features. The mean redshift was estimated to be 3300 ± 500 km/s. Thus, the radial-velocity range used for the HI observations was incorrect.

2.5 NGC 2968

NGC 2968 has a small bright nucleus with a dark lane. The galaxy is in a small group, its nearest neighbour being NGC 2964 which is 5.8 arcmin away. Observations for two days were undertaken with the One-Mile telescope in 1977 January. The aim was to gain information about the spectral index, since the only published radio flux density was 0.10 ± 0.10 Jy at 1400 MHz (Haynes *et al.* 1975). Unfortunately, no radio continuum was detected from the galaxy, with 2σ upper limits of 0.2 Jy at 408 MHz and 0.04 Jy at 1407 MHz. No hydrogen line observations were undertaken.

2.6 NGC 3067

De Vaucouleurs & de Vaucouleurs (1964, RCl) describe NGC 3067 as a 'bright complex bar or lens with bright knots and dark lanes - similar to NGC 972'. Chromey (1974) has investigated the stellar population, and finds that it closely resembles that of a normal Sb galaxy. The galaxy is almost coincident with the strong QSO 3C 232, and Grewing & Mebold (1975) and Hashick & Burke (1975) have detected a narrow HI-absorption feature. Three days of observation were undertaken with the Half-Mile telescope using a 2-MHz bandwidth during 1976 April. The available resolution and sensitivity (Table 1.3, page 1-19) was not sufficient to detect the absorption feature, and no other HI features were seen in the velocity range 1152-1560 km/s.

2.7 NGC 5273

NGC 5273 lies 3.3 arcmin to the NW of a fainter galaxy, NGC 5276. Optical studies (Chromey 1973) suggest a stellar population for NGC 5273 which is similar to that of a normal elliptical galaxy. Three days of observation were undertaken using the Half-Mile telescope in 1976 May (Table 1.3, page 1-19). No hydrogen line was detected in the 2-MHz bandwidth (velocity range 814-1223 km/s) with a 3σ upper limit of 170 mJy. At an assumed distance of 13.6 Mpc this corresponds to $M_H \lesssim 3 \times 10^9 M_\odot$. Subsequent to these observations, Knapp (1977) found $M_H \approx 0.37 \times 10^9 M_\odot$ (assuming a distance of 14.6 Mpc). No 1417-MHz radio continuum was detected from the galaxy (3σ upper limit of 25 mJy).

3 GENERAL PROPERTIES

All available optical and radio data were assembled on the alleged IrII galaxies. Apart from the characteristic optical morphology described in Chapter 1, the IrII sample generally showed a large dispersion in most physical properties. However, some well-defined properties and correlations were found and are described below.

3.1 Spectral type and colour

De Vaucouleurs (1959) was the first to note that several of his IO category seemed to have early-type spectra and yet late-type colour. That is, the spectra suggested a predominance of early-type stars (which are blue) and yet the photometry showed that the galaxy was quite red. Later Markarian (1963) reported that this was a characteristic of most of the 11 'M82-type' galaxies in his list, and Krienke & Hodge (1974) showed that the same was true of many of their sample of 18 IrII galaxies.

The data available on the colours and spectral types of the galaxies in the IrII sample are displayed in Fig. 5.1. The trend noted above is revealed by the fact that the majority of the points lie above the mean line for normal galaxies (de Vaucouleurs 1961). The wide dispersion in colours of the sample is also apparent. (A sample of 'early' or 'late' type spiral galaxies shows a significantly smaller dispersion in colours).

A combination of late-type colour with an early spectrum is in conflict with current ideas on the interstellar medium. Normal early-type galaxies tend to lack (a) internal reddening, (b) dust, (c) HII regions, and (d) the OII (372.7 nm) emission line. These signs are taken to imply little or no interstellar medium. IrII galaxies often

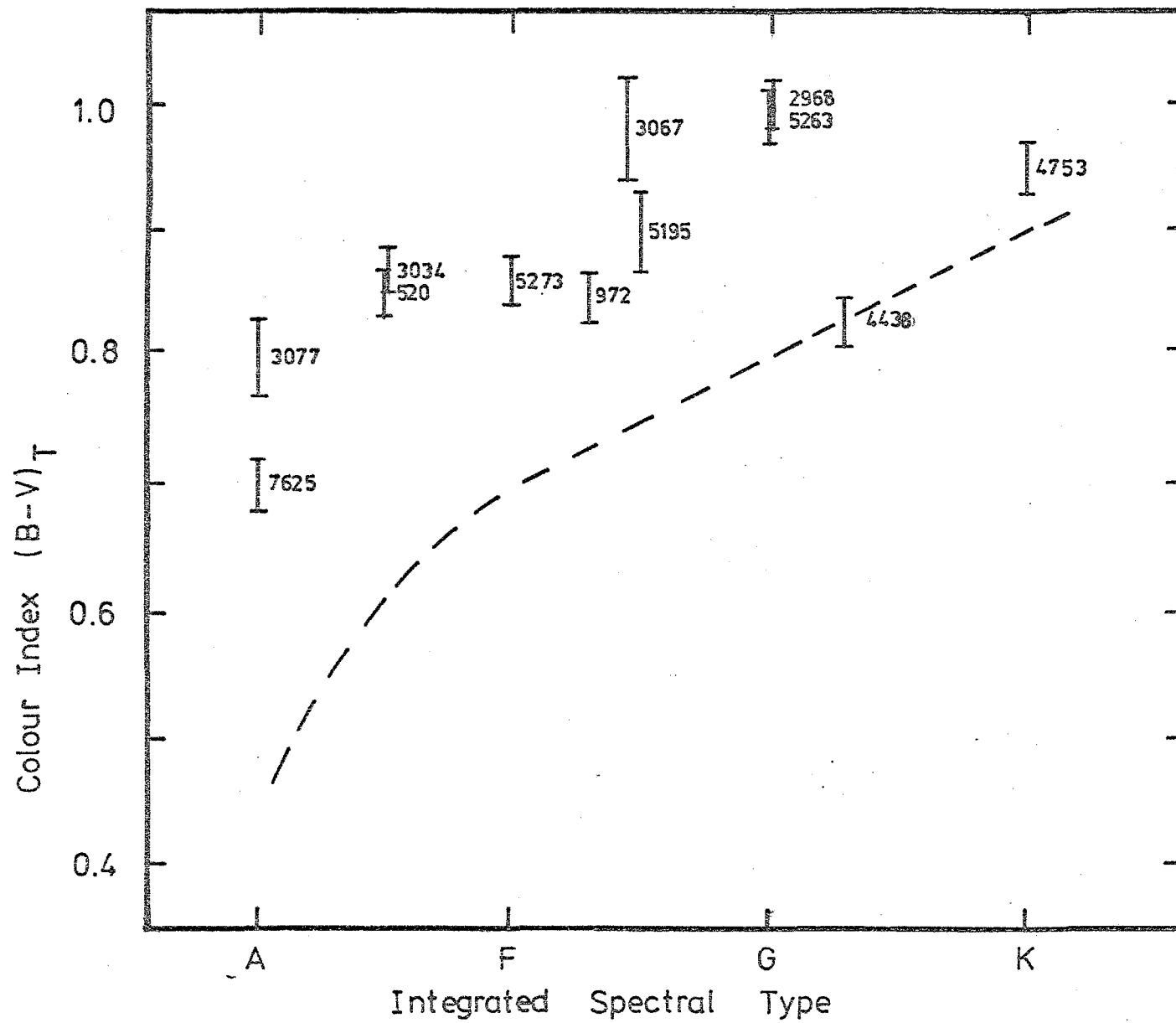


Figure 5.1. Colour-Spectral type plot for IrlI galaxies. The numbers give the NGC identity. The curve indicates a mean value for 'normal galaxies' (de Vaucouleurs 1961).

seem to have a new stellar population while at the same time being red. They often show dust lanes and yet seem to lack HII regions.

3.2 Radio Continuum

Normal galaxies show no correlation between Hubble type and radio luminosity, and there are conflicting claims as to whether peculiar and interacting galaxies have an excess radio flux (Wright 1974; Sulentic 1976). For the sample of IrII galaxies the distribution of radio luminosity is not significantly different from that for normal galaxies.

The distribution of spectral indices (α , where $S \propto \nu^{-\alpha}$) for the IrII galaxies (Fig. 5.2) is generally flatter than that found for normal galaxies. The mean value of α ($\nu < 1400$ MHz) for IrII galaxies is 0.50 ± 0.12 (cf. 0.71 ± 0.07 for normal galaxies, McCutcheon 1972), and the mean value of α ($\nu > 1400$ MHz) is 0.53 ± 0.17 for IrII galaxies (cf. 0.88 ± 0.05 for normal galaxies, McCutcheon 1972). Tovmasyan (1967) also noted the tendency for flat spectral indices for his 'M82-type' galaxies.

3.3 Hydrogen mass to Luminosity Ratio

Values of M_H/L for the IrII sample show a mean value consistent with an early-type galaxy, albeit with a rather large dispersion. It is interesting to plot M_H/L against colour index (Fig. 5.3). Normal galaxies (Gallagher, Faber & Balick 1975) increase in M_H/L and are bluer towards later types. Although the points for IrII galaxies have a considerable scatter, many of the systems with a certain classification as IrII show an excess of M_H/L for their colour when compared with normal galaxies. Nevertheless, there are a few galaxies (notably NGC 3448) for which the opposite is true.

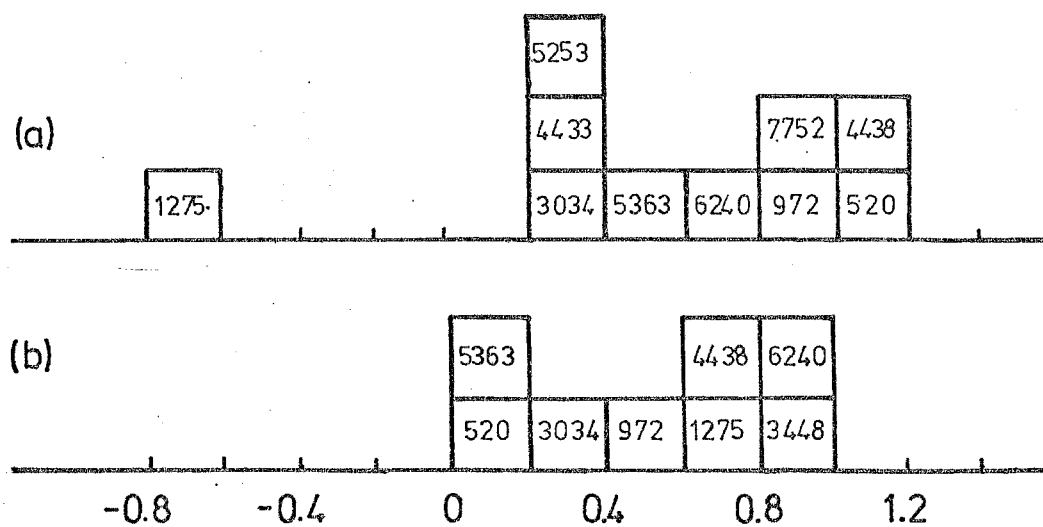
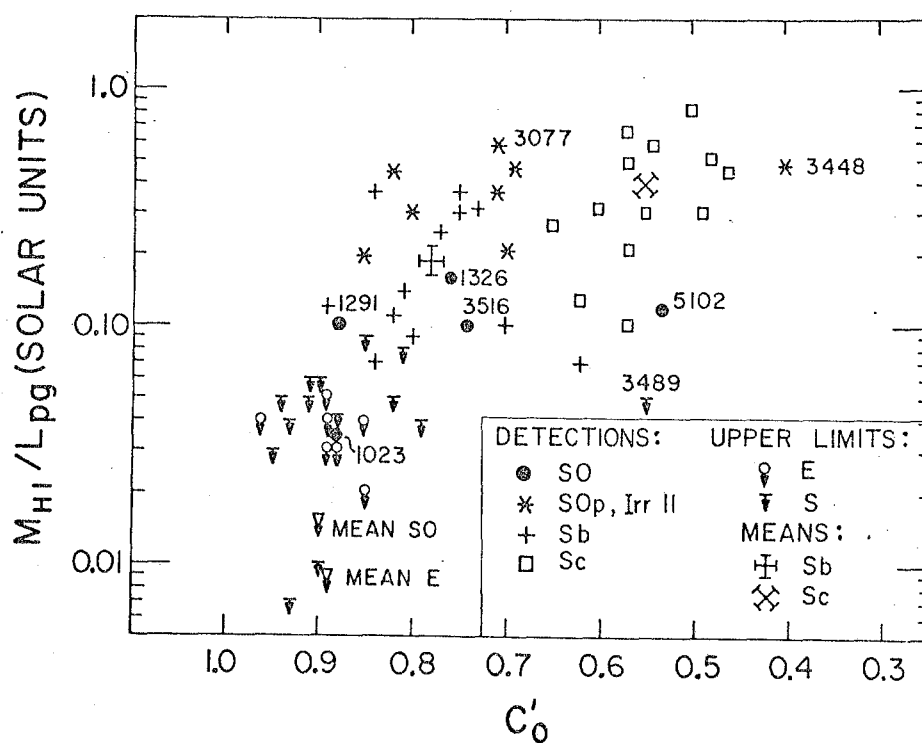


Figure 5.2. Histograms showing the distribution of Radio Spectral Indices for the Iridium sample (the numbers indicate the NGC identity). (a) Spectral index for frequencies greater than 1400 MHz, (b) Spectral index for frequencies less than 1400 MHz.

GALLAGHER, FABER, AND BALICK



Irr II sample

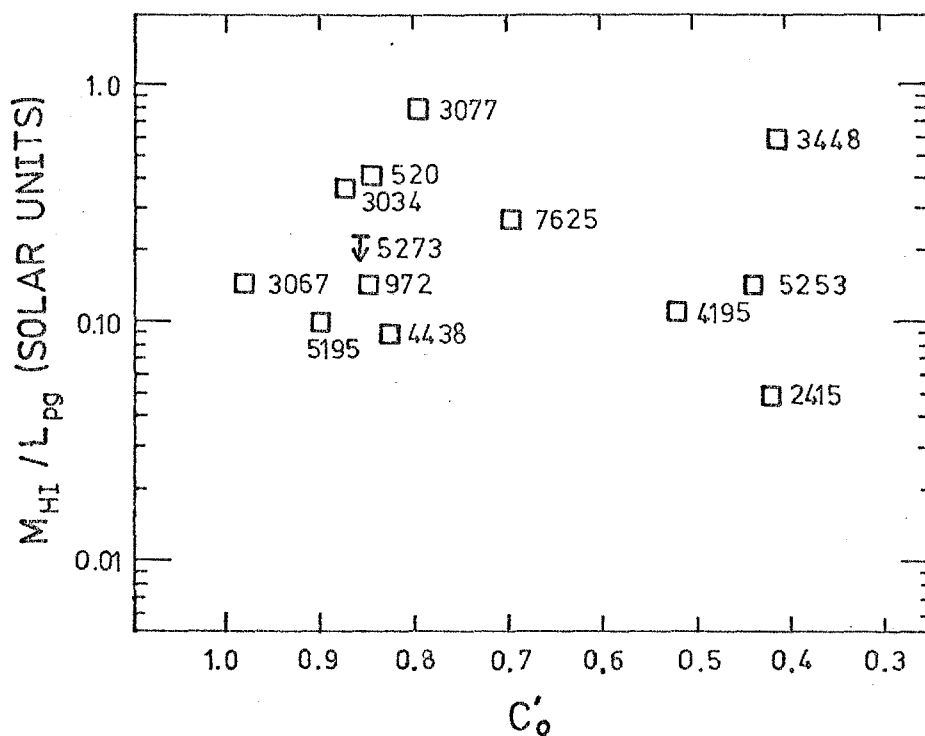


Figure 5.3. Hydrogen mass to Luminosity ratio plotted against colour index, C'_0 . (Top) A sample of Sc and early-type galaxies (Gallagher, Faber & Balick 1975). (Bottom) The Irr II sample. The numbers give the NGC identity.

4 THEORIES

4.1 A Homogeneous class?

The wide dispersion in most properties of IrII galaxies noted in the previous section has been variously interpreted.

Van der Hulst (1977) suggested that the IrII category is not a homogeneous class, but merely a catchment area for unusual and peculiar galaxies. He therefore suggests that IrII galaxies should be treated as individual cases.

Krienke & Hodge (1974) introduced three subclassifications for IrII galaxies, in an attempt to reduce the dispersion of properties. (1) Dusty Galaxies. They suggest that early stellar spectra could co-exist with late-type colours if dust had caused greater than normal reddening. Examples were NGC 972, 2968, 3067, 3955, 4753 5360 and 5363. Many of these galaxies contain normal HII regions, show normal rotation curves, and resemble SO galaxies with an extra dust content. (2) Tidally Interacting Galaxies. Krienke & Hodge suggest that the irregularities of form possessed by this subclass might result from tidal effects, which have distributed material normally confined to spiral arms. Examples are NGC 520, 3448 and 5195. (3) Explosive Galaxies. H α filaments and excess radio emission characterise this subclass. 'Spiral-like' examples are M82 and NGC 4691, while 'E or SO-like' examples are NGC 3077 and NGC 5253.

The subclassifications suggested by Krienke & Hodge have been criticised by Cottrell (1978) on the basis that galaxies such as M82 and NGC 3077 are now known to have suffered the effects of gravitational tides, and so should perhaps be reclassified as 'Tidally Interacting' rather than 'Explosive'. Cottrell suggests that all IrII galaxies have a tidal origin, a theory which is discussed further in the next section.

4.2 A tidal origin for all IrIIs?

Cottrell (1978) suggests that all IrII galaxies have a tidal origin, the mechanism being

$$\text{Galaxy1} + \text{Galaxy2} \xrightarrow[\text{interaction}]{\text{tidal}} \text{Galaxy3} + \text{IrII},$$

where either Galaxy1 or Galaxy2 must be a hydrogen-rich galaxy (i.e. of spiral type). Cottrell considered the populations of galaxy types needed for the process, the efficiency of the process, and how long the tidal relics remain in a state which causes them to be classified as IrII. He concludes that he can account for the observed fraction of IrIIs (about 1% of all classified galaxies) providing they are found in galaxy groups with slightly higher than average density.

An attempt is made, in the next section, to investigate whether the sample of alleged IrII galaxies has an excess of close companions, as might be expected on the basis of Cottrell's theory.

5 A SEARCH FOR COMPANIONS

If gravitational interactions cause the peculiar optical morphology of IrII galaxies, then one might expect a tendency for alleged IrII galaxies (Table 5.1) to have closer companions than a control sample of 'normal' galaxies. The control sample was an equal number of Sc galaxies chosen randomly from UGC but constrained to have an apparent magnitude distribution almost identical to that of the IrII sample. The underlying morphology of many IrII galaxies resembles spiral or SO galaxies rather than ellipticals, so that a control sample constructed from spiral galaxies was considered to be the more suitable. SO galaxies were avoided because of the fine distinction between SO-peculiar and IrII galaxies. It is assumed that Sc galaxies are not implicitly associated with gravitational interactions in the same way as is being suggested for IrIIs. This is thought to be reasonable, but ideally the analysis should have been repeated with control samples selected from other galaxy types. Unfortunately, this was not possible because of the large amount of computer resources required.

The distance from each candidate galaxy to the nearest 'companion' galaxy was determined. This value was expressed in diameters by dividing by the blue major-axis diameter (UGC) of the candidate. A companion galaxy was only counted as such if its magnitude was close (± 2 mag) to that of the candidate. This helped to ensure that the companion galaxy was physically close to the candidate rather than just being a line-of-sight coincidence. Only in three cases were the redshifts of both the candidate and its companion known (NGC 3034, 5195, 4258 and 7752), and in all these the difference in redshifts is small.

The analysis was performed using the IBM 370/165 computer

to scan a catalog containing the positions and magnitudes of all Zwicky galaxies (Zwicky et al. 1960-1968, CGCG). Zwicky's catalog is virtually complete down to 15.5 mag, but covers only declinations above -3° , so that companion searches for only 37 out of the 46 IrII galaxies could be performed. The faintest IrII galaxy was 14.9 mag, and for a few cases the ± 2 -mag search goes outside the range of completeness, but the effect is not considered to be important.

The results of this analysis are displayed in the form of two histograms (Fig. 5.4). The two distributions were compared using the Kolmogorov-Smirnov two-sample test (Siegel 1956). This tests the null hypothesis that the two independent samples have been drawn from the same distribution. With a sample size of 37, the null hypothesis is disproved with more than 95% confidence if a parameter called K_D exceeds the value 12 (i.e. there is less than a 5% chance that the two samples are drawn from the same population entirely by chance). The computed value for K_D is 5; consequently, one cannot say that there is a significant difference between the distribution of nearest neighbours in the IrII sample and those in the control sample of Sc galaxies.

Several of the IrII galaxies which are classified as 'double systems' and others which are known to possess close companions (e.g. NGC 520, 942, 3448, 3656, 6622, 4922B and 7625) are listed in CGCG as only single galaxies. Such cases have been treated as single galaxies in the statistics. If these cases are treated as galaxies whose nearest companion is less than one diameter away, then the IrII sample does have a tendency to possess closer companions than the Sc sample. However, such an adjustment is not considered to be valid because it is by no means obvious whether many of the so-called 'double galaxies' are in

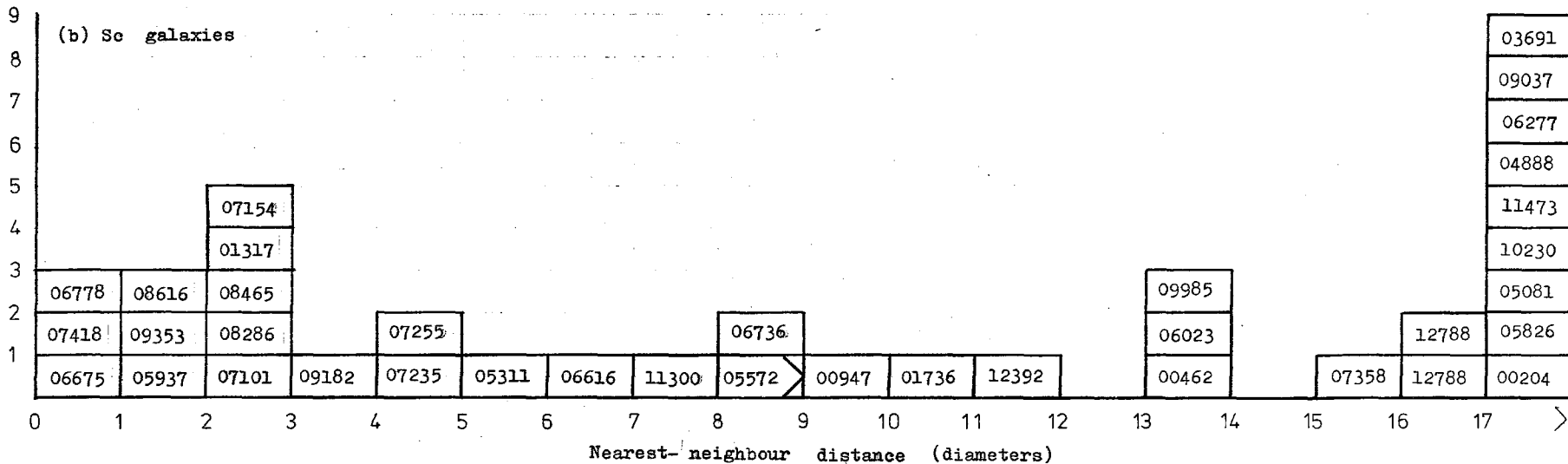
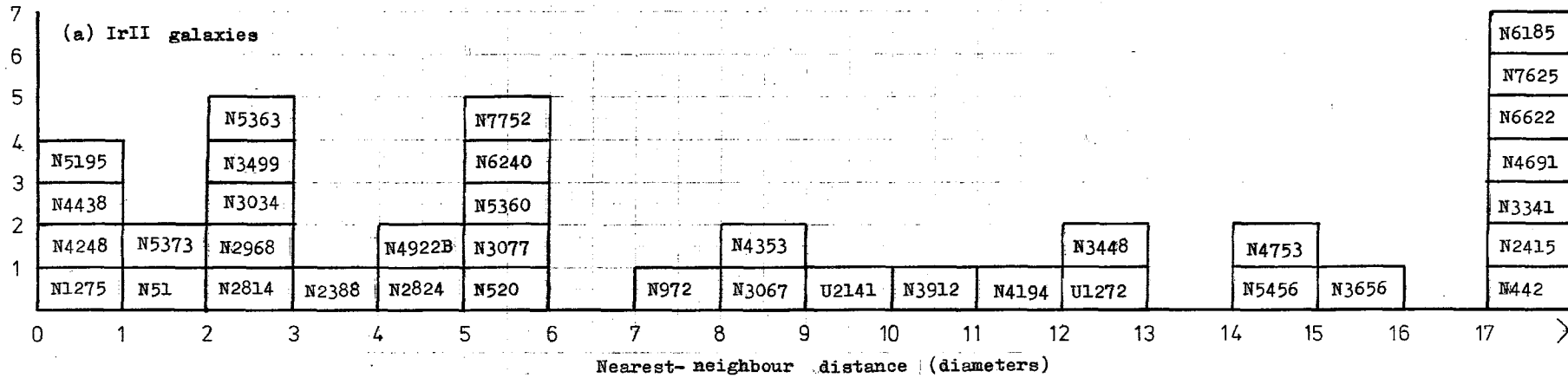


Figure 5.4. Histograms of 'nearest neighbour' distances (defined in the text) for two samples each containing 37 galaxies. (a) Those IrII galaxies from Table 5.1 which appear in CGCG. (b) A control sample of Sc galaxies randomly selected from UGC, but constrained to have the same apparent magnitudes as those in (a). The UGC serial numbers are indicated within each box. The box marked '>' was a candidate which had no valid companion within eight diameters.

fact two separate galaxies or one disturbed galaxy.

On Cottrell's theory (Section 4.2), IrII galaxies are created after certain types of gravitational interactions and last for about 2×10^9 yr thereafter. The companion galaxy involved in the interaction, travelling at about 200 km/s, can therefore lie anywhere within a sphere of radius about 400 kpc (or about $20D$, where $D=20$ kpc is the nominal diameter of a galaxy) centred on the IrII galaxy. This calculation therefore validates the approximate maximum range chosen for the histograms (Fig. 5.4).

The chance that the companion galaxy apparently lies within one diameter of the IrII (where it could be treated as a double galaxy) is thus the volume of a cylinder of radius $1D$ and length $40D$ (along the line of sight) divided by the volume of the sphere radius $20D$, or about 0.4%. The fraction of the alleged IrII sample actually classified as double galaxies or having a close companion within one diameter is about 25%, much greater than expected. To explain this in terms of the ideas above requires that, either the lifetime of an IrII galaxy formed after an interaction should be reduced from 2×10^9 yr to about 0.2×10^9 yr, or the mean separation velocity of the galaxies should be reduced from 200 km/s to about 25 km/s, or a compromise of the two.

In summary: the statistical interpretation of nearest neighbour distances for a sample of IrII galaxies is subject to many difficulties, and no conclusive evidence can be shown for a greater tendency for close companions in the IrII sample than in the control sample of Sc galaxies. The theory that all IrII galaxies originate in gravitational interactions must therefore await a detailed examination of the dynamics of a large sample of IrII galaxies and their companions.

6 SUMMARY

IrII galaxies are apparently a mixture of peculiar systems. In addition to their characteristic optical appearance (irregular morphology, presence of dust lanes, absence of individual stars or HII regions) they also exhibit:

- (1) An earlier spectral type than expected from their colour.
- (2) A wide dispersion in colours.
- (3) A tendency to have 'flat' spectral indices.
- (4) A wide dispersion of M_H/L , but with a mean value similar to that of S0 galaxies.

The tendency of the IrII sample to possess close companions was investigated statistically. No firm evidence was found for a greater tendency in the IrII sample than for a control sample of Sc galaxies.

A detailed study of individual objects is necessary, and for NGC 3448 and NGC 2814 this is pursued in Chapters 6 and 7, respectively.

CHAPTER 6

THE IrII GALAXY NGC 3448

1 INTRODUCTION

Arp 205 (Arp 1966) (Plate 6.1) consists of NGC 3448, a 12.2 m_{pg} galaxy alias UGC 6024 (Nilson 1973, UGC), and a dwarf companion UGC 6016, 3.8 arcmin to the west of NGC 3448, a pair noted to be interacting in RC2. UGC 6016 which has $m_{pg} \sim 17$, is classified 'dwarf irregular' in UGC and SB(s)d pec in RC2. NGC 3448 consists of a bright main body of size 2.7 x 1.0 arcmin with faint extensions along the major axis (RC2). It contains (Hodge 1966) bright knots, possible H α regions and dust lanes. It is classified IO in UGC and RC2, while Krienke & Hodge (1974) place it as type IrII (alias IO). Vorontsov-Velyaminov et al. (1962-74, MCG) and Nilson (1973) point out that the faint extensions suggest the existence of a bridge between the two galaxies.

Arp 205 is a member of the G28 group of galaxies - Ursa Major I(X) (de Vaucouleurs 1975), estimated to be at a distance of $D = 10.7$ Mpc. Adopting this distance for Arp 205 gives a linear scale of 1 arcmin $\cong 3.1$ kpc. Previous HI observations of Arp 205 have been of relatively low angular resolution (Lewis & Davies 1973; Peterson & Shostak 1974; Huchtmeier & Bohenstengel 1975; Bottinelli, Duflot & Gouguenheim 1978). All except Peterson & Shostak (1974) find a large M_H/L ratio, consistent with a late-type galaxy.

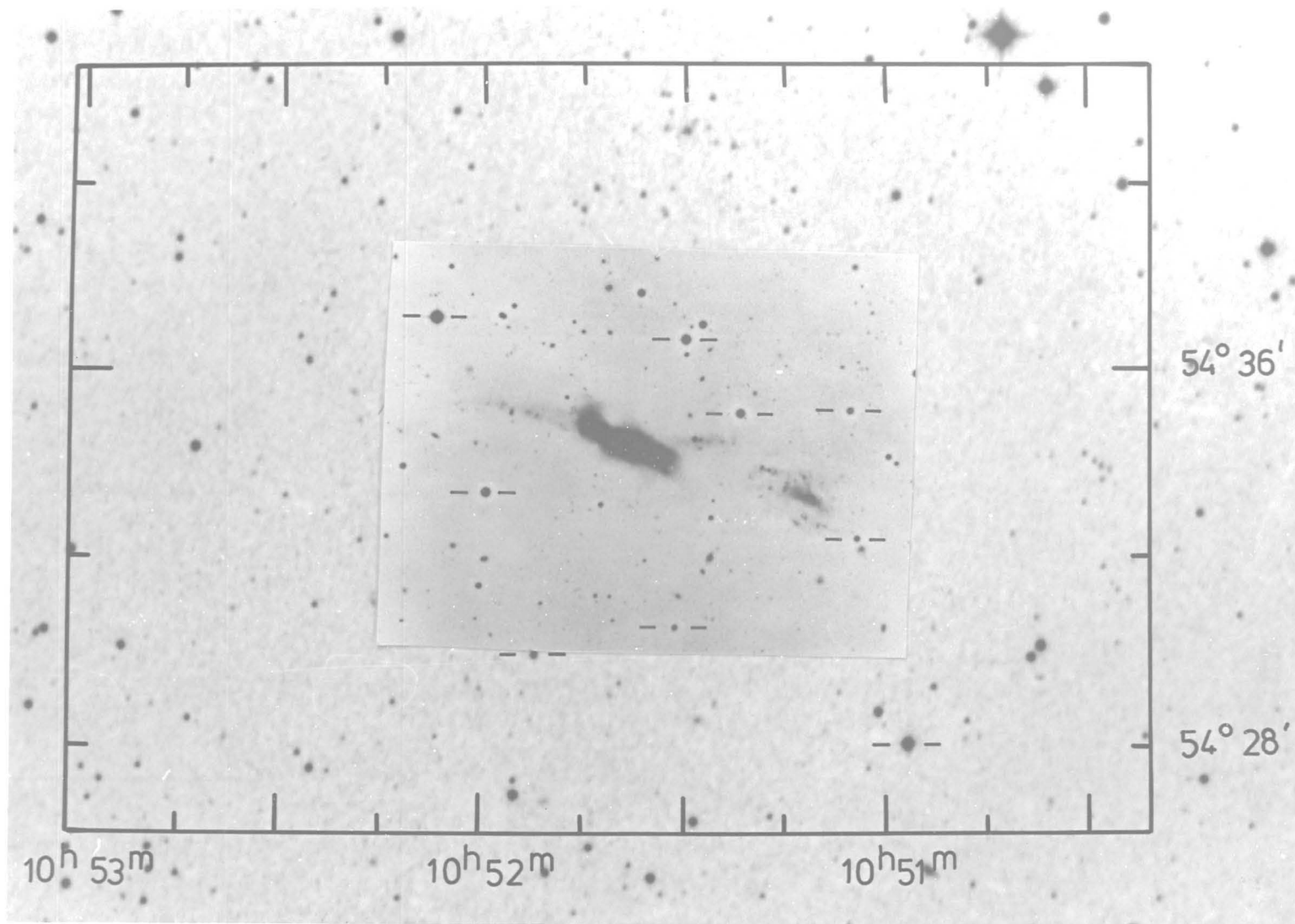


Plate 6.1 Composite photograph of Arp 205. The central region was reproduced with permission from Arp (1966), while the outer region is a photograph of the (blue) Palomar Sky Survey (Copyright by the National Geographic Society). The crosses bars indicate the stars used for alignment with the radio map.

2 OBSERVATIONS

The survey of Arp 205 consisted of 48 equally-spaced interferometer baselines as detailed in Table 6.1. Although observations at two of the spacings were lost due to instrumental faults, nearly full coverage of the u-v plane was achieved. The HI emission was measured using the digital spectrometer over a 4-MHz bandwidth. Continuum radiation in the 10-MHz bandwidth centred at 1417 MHz was also measured and both the surveys were calibrated by observations of 3C 380 and 3C 196.

Channel maps were made at three different spatial resolutions by selecting different sets of interferometer baselines (Table 6.1); the maps at low resolution were more sensitive to low-brightness features than those at the full resolution. At each resolution, a correction for continuum emission was made by averaging those channel maps which contained no line emission (1002 to 1055 km/s and 1583 to 1715 km/s) and subtracting the resulting map from those which did.

Table 6.1 Details of the observations of Arp 205 with the Cambridge Half-Mile telescope.

Dates	1977 February		
Map Centre (1950)			
RA	10 ^h 51 ^m 41 ^s .1		
dec	54° 34' 22"		
Interferometer baselines			
number	48		
smallest	12.2 m		
increment	6.1 m		
largest	298.7 m		
lost due to faults	243.8, 280.4 m		
Calibrator			
name	3C 380	3C 196	
flux	13.8 Jy	13.9 Jy	
reference	Elsmore & Mackay (1969)	Kellermann et al. (1969)	
Response			
structure absent	≥1°		
radius of first grating response in RA	~2°		
Continuum survey			
bandwidth	10 MHz		
centre frequency	1417 MHz		
Hydrogen-line survey			
bandwidth	4 MHz		
heliocentric velocity range	950 to 1767 km/s.		
channel separation	26.4 km/s		
channel width	32 km/s (FWHP Gaussian)		
Resolution and sensitivity			
no. of interferometer baselines included	12	36	46
angular resolution RA x dec (arcmin)	7.4 x 9.1	2.5 x 3.1	1.9 x 2.4
rms noise levels (mJy)			
continuum	-	-	2
one HI-line channel	48	20	18

3 RESULTS

3.1 The overall HI distribution

Fig. 6.1 displays the continuum-free channel maps of Arp 205 at the full resolution of 1.9×2.4 arcmin. The average of the rms noise levels is $18 \text{ mJy } (\sigma)$. Fig. 6.2 displays the emission greater than 3σ in a right ascension-velocity plot (constructed as described in Chapter 1), and identifies the most significant components of emission (C1-C8). Fig. 6.3 shows the relationship between the 3σ envelope of C1-C8 and the optical emission. It should be emphasised that the 'components' are not necessarily separate physical entities or even real features. The emission in Fig. 6.1 has a relatively low signal/noise ratio (a maximum S/N of 6), which makes interpretation difficult, and it is to aid this interpretation that the nomenclature is used. It is clear that more sensitive observations would show a more continuous distribution of hydrogen not needing this type of description.

There is little doubt that components C1-C5 are real. All appear greater than 3σ on at least three adjacent channels, and all are seen with equal or better S/N ratios on the maps made at the lowest resolution. The reality of C6, C7 and C8 is uncertain: C6 appears on two adjacent channels above the 3σ level, but it is possible to find two negative features in Fig. 6.1 (assumed to be unreal) which also satisfy this criterion (at 1372 and 1398 km/s , and at 1530 and 1556 km/s). C7 appears on Fig. 6.1 in three adjacent channels above the 3σ level, but only appears at $\sim 2\sigma$ on the low-resolution maps. This implies that if C7 is real, it must be isolated emission with an angular scale of less than 2 arcmin. C8 is seen at the 4σ level, but only on one

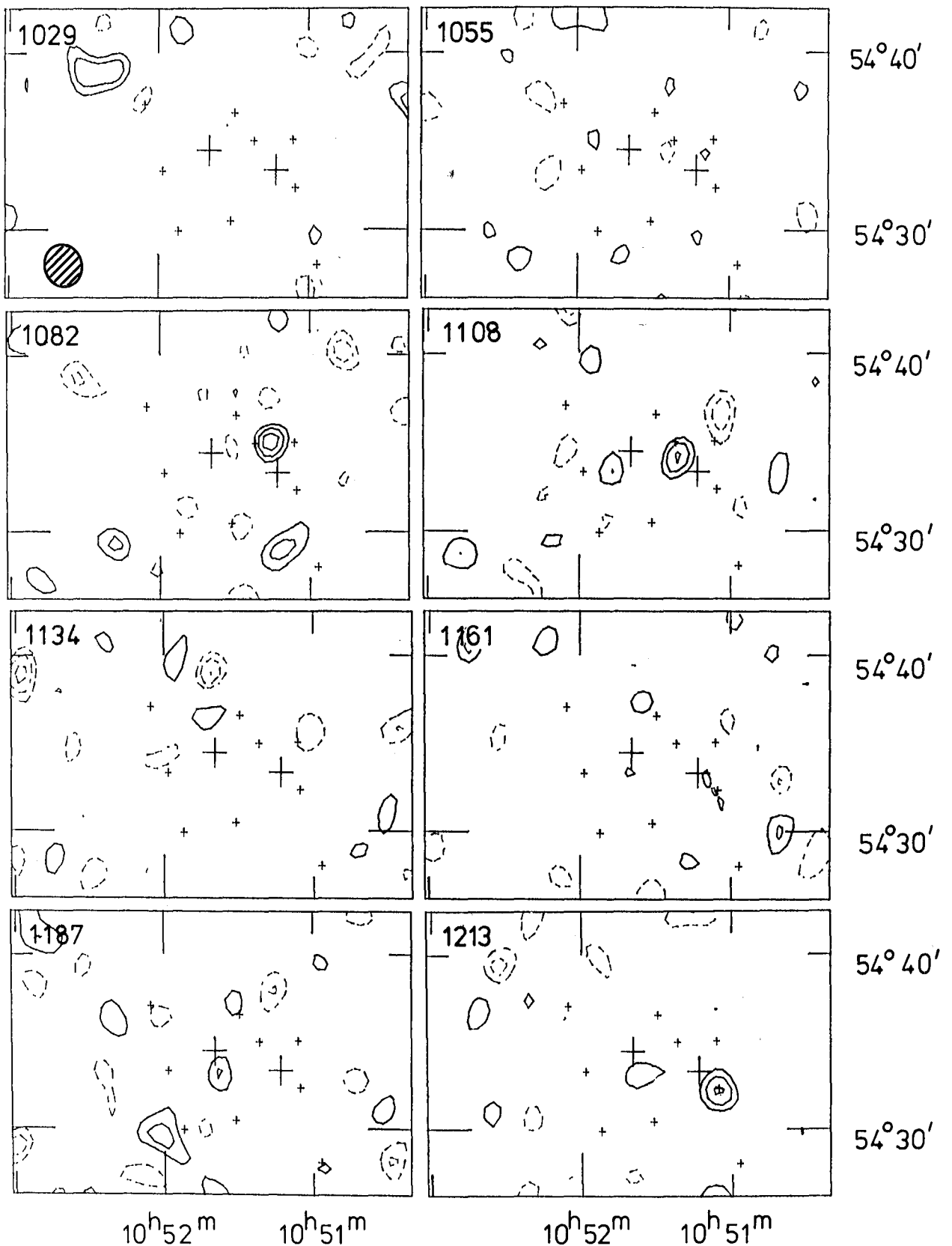


Figure 6.1 Continuum-free channel maps with HPFW resolution of 1.9×2.4 arcmin (hatched ellipse). The contour interval is 20 mJy, positive contours are solid and negative contours are dashed. The zero contour and those at +20 and -20 mJy have been omitted for clarity. The large crosses represent the optical nuclei of NGC 3448 (east) and UGC 6016 (west), and the small crosses are the positions of fiducial stars on Plate 6.1. No polar diagram correction has been applied in this or subsequent diagrams.

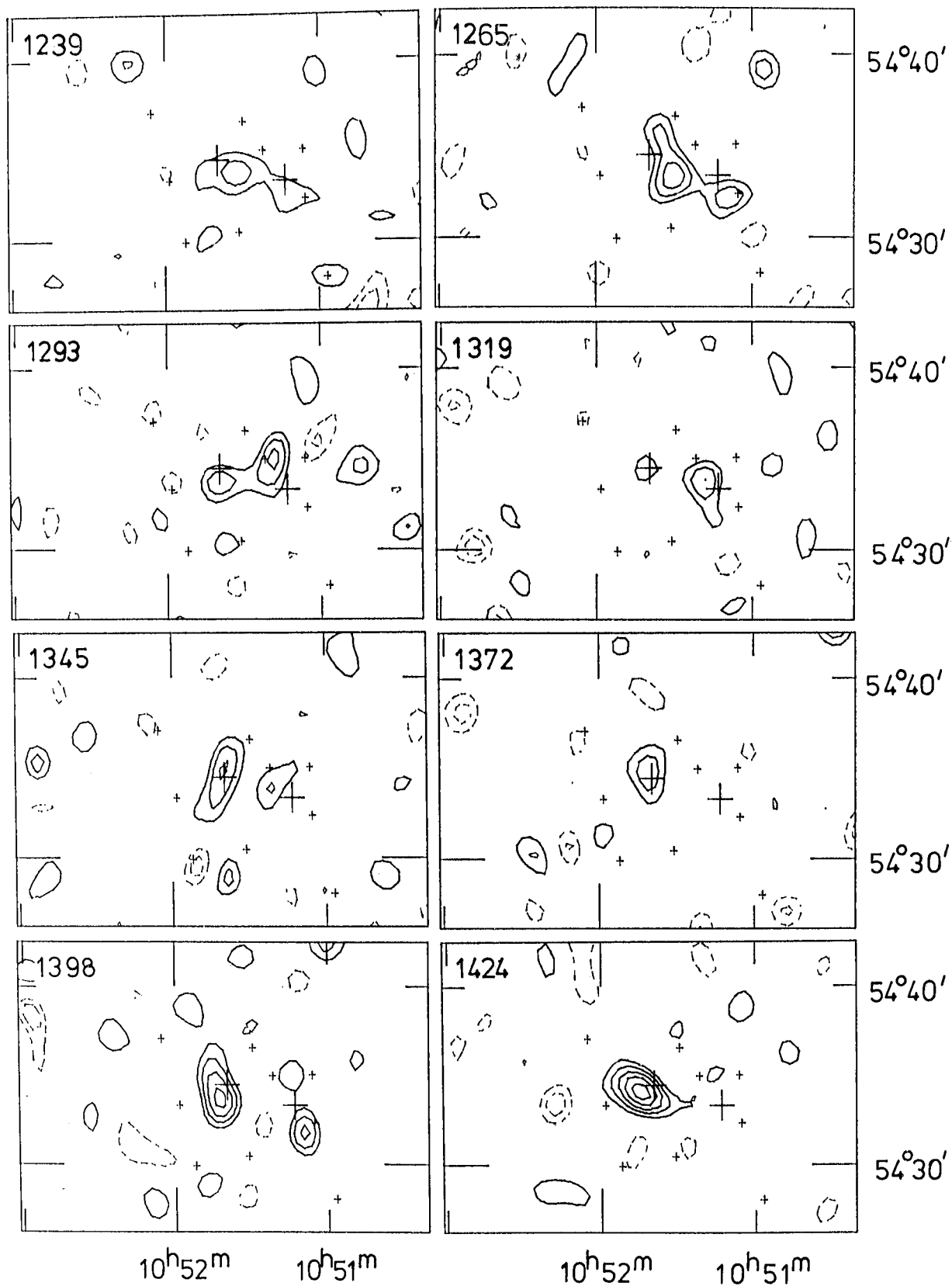


Figure 6.1 (continued)

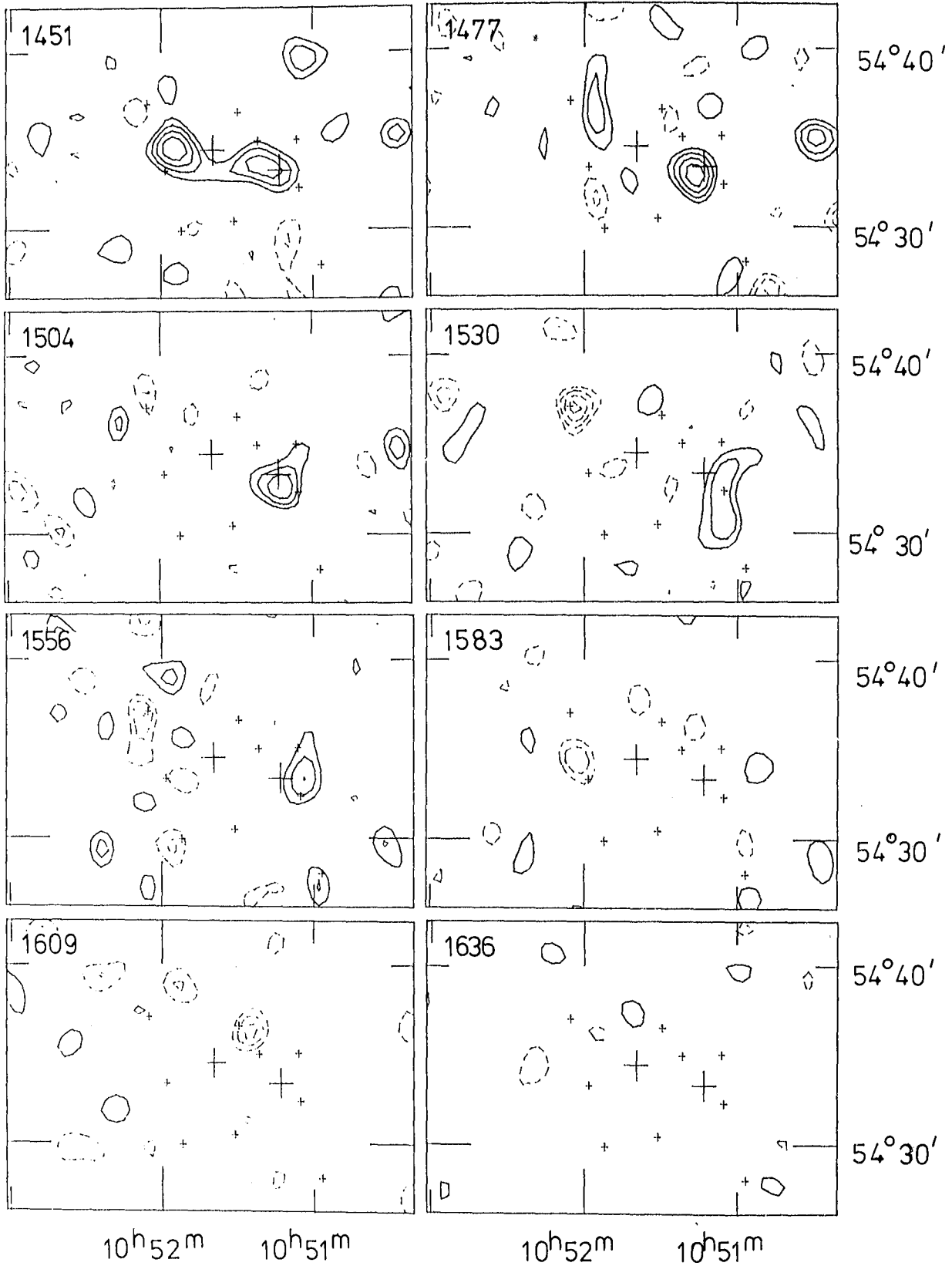


Figure 6.1 (continued)

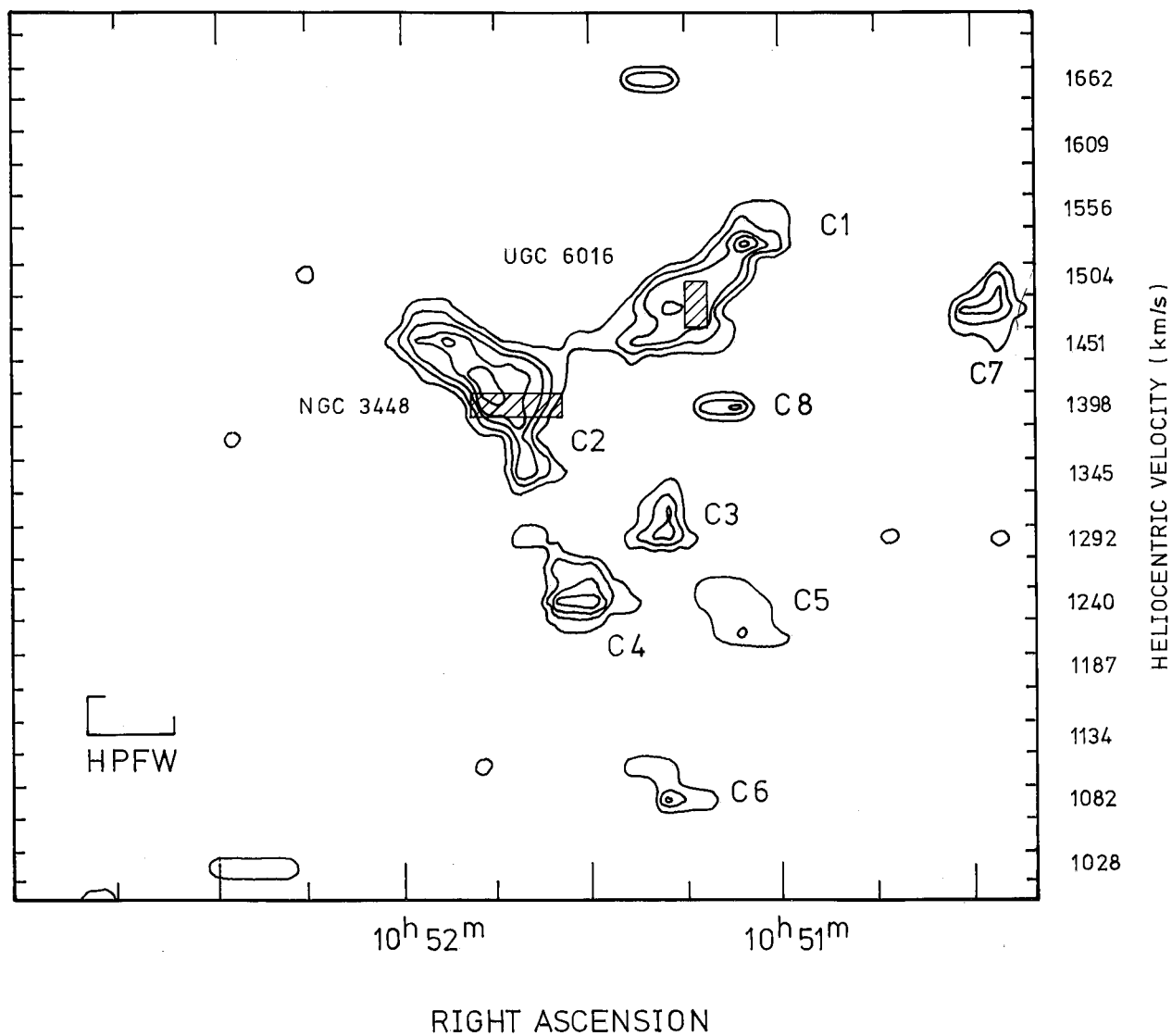


Figure 6.2 Right ascension-velocity plot constructed from the data of Fig. 6.1, including only signals above 3σ . The contour interval is uniform and the units are arbitrary. The HPFW resolution is $1.9 \text{ arcmin} \times 32 \text{ km/s}$. The hatched rectangles represent the optical positions and velocities of the labelled galaxies. Eight components are identified (C1-C8) for discussion purposes.

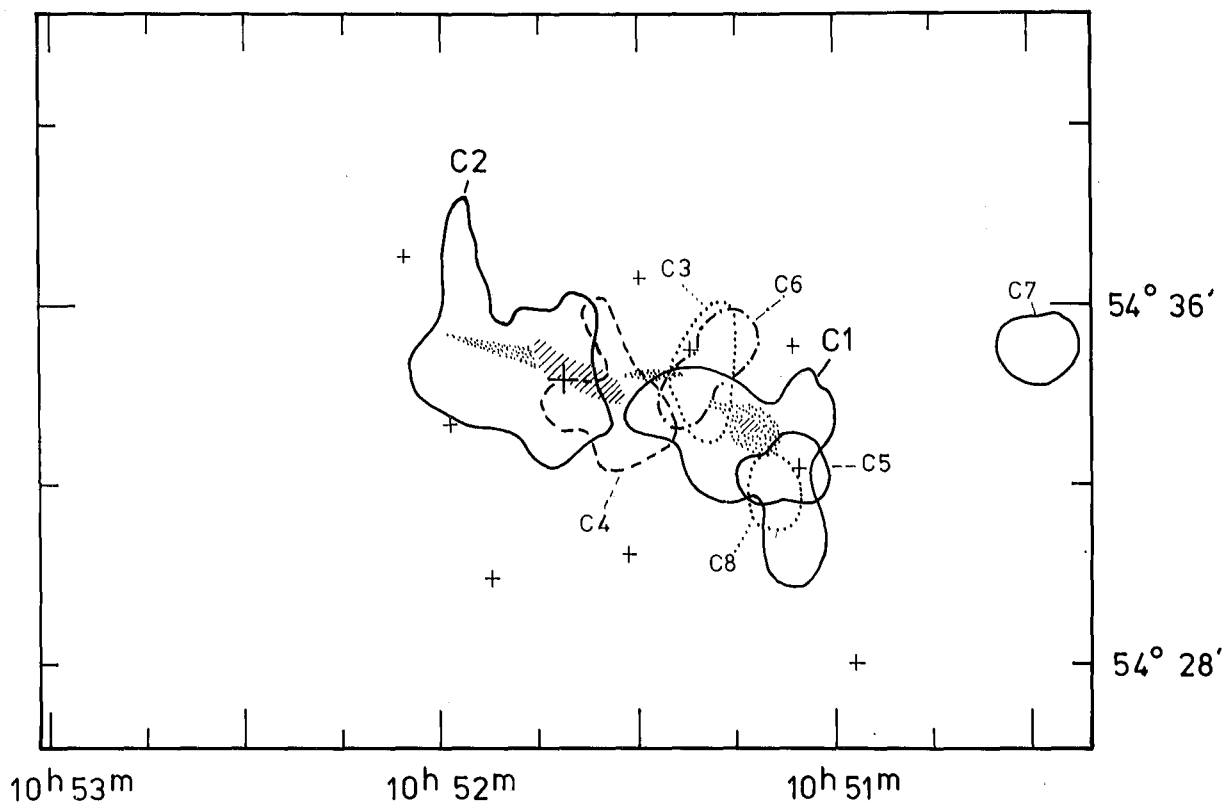


Figure 6.3 Comparison of the HI components (Fig. 6.2) with the optical emission. Each contour is the outer envelope of emission from the continuum-free channel maps (Fig. 6.1) at 3σ . The shading represents the regions of optical emission from the galaxies, the smaller crosses are star positions, and the larger cross is at the map centre.

channel.

C1 agrees in position with the dwarf galaxy UGC 6016 and shows a systematic shift from channel to channel (Fig. 6.1), so is presumably due to HI in ordered rotation about UGC 6016. C2 is coincident with the eastern edge of NGC 3448 and shows a similar shift with velocity. C4 is in positional agreement with the western edge of NGC 3448 and also shows a similar shift, but is separated from C2 because of the lack of emission (greater than 3σ) joining these two components on the channel map at 1319 km/s. C2 and C4 may be plausibly interpreted as forming the HI in rotation about NGC 3448, despite the lack of emission at 1319 km/s. Such emission is in fact seen at about 2σ on this channel map, and the absence of emission above the 3σ level may simply be due to the poor S/N ratio. An alternative interpretation would be to treat C2, C3 and C5 as forming a single rotating system, but this is unlikely because of the lack of corresponding optical features, and the spatial and velocity discontinuity of the HI (Figs 6.1, 6.2). The presence of HI to the west of NGC 3448 (C3 and C5) is interpreted as clear evidence that NGC 3448 is a disturbed system. If C7 and C8 are real features, they also give an indication that the HI surrounding UGC 6016 is disturbed. The origin of these disturbances is discussed in Section 4.

By including only the 12 smallest interferometer baselines, continuum-free maps were made at a resolution of 7.4×9 arcmin. Nineteen of these channel maps over the velocity range 1082-1556 km/s were combined as described in Chapter 1 to make an integrated HI map (Fig. 6.4). This map is more sensitive to low-brightness emission than a similar map made

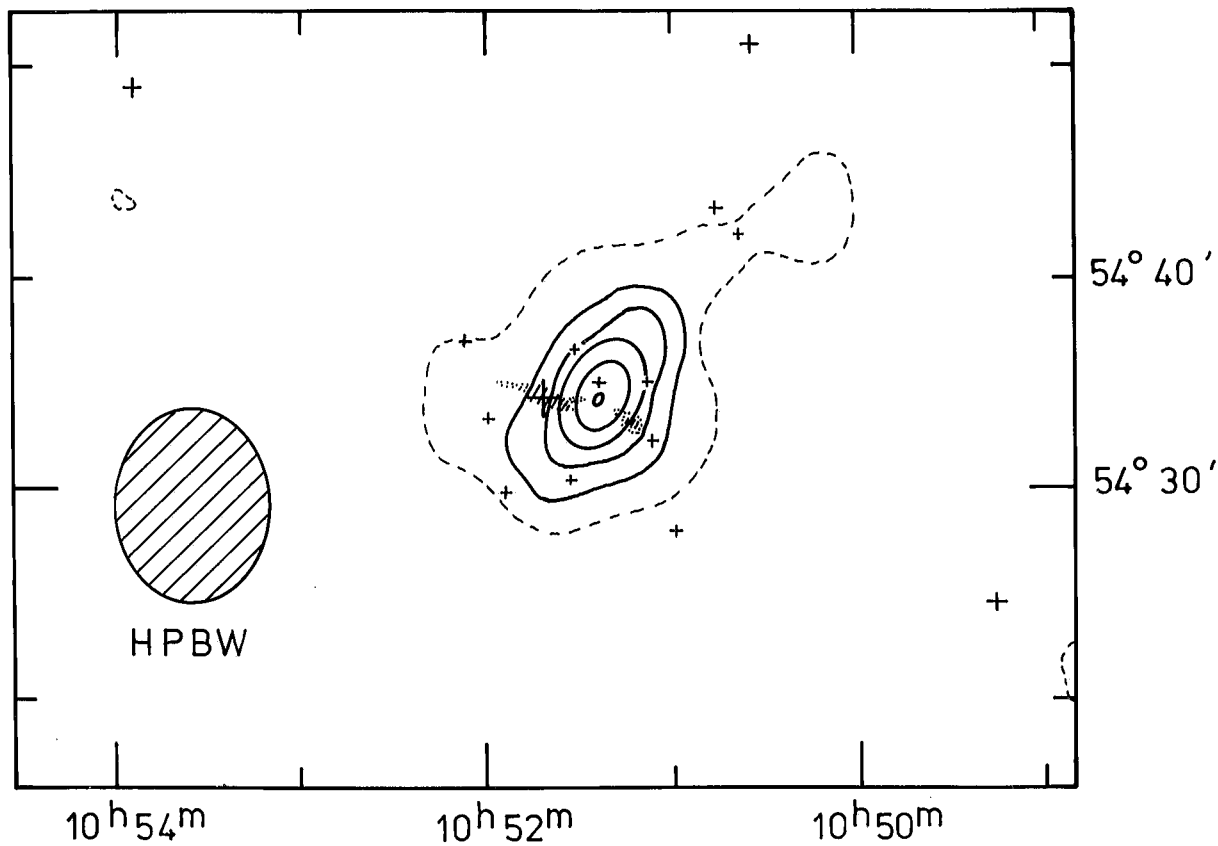


Figure 6.4 Low-resolution integrated HI map of Arp 205 incorporating 19 continuum-free channel maps over the velocity range 1082-1556 km/s. The HPBW resolution of $7.4 \times 9'$ arcmin is shown by the hatched ellipse. The outer dashed contour is 20 K km/s, while the first solid contour is at 50 K km/s and higher contours are at intervals of 30 K km/s. The noise on this map varies as the number of channels added at any point, and is typically 8 K km/s. The shading and crosses are as in Fig. 6.3.

at high resolution. The peak of HI emission in Fig. 6.4 is displaced 3.2 arcmin to the west of the nucleus of NGC 3448, and an extension to the northwest at the 20 K km/s level is a prominent feature. These features indicate the presence of low-brightness emission surrounding Arp 205, not seen in the maps at higher resolution. No corresponding optical emission is seen on the PSS plates.

The total HI mass in Arp 205 was derived using the relation given in Section 2.4c of Chapter 1. The result (Table 6.2) agrees well with that of Bottinelli et al. (1978). The fraction of the total mass contained in each of the components (Table 6.2) was evaluated by comparing the emission seen above the 3σ level on the maps at high resolution (Fig. 6.1).

Fig. 6.5 shows the high-resolution map of HI integrated over the velocity range which includes all the significant HI (1082-1556 km/s). The morphology of the HI resembles two systems joined by a bridge, implying that both galaxies are physically very close to each other and confirming the optical evidence of interaction referred to in the Introduction. The isolated emission in the west of Fig. 6.5 is due to component 7, which does not appear to be coincident with any galaxy or other optical feature.

3.2 UGC 6016

Parameters for UGC 6016 are displayed in Table 6.3. The systemic velocity was derived by calculating the 'centre of gravity' of component 1 in Fig. 6.2, and the value is slightly higher than that of Botinelli et al. (1978). The neutral hydrogen diameter was measured along PA 70° , and

Table 6.2 The distribution of hydrogen in Arp 205

Item	HI mass/ $10^8 M_{\odot}$	Source
Arp 205 total	22 ± 5 21.8	Fig. 6.4 Bottinelli <u>et al.</u> (1978)
Individual components		
C1 (UGC 6016)	6.8	31% of Arp 205 total (Fig. 6.1)
C2 (NGC 3448 east)	8.4	38% do.
C3*	1.3	6% do.
C4 (NGC 3448 west)	3.1	14% do.
C5*	1.1	5% do.
C6 ?	1.3	6% do.
C7* ?	1.4 ± 0.3	Fig. 6.1
C8* ?	0.9 ± 0.3	Fig. 6.1
UGC 6016	6.8 3.6	C1 Bottinelli <u>et al.</u> (1978)
NGC 3448	11.5 18.2	C2 and C4 Bottinelli <u>et al.</u> (1978)

* It is argued in Section 4 that C3 and C5 form part of a tidal arm of NGC 3448, and that C7 and C8 is matter close to UGC 6016. Refer to Fig. 6.7.

? The reality of this emission is in some doubt - see Section 3.1.

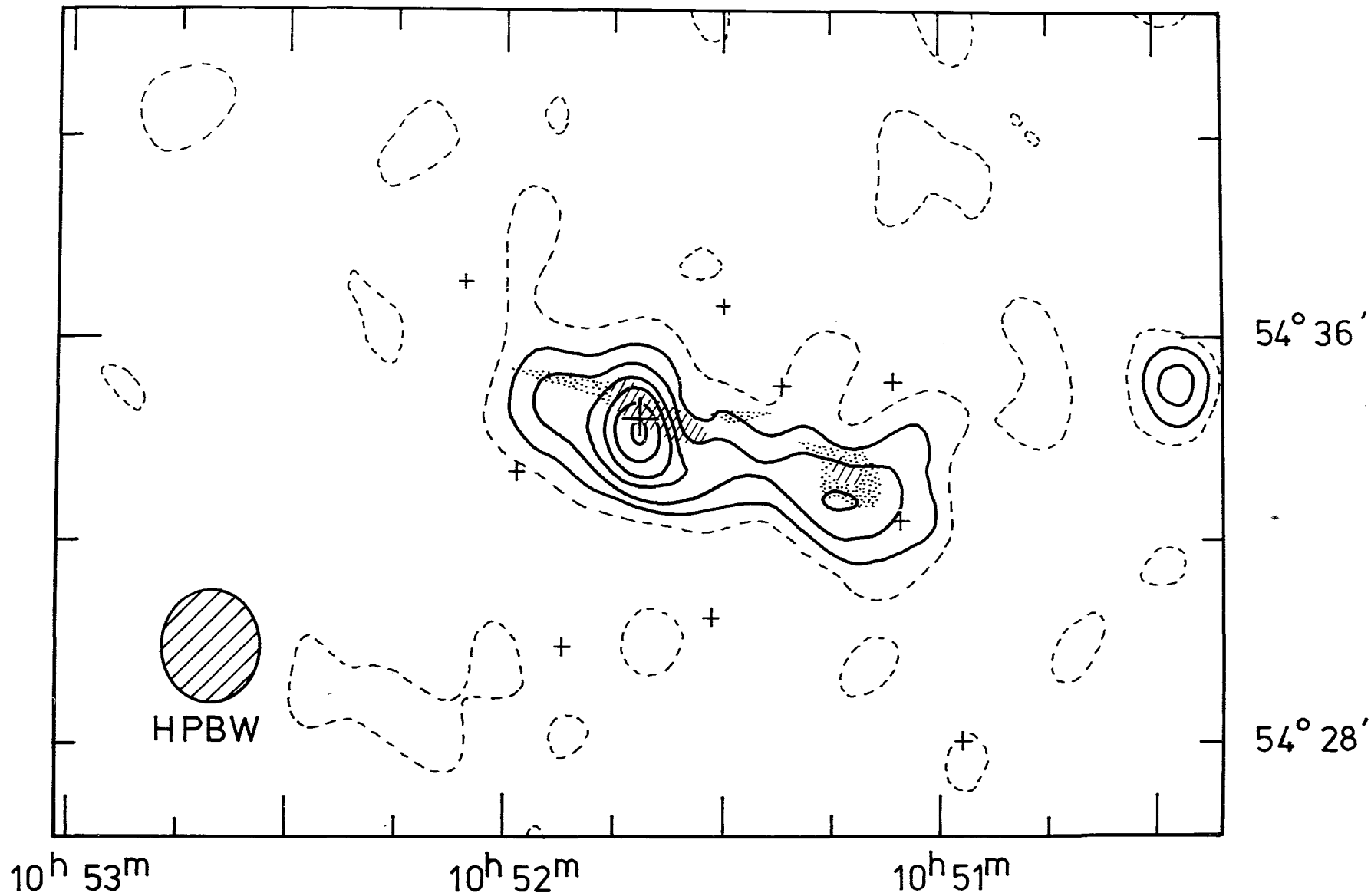


Figure 6.5 High-resolution integrated HI map of Arp 205 incorporating 19 continuum-free channel maps over the velocity range 1082-1556 km/s. The HPBW resolution of 1.9 x 2.4 arcmin is shown by the hatched ellipse. The dashed contour is 100 K km/s, and solid contours start at 200 K km/s and are at 100 K km/s intervals. The noise on this map varies as the number of channels added at any point, and is typically ~45 K km/s. The shading and crosses are as Fig. 6.3.

Table 6.3 Parameters for UGC 6016

Parameter	Value	Source
Optical nucleus (1950)		UGC
RA	10 ^h 51 ^m .2	
dec	53° 34'	
Classification	SB(s)d pec	RC2
	dwarf irregular	UGC
Photographic magnitude, m_{pg}	~17	UGC
	~15 #	MCG
Optical dimensions	2.2 x 1.6 arcmin ?#	UGC (blue PSS)
	2 x 1 arcmin	MCG
Systemic velocity from HI studies	1500 ± 10 km/s	Fig. 6.2
	1480 ± 20 km/s	Bottinelli <i>et al.</i> (1978)
PA of optical major axis	80 ± 5°	blue PSS print
PA of HI major axis	70 ± 5°	Map not shown
Distance, D	10.7 Mpc	de Vaucouleurs (1975)
Photometric linear diameter, a_0	6.8 kpc	Optical dimensions
HI diameter, a_H	11.7 ± 0.5 kpc	Map not shown (PA 70°)
Total width of the HI line profile, ΔV	132 ± 16 km/s	Fig. 6.2
	180 km/s	Bottinelli <i>et al.</i> (1978)
Inclination wrt plane of sky, i	45° #	see text
	range 45 to 62°	
HI mass M_H ($\propto D^2$)	(6.8 ± 1.7) × 10 ⁸ M _⊙	Table 6.2
Total mass M_T ($\propto D^1$)	(3.0 ± 1.0) × 10 ⁹ M _⊙	see text
(within 5.6 kpc of nucleus)		
Luminosity, L ($\propto D^2$)	(1.7 ± 1.0) × 10 ⁸ L _⊙	Based on m_{pg}
M_H/L	4	This table
M_T/L	18	This table
M_H/M_T	0.2	This table
a_H/a_0	1.8	This table

Notes # identifies adopted values where more than one value is quoted. The HI parameters assume UGC 6016 to be composed solely of Cl. (See Section 4 and Figs 6.2, 6.3 and 6.6). The value marked ? is uncertain.

takes account of convolution with the synthesised beam. Emission from UGC 6016 appears on five consecutive channels at high resolution, giving a profile width, ΔV , of 132 km/s. This value is significantly less than that of Bottinelli et al. (1978), but their larger beam area will have included HI other than that of component 1. The inclination was computed as described in Section 2.4e of Chapter 1, taking the ratio of the observed major to observed minor axis from Table 6.3 and the ratio of the intrinsic principal axes of the light distribution as 0.2 (Heidmann, Heidmann & de Vaucouleurs 1971). The majority of the error in inclination arises from the uncertain optical dimensions. The total mass, M_T , was estimated as described in Section 2.4f of Chapter 1.

The integral parameters of UGC 6016 are, in general, typical of a dwarf irregular (Im) galaxy, in agreement with Bottinelli et al. (1978). Because of the small number of beam areas over this galaxy, modelling has not been attempted, but the velocity field (not shown) resembles that expected from rotation of a HI disc with the PA and inclination as given in Table 6.3.

3.3 NGC 3448

Parameters for NGC 3448, obtained in the same way as for UGC 6016, are displayed in Table 6.4. The HI parameters assume NGC 3448 to be composed of components C2 and C4, and they are (in general) similar to those expected from Sc-type galaxies (Balkowski 1973); this is an earlier type than the Sd or Sm category suggested by Bottinelli et al., but there is better agreement if NGC 3448 also includes components C3 and C5, as suggested in Section 4. The velocity field (not

Table 6.4 Parameters for NGC 3448

Parameter	Value	Source
Optical nucleus (1950)		RC2
RA	10 ^h 51 ^m 39 ^s .6	
dec	54° 34' 30"	
Peak of HI (1950)		
RA	10 ^h 51 ^m 41 ^s .1	
dec	54° 34' 12 ⁿ .5	
Classification	IO	RC2, UGC
Total 'face-on' magnitude corrected for galactic and internal absorption	11.59 mag	RC2
Isophotal major diameter corrected to face on	4.27 arcmin	RC2
Ratio of major to minor diameter	2.88 ± 0.03	RC2
Systemic velocity from HI study	1370 ± 15 km/s	Fig. 6.2
PA of optical major axis		Blue PSS print
Bright nucleus	65 ± 5°	
Faint outer emission	80 ± 5°	
PA of HI major axis	75 ± 5°	Map not shown
Distance, D	10.7 Mpc	de Vaucouleurs (1975)
Photometric linear diameter, a ₀	13.2 kpc	RC2
HI diameter, a _H	17.4 kpc	Map not shown (PA 70°)
Total width of the HI line profile, ΔV	317 km/s	Fig. 6.2
Inclination wrt plane of sky, i	73° ± 1°	See text
HI mass, M _{HI}	(11.5 ± 2.6) × 10 ⁸ M _⊙	Table 6.2
Total mass, M _T	(1.40 ± 0.5) × 10 ¹⁰ M _⊙	See text
Luminosity, L	(3.9 ± 0.3) × 10 ⁹ L _⊙	
M _H /L	0.30	This table
	0.48	Bottinelli <u>et al.</u> (1978)
M _T /L	3.6	This table
M _H /M _T	0.08	This table
a _H /a ₀	1.32	This table
	0.92	Bottinelli <u>et al.</u> (1978)

Note The HI parameters assume NGC 3448 to be composed solely of C2 and C4. See Section 4 and Figs 6.2, 6.3 and 6.6.

shown) is difficult to interpret because of beam-smearing effects, but may well be compatible with normal differential rotation.

NGC 3448 has a continuum source associated with its nucleus. Observations of this have been made at various frequencies and the results are displayed in Table 6.5, from which the spectral index (α , defined as $S \propto \nu^{-\alpha}$) has a value of about 1.0, typical of many normal spiral galaxies. Flux densities quoted by Haynes et al. (1975) are inconsistent with those presented here, being a factor ~ 2 higher, but the observations by Pfleiderer would have included flux from a background source about 10 arcmin north of NGC 3448.

The radio luminosity of the nuclear source at 1417 MHz, based on a flux density of 30 mJy and a distance estimate of 10.7 Mpc is 4.1×10^{21} W/Hz. This value is typical of normal spiral galaxies, and is in accord with the findings of Burke & Miley (1978) and others that radio luminosities of peculiar galaxies are not significantly different from those of normal ones.

Table 6.5 Radio continuum observations of the nuclear source in NGC 3448

Telescope	6C*	One-Mile	One-Mile	Half-Mile	5-km
Frequency (MHz)	151	408	1407	1417	2700
Resolution RA x dec	4 x 5 arcmin	1.2 x 1.4 arcmin	26 x 32 arcsec	1.9 x 2.4 arcmin	23 x 29 [#] arcsec
Integrated flux (mJy)	260	60 ± 30	31 ± 8	30 ± 5	15
Position (1950)					
RA		10 ^h 51 ^m 37. ^s 6	10 ^h 51 ^m 38. ^s 6	10 ^h 51 ^m 38. ^s 1	10 ^h 51 ^m 39. ^s
dec		54°34'27"	54°34'20".4	54°34'22"	54°34'20"

*C.R. Masson, private communication.

[#]Convolved from 4 x 5 arcsec.

4 ANALYSIS

The optical morphology of Arp 205 is peculiar (Plate 6.1); outer emission seen both to the east and west of NGC 3448 contrasts with its bright nucleus - the outer emission is much fainter than the nuclear emission, significantly bluer, and oriented at a significantly different position angle (Table 6.4). The observations presented in Section 3 also show that the HI around NGC 3448 is clearly disturbed (C3, C5 and possibly C6) and around UGC 6016 (C7 and C8) the HI is possibly disturbed. This section examines two different theories to account for this disturbance.

4.1 NGC 3448 as a double interacting system

Bottinelli et al. (1978) obtained optical spectra in the eastern part of the nucleus of NGC 3448, which showed a 'very unusual double-valued velocity field'. One interpretation of this was that NGC 3448 consists of two separate but interacting galaxies. This section examines the HI evidence for this hypothesis.

A case can be put forward that the HI components C3 and C5 form an independent rotating system, but such a system does not coincide with any clearly defined optical feature, and is not in the region where the optical spectra are double. This region exhibits ordered rotation of the HI (component 2), with no sign of double HI profiles. This evidence also argues against an hypothesis by Hodge (1975), who considers that a patch of emission near the eastern end of the nuclear disc (clearly shown in Hodge 1975, Fig. 4) may constitute a separate rotating system. A dust lane seems a more likely interpretation.

It is possible that the faint optical extensions surrounding NGC 3448 are part of a separate system along the same line of sight as the bright nucleus, perhaps a long stream of matter joining UGC 6016. It is interesting that components C2 and C4 more closely match these faint optical extensions than they do the bright nucleus. Although this hypothesis may also be able to explain the double optical profiles of Bottinelli et al., it does not unify all the available optical and HI data.

4.2 Tidal-Interaction theories

In this section evidence for a tidal interaction in Arp 205 is discussed. One might hope that such an hypothesis will account both for the disturbed optical nature of Arp 205 as a natural consequence of gas compression during an interaction, and for the remaining HI components (notably components C3 and C5 which have similar velocity fields).

Are there any massive galaxies close to Arp 205 which could be responsible for its peculiarities? All other members of the G28 group of galaxies (de Vaucouleurs 1975) are more than 2° away, and the only other galaxy within a radius of $1^\circ.5$, and brighter than 15 mag is ZWG 267.018 = UGC 05954 = IC 664, a 14.4 mag galaxy 66 arcmin away with an unknown redshift. None of these galaxies seems capable of producing the disruption observed in Arp 205, so only UGC 6016 and NGC 3448 themselves could have been involved.

Since both UGC 6016 and all the observed HI components lie close to the plane of NGC 3448, any proposed orbit is most likely to be approximately co-planar. Other constraints are the radial velocities of both galaxies and their mass

ratio (UGC 6016/NGC 3448) ~ 0.5 . The distribution of test particles following various idealized gravitational interactions are given by Toomre & Toomre (1972) and Wright (1972), and shown in the Appendix. The galaxies UGC 6016 and NGC 3448 are rotating with nearly the opposite sense (Fig. 6.2 and inclinations in Tables 6.4 and 6.5), and so a retrograde collision for one galaxy will be a prograde collision for the other. Retrograde collisions have been shown to be less likely to cause disruption than prograde collisions, and have no appreciable effect if the mass ratio (intruder/galaxy) is as low as $u \sim 0.5$. Hence orbits in which NGC 3448 suffers a retrograde collision (with UGC 6016 as the intruder) can be ruled out. Furthermore, this orbit also implies a prograde collision for UGC 6016 with $u \sim 2$ which would produce much more disruption to UGC 6016 than is observed. However, orbits for which UGC 6016 has a perigalacticon on the east side of NGC 3448 cause the latter to suffer a prograde collision with $u \sim 0.5$, which is capable of pulling an arm of material from the disc, and thus explaining both the positions and velocities of components C3 and C5. These orbits also imply a retrograde collision for UGC 6016 with $u \sim 2$, which could have produced enough disruption to explain C7 and C8 if more sensitive observations confirm their reality.

Fig. 6.6 represents a reasonably self-consistent model of Arp 205 which explains the optical and HI peculiarities described earlier. The positions and radial velocities of the optical galaxies and the HI components (except C6) are correctly represented, and this model can result from the type of gravitational interaction described above, namely, a co-planar orbit which involves a prograde collision for

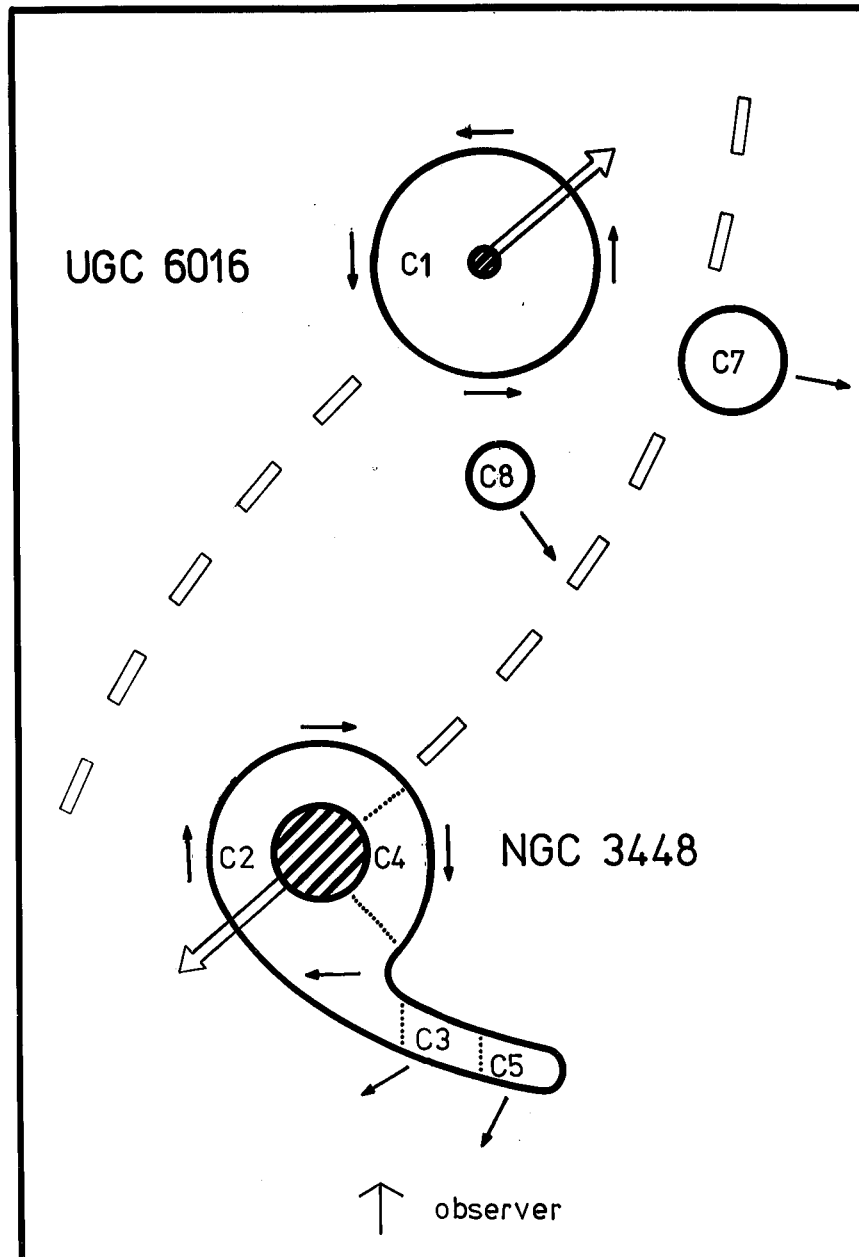


Figure 6.6 Schematic model for Arp 205, arranged such that the plane of the paper represents the plane containing NGC 3448. The hatched areas are the brightest parts of the optical emission, as in Fig. 6.3. The approximate extent of the HI components are shown, together with their velocity vectors relative to the systemic velocity of NGC 3448 and UGC 6016 (arrows). This model is consistent with the observations (cf. Figs 6.2 and 6.3), and can be produced by a gravitational interaction (see text). The orbits of the galaxies are indicated by the dashed lines.

NGC 3448 and a retrograde collision for UGC 6016. The galaxies are apparently seen about $4-8 \times 10^8$ yr after a perigalacticon at a distance of about 10-15 kpc. If the orbit were inclined by a small angle from the plane of NGC 3448 (so that UGC 6016 was slightly below the plane of NGC 3448 at perigalacticon), then it is possible to explain the observed warp of the optical filaments - downward on the east side of NGC 3448 and upward on the west side. The HI is also warped since the orientation of C2 and C4 matches more closely the position angle of the optical filaments than that of the bright nucleus. Component C6 has not been included in Fig. 6.6, because its position and velocity are not continuous with that of C3 and C5, so it is unlikely to be part of the tidal arm pulled from NGC 3448. If C6 is real, it is more likely to be outlying HI in a rotation pattern similar to that of C2 and C4 (cf. Fig. 6.2).

5 CONCLUSIONS

Arp 205 consists of HI in rotation about NGC 3448, plus HI rotating in almost the opposite sense about UGC 6016, a dwarf irregular galaxy. The system also contains emission to the west of NGC 3448, with a smaller recession velocity than NGC 3448. Parameters observed for NGC 3448 and UGC 6016 are displayed in Tables 6.2 and 6.3. Radio continuum observations of the nuclear source in NGC 3448 (Table 6.5) reveal a spectral index and radio luminosity typical of nuclear sources in many normal spiral galaxies.

The HI data provide little evidence to support the theory of Bottinelli et al. (1978) that NGC 3448 may be a double interacting system. The HI dynamics in Arp 205 can be modeled as shown in Fig. 6.6, suggesting that there has been a planar tidal interaction between NGC 3448 and UGC 6016.

CHAPTER 7THE GROUP OF GALAXIES NGC 2805, NGC 2814, NGC 2820 AND IC 24581 INTRODUCTION

NGC 2805, 2814, 2820 and IC 2458 form a compact group of galaxies of which NGC 2805 is the brightest. Optical data from RC2 are given in Table 7.1, and Plate 7.1 includes a reproduction of the Palomar Sky Survey print of the region. NGC 2805 is a 'disturbed' late-type spiral viewed nearly face-on, and closely resembles M101 (Arp 1966). NGC 2820 is an edge-on disc system, probably of late spiral type, having a close companion, IC 2458, of uncertain type, which is number 108 in Markarian's list of objects with ultraviolet excesses (Markarian 1969), and shows strong emission lines. The Palomar Sky Survey prints reveal a filamentary structure which appears to link the eastern edge of NGC 2820 with IC 2458; since these filaments appear on both the red and blue plates, they must contain some old stars. NGC 2814 was originally classified IO? by de Vaucouleurs & de Vaucouleurs (1964, RC1), but the classification was subsequently withdrawn (RC2). Krienke & Hodge (1974) point out that photographs of NGC 2814 have a 'smooth texture' with no resolution into stars and HII regions, and also indications of dust lanes, all characteristics of IO (alias IrII) galaxies.

According to de Vaucouleurs (1975), NGC 2805 is one of six galaxies forming the G41 (alias NGC 2768) group at a distance of 13.7 Mpc, but NGC 2820, 2814 and IC 2458 are not listed as members of this group although they all have similar redshifts. The distance of 13.7 Mpc has been assumed for all the galaxies discussed in this Chapter, leading to a linear scale of 1 arcmin \approx 4 kpc, but it should be noted that this

Table 7.1 Optical parameters (from RC2 unless stated)

Name	NGC 2805	NGC 2814	IC 2458 Mk 108	NGC 2820
RA 1950.0	09 ^h 16 ^m .29	09 ^h 17 ^m .4	09 ^h 17 ^m .45	09 ^h 17 ^m .71
Dec 1950.0	64° 19'.1	64° 27'.9	64° 27'.1	64° 28'.3
Classification	SAB(rs)d	I0?*	?	SB(s)c pec*
Total 'face-on' <i>B</i> magnitude corrected for galactic and internal absorption	11.40	13.61	15†	12.37
Isophotal major diameter (arcmin), corrected to 'face-on'	6.2	1.2	0.5	3.0
Ratio of major to minor diameter <i>R</i>	1.26 ± 0.02	3.39 ± 0.03	2.14 ± 0.04	6.03 ± 0.03
Heliocentric radial velocity (km/s)	1726 ± 11	1663 ± 95	1467 ± 20	1686 ± 18
Colour index (<i>B</i> - <i>V</i>)	0.51 ± 0.07	0.55 ± 0.04	—	0.50 ± 0.07

* From Nilson (1973).

† Photographic magnitude from Markarian (1969).

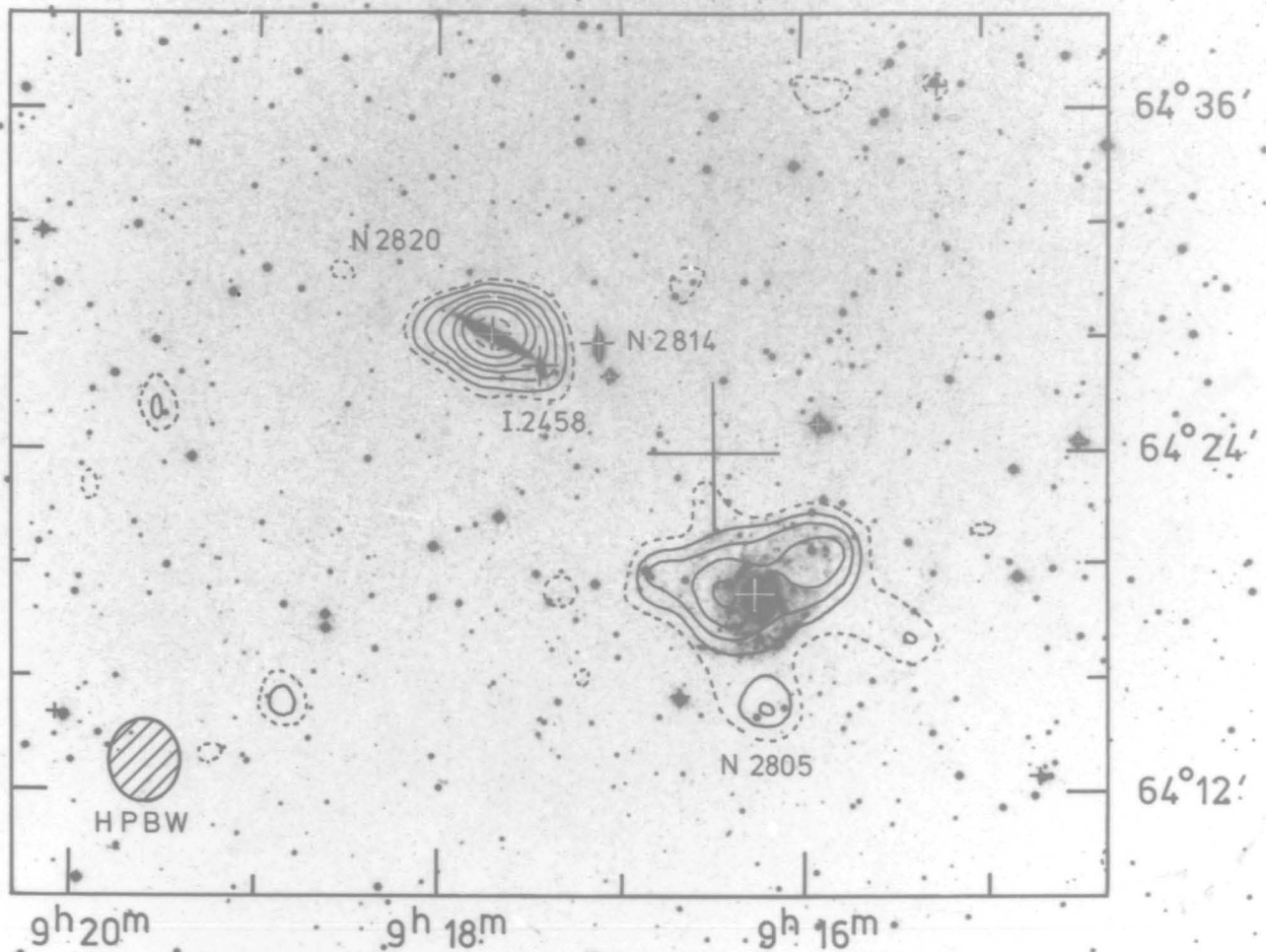


Plate 7.1 Hydrogen integrated over the velocity range 1451-1767 km/s, and superimposed on a blue photograph from the Palomar Sky Survey (copyright by the National Geographic Society and reproduced with permission from the Hale Observatories). The dashed contour is 200 K km/s. Solid contours start at 300 K km/s and are at intervals of 100 K km/s. Small crosses are star positions for alignment. The large cross is at the map centre. The labels refer to the medium-sized crosses which are at the optical centres of these galaxies. The hatched ellipse represents the HPPW resolution of 2.5 x 2.8 arcmin. No polar diagram correction has been applied, but this correction increases values at the nucleus of NGC 2805 by only 1 per cent, and values at the nucleus of NGC 2820 by 3 per cent.

value is uncertain by about a factor of 2 and the assumption $H_0 = 75 \text{ km}/(\text{s Mpc})$ leads to distances of about 20 Mpc.

The only published radio observations are a detection of the 21-cm line in NGC 2805 by Dickel & Rood (1978), but Bottinelli & Gouguenheim (private communication) have used the radio telescope at Nançay to obtain an HI line profile centred on NGC 2814. This profile shows two emission peaks - one from NGC 2805 at about 1710 km/s, and one at about 1456 km/s. The present survey was undertaken primarily to discriminate between the HI from the various galaxies in this group. Bosma (1978) is currently preparing a paper on similar observations made with the Westerbork Synthesis Radio Telescope.

2 OBSERVATIONS

This survey consisted of 36 equally-spaced interferometer baselines as detailed in Table 7.2. HI emission was measured using the digital cross-correlation spectrometer over a 4-MHz bandwidth. Continuum emission was simultaneously measured over the 10-MHz bandwidth, and both the surveys were calibrated by observations of 3C 268.3 and 3C 468.1 (the latter was used for phase calibration only).

The HI channel maps were corrected for the presence of continuum emission by averaging those channels which contained no significant line-emission (1952 to 1820 km/s and 1372 to 1293 km/s), and subtracting the resulting map from those which did. The resulting 'continuum-free' channel maps were analysed to produce an integrated HI map, a RA-velocity plot, a dec-velocity plot and the velocity field as described in Chapter 1.

Table 7.2 Details of the observations of NGC 2805, 2814, 2820 and IC 2458 with the Cambridge Half-Mile Telescope

Dates	1978 January/February	
Map centre (1950)		
RA	09 ^h 16 ^m 30 ^s	
dec	64° 24' 00"	
Interferometer baselines		
number	36	
smallest	12.2 m	
increment	6.1 m	
largest	225.6 m	
Calibrators		
name	3C 268.3	3C 468.1
flux density	4.4 Jy	5.3 Jy
reference	Elsmore & Mackay (1969)	See text
Response		
synthesised beam (HPFW)		
RA x dec	2.5 x 2.8 arcmin	
structure absent	greater than 1°	
radius of first grating response	~2°	
Continuum Survey		
bandwidth	10 MHz	
centre frequency	1415 MHz	
noise per beam area	2 mJy	
Hydrogen-line survey		
bandwidth	4 MHz	
heliocentric velocity range	1266 to 2084 km/s	
channel separation	26.4 km/s	
channel width	32 km/s (FWHP Gaussian)	
mean rms sensitivity per beam area per channel	28 mJy	

3 RESULTS

3.1 The HI distribution

Plate 7.1 shows the integrated HI superimposed on a blue print of the Palomar Sky Survey, and it can be seen that HI surrounds NGC 2805, 2820 and IC 2458, but not NGC 2814. Fig. 7.1 and 7.2 show the RA-velocity and the dec-velocity plots. The bars indicate the optical positions and velocities of the galaxies from RC2. According to Dickel & Rood (1978), the mean velocity errors quoted in RC2 are underestimates, and the velocity error-bars have therefore been increased by 50 % from the RC2 values. The HI systemic velocities, V_{sys} , derived by calculating the 'centres of gravity' in Figs 7.1 and 7.2 are given in Table 7.3 and are confirmed by the Nançay line-profiles. The systemic velocity of NGC 2805 derived in this study agrees with the optical value (Table 7.1) and with the value of 1733 km/s quoted by Dickel & Rood. The optical and HI positions for NGC 2805 also agree well (Figs 7.1 and 7.2).

From the integrated HI distribution alone (Plate 7.1), it appears that the gas seen around the NGC 2820/IC 2458 system is confined to an envelope around the disc galaxy NGC 2820, as might be expected if the galaxy was undisturbed. However, there are several reasons to suppose that this is not the case. Figs 7.1 and 7.2 show that the systemic velocity ($V_{\text{sys}} = 1561 \pm 13$ km/s) of HI surrounding the system, taken as a whole, is significantly different from the optical values for both NGC 2820 and IC 2458 (differences of 125 ± 21 and 94 ± 33 km/s respectively). The optical redshift for NGC 2820 is based on two measurements, both by Page (1970). He used red-sensitive plates, so avoiding

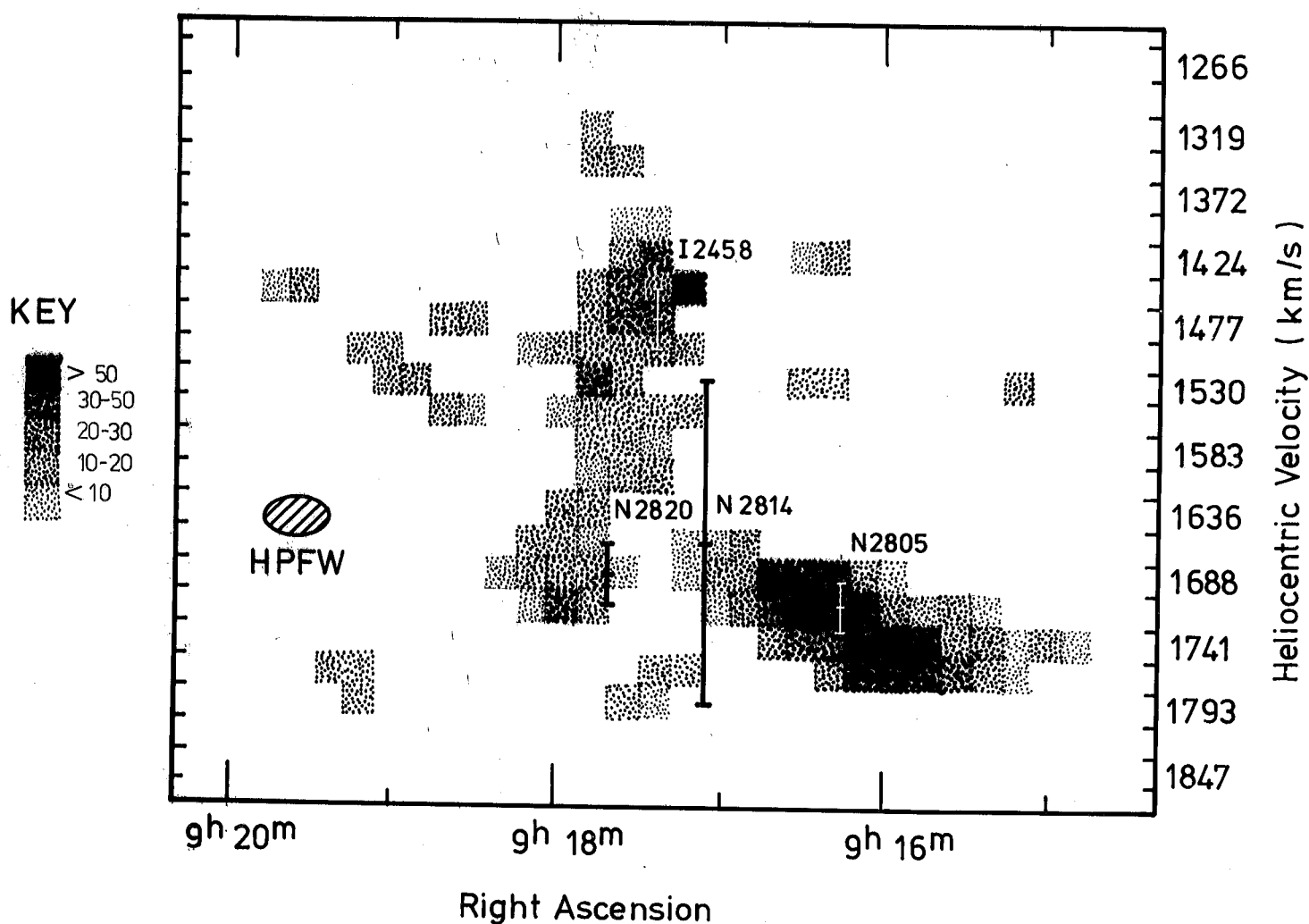


Figure 7.1. Right ascension-velocity plot constructed as described in Chapter 1. Each shaded rectangle represents the HI intensity in a 70 arcsec x 32 km/s cell (arbitrary units). The crosses represent the optical positions and velocities of the labelled galaxies. The HPFW resolution of 2.5 arcmin x 32 km/s is shown by the hatched ellipse. Only signals which exceed 3σ have been included in this plot.

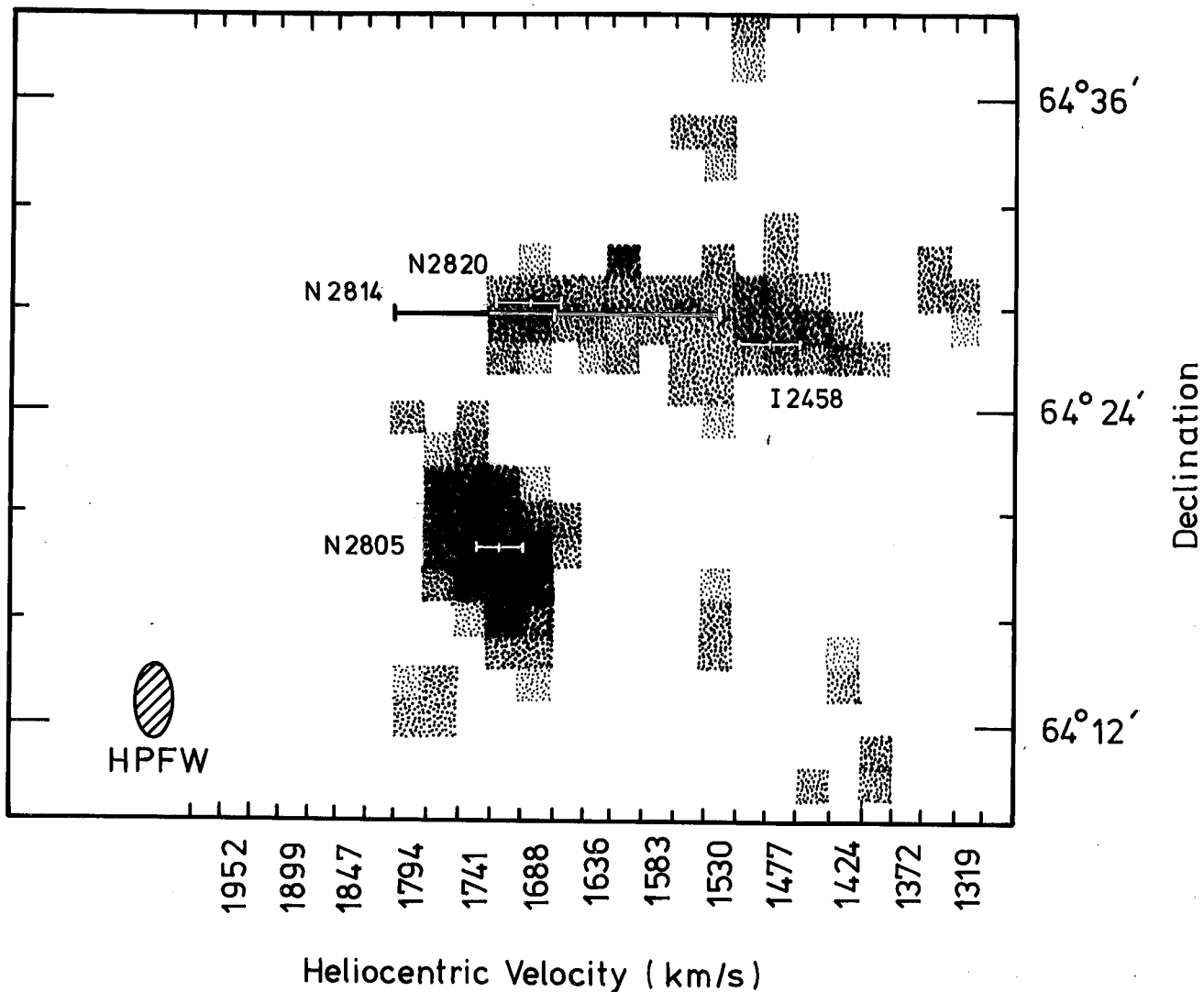


Figure 7.2. Declination-velocity plot constructed as described in Chapter 1. The key to the symbols is the same as for Fig. 7.1. The crosses represent the optical positions and velocities of the labelled galaxies. The HPFW resolution of 2.8 arcmin x 32 km/s is shown by the hatched ellipse. Only signals above 3σ have been included in this plot.

Table 7.3. HI properties.

Parameter	Symbol	NGC 2805	Total NGC 2820/ IC 2458 system =	NGC 2820 +	IC 2458 +	Bridge	NGC 2814
Optical type	(from Table 1)	SAB(rs)d	—	SB(s)c pec	?	—	I0?
HI systemic velocity	$V_{\text{sys}} (\pm 26)$ km/s	1726 ± 13	1561 ± 13	1692	1480	1591	—
HI velocity width	$\Delta V (\pm 26)$ km/s	158	341	79	158	104	—
HI mass distance ⁻²	$M_{\text{H}}/D^2 \times 10^7 M_{\odot} \text{Mpc}^{-2}$	1.9 ± 0.2	1.5 ± 0.2	0.4 (24%)	0.8 (52%)	0.4 (24%)	<0.07
HI diameter	a_{H} arcmin	12 ± 1	5.8 ± 0.5	<2.5	<2.5	<2.5	—
Inclination	i degree	38 ± 2	90	90	?	—	77 ± 1
Distance	D Mpc	13.7	13.7	13.7	13.7	13.7	13.7
HI mass	$M_{\text{H}} \times 10^9 M_{\odot} (D^2)$	3.2 ± 0.4	2.9 ± 0.4	0.7	1.5	0.7	<0.14
Total mass	$M_{\text{T}} \times 10^9 M_{\odot} (D)$	50 ± 20	50 ± 10	2 ± 2	$1 \pm 1 \dagger$	—	10^*
Luminosity	$L \times 10^9 M_{\odot} (D^2)$	8 ± 1	3.1	2.7	0.3	—	0.9
Integral parameters	$M_{\text{H}}/L (D^0)$	0.4	1.0	0.3	5	—	<0.16
	$M_{\text{T}}/L (1/D)$	7	16	0.8	4.0	—	—
	$M_{\text{H}}/M_{\text{T}} (D)$	0.06	0.06	0.4	1.5	—	—

* Assuming $M_{\text{T}}/L = 11$ (Dickel & Rood 1978).

† Assuming an inclination of 90° .

? Uncertain.

the Roberts (1975) correction, and it is most unlikely that the redshift is in error by 125 km/s. It is also unlikely that all the HI is associated with IC 2458, since this results in an abnormal M_H/L ratio. Figs 7.1 and 7.2 show that the HI around NGC 2820 and IC 2458 has two distinct peaks of emission at 1714 and 1450 km/s, corresponding closely with their optical velocities (differences of 28 km/s for NGC 2820 and 17 km/s for IC 2458). This suggests that the optical velocities are correct to within their quoted errors, from which the following conclusions can be drawn about the HI surrounding the NGC 2820/IC 2458 system: (1) the HI seen on the channels between 1662 and 1715 km/s surrounds the eastern half of the stellar disc of NGC 2820; (2) the HI seen on the channels between 1398 and 1530 km/s surrounds IC 2458; (3) the remaining HI (i.e. on channels between 1556 and 1636 km/s inclusive) forms an intergalactic bridge between the two galaxies. This is discussed further in Section 4.

Fig. 7.3 shows the velocity field. That over NGC 2805 is typical of a spiral galaxy with PA about 125° . Model-fitting was not attempted, because of the small number of beam areas over the galaxy. The velocity field between NGC 2820 and IC 2458 is apparently discontinuous, having velocities over IC 2458 of about 1478 km/s and then abruptly changing to about 1689 km/s over NGC 2820. This apparent discontinuity is to be expected from the fitting procedure used (see Figs 7.1 and 7.2) and does not necessarily imply a true discontinuity. In view of the HI bridge between NGC 2820 and IC 2458, and the disturbed nature of NGC 2805 (Nilson 1973), a search was made for faint HI between the other galaxies. Continuum-free channel maps were constructed for this purpose using data

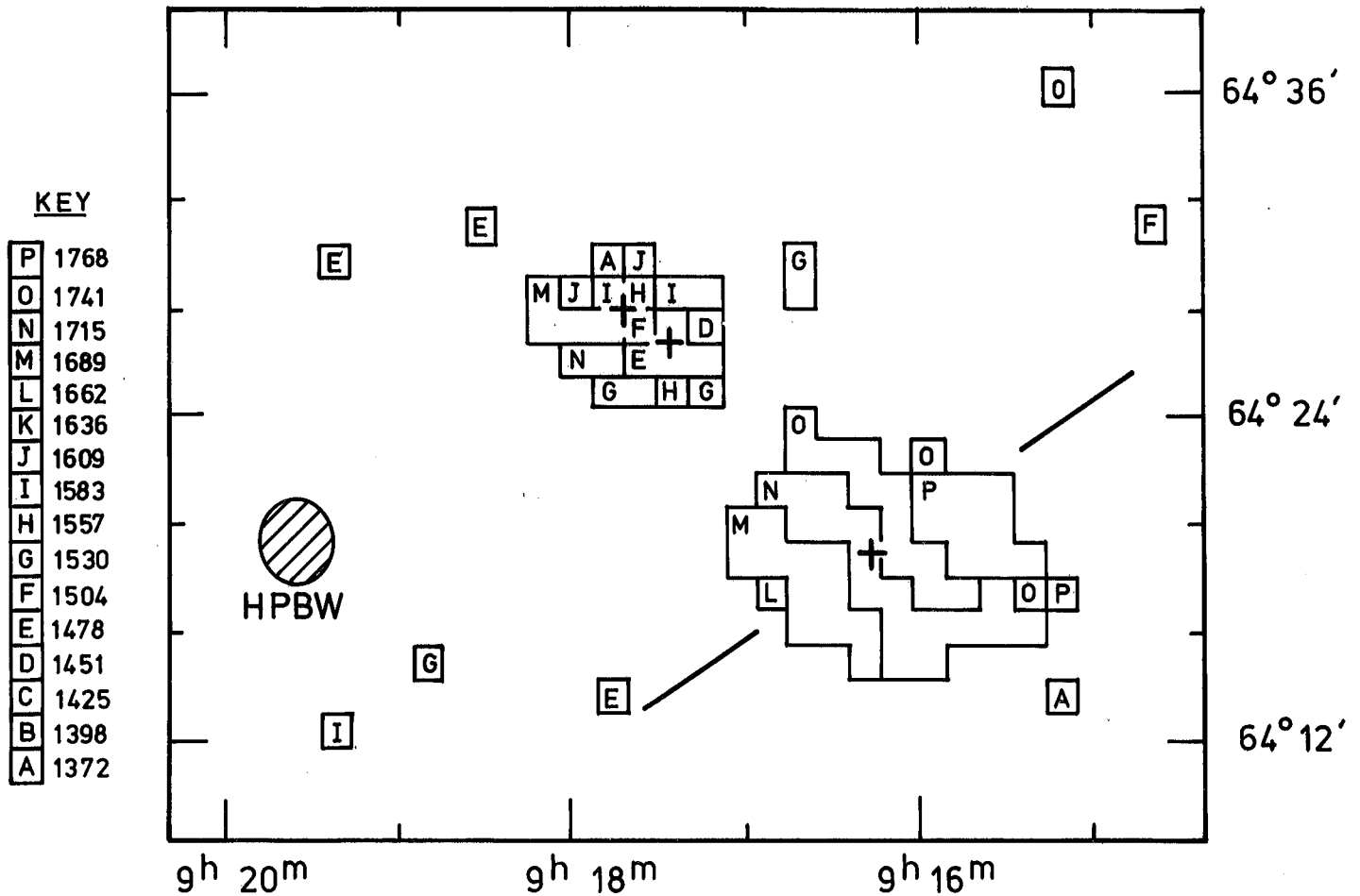


Figure 7.3. The velocity field, obtained by fitting Gaussian profiles at each point as described in Chapter 1. Each symbol represents the fitted heliocentric velocity (km/s) in 70×78 arcsec cells. The crosses indicate the optical nuclei, and the line represents the major axis PA of NGC 2805 (125°). The HPBW resolution of 2.5×2.8 arcmin is shown by the hatched ellipse.

from the 12 smallest interferometer baselines. These maps were more sensitive to low-brightness emission than the maps made at full resolution, and had a resolution of 7.4×8.2 arcmin and a mean rms noise level of 50 mJy. No convincing evidence was found for HI except between NGC 2820 and IC 2458.

The hydrogen masses (Table 7.3) of NGC 2805 and NGC 2820/IC 2458 were determined from the low-resolution channel maps (described above) as described in Section 2.4c of Chapter 1. On these maps the NGC 2805 and the NGC 2820/IC 2458 systems were each unresolved, but still well separated. The hydrogen masses agree to within a factor of 2 with those determined from the maps at high resolution, and from the Nançay line-profiles. In Table 7.3 the HI masses of NGC 2820, IC 2458 and of the intergalactic bridge were evaluated from Figs 7.1 and 7.2 by calculating the fraction of the total HI mass of this system which each occupies. This was done in accordance with the earlier assumption that HI in the channels centred between 1398 and 1530 km/s is associated with IC 2458, HI between 1662 and 1715 km/s is associated with NGC 2820, and HI between 1556 and 1636 km/s forms the intergalactic bridge.

The neutral hydrogen diameter a_H was measured at PA 70° for NGC 2805 and the NGC 2820/IC 2458 system, and the values take account of convolution with the synthesised beam. The inclination was computed as described in Section 2.4e of Chapter 1, taking the ratio of the observed major to observed minor axis from Table 7.1, and assuming the ratio of the intrinsic principal axes of the light distribution to be 0.2 (Heidmann, Heidmann & de Vaucouleurs 1971).

The observed radial velocities along the major axis of NGC 2805 are shown in Fig. 7.4. From this curve, a difference

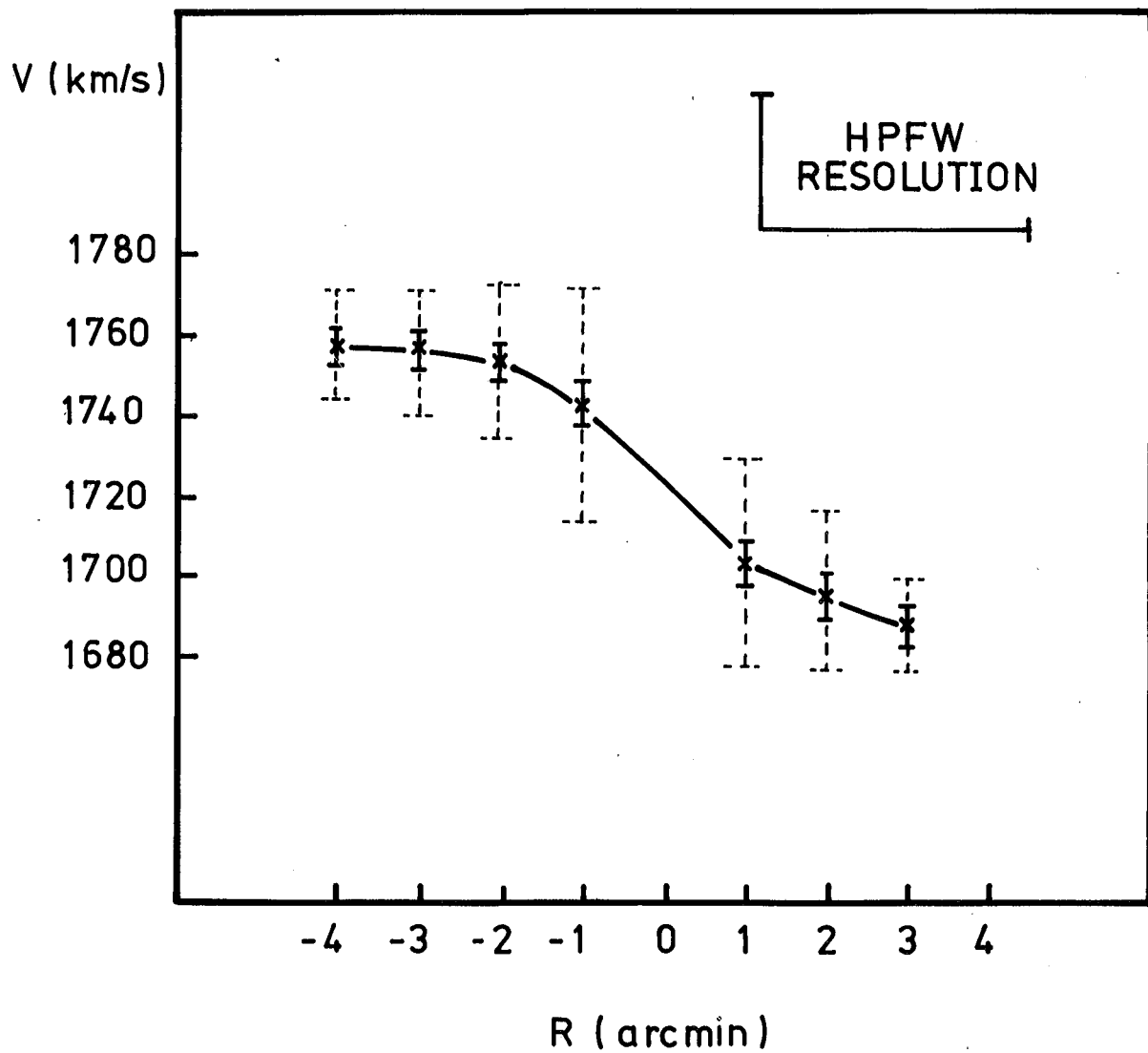


Figure 7.4. Rotation curve for NGC 2805, derived by interpolating velocities from Fig. 7.3 along a line defined by the optical centre and position angle (Table 7.1). The errors are rms (solid line) and fitted widths at half power (dashed line).

of 34 ± 4 km/s from the systemic velocity is observed at a radius of 3.5 arcmin. In fact this velocity difference is underestimated because of beam-smearing, for which a simple correction is to take velocities at the 10 % level of the Gaussian profiles, rather than at the peak. This correction gives 78 ± 8 km/s at 3.5 arcmin from the nucleus and, following the method outlined in Section 2.4f of Chapter 1, results in a total mass for NGC 2805 of $M_T \sim 50 M_\odot$.

All the values of M_T quoted in Table 7.3 are indicative total masses, and for NGC 2805 the value is in close agreement with that quoted above. Luminosities are based on values from Table 7.1 and the distance estimate of 13.7 Mpc. All the galaxies have typical luminosities (Roberts 1975). The M_T value and colour index of NGC 2805 are typical of its Sd type, while the M_H/L value is more consistent with an Sc type (Balkowski 1973). If the HI seen around NGC 2820 and IC 2458 comprises one system, its M_T value is typical of a Sc galaxy, although the M_H/L and M_H/M_T both indicate the system to be of a later type (Sd to Ir). As independent galaxies, NGC 2820 and IC 2458 both have total masses which are low, especially for NGC 2820 (a Sc type). The resulting M_H/M_T and M_T/L values for NGC 2820 and IC 2458 are also abnormal. Both the M_H/L ratio and colour of NGC 2820 are typical of a Sc galaxy, but the M_H/L value of IC 2458 is very high and points strongly to its being of Ir type.

The M_H/L limit of NGC 2814 is indicative of a S0 galaxy, as are the M_H/L values of many other IO galaxies (Chapter 5). Its colour ($B-V = 0.55$) is somewhat redder than those of the other galaxies in this group, although still rather blue for a S0 galaxy.

3.2 Radio Continuum

Fig. 7.5 shows the radio continuum map, which in fact also includes line emission over the 10-MHz bandwidth. The line emission accounts for about 10 mJy in the region of NGC 2820, IC 2458 and NGC 2805. The continuum distribution can be explained solely as a result of two (or possibly three) nuclear sources, as shown in Table 7.4, and there is no need to invoke disc components or intergalactic emission. The radio luminosities (Table 7.4) are characteristic of normal galaxies, as Burke & Miley (1978) also found for a sample of optically 'peculiar' galaxies.

Table 7.4 Radio-Continuum properties of NGC 2805, 2820, 2814, and IC 2458.

Galaxy	S_{151}^* (mJy)	S_{1415} (mJy)	L_{1415} (10^{21} W/Hz)
NGC 2805	130	10	0.2
NGC 2820	130	50 ± 10	1.1 ± 0.2
NGC 2814	130	20 ± 10	0.4 ± 0.2
IC 2458	130	$20 \pm 20?$	$0.4 \pm 0.4?$

Notes * From the Cambridge 6C survey (C.J. Mayer, private communication).

? Uncertain.

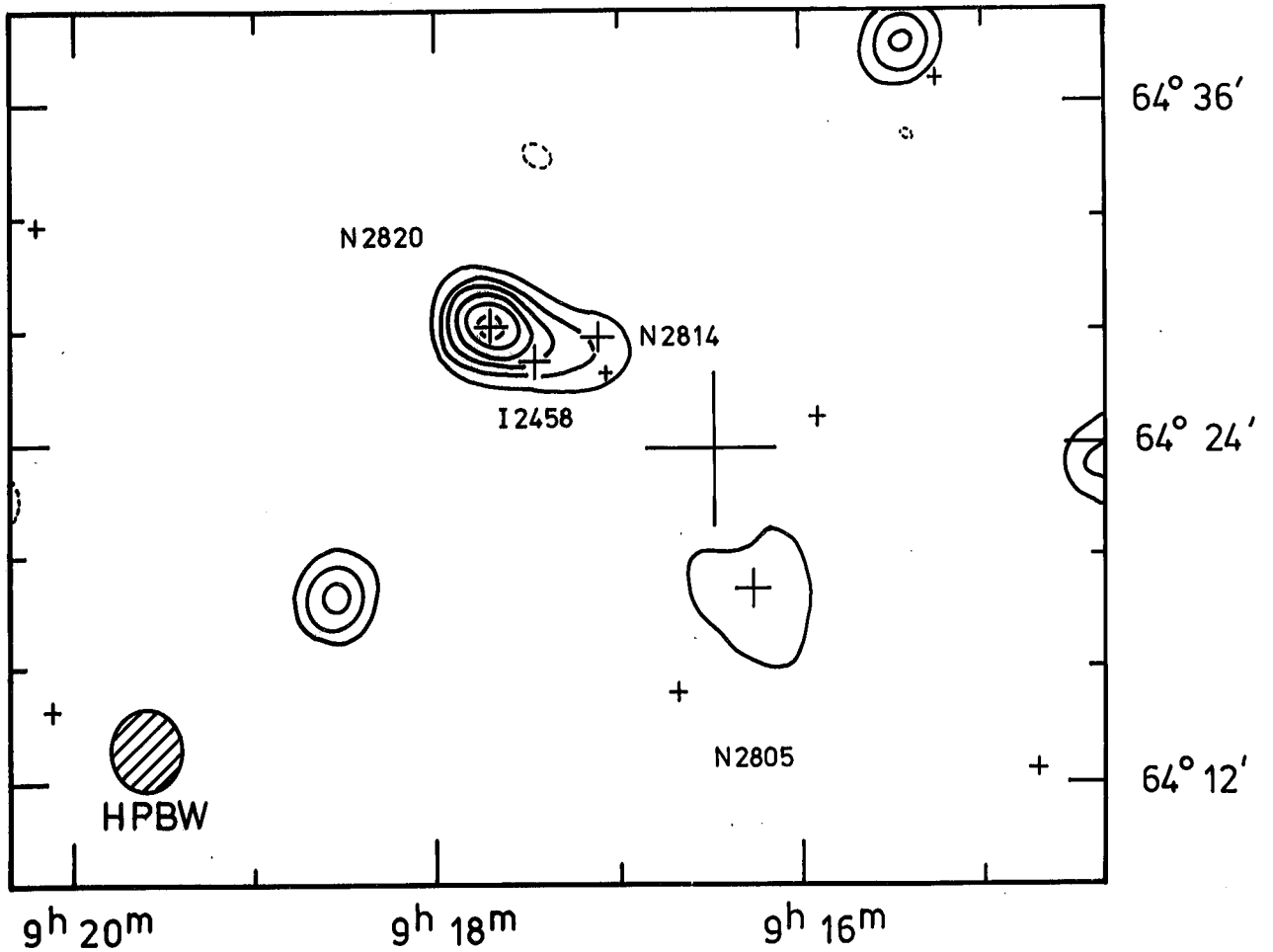


Figure 7.5. Map of radio-continuum emission over a 10-MHz bandwidth centred at 1415 MHz. Solid contours start at 10 mJy and are in 10 mJy intervals. The dashed contour is -10 mJy. The HPBW resolution of 2.5×2.8 arcmin is shown by the hatched ellipse. The crosses are as in Plate 7.1

4.1 Dynamics

In order to investigate if any of the galaxy pairs are in bound orbits, the minimum mass necessary to sustain circular motion was evaluated,

$$M_c = 2.3 \times 10^5 S_{\text{proj}} (V_c)^2,$$

where M_c is expressed in solar masses, S_{proj} is the projected linear separation (kpc) of the two galaxies, and V_c is the difference in radial velocities (km/s). If M_c is greater than the mass of the satellite galaxy, then the system is not bound. On the basis of the values given in Table 7.3, neither the NGC 2820/IC 2458 pair nor the NGC 2820/IC 2458/NGC 2805 system has the necessary mass, about $100 GM_{\odot}$. It is nevertheless very hard to believe that such a compact group of galaxies is not in fact bound, and it seems likely that the M_T values in Table 7.3 are underestimates.

4.2 Tidal Interaction Hypothesis

One interpretation of the NGC 2820/IC 2458 system, which correctly represents the positions and velocities of the two galaxies, as well as those of the HI, is shown in Fig. 7.6, where NGC 2820 is more distant than IC 2458 and the two galaxies are connected by an HI bridge. It is suggested that there has been a tidal interaction in which a perturbing body has disrupted a proto-NGC 2820, consisting of a normal late-type galaxy (e.g. Sc or Sd), drawing out HI to form a large tidal arm. On this picture, IC 2458 represents stars either drawn from NGC 2820 or the perturbing body, or formed as a result of gas compressed during the encounter.

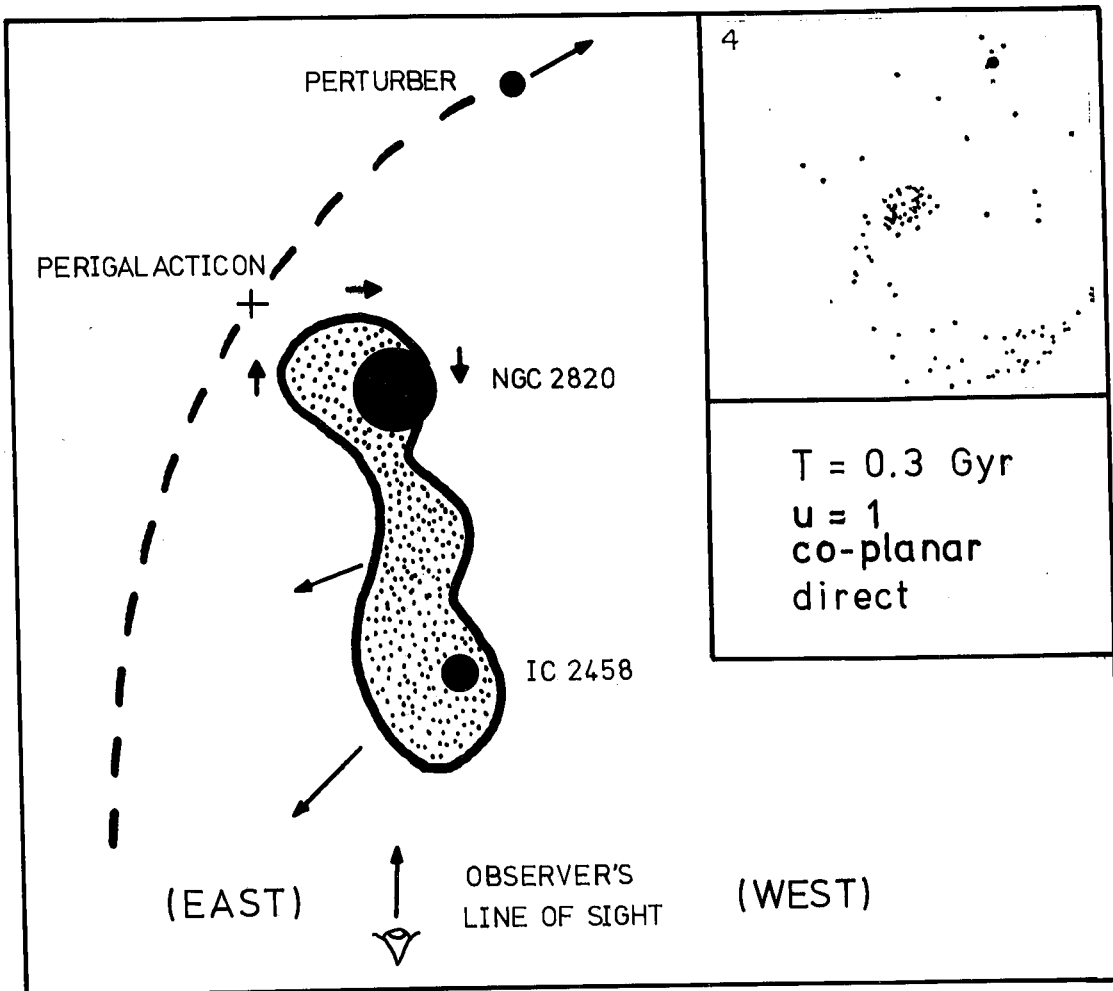


Figure 7.6. Illustration of the proposed model for the NGC 2820/IC 2458 system, drawn in the plane of NGC 2820. The diagram (which is not to scale) shows the distribution of HI (dotted areas), and its approximate velocity relative to the centre of NGC 2820 (arrows). The type of orbit required to produce the disruption is indicated by the dashed line. The inset (reproduced with permission from Wright 1972) shows the disruption of test particles and the position of the perturbing body 0.3 Gyr after a co-planar, direct collision with $u = 1$, and with a perigalacticon of one galactic radii.

Two obvious candidates to cause such disruption to the proto-NGC 2820 are NGC 2805 and 2814.

Toomre & Toomre (1972) and Wright (1972) have shown that, in idealized models, gravitational interactions alone can produce a variety of 'bridges' and 'tails'. Simulations which reproduce the tidal arm are shown in the Appendix. They require a co-planar, direct collision with mass ratios (perturber/galaxy), u , between 0.25 and 1, and are seen at a time of about 0.3-0.7 Gyr after a perigalacticon of about one galactic radii. One such distribution of test particles is reproduced in Fig. 7.6 (inset). The proposed orbits are consistent with the sense of the velocity gradient along the tidal arm (cf. Fig. 7.1), and the arm appears to join NGC 2820 on its eastern side and bend westward toward IC 2458.

It is not easy to identify whether NGC 2805 or 2814 is the correct candidate for the role of perturber. Both galaxies could be in orbits (illustrated in Fig. 7.6) which would produce the requisite disruption to the proto-NGC 2820 and also match the positions and radial velocities of the galaxies. For an encounter between the proto-NGC 2820 and 2805, the mass ratio u is of order 1, while, for an encounter with NGC 2814, u is of order 0.5 (Table 7.3). Although the larger disturbance envisaged in Fig. 7.6 would favour the larger mass-ratio (implying NGC 2805 as perturber), one cannot rule out perturbations by NGC 2814 in a relatively closer orbit.

The gravitational influence of NGC 2820 is not likely to produce any extensive 'bridges' or 'tails' to the perturbers, since neither suffer sufficiently prograde or co-planar collisions. Tidal effects may, however, account for the

peculiar optical appearance and associated IO? classification of the gas-poor galaxy NGC 2814, or the 'disturbed' nature of NGC 2805. The IO classification was discussed in Chapter 5, and NGC 2814 may be another example of this type of galaxy whose properties have resulted from a tidal interaction.

Neither NGC 2805 nor 2814 are in the plane of NGC 2820's disc (Plate 7.1), so that the orbit of either perturber cannot be exactly co-planar. Although a slightly inclined orbit for either body would still produce a tidal arm (e.g. fig. 9 in Wright 1972), such an orbit would be expected to leave the arm warped slightly out of the plane in the direction of the perturbing body before perigalacticon. In fact IC 2458 lies slightly below the plane of NGC 2820 (Plate 7.1), and according to the model so also does the HI arm. This is compatible with NGC 2814 as the perturber, since its orbit is below the plane of NGC 2820 before perigalacticon and above it afterwards, but not with NGC 2805 as perturber since it is now below NGC 2820's plane and was presumably above it before perigalacticon.

The filamentary structure which appears to link NGC 2820 and IC 2458 on the PSS plates adds weight to the interpretation of the HI data in terms of a tidal arm, however caused. These filaments appear on both red and blue plates, and therefore must contain some old stars. If these were newly formed in the encounter, there has been time for them to evolve to their present colour during the 0.3 Gyr since perigalacticon (Freeman 1975).

5 CONCLUSIONS

In this Chapter HI and radio continuum observations of the close group of galaxies NGC 2805, NGC 2814, NGC 2820 and IC 2458 have been presented. HI was detected in all except NGC 2814, and there is good evidence for a HI bridge linking NGC 2820 and IC 2458. The radio continuum emission is not significantly different from that of 'normal' galaxies, being consistent with nuclear sources in NGC 2820, NGC 2814 and possibly IC 2458.

It is postulated that the HI bridge and disturbed nature of this group are the result of a tidal interaction, in which either NGC 2814 or NGC 2805 passed within one galactic radii of a proto-NGC 2820 about 3 Gyr ago, in an approximately co-planar orbit. As a result the HI (originally surrounding NGC 2820) was drawn out to form a large tidal arm, in which IC 2458 is now embedded.

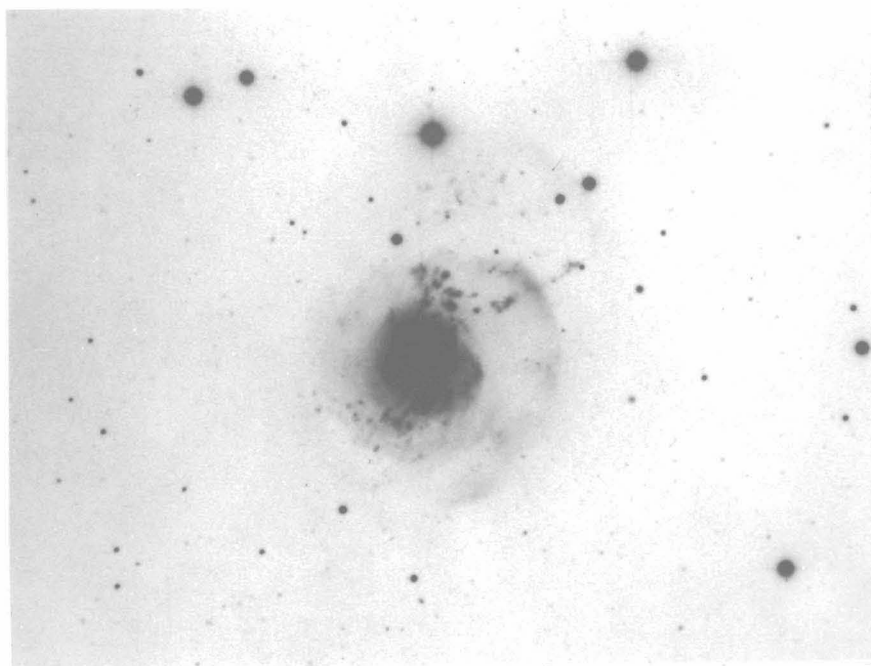
CHAPTER 8THE PECULIAR GALAXIES NGC 3310 AND NGC 34321 INTRODUCTION

The galaxy NGC 3310 is number 217 in Arp (1966) and the photograph is reproduced in Plate 8.1a. The main optical parameters are shown in Table 8.1. NGC 3310 is classified as 'SAB(r)bc pec' in RC2, and an excellent review of its properties appears in van der Kruit & de Bruyn (1976). The galaxy is notable for: a disturbed ('bow-and-arrow') structure in the outer parts to the north-west; a very symmetrical spiral structure in the inner parts of the disc, which is especially clear on H α plates such as Plate 8.1b; highly intense optical emission lines; a high value for the radio-continuum flux and a very blue colour.

Recently the ionized gas in NGC 3310 was investigated by van der Kruit (1976), who assumed a flat plane and large-scale organisation of the velocity field to model the observed velocities in terms of (a) circular rotation plus streaming motions coincident and parallel with the two spiral arms, or (b) a kinematic density wave. He concluded that something very similar to a strong density wave exists in NGC 3310. He points out that this is consistent with all other known properties of the system, and these also suggest the phenomenon is relatively young (probably 10^9 yr or less).

A study of the physical conditions in the nucleus of NGC 3310 (Andrillat & Collin-Souffrin 1976) shows that there is an overabundance of oxygen, and that the synthesised stellar pop-

(a)



(b)

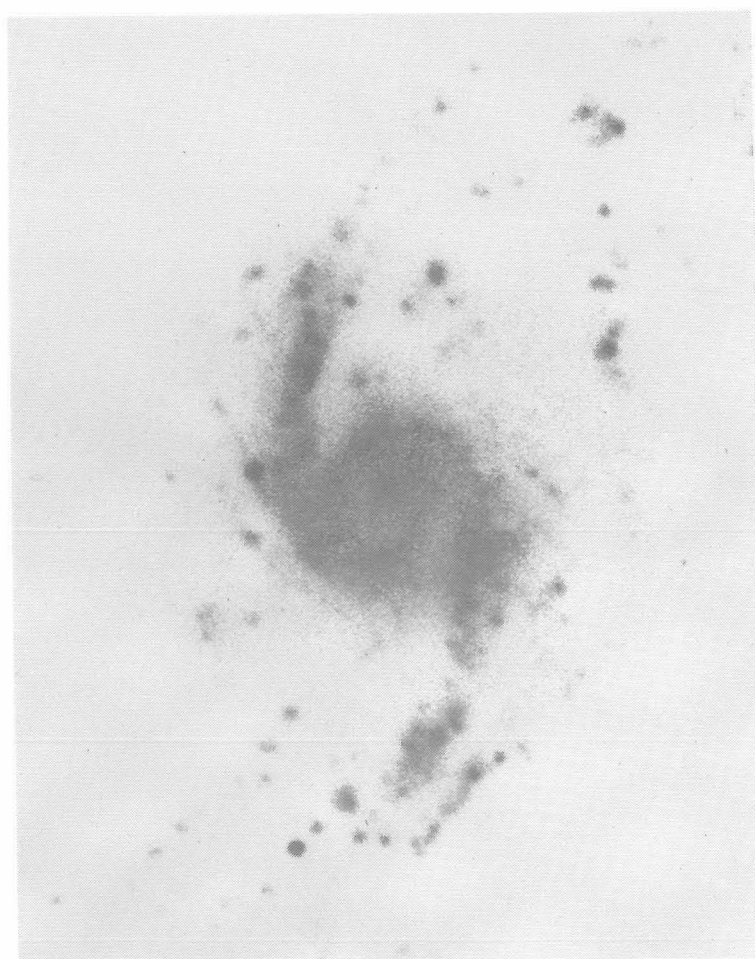


Plate 8.1 (a) Photograph of NGC 3310 from Arp 1966. The photograph measures approximately 10.7×8.3 arcmin. (b) $H\alpha$ photograph from van der Kruit & de Bruyn 1976. The photograph measures approximately 1.8×1.4 arcmin. Both photographs have north at the top and east at the left.

Table 8.1 Optical Parameters for NGC 3310

<u>Parameter</u>	<u>Value</u>	<u>Source</u>
Optical nucleus (1950)		RC2
RA	$10^{\text{h}}35^{\text{m}}39^{\text{s}}.5$	
dec	$53^{\circ}45'54''$	
Classification	SAB(r)bc pec	RC2
Total B magnitude*	10.9	RC2
Colour Index, (B-V)*	0.24 mag	RC2
Inclination wrt plane of sky, i	$32 \pm 6^{\circ}$	van der Kruit 1976
Distance, D	20.5 Mpc	van der Kruit & de Bruyn 1976
Linear Scale	1 arcmin \cong 5.96 kpc	
Dimensions (major axis x minor axis)	3.6 x 3.5 arcmin	RC2
Systemic velocity	994 ± 7 km/s	RC2
	1019 ± 3 km/s	van der Kruit 1976
PA of major axis	$172 \pm 4^{\circ}$	van der Kruit 1976

* corrected for galactic and internal absorption, and to 'face-on' view.

ulation contains a large fraction of O and B stars which account for the intense ultraviolet continuum from the nucleus. Seaquist & Bignell (1977) have presented aperture synthesis observations of the radio continuum at 2.7 and 8.1 GHz. The maps show the emission resolved into components associated with the nucleus and inner spiral structure seen in H α .

NGC 3432 is classified 'SB(s)m sp' in RC2, and the main optical parameters are displayed in Table 8.2. NGC 3432 is number 206 in Arp (1966) and the photograph (Plate 8.2) clearly shows two condensations: one about 3 arcmin to the NE of the nucleus which was reported by Vorontsov-Velyaminov (1959), and one to the west which was noted by Bertola (1966). The latter author found evidence for non-circular motions of about 30 km/s in the central part of the disc from an optical study. The western condensation (a dwarf companion according to RC2) appears as number 05983 in UGC which catalogues the main body plus the condensation to the NE as number 05986. Van der Kruit (1973) has published a radio continuum map of NGC 3432 at 1415 MHz, which shows a disc of emission coincident with the main body of the galaxy and an extended source close to but not coincident with the NE companion (and presumed not to be associated with it).

Previous published HI observations of NGC 3310 (Bottinelli et al. 1970; Balkowski 1973; Peterson & Shostak 1974) and NGC 3432 (Roberts 1968; Balkowski 1973; Bottinelli & Gouguenheim 1974; Dickel & Rood 1978) have used single-dish instruments. Both galaxies were observed in February 1978 using the Half-Mile telescope, and the results (which are described together in this chapter) provide the first detailed maps of the HI distribution and radial velocity field. Van der Kruit & de Bruyn (1976) mention that HI observations of NGC 3310 with the WSRT are in preparation.

Table 8.2 Optical Parameters for NGC 3432

<u>Parameter</u>	<u>Value</u>	<u>Source</u>
Optical nucleus (1950)		RC2
RA	$10^{\text{h}}49^{\text{m}}42^{\text{s}}.6$	
dec	$36^{\circ}53'06''$	
Classification	SB(s)m sp	RC2
Total B magnitude*	11.0	RC2
Colour Index, (B-V)*	0.30	RC2
Inclination wrt plane of sky, i	77°	Dickel & Rood 1978
Distance, D	7.9 Mpc	van der Kruit 1973
Linear scale	1 arcmin = 2.3 kpc	
Dimensions (major axis x minor axis)	6.2 x 6.1 arcmin	RC2
Systemic velocity	636 ± 13 km/s	RC2
PA of major axis	$38 \pm 1^{\circ}$	Plate 8.2

* corrected for galactic and internal absorption, and to 'face-on' view.

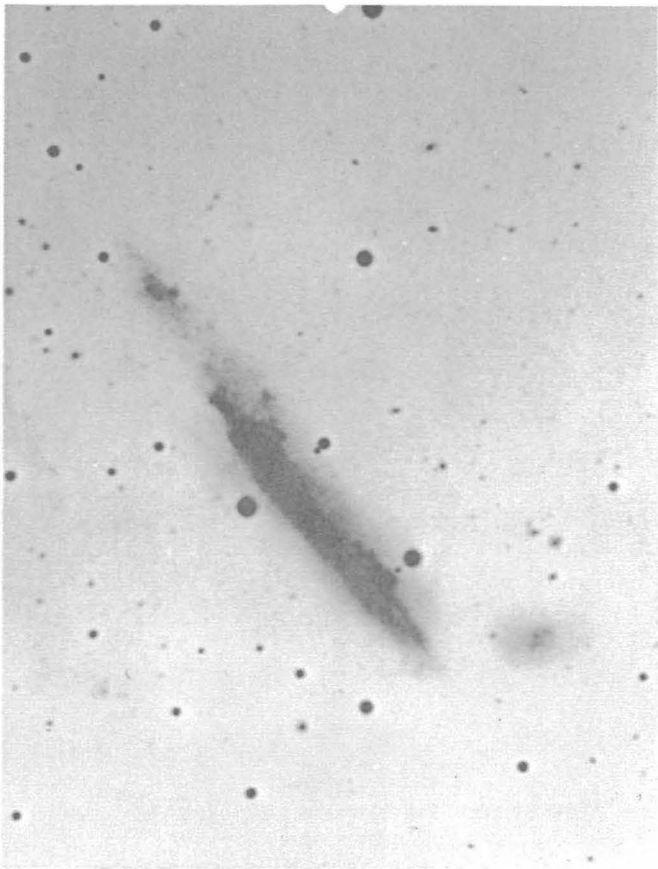


Plate 8.2 Photograph of NGC 3432 from Arp 1966. North is at the top and east is at the left. The photograph measures approximately 10.7 x 8.3 arcmin

2 OBSERVATIONS

The surveys of both NGC 3310 and 3432 consisted of 12 equally-spaced interferometer baselines as indicated in Table 8.3. The HI emission was measured using the digital spectrometer over a 4-MHz bandwidth, and continuum radiation was measured in the 10-MHz bandwidth centred on 1417 MHz. The survey of NGC 3310 was calibrated by observations of 3C 380 and that of NGC 3432 by observations of 3C 48.

In order to correct for the presence of continuum emission, the channel maps which contained no significant line emission (649-728 plus 1203-1335 km/s for NGC 3310, and 390-417 plus 839-1024 km/s for NGC 3432) were averaged and subtracted from those which did. The resulting 'continuum-free' channel maps are shown in Figs 8.1 and 8.2.

Table 8.3 Details of the observations of NGC 3310 and 3432 with the Cambridge Half-Mile telescope.

	<u>NGC 3310</u>	<u>NGC 3432</u>
Dates	1978 February	1978 February
Map centre (1950)		
RA	10 ^h 35 ^m 39 ^s .0	10 ^h 49 ^m 42 ^s .6
dec	53°45'54"	36°53'06"
Interferometer baselines		
number	12	12
smallest	12.2 m	12.2 m
increment	6.1 m	6.1 m
largest	79.3 m	79.3 m
Calibrator		
name	3C 380	3C 48
flux density	13.8	15.3
reference	Elsmore & Mackay (1969)	Kellermann <u>et al.</u> (1969)
Response		
synthesised beam (HPFW)		
RA x dec	7.4 x 9.2 arcmin	7.4 x 12.3 arcmin
structure absent	>1°	>1°
radius of first grating response in RA	~2°	~2°
Continuum survey		
bandwidth	10 MHz	10 MHz
centre frequency	1417 MHz	1417 MHz
sensitivity/beam area	2.8 mJy	2.8 mJy
Hydrogen-line survey		
bandwidth	4 MHz	4 MHz
heliocentric velocity range	570-1388 km/s	232-1050 km/s
channel separation	26.4 km/s	26.4 km/s
channel width (FWHP Gaussian)	32 km/s	32 km/s
mean rms sensitivity/ beam area	38 mJy	34 mJy

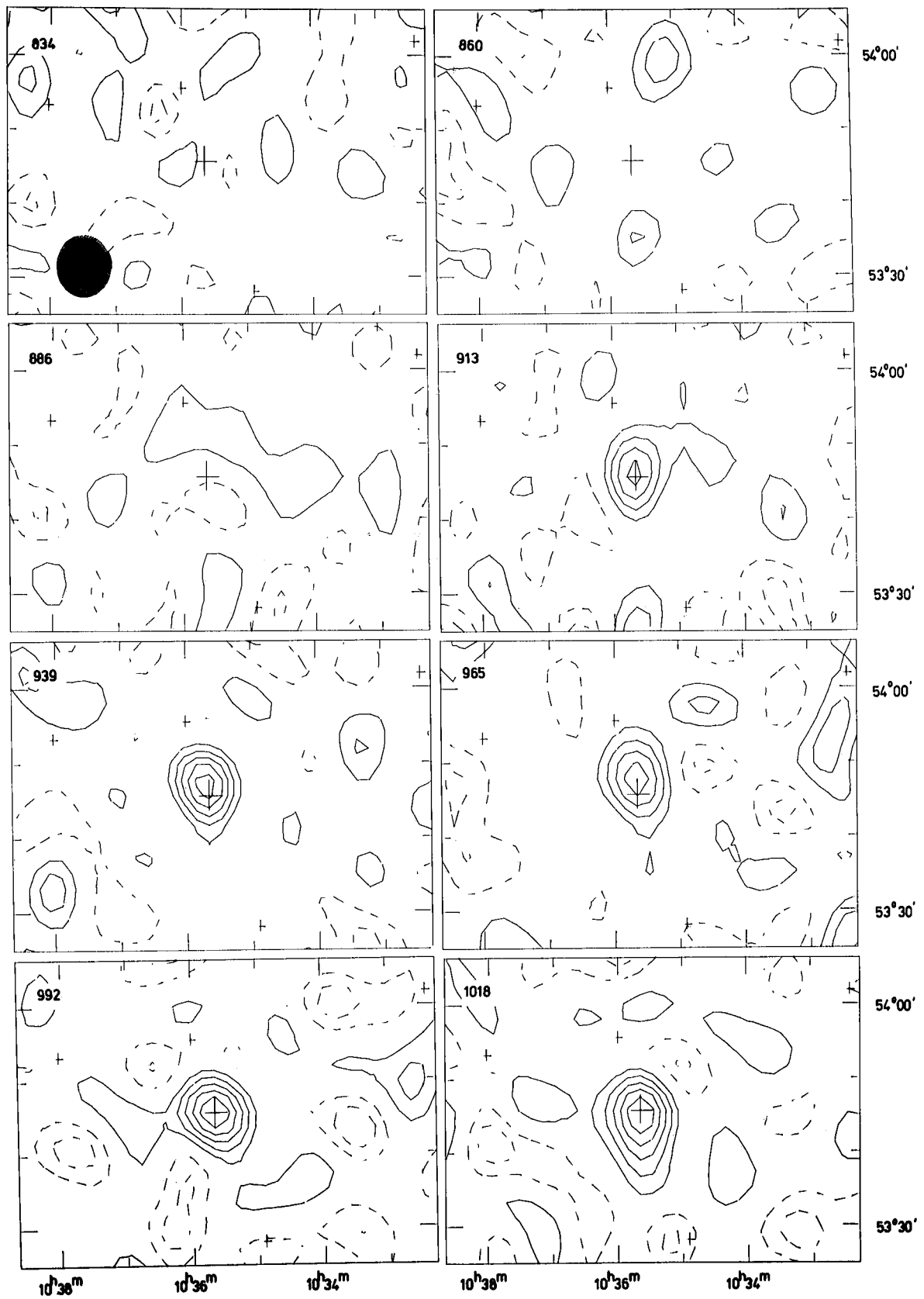


Figure 8.1 Channel maps for NGC 3310, free from continuum emission. Contours start at 50 mJy with the same contour interval ($\sigma \sim 38$ mJy). The large cross is the map centre and the small crosses are star positions for alignment with optical photographs. The hatched ellipse represents the HPBW resolution (Table 8.3). The numbers at the top-left of each box indicate the heliocentric velocity in km/s.

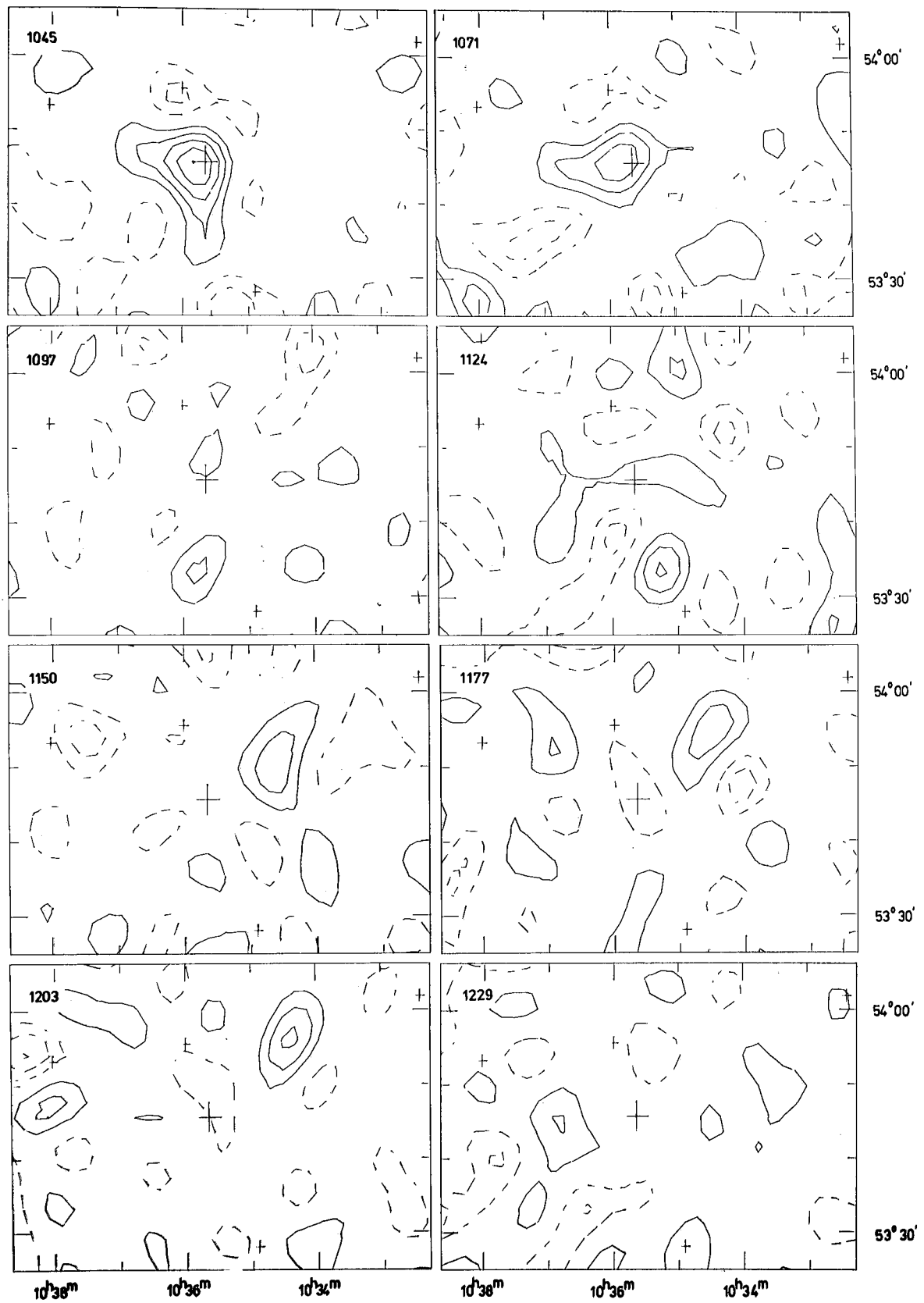


Figure 8.1 continued

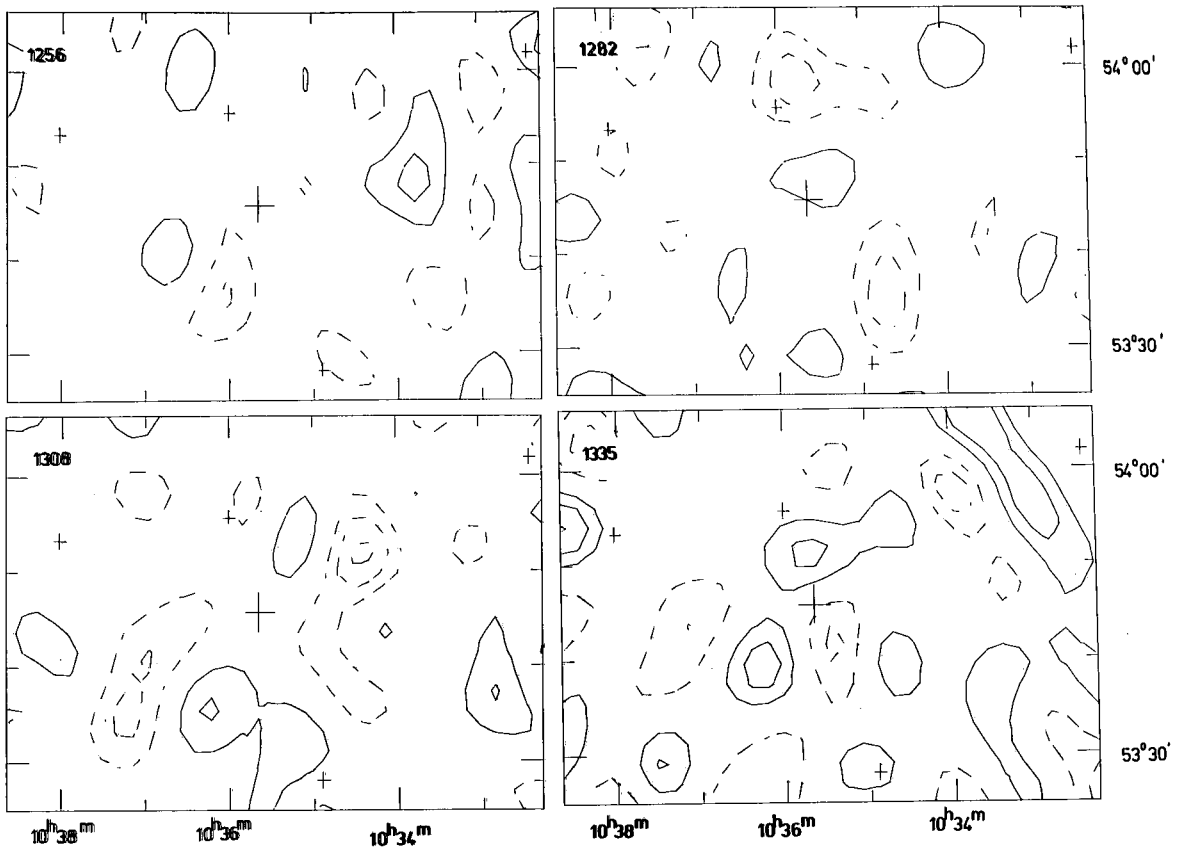


Figure 8.1 continued

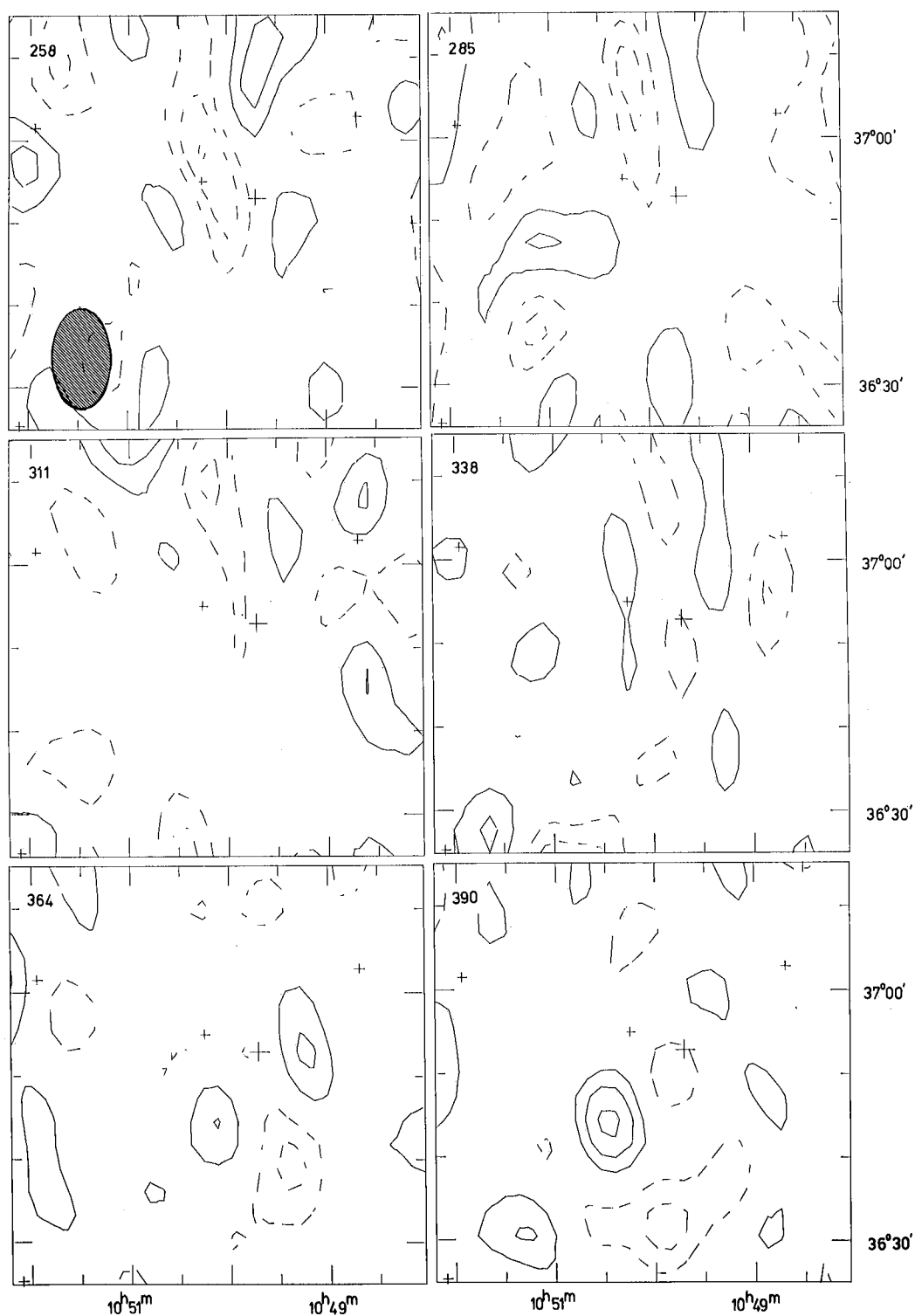


Figure 8.2 Channel maps for NGC 3432, free from continuum emission. Contours start at 50 mJy with the same contour interval ($\sigma \sim 35$ mJy). The large cross is the map centre and the small crosses are star positions for alignment with optical photographs. The hatched ellipse represents the HPBW resolution (Table 8.3). The numbers at the top-left of each box indicate the heliocentric velocity in km/s.

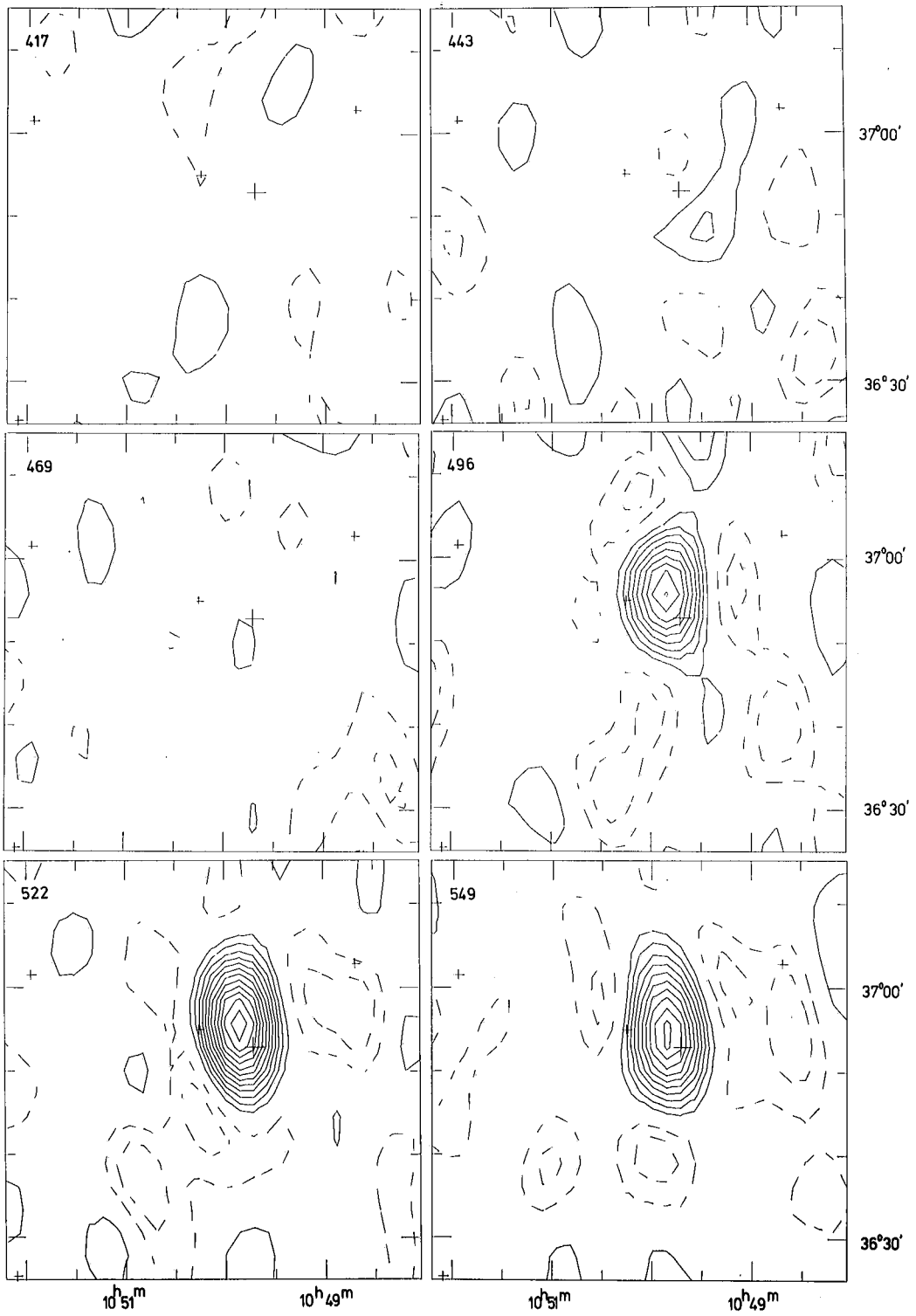


Figure 8.2 continued

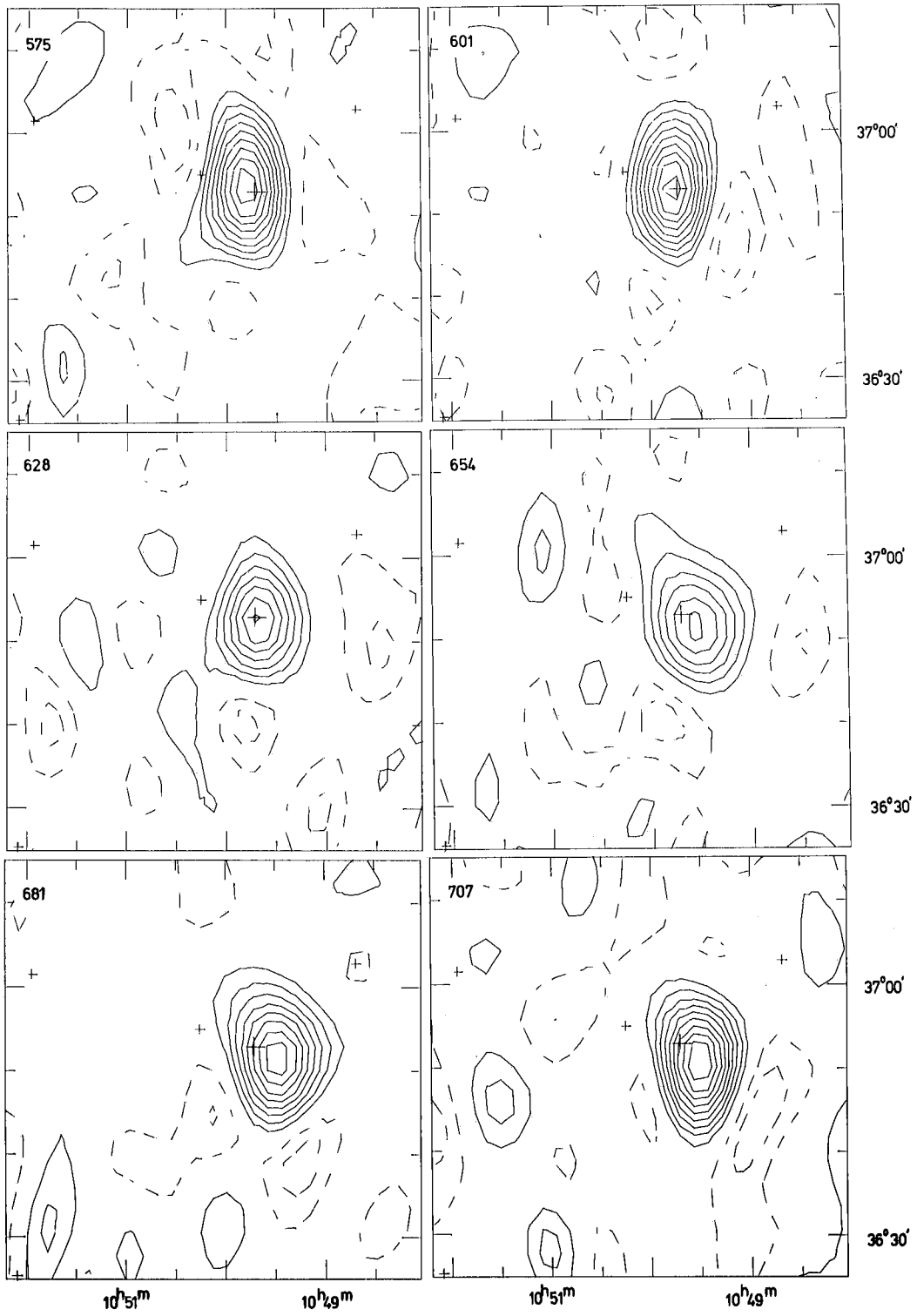


Figure 8.2 continued

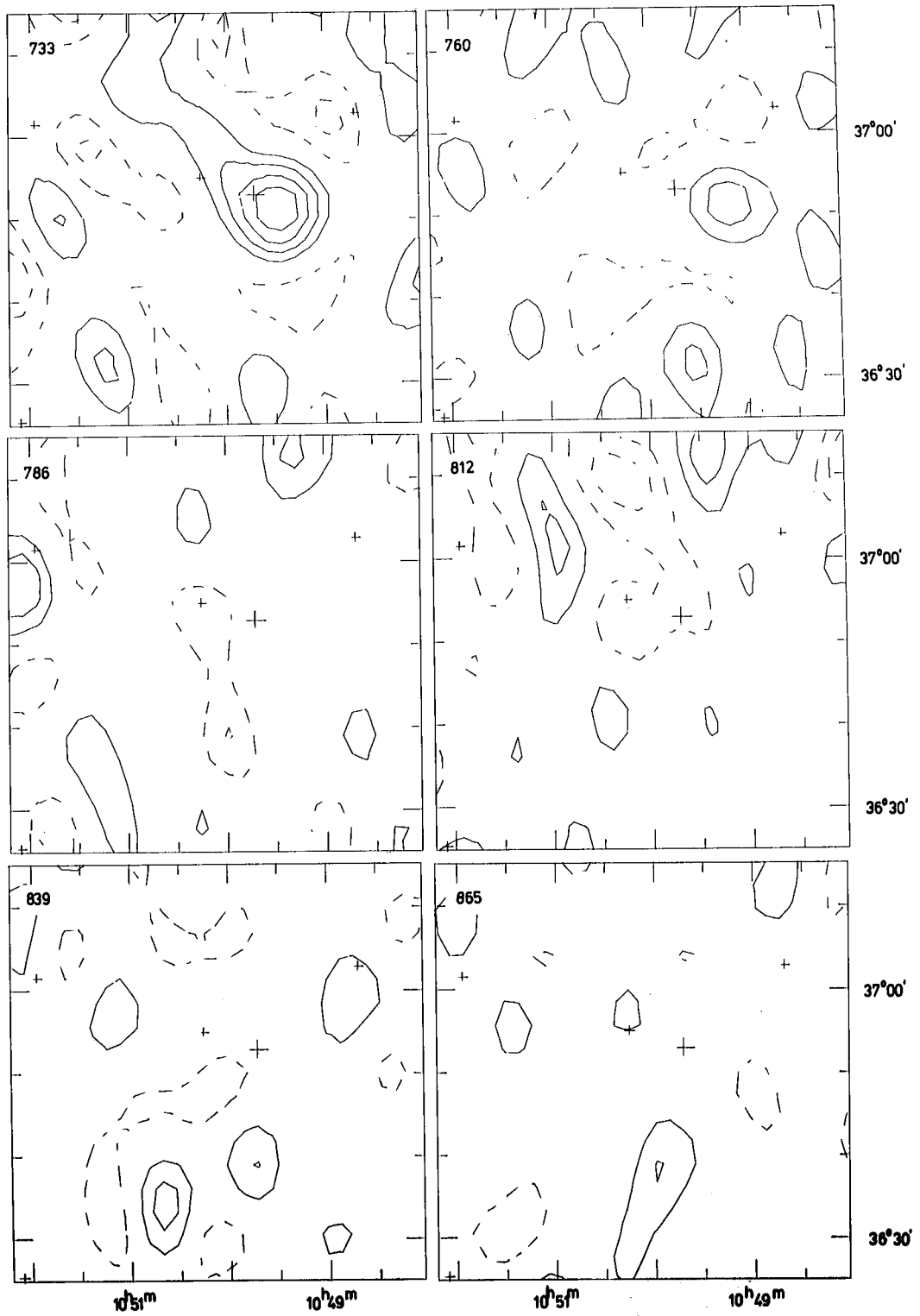


Figure 8.2 continued

3 RESULTS AND ANALYSIS

3.1 NGC 3310

3.1.1 RADIO CONTINUUM

At the resolution of these observations the continuum radiation in a 10-MHz bandwidth centred on 1417 MHz consists of two unresolved sources near NGC 3310. The first, of flux density 0.40 ± 0.01 Jy, lies exactly at the map centre, RA $10^{\text{h}}35^{\text{m}}39^{\text{s}}.0$ dec $53^{\circ}45'54''$ (Table 8.3). High-resolution observations (van der Kruit & de Bruyn 1976) confirm this flux density and reveal that the emission originates from the two spiral arms seen in H α light. The second source seen in the present observations is of flux density 0.10 ± 0.01 Jy, and is at RA $10^{\text{h}}36^{\text{m}}27^{\text{s}}$ dec $53^{\circ}55'16''$. A box is positioned at these coordinates on Plate 8.3 and encloses a possible identification with an elliptical galaxy near the plate limit (not visible on Plate 8.3).

3.1.2 INTEGRAL PARAMETERS

The integrated spectrum of NGC 3310 is displayed in Fig. 8.3, and was used to derive an estimate for the systemic velocity of 999 ± 10 km/s (Table 8.4), in good agreement with the optical value of 994 ± 7 km/s by RC2 but somewhat lower than the value of 1019 ± 3 km/s by van der Kruit (Table 8.1). By evaluating the area under the integrated spectrum, the total mass of hydrogen was estimated to be $(5.5 \pm 1.3) \times 10^9 M_{\odot}$ at the adopted distance of 20.5 Mpc (Table 8.1). This value agrees with the previous determinations (Table 8.4). The resultant M_{H}/L ratio is 0.20, typical of galaxies of type Sb or Sc and thus confirming the optical classification.

The total width of the line-profile is 211 ± 20 km/s. Using the formula given in Section 2.4(f) of Chapter 1 (which assumes circular rotation), and adopting values given in Tables 8.1 and

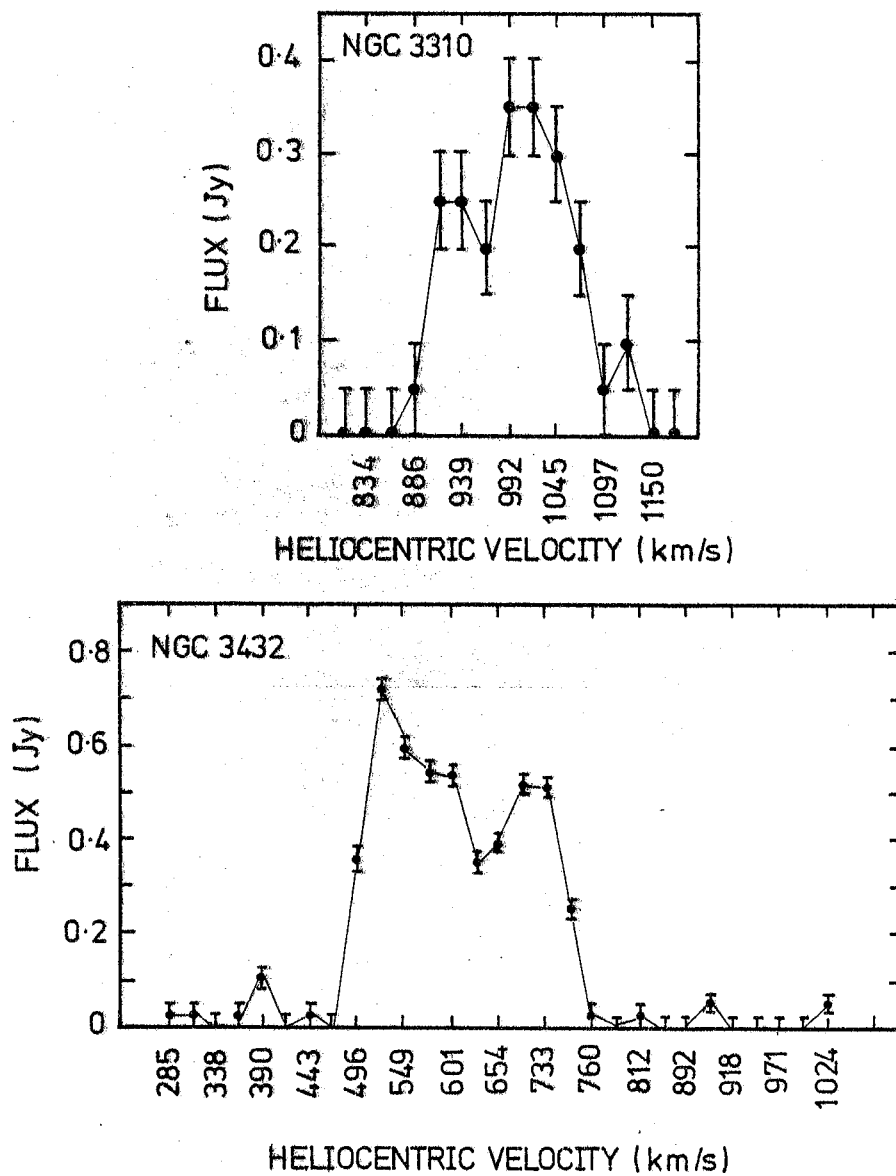


Figure 8.3 The integrated HI spectra for NGC 3310 and NGC 3432. The lines join the points but have no other significance.

Table 8.4 Integral Parameters for NGC 3310

<u>Parameter</u>	<u>Value</u>	<u>Source</u>
HI dimensions (taking into account convolution with the synthesised beam)		Plate 8.3 at PA 0°
major axis	4.4 arcmin	
minor axis	unresolved	
HI systemic velocity	999 ± 10 km/s	Fig. 8.3
Total width of HI line profile at 3σ level.	211 ± 20 km/s	Fig. 8.3
HI mass, M _H (∝D ²)	(5.5 ± 1.3) × 10 ⁹ M _⊙	Fig. 8.3
	9.1 × 10 ⁹ M _⊙	Balkowski 1973
	5.6 × 10 ⁹ M _⊙	Peterson & Shostak 1974
Total mass within 2 arcmin of nucleus, M _T (∝D)	~ 1.2 × 10 ¹¹ M _⊙	This table & Table 8.1
Luminosity, L (∝D ²)	2.69 × 10 ¹⁰ L _⊙	Table 8.1
M _H /L	0.20	this table
M _T /L	~ 4.4	this table
	4	Peterson & Shostak 1974
	~ 10	Balkowski 1973
M _H /M _T	0.05	this table

8.4, the total mass, M_T , was found to be of the order $10^{11} M_\odot$.

3.1.3 THE HI DISTRIBUTION

Significant emission (greater than 3σ) is seen on Fig. 8.1 in the channels between 913 and 1071 km/s. This is assumed to be associated with NGC 3310, since there is a systematic shift from NW to SE with increasing radial velocity. The isolated emission seen to the east of the nucleus at 992 and 1018 km/s is probably real, and joins smoothly with the brighter emission around the galaxy at 1045 and 1071 km/s. This feature will be termed the 'Eastern Extension'.

Plate 8.3 shows the map of integrated HI superimposed on a blue PSS photograph. The eastern extension is prominent, but no corresponding optical feature can be seen. The HI in the extension reaches 10 arcmin (or about 60 kpc) from the optical nucleus of NGC 3310, which is itself displaced 1.5 arcmin to the SW of the peak of HI emission. The bright emission surrounding the nucleus is resolved in declination and has an angular size of about 4 arcmin.

The velocity field of NGC 3310 is shown in Fig. 8.4. The maximum velocity gradient is at approximately PA 0° in the northern half of the galaxy and PA 140° in the south (cf. the optical PA of $172 \pm 4^\circ$ given in Table 8.2). The velocity contours clearly indicate a rotating disc, but the limited spatial resolution does not permit a more detailed analysis. The small irregularities displayed by some of the contours result from local enhancements of the HI column density (Fig. 8.1). As would be expected, there is no sign of the density waves apparent in the $H\alpha$ velocity field.

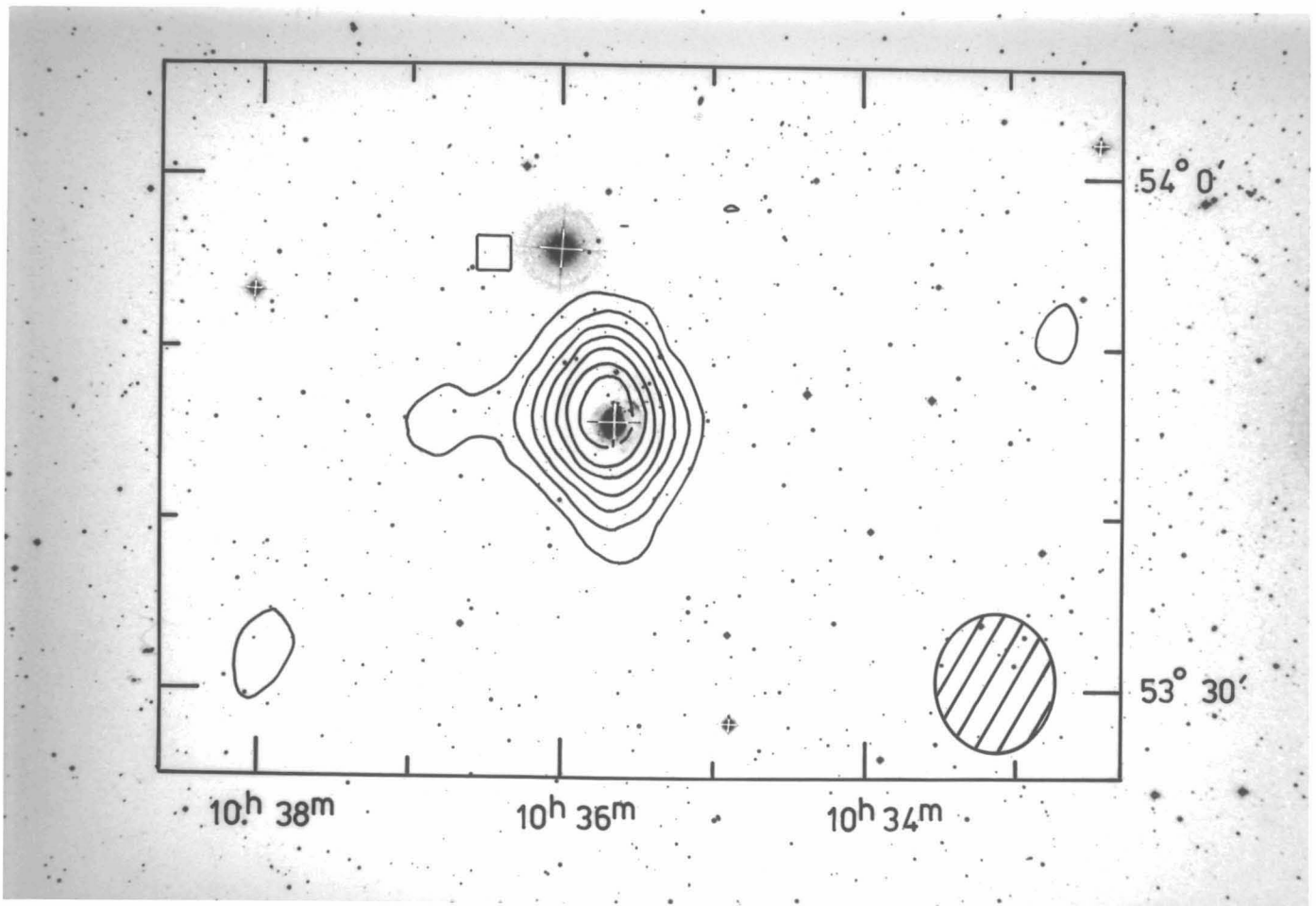


Plate 8.3 Map of integrated HI superimposed on a blue photograph of NGC 3310 (copyright by the National Geographic Society - Palomar Sky Survey, reproduced by permission from the Hale observatories). The integration was performed over the velocity range 860-1124 km/s and employed a gate of 60 mJy. The contours start at 20 K km/s and are at the same interval. The rms noise is typically ~ 6 K km/s. The large cross is the map centre and the smaller crosses are star positions used for alignment. The hatched ellipse represents the HPBW of 7.4×9.2 arcmin. No polar diagram correction has been applied. The box is centred at RA $10^{\text{h}}36^{\text{m}}27^{\text{s}}$ dec $53^{\circ}55'16''$, the position of a bright radio-continuum source (see text).

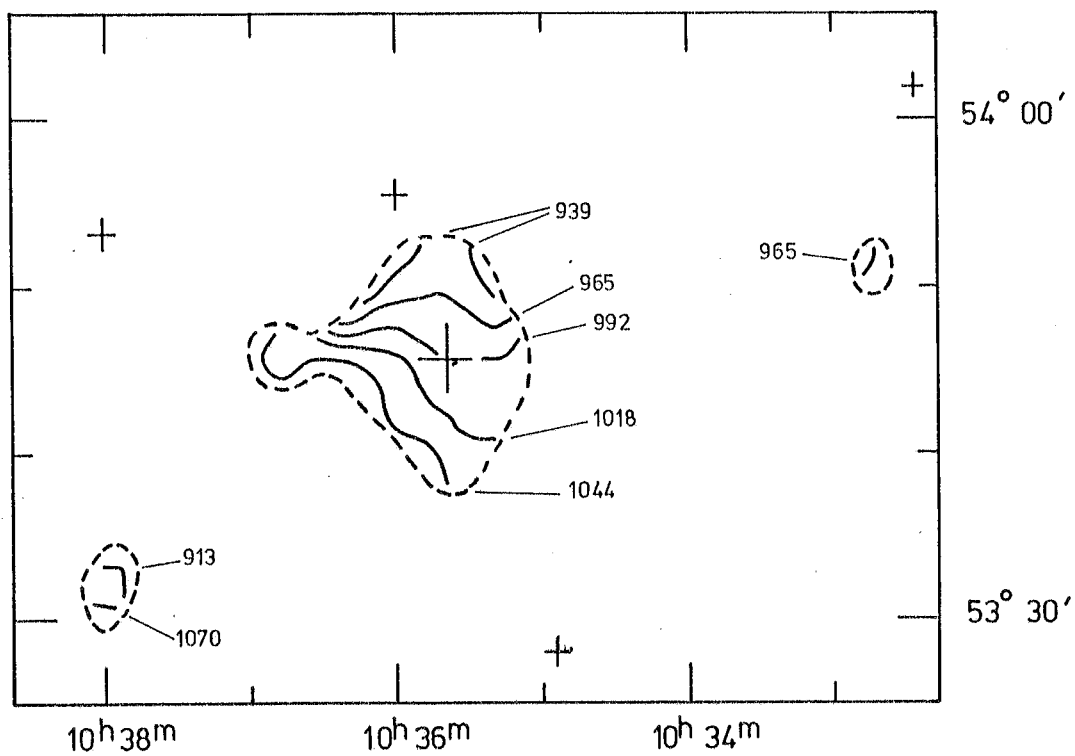


Figure 8.4 Velocity field of NGC 3310 corresponding to the integrated HI map of Plate 8.3

The isolated patch of emission seen at RA $10^{\text{h}}33^{\text{m}}$ dec $53^{\circ}50'$ in Plate 8.3 can be traced to emission at the 3σ level on the channels at 965 and 992 km/s (Fig. 8.1). The emission is probably real but no corresponding optical feature is evident. The isolated emission at RA $10^{\text{h}}38^{\text{m}}$ dec $53^{\circ}30'$ arises from a superposition of two separate 3σ peaks on the channels at 939 and 1071 km/s (Fig. 8.1). This is reflected in the large velocity gradient shown in Fig. 8.3, and the feature is probably not real, nor the $1.5\text{-}\sigma$ extension seen to the west of the bright emission on the 913 km/s channel (Fig. 8.1).

The three channel-maps at 1150-1203 km/s (Fig. 8.1) show an interesting feature located about 14 arcmin to the NW of the nucleus. This emission, almost certainly real, shifts systematically from SE to NW with increasing radial velocity. There is no corresponding optical emission, although the 'bow' (see the Introduction) points towards the HI emission. There is no evidence from the present observations that this HI emission is contiguous with the bright emission surrounding NGC 3310. Note that the velocity range incorporated in Plate 8.3 excludes this feature.

The eastern extension and isolated HI to the NW of the nucleus (noted above) are unexplained features which indicate some disturbance to the HI in the outer parts of NGC 3310. Van der Kruit & de Bruyn (1976) discussed tidal theories to explain the unusual optical properties of NGC 3310, but concluded that an interaction with either of the two nearest bright galaxies (NGC 3353 and 3448, which are both about $2^{\circ}.5$ away - the latter being the subject of Chapter 6) was unlikely. UGC 05734 is a disturbed SOa galaxy (14 mag) which lies 39 arcmin to the SW of NGC 3310, and UGC 05720 is a peculiar galaxy (13.2 mag) which lies 54 arcmin to the NW. Both galaxies are more likely candidates for an interaction.

3.2 NGC 3432

3.2.1 RADIO CONTINUUM

The radio-continuum emission at 1417 MHz within the area shown in Plate 8.4 consists of three bright sources. Firstly there is the emission from NGC 3432, with a peak coincident with the map centre (RA $10^{\text{h}}49^{\text{m}}43^{\text{s}}$ dec $36^{\circ}53'06''$). This source appears to be very slightly resolved towards the NW. The flux density on the broad-band map is 145 ± 10 mJy, but this includes the effects of line emission. A better estimate of the flux density, 115 ± 10 mJy, was derived from the map of 'average-continuum' radiation (Section 2).

The second and brightest source lies at RA $10^{\text{h}}51^{\text{m}}49^{\text{s}}_{+2}$ dec $36^{\circ}54'_{+1}$, as indicated by a box on Plate 8.4. The source is essentially unresolved in these observations, and has a flux density of 280 ± 10 mJy (after a polar diagram correction has been applied). One possible identification is a Seyfert-like galaxy seen at the southern end of the 1σ box.

The third source has a peak flux density of 112 ± 13 mJy (corrected for polar diagram) and lies at coordinates RA $10^{\text{h}}48^{\text{m}}51^{\text{s}}_{+2}$ dec $36^{\circ}31'_{+1}$. The source appears resolved, but this is probably due to the confusion of several distinct point sources. No obvious optical feature is coincident with this object.

The area surrounding NGC 3432 contains two other interesting objects: an edge-on spiral galaxy (UGC 6036 at RA $10^{\text{h}}53^{\text{m}}00^{\text{s}}$ dec $37^{\circ}07'$) and a peculiar galaxy (MCG+06-24-019 at RA $10^{\text{h}}47^{\text{m}}21^{\text{s}}$ dec $36^{\circ}37'$). Neither of these features is coincident with any of the continuum sources.

3.2.2 INTEGRAL PARAMETERS

The integrated spectrum of NGC 3432 is displayed in Fig. 8.3 and the systemic velocity derived from it is 606 ± 10 km/s. This value is in good agreement with the determination by Dickel & Rood 1978 (Table 8.5). By evaluating the area under the integrated spectrum, the total mass of hydrogen in NGC 3432 was estimated to be $(19 \pm 2) \times 10^8 M_{\odot}$ at the adopted distance of 7.9 Mpc. This value is 20 per cent larger than the previous determinations (Table 8.5), but is not inconsistent with them when allowance is made for the errors. The resulting M_H/L ratio is 0.53 ± 0.10 and suggests a galaxy of type Scd to Sm, confirming the optical classification.

The total width of the integrated spectrum was 264 ± 26 km/s (cf. 272 km/s by Dickel & Rood 1978). The total mass within 3 arcmin of the nucleus was computed in the same way as described for NGC 3310, and found to be $M_T \approx (30 \pm 10) \times 10^9 M_{\odot}$. The range of values of M_T in Table 8.5 reflects the different methods of calculation used.

3.2.3 THE HI DISTRIBUTION

Significant HI emission is seen on the channel maps (Fig. 8.2) between 496 and 760 km/s. The peak emission on each channel shifts from NE to SW with increasing radial velocity. Plate 8.4 shows the map of integrated HI superimposed on a blue PSS photograph. The peak of HI emission is nearly coincident (~ 0.5 arcmin to the NE) with the nucleus of NGC 3432, and the HI is distributed with an apparent major axis at PA $20 \pm 5^{\circ}$. After correcting for the convolution with the synthesised beam, the HI dimensions are 6.3×2.0 arcmin.

The HI shows an apparent extension (Plate 8.4) reaching 2

Table 8.5 Integral Parameters for NGC 3432

<u>Parameter</u>	<u>Value</u>	<u>Source</u>
PA of HI major axis	$20 \pm 5^\circ$	Plate 8.4
HI dimensions (taking into account convolution with the synthesised beam)		Plate 8.4 at PA 20°
major axis	6.3 arcmin	
minor axis	2.0 arcmin	
HI systemic velocity	606 ± 10 km/s 615	Fig. 8.3 Dickel & Rood 1978
Total width of the HI line profile at 3σ level	264 ± 26 km/s 272	Fig. 8.3 Dickel & Rood 1978
HI mass, M_H ($\propto D^2$)	$(19 \pm 2) \times 10^8 M_\odot$ $15 \times 10^8 M_\odot$ $16 \times 10^8 M_\odot$	Fig. 8.3 Dickel & Rood 1978* Balkowski 1973*
Total mass within 3 arcmin of nucleus, M_T ($\propto D$)	$(30 \pm 10) \times 10^9 M_\odot$ $112 \times 10^9 M_\odot$ $66 \times 10^9 M_\odot$	this table & Table 8.2 Dickel & Rood 1978* Balkowski 1973*
Luminosity, L ($\propto D^2$)	$(36 \pm 3) \times 10^8 L_\odot$	Table 8.2
M_H/L	0.53 ± 0.10 0.42 0.45	this table Dickel & Rood 1978* Balkowski 1973*
M_T/L	8 ± 3 31 13	this table Dickel & Rood 1978* Balkowski 1973*
M_H/M_T	0.063 0.013 0.036	this table Dickel & Rood 1978* Balkowski 1973*

*Corrected to a distance of 7.9 Mpc and, where applicable, using the luminosity given in Table 8.2.

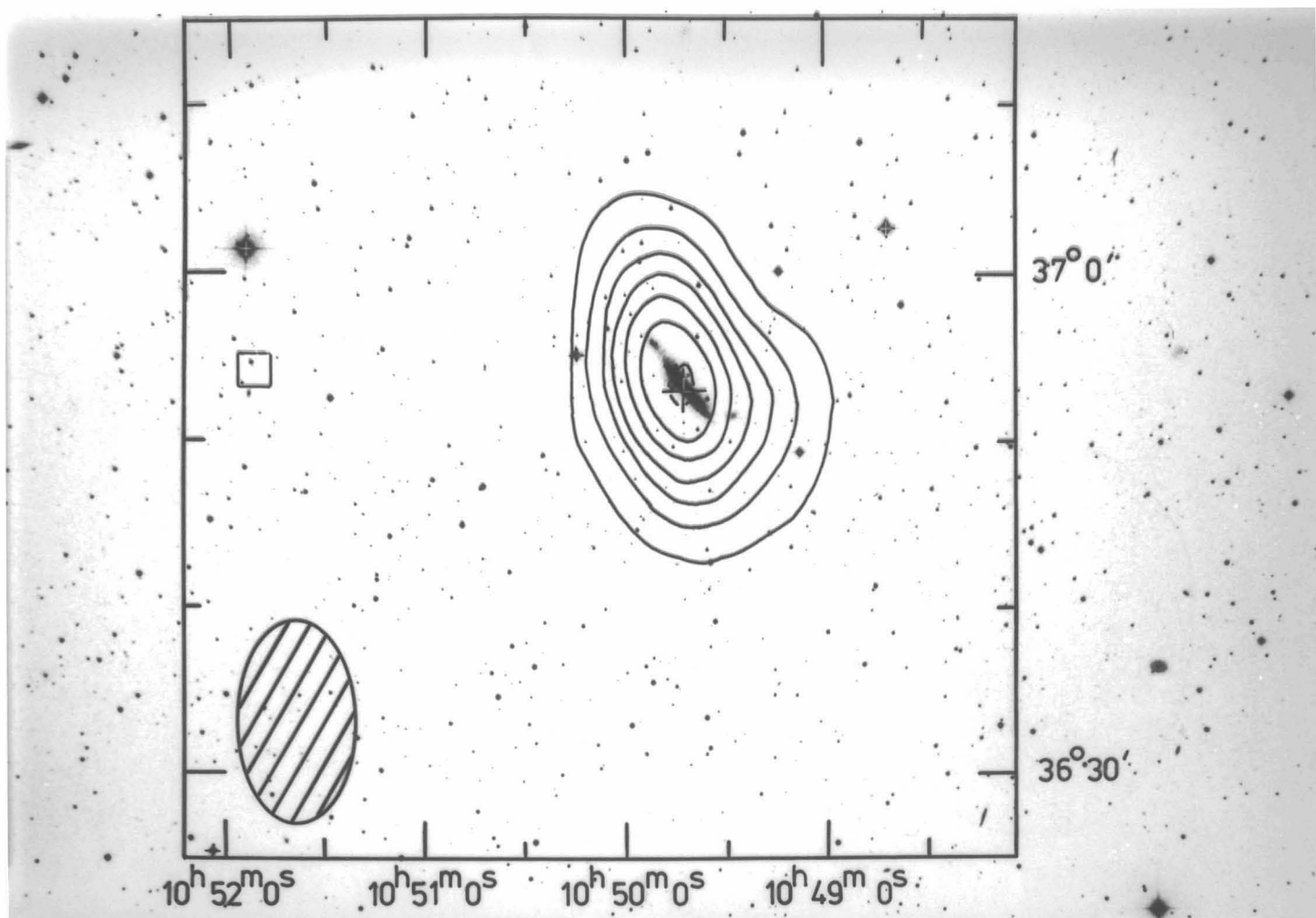


Plate 8.4 Integrated HI map of NGC 3432 superimposed on a blue photograph (copyright by the National Geographic Society-Palomar Sky Survey, and reproduced with permission from the Hale Observatories). The contours start at 20 K km/s and higher contours are at intervals of 40 K km/s. The rms noise level is typically about 4 K km/s. The large cross is the map centre and the smaller crosses are star positions used for alignment. The hatched ellipse represents the HPBW of 7.4 x 9.2 arcmin. No polar diagram correction has been applied. The box indicates the position of a bright radio continuum source (see text).

arcmin to the west of the dwarf companion (UGC 5983). Examination of Fig. 8.2 reveals a channel-to-channel shift of the peaks of HI emission in the velocity range 654-760 km/s, predominantly along an east-to-west line. This is at variance with the HI peaks at remaining velocities, which shift along a NE-SW line (approximately coincident with the optical major axis of NGC 3432).

It is difficult to determine from the present observations whether the feature noted above is a warp of the HI layer (e.g. similar to that seen in M33), or is due to HI around the dwarf companion UGC 5983. There is a large displacement (about 2.3 arcmin) between the peaks of HI emission on the channels at 628 km/s and 654 km/s, which suggests that the emission at velocities greater than and including 654 km/s may belong to a separate feature, in accordance with the latter theory. The peaks of HI emission at 654, 681 and 707 km/s lie very close to the position of UGC 5983 and so do not exclude this theory.

Fig. 8.5 shows the velocity field. As discussed above, the velocity gradient to the SW of the nucleus lies along an east-west line, whereas to the NE of the nucleus the gradient is more along the the optical major axis of NGC 3432. It is also apparent that the magnitude of the velocity gradient to the SW of the nucleus is approximately twice that in the NE.

The inverted velocity gradient seen at the extreme NE end of the major axis is an artefact. In fact these near-to-systemic velocities arise from very bright HI near the nucleus which has been spread outwards by the response of the synthesised beam. The phenomenon is enhanced by the extremely sharp cutoff in emission at velocities less than 496 km/s (Figs 8.2 and 8.3).

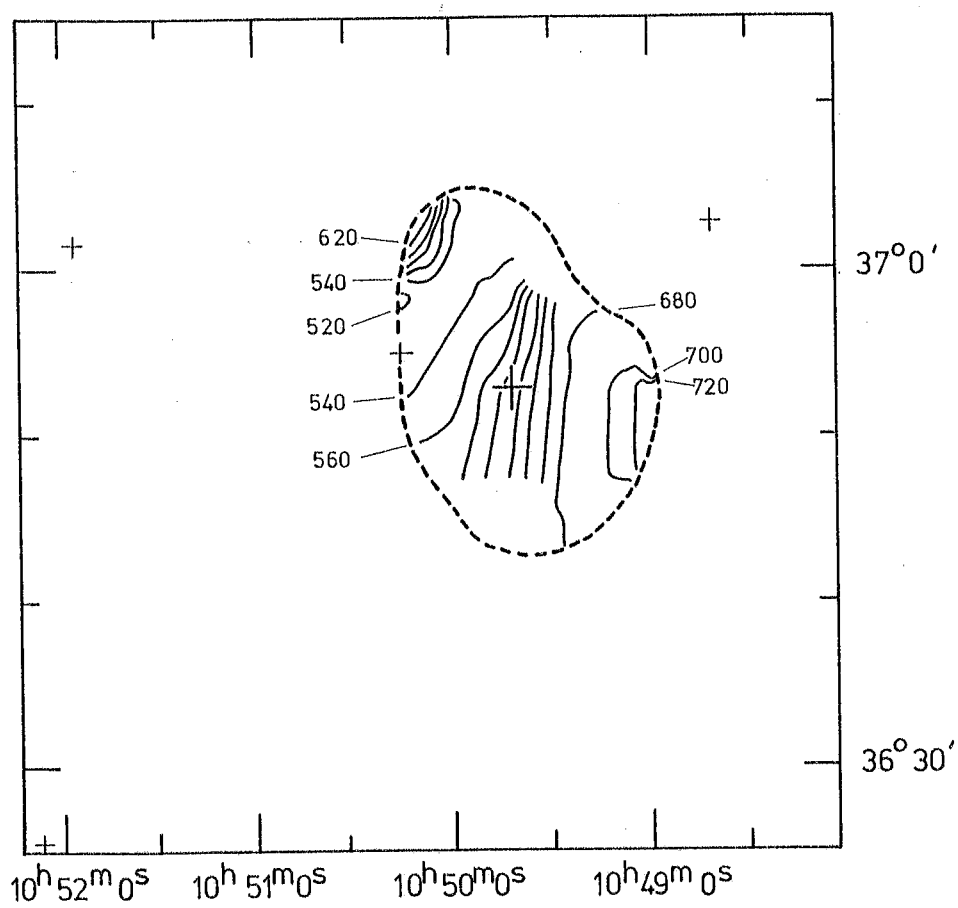


Figure 8.5 Velocity field of NGC 3432, corresponding to the integrated HI map of Plate 8.4.

Finally, the presence of a 3σ unresolved source about 13 arcmin to the SE of the nucleus on the channel at 390 km/s is noted (Fig. 8.2). The emission is nearly coincident with a very faint elliptical galaxy, but is probably not real since it appears on only one channel. For a similar reason, the $1.5\text{-}\sigma$ tails apparently emerging from the brighter emission of NGC 3432 at 496 and 733 km/s are also probably unreal.

3 CONCLUSIONS

In this chapter, radio-continuum and neutral-hydrogen observations of NGC 3310 and NGC 3432 have been presented. The spatial resolution was 7.4 arcmin in RA, and the velocity resolution was 32 km/s.

The HI in the outer parts of NGC 3310 appears to be disturbed, as witnessed by an extension reaching 10 arcmin to the east of the nucleus, and isolated emission 14 arcmin to the NW of the nucleus. No corresponding optical emission is seen, and it is likely that these disturbances have been caused by a gravitational interaction.

The HI surrounding the galaxy NGC 3432 is generally consistent with a rotating disc which is nearly edge-on. However, at the SW end of the major axis, the HI extends westward, away from the optical major axis, reaching 2 arcmin to the west of the dwarf companion UGC 5983. It is not clear from the present observations whether the HI in this feature is in rotation about NGC 3432 or forms a separate rotating system surrounding UGC 5983.

CHAPTER 9SUMMARY

This thesis has described hydrogen-line observations using the Cambridge Half-Mile telescope. This chapter is intended to summarize the main conclusions of this work.

Chapters 2 and 3 described observations of two nearby galaxies of late-spiral type, namely M33 and NGC 2403. The severe warping of the HI layer in the outer parts of M33 was clearly seen, and a revised geometry for the warp was presented. A gravitational interaction between M31 and M33 is a possible explanation for the large-scale distortions observed in M33.

Sensitive low-resolution maps revealed only a very slight warp in NGC 2403. Comparison of the magnitude of this warp with that in M33 was hampered by uncertainties in the distance of NGC 2403, and even more sensitive observations are required for a detailed study of the warping in NGC 2403. HI maps at a higher resolution allowed the dynamical parameters to be investigated, and confirmed the values of Shostak (1973). Several HI spiral features were seen, and these appear (as far as the limited resolution allowed) to be correlated with the optical spiral arms and HII regions. The velocity field showed several perturbations associated with the optical spiral arms, in qualitative agreement with the density-wave theory of spiral structure.

The remaining chapters described observations of irregular and peculiar galaxies. Chapter 4 described observations of a dwarf irregular galaxy, NGC 1569. This galaxy has been the subject of interest due to its prominent H α filaments, which previous

authors have thought to originate from an explosion in the nucleus. Observations revealed that the overall HI distribution was that expected of a disc in normal rotation, although several unusual features were noted. No correspondence was observed between the velocity fields of the HI and H α , the latter (de Vaucouleurs et al., 1974) being chaotic and displaying a general velocity gradient perpendicular to the major axis. The similarities between NGC 1569 and the well-studied galaxy M82 were noted, and it was suggested that many features of NGC 1569 are due to the galaxy having drifted into a tenuous cloud of dust and gas, as originally advocated by Solinger et al. (1977) for M82.

Irregular galaxies of class II (IrII) were the subject of particular interest in this thesis. In Chapter 5, a list of 46 galaxies alleged to belong to this class was presented, and as many optical and radio data as possible were collected and examined for unusual correlations and well-defined properties. Apart from their characteristic optical appearance (irregular morphology, presence of dust lanes, absence of stars or HII regions), the sample displayed few common properties. A tendency was noted for: (i) an earlier spectral type than normal for their colour; (ii) 'flat' spectral indices; (iii) a wide dispersion in M_H/L , but with a mean value similar to that of S0 galaxies. The tendency of the IrII sample to possess close companions was investigated statistically, in order to verify the hypothesis that all such galaxies have a tidal origin. No firm evidence was found for a greater tendency in the IrII sample than a control sample of Sc galaxies. A detailed study of individual objects is necessary, and for NGC 3448 and NGC 2814 this is pursued in Chapters 6 and 7, respectively.

Arp 205 consists of an IrII galaxy (NGC 3448) and a dwarf irregular companion (UGC 6016) less than one diameter away. Observations revealed HI in rotation about NGC 3448, HI rotating in almost the opposite sense about UGC 6016, plus emission to the west of NGC 3448 with a smaller recession velocity than it. A model was constructed for the HI dynamics which suggested that there had been a planar tidal interaction between these two galaxies.

NGC 2805, NGC 2814, NGC 2820 and IC 2458 form a compact group of galaxies of which NGC 2805 is the brightest. HI was detected in all except NGC 2814, and there is good evidence for a HI bridge linking NGC 2820 and IC 2458. It is postulated that the HI bridge and disturbed nature of this group are the result of a tidal interaction, in which either NGC 2814 or NGC 2805 passed within one galactic radii of a proto-NGC 2820 about 3 Gyr ago, in an approximately co-planar orbit. As a result the HI (originally surrounding NGC 2820) was drawn out to form a large tidal arm, in which IC 2458 is now embedded.

Thus two more IrII galaxies are likely to have been involved in gravitational interactions. It is becoming increasingly clear that gravitational interactions are the originators of many of the galaxies classified as IrII. Nevertheless, as a whole the IrII category exhibits such a diversity of properties that it is wise to treat the cases individually, rather than as members of a homogeneous class with the same mechanism of formation.

Finally in Chapter 8, observations of two optically peculiar galaxies, NGC 3310 and NGC 3432 were described. The HI in the outer parts of NGC 3310 appears to be disturbed, but no corresponding optical emission is seen. It was postulated that these disturbances were caused by a gravitational inter-

action. The HI surrounding the galaxy NGC 3432 is generally consistent with a rotating disc which is nearly edge-on. However, at the SW end of the major axis the HI extends westward towards the dwarf companion UGC 5983. Observations with higher spatial resolution are required to determine if this feature is HI in rotation about NGC 3432 or a separate rotating system surrounding UGC 5983.

APPENDIXCOMPUTER SIMULATIONS OF GRAVITATIONAL INTERACTIONS IN GALAXIES

This appendix is based on the work of Wright 1972. The galaxy to be simulated is taken in each case to be a point mass surrounded by test particles which can be considered as mass elements of a pressure-free gas. Initially, the test particles are distributed in a flat disc, each particle having a circular velocity appropriate to its particular radius. The intruder galaxy, represented as a point mass, is allowed to approach the main galaxy from a distance. Each test particle is considered to experience the attractive forces of the main and intruder galaxies (represented as point masses) and thus the equation of motion can be solved. The main galaxy is assumed to have a spherically-symmetric gravitational potential, which does not change with time (during which the galaxy may become distorted). This assumption is reasonable in all but the most violent interactions where the nucleus is disturbed. Self-gravitation effects are ignored.

In this idealized situation, the free parameters are:

- (1) The mass ratio, $u = \frac{(\text{mass of intruder galaxy})}{(\text{mass of main galaxy})}$.
- (2) The eccentricity of the intruder's orbit, e . If $e > 1$ then the orbit is hyperbolic, if $e = 1$ the orbit is parabolic, and if $e < 1$ then the orbit is elliptical (i.e. a bound orbit).
- (3) The perigalacticon distance, or distance of closest approach between the nucleus of the main galaxy and the point-mass intruder.
- (4) Two angles defining the orientation of the intruder's orbit relative to the disc of the main galaxy. The exact definitions are given in Wright (1972) and Toomre & Toomre (1972) but are

not included here since only co-planar (or approximately co-planar) orbits are employed in this thesis. There are two types of co-planar collisions: 'prograde' (or 'direct') and 'retrograde' (Fig. A.1).

(5) The viewing time, T . $T = 0$ corresponds to perigalacticon.

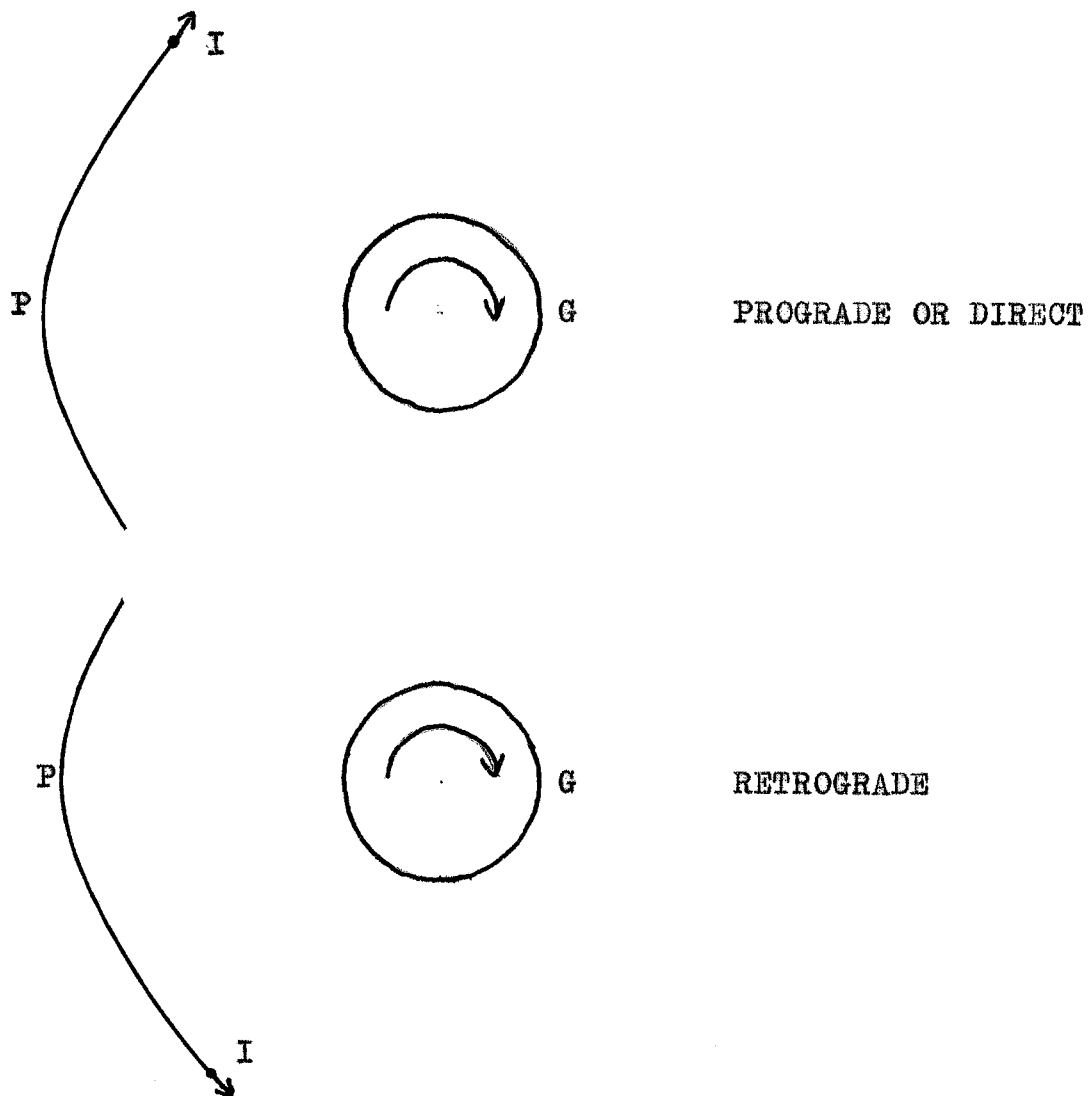


Figure A.1. The definition of prograde and retrograde collisions. 'I' indicates the intruder galaxy (arrow shows its velocity). 'G' is the disc of test particles (arrow shows sense of rotation). 'P' marks the perigalacticon.

Figs. A.2, A.3 and A.4 show examples of the simulations, and a summary of the discussion relevant to this thesis is reproduced below:

- (1) 'Tails' are normally produced whenever a galaxy suffers a direct, close approach from a similar, or smaller galaxy along a parabolic, or near parabolic orbit.
- (2) Tails are both easier to form and substantially more long-lived than 'bridges'.
- (3) Purely retrograde interactions do not produce either tails or bridges, although a small amount of inclination can produce such effects.
- (4) 'Overhead' encounters produce some evidence of both tails and bridges lying in the plane of the main galaxy, but these are both small and short-lived.
- (5) The production of tails is very sensitive to the perigalacticon distance of the perturbing body.
- (6) The amount of mass captured by the perturbing galaxy from the main galaxy is small, and even in the most favourable cases does not exceed a few percent of the total mass.
- (7) The amount of material which escapes completely from closely interacting systems is often a substantial fraction (10-20%) of each galaxy's initial mass.
- (8) In an interaction between two galaxies, one having a lower mass but being more compact, and the other having a greater mass but being more diffuse, the compact galaxy is much less susceptible to distortion.

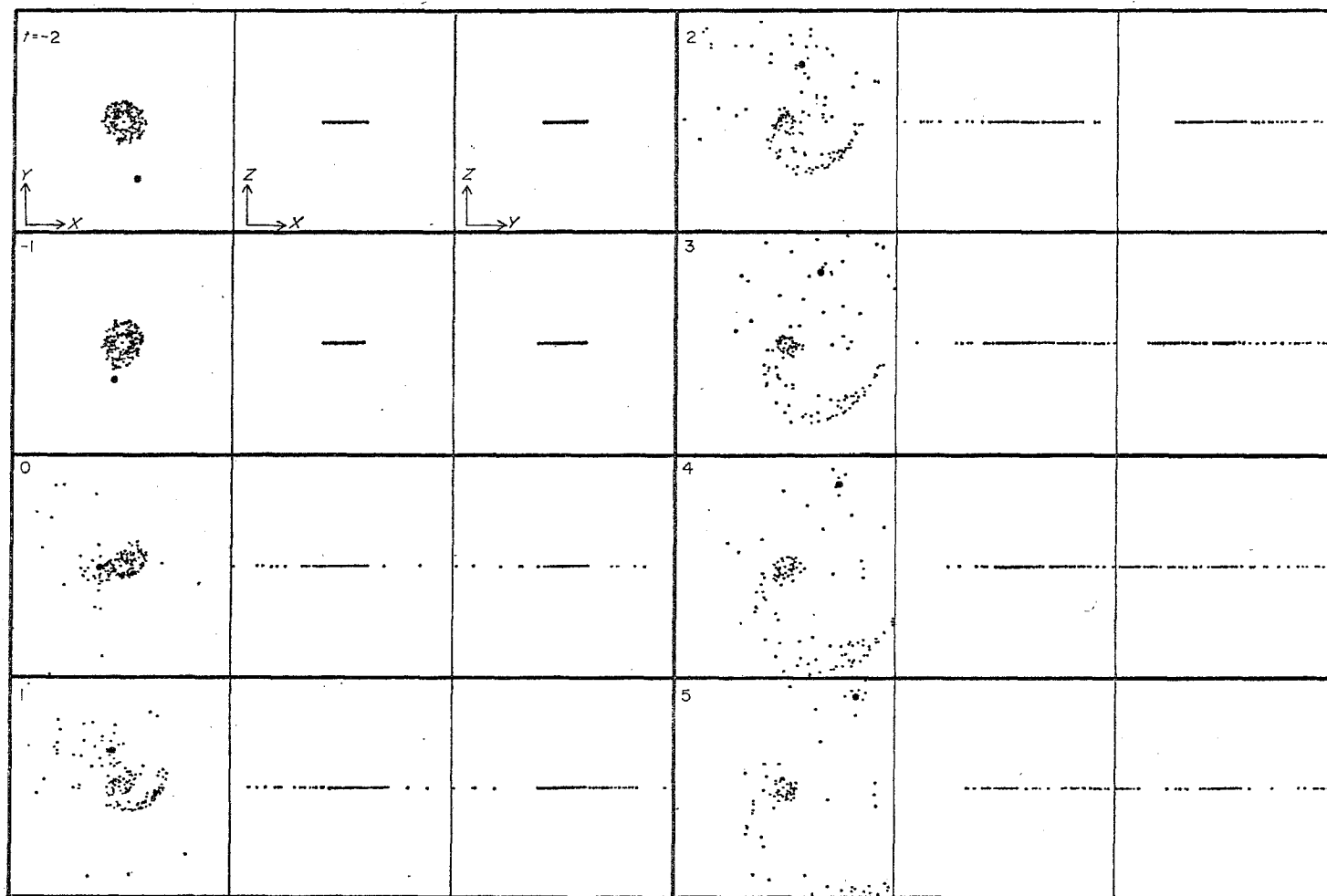


Figure A.2. A co-planar, direct collision with $u = 1$. The unit of time is $\frac{85}{94}$ Myr.

$$\sqrt{\frac{Q^3}{G(M_0 + M_1)}} \quad \text{with } Q = 20 \text{ kpc} \\ M_0 + M_1 = 2 \times 10^{11} M_\odot$$

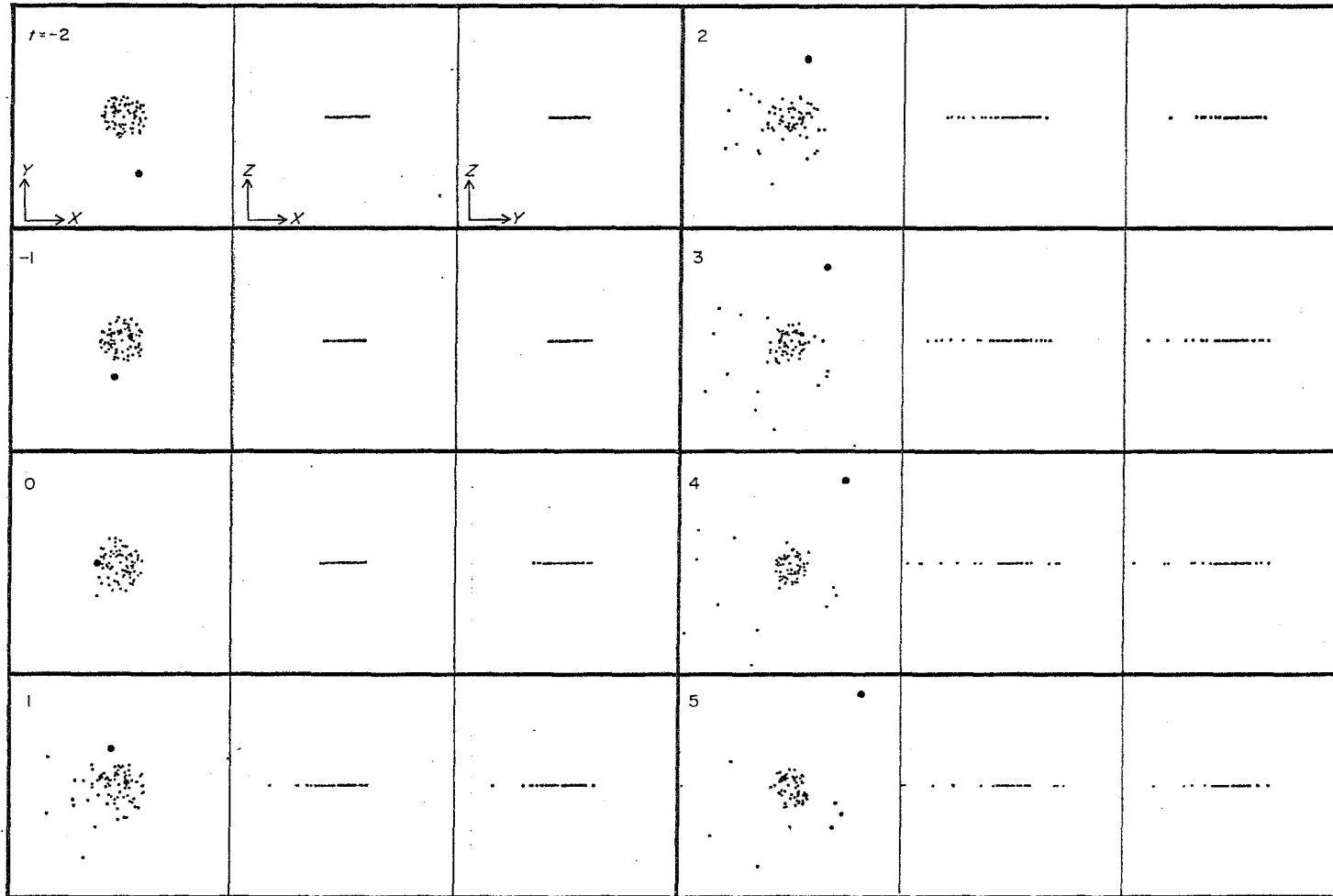


Figure A.3. A co-planar, retrograde collision with $u = 1$.

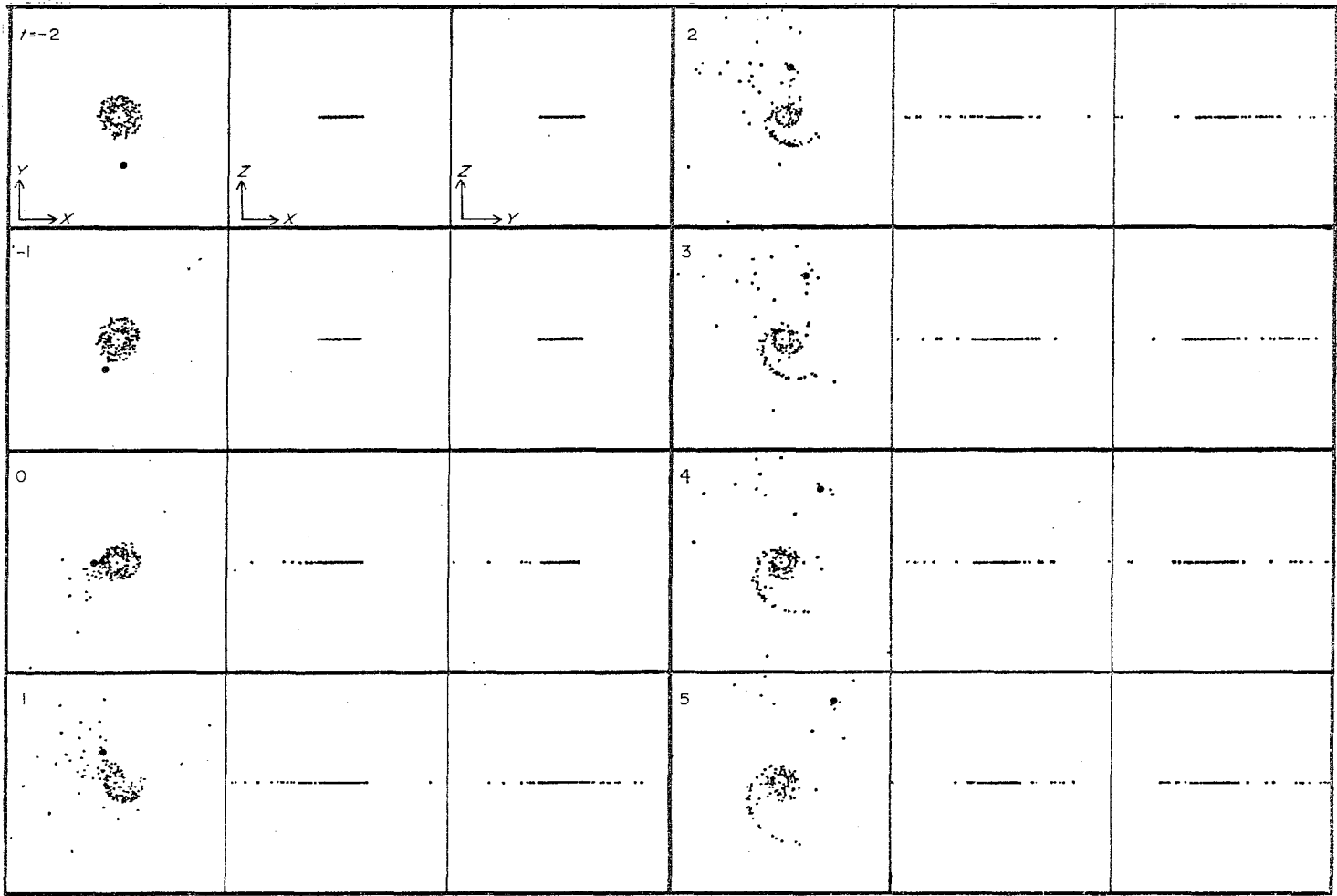


Figure A.4. A co-planar, direct collision with $u = \frac{1}{4}$. The unit of time is 130 Myr.

REFERENCES

- Ables, H.D., 1971. Publ. U.S. Naval Obs., XX, Part IV, 60.
- Allsopp, N.J.A., 1978. Mon. Not. R. astr. Soc., 184, 397.
- Andrillat, Y. & Collin-Souffrin, S., 1976. Astron. & Astrophys., 49, 251.
- Arp, H., 1966. Atlas of Peculiar Galaxies, California Institute of Technology, Pasadena, California.
- Baade, W., 1963. Evolution of Stars and Galaxies, page 73, ed. C. Payne-Gaposchkin, Harvard University Press, Cambridge, Massachusetts.
- Baldwin, J.E., 1978. Proc. IAU Symp. 77, Structure and Properties of Nearby Galaxies, D. Reidel, Dordrecht, Holland.
- Baldwin, J.E., Jennings, J.E., Shakeshaft, J.R., Warner, P.J., Wilson, D.M.A. & Wright, M.C.H., 1970. Mon. Not. R. astr. Soc., 150, 253.
- Baldwin, J.E., Field, C., Warner, P.J. & Wright, M.C.H., 1971. Mon. Not. R. astr. Soc., 154, 445.
- Balkowski, C., 1973. Astron. & Astrophys., 29, 43.
- Bertola, C., 1966. Contr. Obs. Ap. Asiago., no. 172.
- Bosma, A., 1978. PhD thesis, University of Groningen.
- Bottinelli, L., Chamaraux, P., Gouguenheim, L. & Lauqué, R., 1970. Astron. & Astrophys., 6, 453.
- Bottinelli, L., Duflot, R. & Gouguenheim, L., 1978. Astron. & Astrophys., 63, 363.
- Bottinelli, L. & Gouguenheim, L., 1974. Astron. & Astrophys., 33, 269.
- Burbidge, E.M., Burbidge, G.R. & Prendergast, K.H., 1959. Astrophys. J., 130, 739.
- Burke, B.F., 1957. Astron. J., 62, 90.
- Burke, B.F. & Miley, G.K., 1978. Astron. & Astrophys., 28, 379.
- Burns, W.R. & Roberts, M.S., 1971. Astrophys. J., 166, 265.
- Butslov, M.M., Kopylov, I.M., Nikonov, V.B., Severnyi, A.B. & Chuvayev, K.K., 1962. Soviet Astr. - AJ, 6, 244.
- Carnochan, D.J., Navach, C. & Wilson, R., 1975. Mon. Not. R. astr. Soc., 172, 27P.
- Chromey, F.R., 1973. Astron. & Astrophys., 29, 77.
- Chromey, F.R., 1974. Astron. & Astrophys., 37, 7.
- Clutton-Brock, M., 1972. Astrophys. Space Sci., 17, 292.
- Coombes, F., 1978. Astron. & Astrophys., 65, 47.
- Cooper, B.F.C., Epstein, E.E., Goldstein, S.J., Jolley, J.V. & Kaftan-Kassim, M.A., 1960. Astron. J., 65, 486.

- Corwin, H.G., 1970. Revised Classifications for 1200 Bright Galaxies, University of Texas, Publ. in Astron. No. 4.
- Cottrell, G.A.C., 1976. PhD thesis, University of Cambridge, England.
- Cottrell, G.A.C., 1978. Mon. Not. R. astr. Soc., 184, 259.
- Davies, R.D., 1975. Mon. Not. R. astr. Soc., 170, 45P.
- Dean, J.F. & Davies, R.D., 1975. Mon. Not. R. astr. Soc., 170, 503.
- Deharveng, J.M. & Pellet, A., 1970. Astron. & Astrophys., 7, 210.
- Demoulin, M.-H., 1969. Astrophys. J., 157, 69.
- de Vaucouleurs, G., 1959. Handbuch der Physik, 53, 275, Springer-Verlag, Berlin.
- de Vaucouleurs, G., 1961. Astrophys. J., 5, 233.
- de Vaucouleurs, G., 1975. Stars & Stellar systems, vol. IX, page 578. University of Chicago Press.
- de Vaucouleurs, G. & de Vaucouleurs, A., 1964 (RC1). Reference Catalog of Bright Galaxies, University of Texas Press, Austin.
- de Vaucouleurs, G., de Vaucouleurs, A. & Pence, W., 1974. Astrophys. J., 194, L119.
- de Vaucouleurs, G., de Vaucouleurs, A. & Corwin, H.G., 1976 (RC2). Second Reference Catalog of Bright Galaxies, University of Texas Press, Austin.
- Dickel, J.R. & Rood, H.J., 1978. Astrophys. J., 223, 391.
- Elsmore, B., Kenderdine, S. & Ryle, M., 1966. Mon. Not. R. astr. Soc., 134, 87.
- Elsmore, B. & Mackay, C.D., 1969. Mon. Not. R. astr. Soc., 146, 361.
- Eneev, T.M., Kozlov, N.N. & Sunyaev, R.A., 1973. Astron. & Astrophys., 22, 41.
- Freeman, K.C., 1975. Stars & Stellar Systems, vol. IX, page 409. University of Chicago Press.
- Gallagher, J.S., Faber, S.M. & Balick, B., 1975. Astrophys. J., 202, 7.
- Gordon, K.J., 1971. Astrophys. J., 169, 235.
- Grewing, M. & Mebold, U., 1975. Astron. & Astrophys., 42, 119.
- Guelin, M. & Weliachew, L., 1969. Astron. & Astrophys., 1, 10.
- Guibert, J., 1974. Astron. & Astrophys., 30, 353.
- Hamijima, K. & Tosa, M., 1975. Publ. Astron. Soc. Japan, 27, 561.
- Haschick, A.D. & Burke, B.F., 1975. Astrophys. J., 200, L137.

- Haynes, B.F., Huchtmeier, W.K.H., Siegmann, B.C. & Wright, A.E., 1975. A Compendium of Radio Measurements of Bright Galaxies, C.S.I.R.O., Melbourne.
- Haud, U. & Einasto, J., 1977. Astr. Circ. No. 958, 1977.
- Heidmann, J., Heidmann, N. & de Vaucouleurs, G., 1971. Mem. R. astr. Soc., 75, 85.
- Hodge, P.W., 1966. Astrophys. J., 146, 593.
- Hodge, P.W., 1969A. Astrophys. J., 155, 417.
- Hodge, P.W., 1969B. Astrophys. J., 157, 73.
- Hodge, P.W., 1974. Astrophys. J., 191, L21.
- Hodge, P.W., 1975. Astrophys. J., 202, 619.
- Holmberg, E., 1940. Astrophys. J., 92, 200.
- Holmberg, E., 1941. Astrophys. J., 94, 385.
- Holmberg, E., 1946. Meddn. Lunds. astr. Obs., Ser. II, No. 117.
- Holmberg, E., 1958. Meddn. Lunds. astr. Obs., Ser. II, No. 136.
- Huchtmeier, W.K., 1973. Astron. & Astrophys., 22, 91.
- Huchtmeier, W.K., 1975. Astron. & Astrophys., 45, 259.
- Huchtmeier, W.K. & Bohenstengel, H.D., 1975. Astron. & Astrophys., 74, 479.
- Hunter, C. & Toomre, A., 1969. Astrophys. J., 155, 747.
- Kahn, F.D. & Woltjer, L., 1959. Astrophys. J., 130, 712.
- Kellermann, K.I., Pauliny-Toth, I.I.K. & Williams, P.J.S., 1969. Astrophys. J., 157, 1.
- Kerr, F.J., 1957. Astron. J., 62, 93.
- Knapp, G.R., 1977. Astron. J., 82, 106.
- Krienker, O.K. & Hodge, P.W., 1974. Astron. J., 79, 1242.
- Lequeux, J., 1971. Astr. & Astrophys., 15, 30.
- Lewis, B.M. & Davies, R.D., 1973. Mon. Not. R. astr. Soc., 165, 213.
- Love, R., 1975. PhD thesis, University of Cambridge, England.
- Lin, C.C., Yuan, C. & Shu, F.H., 1969. Astrophys. J., 155, 721.
- Lynden-Bell, D., 1964. Mon. Not. R. astr. Soc., 129, 19.
- Lynds, C.R. & Sandage, A.R., 1963. Astrophys. J., 137, 1005.
- McCutcheon, W.H., 1972. Astron. J., 78, 18.
- McCutcheon, W.H. & Davies, R.D., 1970. Mon. Not. R. astr. Soc., 150, 357.
- Madore, B.F., 1976. Mon. Not. R. astr. Soc., 177, 157.
- Markarian, B.E., 1963. Soobs. Byurak. Obs., 34, 19.
- Markarian, B.E., 1969. Astrophys. (translation), 5, 206.
- Newton, K., 1978. PhD thesis, University of Cambridge, England.

- Newton, K. & Emerson, D.T., 1977. Mon. Not. R. astr. Soc., 181, 573.
- Nilson, P.N., 1973 (UGC). Uppsala General Catalogue of Galaxies, Uppsala Obs. Ann., vol. 6.
- Okamura, S., Takase, B. & Kodaira, K., 1977. Publ. Astron. Soc. Japan, 29, 567.
- Page, T.L., 1970. Astrophys. J., 159, 791.
- Pearson, T.J. & Warner, P.J., 1977. Users' Guide to the Radio-Astronomy Programs, MRAD Internal Report.
- Peterson, S.D. & Shostak, G.S., 1974. Astrophys. J., 79, 767.
- Reakes, M., 1979A. Mon. Not. R. astr. Soc., 187, 509.
- Reakes, M., 1979B. Mon. Not. R. astr. Soc., 187, 525.
- Reakes, M. & Newton K., 1978. Mon. Not. R. astr. Soc., 185, 277.
- Richer, H.B., Sharpless, S. & Olson, B.I., 1972. Astrophys. J., 171, 13.
- Roberts, M.S., 1962. Astron. J., 63, 437.
- Roberts, M.S., 1968 (Chapter 4). Stars & Stellar Systems, vol. IX, page 337. University of Chicago Press.
- Roberts, M.S., 1968 (Chapter 8). Astrophys. J., 73, 945.
- Roberts, M.S., 1969 (Chapter 1). Astrophys. J., 74, 859.
- Roberts, M.S., 1975. Stars & Stellar Systems, vol. IX, page 309. University of Chicago Press.
- Roberts, M.S. & Whitehurst, R.N., 1975. Astrophys. J., 201, 327.
- Roberts, W.W., 1969 (Chapter 3). Astrophys. J., 158, 123.
- Roberts, W.W., Roberts, M.S. & Shu, F.H., 1975. Astrophys. J., 196, 381.
- Rogstad, D.H., Lockhart, I.A. & Wright, M.C.H., 1974. Astrophys. J., 193, 309.
- Rogstad, D.H., Rougoor, G.W. & Whiteoak, J.B., 1967. Astrophys. J., 150, 9.
- Rogstad, D.H., Wright, M.C.H. & Lockhart, I.A., 1976. Astrophys. J., 204, 703.
- Rots, A.H. & Shane, W.W., 1975. Astron. & Astrophys., 45, 25.
- Sancisi, R., 1976. Astron. & Astrophys., 53, 159.
- Sandage, A., 1961. The Hubble Atlas of Galaxies, Carnegie Institute of Washington.
- Sandage, A., 1975. Stars & Stellar Systems, Vol. IX, page 1. University of Chicago Press.
- Sandage, A. & Tammann, G.A., 1974. Astrophys. J., 191, 603.
- Sandage, A. & Tammann, G.A., 1976. Astrophys. J., 210, 7.
- Seaquist, E.R. & Bignell, R.C., 1976. Astron. & Astrophys., 48, 421.

- Seaquist, E.R. & Bignell, R.C., 1977. Astron. & Astrophys., 55, 163.
- Searle, L., 1971. Astrophys. J., 168, 327.
- Seielstad, G.A. & Whiteoak, J.B., 1965. Astrophys. J., 142, 616.
- Shostak, G.S., 1973. Astron. & Astrophys., 24, 411.
- Shostak, G.S. & Rogstad, D.H., 1973. Astron. & Astrophys., 24, 405.
- Siegel, F., 1956. Non-Parametric Statistics for the Behavioural Sciences, McGraw-Hill.
- Solinger, A., Morrison, P. & Markert, T., 1977. Astrophys. J., 211, 701.
- Sulentic, J.W., 1976. Astrophys. J. Suppl. Ser., 32, No. 2.
- Tammann, G.A. & Sandage, A., 1968. Astrophys. J., 151, 825.
- Toomre, A. & Toomre, J., 1972. Astrophys. J., 178, 623.
- Tovmasyan, G.M., 1967. Astrofizika, Vol. 3, 427.
- Tully, R.B., Bottinelli, L., Fisher, J.R., Gouguenheim, L., Sancisi, R. & van Woerden, H., 1977. Astron. & Astrophys., 63, 31.
- van der Hulst, J.M., 1977. PhD thesis, University of Groningen.
- van der Kruit, P.C., 1973 (Chapter 3). Astron. & Astrophys., 29, 231.
- van der Kruit, P.C., 1973 (Chapter 8). Astron. & Astrophys., 29, 249.
- van der Kruit, P.C., 1976. Astron. & Astrophys., 49, 161.
- van der Kruit, P.C. & de Bruyn, A.G., 1976. Astron. & Astrophys., 48, 373.
- Véron, P. & Sauvayre, A., 1965. Ann. Astrophys., 28, 698.
- vershuur, G. 1973. Astr. Astrophys. 22, 139.
- Vorontsov-Vel'yaminov, B.A., 1959. Atlas of Interacting Galaxies, Moscow.
- Voronstov-Vel'yaminov, B.A., 1961. Problems of Extragalactic Research, IAU Symp. no. 15 (Editor G.C. McVittie), page 194.
- Vorontsov-Vel'yaminov, B.A. et al., 1962-1974 (MCG). Morphological Catalogue of Galaxies, Sternberg Institute, Moscow.
- Walker, M.F. & Chincarini, G., 1967. Astrophys. J., 147, 416.
- Warner, P.J., Wright, M.C.H. & Baldwin, J.E., 1973. Mon. Not. R. astr. Soc., 163, 163.
- Weaver, H. & Williams, D.R.W., 1973. Astron. & Astrophys. Suppl. Series., 8, 1.
- Weliachew, L., Sancisi, R. & Guelin, M., 1978. Astron. & Astrophys., 65, 37.

- Winter, A.J.B., 1975. PhD thesis, University of Cambridge, England.
- Wright, A.E., 1972. Mon. Not. R. astr. Soc., 157, 309.
- Wright, A.E., 1974. Mon. Not. R. astr. Soc., 167, 251.
- Wright, M.C.H., Warner, P.J. & Baldwin, J.E., 1972. Mon. Not. R. astr. Soc., 155, 337.
- Zwicky, F., 1953. Phys. Today, 6, No. 4, 7.
- Zwicky, F., 1956. Ergebnisse der Exakten Naturwissenschaften, 29, 344.
- Zwicky, F., 1971. Catalogue of selected Compact Galaxies and of Post-Eruptive Galaxies, Speich, Zurich.
- Zwicky, F. et al., 1960-1968 (CGCG). Catalog of Galaxies and Clusters of Galaxies, Vols 1-6. California Institute of Technology, Pasadena.